Challenges and potential of 7T (f)MRI for investigating attention and perception

Doctoral thesis

CHALLENGES AND POTENTIAL OF 7T (F)MRI FOR INVESTIGATING ATTENTION AND PERCEPTION

Yawen Wang

2023

ISBN	978-94-6469-380-5
Printed by	ProefschriftMaken || www.proefschriftmaken.nl
Layout by	ProefschriftMaken || Yawen Wang
Cover design by	ProefschriftMaken || Yawen Wang

CHALLENGES AND POTENTIAL OF 7T (F)MRI FOR INVESTIGATING ATTENTION AND PERCEPTION

Dissertation

To obtain the degree of Doctor at Maastricht University,
on the authority of the Rector Magnificus, Prof. dr. Pamela Habibović,
in accordance with the decision of the Board of Deans,
to be defended in public
on Wednesday 28th of June 2023, at 16.00 hours

by

Yawen Wang

Supervisor
Prof. Dr. Peter De Weerd

Co-supervisors
Dr. Mark J. Roberts
Dr. Sriranga Kashyap, University Health Network

Assessment Committee
Prof. Dr. Federico de Martino (Chair)
Prof. Dr. Kâmil Uludağ (University of Toronto, Canada)
Prof. Dr. Floris de Lange (Radboud University, The Netherlands)
Dr. Vincent van de Ven

The research presented in this thesis was conducted at Maastricht University and supported by Maastricht University, Maastricht Brain Imaging center and China Scholarship Council.

Contents

1

General Introduction

1.1 Overview

The work presented in this thesis emanated from two research goals. The first research goal focused on the function of the Nucleus Basalis of Meynert (nbM) in attention. To that aim, we wanted to investigate the potential of ultra-high field magnetic resonance imaging (MRI) in making volumetric and functional measures of this small open subcortical structure. In addition, we aimed to map separate functional domains in this nucleus associated with visual and auditory attention using functional MRI at 7 Tesla (7T). The second research goal of this thesis was the use of functional 7T MRI to elucidate the role of early visual cortex in surface perception. This research goal was inspired by the hypothesised differential involvement of different cortical layers in feedforward and feedback processes during the perception of surfaces. Both projects tested the limits of current technology to answer fundamental and long-standing questions in modern neuroscience. The current chapter will elaborate on the scientific rationale and background for both of these research projects and on the methods we used to investigate these questions.

Perception and attention are elements of the mind. It is a Buddhist belief that ‘All phenomena are mind by nature’. Philosophy of mind is the philosophical study of the nature of the mind, mental events, mental functions, mental properties, and consciousness, and of the nature of their relationship with the physical body. Thus, a key question is: what is the mind? In the domain of cognitive neuroscience, researchers link measures of brain activity to operations of the mind to understand how the brain enables the mind (Gazzaniga and Rakoff 2010; Teller 1984). Single neuron recording, optogenetics, light microscopy, electroencephalography (EEG), magnetoencephalography (MEG) and functional magnetic resonance imaging (fMRI) all constitute imaging techniques that provide unique and powerful information that contribute towards understanding cognition (Sejnowski et al. 2014). Confucius says, “the mechanic who wishes to do his work well, must first sharpen his tools” . Over the last decades, fMRI has been widely used in the field of

cognitive neuroscience, due to its noninvasive nature, ever-increasing availability, relatively high spatiotemporal resolution, and its capacity to demonstrate the entire network of brain areas engaged when subjects undertake particular tasks (Logothetis 2008). Advances in scanner technology, image acquisition protocols, experimental design, and analysis methods push forward fMRI from mere cartography to the true study of brain organisation (Logothetis 2008). The present thesis reports on our research efforts, and in Confucius' terms, it also considers how we could sharpen our tools further to provide better answers in the future to the scientific questions asked in the present thesis.

1.2 Ultra-high field (f)MRI: new opportunities

1.2.1 The nuclear magnetic resonance phenomenon

The principle of MRI can be explained by quantum physics. In classical physics, a rotating object possesses a property known as angular momentum. Atomic and subatomic particles possess an angular momentum known as spin or spin angular momentum. Only nuclei with non-zero spins ($I \neq 0$) can absorb and emit electromagnetic radiation and undergo resonance when placed in a magnetic field (Atta-Ur-Rahman 2012). Hydrogen, for which it is the case that $I = \frac{1}{2}$, makes up around 10% of the human body mass and exists mainly in water and fat. It has properties that make it very useful in (f)MRI. The 1H nucleus has two spin states, which are commonly denoted as $|+\frac{1}{2}>$ and $|-\frac{1}{2}>$ and are often referred to as 'parallel/spin-up' and 'anti-parallel/spin-down' respectively (Levitt 2013).

In the absence of an external magnetic field, these hydrogen proton spin in the body with their axis randomly aligned and those two spin states are not observable. When the body is placed in a strong magnetic field (B_0), the two spin states split up. In the parallel state, the detected component of nuclear angular momentum is in the same direction as B_0. In the anti-parallel state, it is in the opposite direction. Since the lower energy state for a nuclear spin in B_0 is spin-up/parallel, an

energy gap is generated. The amount of the energy gap depends on the Larmor frequency and strength of the external magnetic field. In practice, we focus on the aggregate of protons from millions to billions. The average of summation of magnetic properties from all protons is net magnetization (M). At equilibrium, M/M_0 precess in the direction of B_0. The direction of the B_0 field is commonly designated as the z-axis. Correspondingly, M is considered to have both longitudinal (M_Z) and transverse components (M_{XY}).

When a radio frequency (RF, B_1) with the same Larmor frequency is applied to the B_0, it excites protons from parallel (low energy) to anti-parallel (high-energy) alignment and causes protons/M to precess away from the initial alignment with B_0. After switching off the B_1, due to the interaction of individual spins with each other and with their environment, M returns to its initial alignment, parallel to B_0. To do this, protons have to release their energy to the environment in a process called relaxation. The MR signal is the small electrical current induced in the receiver coil by the precession of the M during the relaxation. T_1/longitudinal relaxation is the process of M returning to its initial maximal value (M_0) parallel to B_0. T_1 can be viewed as the time required for the M_Z to reach $(1 - \frac{1}{e})$ or about 63% of M_0. T_2/transverse relaxation is the process by which M_{XY} decays or dephases. T_2 is the time required for the M_{XY} to fall to approximately 37% ($\frac{1}{e}$) of its initial value as predicted by natural atomic and molecular mechanisms. However, in practice, the T_2 decay rate is much faster than theoretically predicted, due to the inhomogeneities of B_0. This much faster than expected decay rate is denoted T_2^* ($T_2 + T_2'$). The inducted MR signal increases as the M precesses around the z-axis. But signal in the transverse plane decays as a style of T_2^* at the same time, namely, free induction decay (FID). To reduce the effect of FID, gradient echo technique and spin echo technique are applied after applying an RF pulse. A gradient-echo is created when the frequency-encoding positive gradient counterbalances the initial negative gradient, the signal relaxes with T_2^*. A spin-echo is created by using an additional 180° RF pulse at half echo time to refocus the dephasing signal so it relaxes at a rate

comparable to T_2 (Uludağ et al. 2005).

1.2.2 High-resolution imaging at UHF

Higher sensitivity

The increase in main magnetic field strength (B_0) has been one of the most fundamental developments in the field of MRI (Dumoulin et al. 2018). Increased field strength leads to increased signal to noise ratio (SNR), which can be traded for increased spatial resolution or for advancements of other aspects of MRI measurement. At UHF, SNR variation in the main magnetic field strength becomes a complex function of size and shape of the head, tissue composition and position within the head (Ladd et al. 2018). Generally, most estimations predict a more than linear increase in SNR above 3T (Ladd et al. 2018). It has been shown that the SNR increases roughly in proportion to a power factor B_0^x, where x is approximately 1.2 near the surface and 2.1 near the centre of the head (Guérin et al. 2017). Additionally, the SNR increase is influenced by the acceleration factor in parallel imaging. The advantage of higher field strength is greater with higher acceleration factors (Guérin et al. 2017). Elevated SNR can be beneficial to multiple aspects of MRI including reducing scanning time. However, the most common use of the benefits of higher field strength is to achieve higher spatial resolution (Polimeni et al. 2018). For example, at 7T, an in vivo T_1-weighted whole brain MRI dataset can be acquired at resolution of 250 μm isotropic (Lüsebrink et al. 2017).

Higher specificity and MR contrast

Contrast-to-noise ratio (CNR) is defined as the difference in signal distribution across tissues, divided by the background noise. It is a measure of image quality. By moving to UHF, the image contrast can be enhanced in many applications, including techniques used for anatomical and functional imaging and spectroscopic techniques. The advantages of increased field strength for image contrast result from the signifi-

cant changes in relaxation time constants (Longer T_1; Shorter: T_2 and T_2^*) and in spectral and spatial frequency contrast (Enhanced) due to chemical shift and magnetic susceptibility effects (Duyn 2012).

The MR properties that are enhanced by higher field strength can give crucial information about the local microstructure, especially cell membrane, myelin and iron (Möller et al. 2019; Stüber et al. 2014). Myelin is diamagnetic due to its phospholipid layers (Lonsdale and Bragg 1939). Water protons frequently interact with non-aqueous components between the adjacent myelin membrane layers, thereby accelerating longitudinal and transverse relaxation and inducing magnetic transfer between water and macromolecular protons (Sled 2018). Myelin has been estimated using T_1 (Bock et al. 2013; Lutti et al. 2014), R_2^* and R_2 (Reciprocal of T_2^* and T_2) (Alonso-Ortiz et al. 2018; Du et al. 2007; Prasloski et al. 2012) and magnetic transfer contrast (Schmierer et al. 2007). Iron is paramagnetic and a major contributor to the T_2 and T_2^* relaxation and magnetic susceptibility of brain tissue (Drayer et al. 1986). But it also plays a role in the generation of T_1 contrast (Rooney et al. 2007). Through the use of UHF, the MR contrast among tissues with different microstructure is enhanced. Together with high resolution acquisition, UHF MRI facilitates the visualisation of finer structures, for example improving segregation of lesions from surrounding tissues (Verma and Balchandani 2019). These improvements have further promoted more accurate segmentation and volumetric measurement of smaller structures such as hippocampus (Thomas et al. 2008; Wisse et al. 2012; Wisse et al. 2016) and the nuclei of the amygdala (Solano-Castiella et al. 2011).

Ex vivo MRI of human postmortem brain

Ex vivo MRI is the MRI measurement closest to histology. It has been validated against histology techniques applied in situ to the same sample and so forms a stepping stone to investigate MRI contrast. The comparison between MRI and histology is essential to investigate the necessary resolutions to translate ex vivo MRI observations and histological ob-

servations to in vivo UHF MRI (Sengupta et al. 2018). Compared to in vivo MRI, postmortem ex vivo MRI offers pronounced advantages for visualising the microstructural neuroanatomy of the human brain (Edlow et al. 2019). Unlike in vivo MRI acquisitions, ex vivo MRI can be performed with long scanning time (e.g. ~days) and it is free from cardiorespiratory and head-motion effects on the data. These advantages are crucial for identifying subcortical nuclei and cortical layers at microscale, which are difficult to visualise even in the highest-resolution in vivo MRI datasets (Edlow et al. 2019). Many ex vivo MRI datasets at UHF have high spatial resolution (such as 60 μm isotropic from Sengupta et al. (2018); 100 μm isotropic from Amunts et al. (2013), Edlow et al. (2019), and Iglesias et al. (2015); 200 μm from Ding et al. (2016) and Sengupta et al. (2018)) and have revealed detailed neuroanatomy. The detailed structural information from ex vivo MRI can guide in vivo parcellations and segmentations (Ding et al. 2016; Finn et al. 2021; Iglesias et al. 2015; Wisse et al. 2017). Accurate segmentation is essential for the visualisation and measurement of anatomical structures and the quantification of changes in brain structures (Akkus et al. 2017) associated with e.g. disease or ageing. While very high resolution ex vivo datasets have their advantages, ex vivo MRI datasets acquired at conventional field strength (1.5 T, and 3T) with relatively low resolution (such as 1 mm isotropic) and validated against histology (Kilimann et al. 2014; Teipel et al. 2005; Zaborszky et al. 2008) are also advantageous. Probabilistic atlases based on these histology-validated ex vivo MRI datasets (e.g. Zaborszky et al. (2008)), are used to guide the segmentation of subcortical or other hard-to-image structures required to interpret low-resolution in vivo functional and structural MRI data (Fernández-Cabello et al. 2020; Gang et al. 2020; Markello et al. 2018; Schulz et al. 2018; Yuan et al. 2019).

Visualisation of human subcortical structures at UHF

To fully comprehend how cognition is implemented in the brain, it is necessary to investigate the full network of structures that may be functionally involved (Keuken et al. 2018). Subcortical structures play an

important role in cognitive functions, and structural and functional deformity in these structures have been associated with various psychiatric disorders (Koshiyama et al. 2018). Compared to the cortex, the subcortex is about five times smaller but contains a large number of small and unique structures. Studying these structures is complicated, not only by their small size, but also because their locations vary significantly among individuals (Keuken et al. 2018). Additionally, the SNR in the middle of the brain is low because it is further away from the modern head coils (de Hollander et al. 2017; Wiggins et al. 2009). The low SNR challenges involved in imaging subcortical structures point to the potential of UHF MRI for advancing subcortical imaging research. At UHF, g-factor penalties in the middle of the brain are lower than at conventional field strength, which means a higher acceleration factor can be applied during acquisition with less SNR loss (Wen et al. 2015). UHF imaging is essential to visualise the subcortex, because it permits the localisation and parcellation of subcortical structures at an individual level in vivo (Keuken et al. 2018).

Significant progress has been made in visualising subcortical structures using 7T scanners. Using optimised T_1-weighted sequences acquired at submillimetre resolution (in plane), researchers have been able to visualise the thalamic subnuclei (Aldusary et al. 2019; Kanowski et al. 2014; Saranathan et al. 2015; Tourdias et al. 2014). For example, using high resolution T_2^*-weighted acquisition (0.5 mm isotropic), in vivo data from Forstmann et al. (2017) visualised the boundary between the substantia nigra and the globus pallidus. Moreover, they were able to separate these iron rich structures (globus pallidus interna and externa) thanks to the enhanced T_2^* contrast at 7T. In another example, by acquiring 0.7 mm isotropic T_2-weighted images at 7T, Wisse et al. (2012) and Wisse et al. (2016) achieved a higher accuracy for segmentation and volumetric measurement of hippocampal subfields. Finally, diffusion data acquired at 7T (Sitek et al. 2019) permitted the structural connectivity maps of subcortical auditory pathways in humans.

1.2.3 Functional magnetic resonance imaging (fMRI)

fMRI emerged from two crucial discoveries. Firstly, Pauling and Coryell (1936) discovered that haemoglobin possesses magnetic properties. Haemoglobin is the iron-containing oxygen-transport metalloprotein in red blood cells of almost all vertebrates (Maton 1993). Pauling and Coryell (1936) found oxyhaemoglobin had no unpaired electrons and is weakly diamagnetic. When oxyhaemoglobin releases its oxygen, four unpaired electrons are exposed at each iron centre, rendering the molecule strongly paramagnetic. Paramagnetic deoxyhemoglobin induces local magnetic field distortions in and around blood vessels. Thus, it causes different resonance frequency and phase shifts to nearby spins. This accelerates intravoxel dephasing and results in a shorter T_2^* time.

Secondly, changes in brain activity are associated with local changes in blood oxygenation that can be measured during acquisition. Ogawa et al. (1990) reported that deoxyhemoglobin in venous blood is a natural contrast for MRI, meaning that this contrast is sensitive to different levels of blood oxygenation, without the need for an injected contrast agent, and thus to different levels of local brain activity. Ogawa and colleagues showed that gradient-echo techniques in high fields were particularly effective for measuring blood oxygenation levels (Ogawa et al. 1990; Ogawa and Lee 1990). They labelled this natural contrast as the blood oxygenation level-dependent (BOLD) contrast. The discovery of the BOLD contrast opened the era of noninvasive fMRI. It has become a mainstay of human neuroimaging (Logothetis 2008) thanks to its reasonably good spatial and temporal resolution, and the development of fast imaging sequences, including echo planar imaging (Mansfield 1977) and other MR pulse sequences (Uludağ et al. 2005). The association between neuronal activation and changes in regional blood flow, blood volume and oxygen metabolism is termed neurovascular coupling. Without going into detail, increased activity of neurons in a region, for example in response to a stimulus onset, is accompanied by increased metabolism ($CMRO_2$) in the

region. This leads to an initial lowering of oxygenation, which may be measured as a small decrease in the BOLD signal related to the stimulus onset (the so-called 'undershoot'). This is followed by a pronounced increase of oxygenated blood to the activated region resulting in hyper-oxygenation and an increase in the BOLD signal. This is the reason why we observe a positive BOLD response after stimulus presentation. For stimuli represented in a block design, the dominant peak becomes a broad plateau, which stays until the end of stimulation. A small overshoot may be observed just prior to the positive plateau. By simultaneously measuring BOLD and neuronal activity including single- and multi-unit activity (MUA) and local field potential (LFP), studies have found a higher correlation between BOLD and LFP (Goense and Logothetis 2008; Logothetis et al. 2001). These studies also demonstrated that the BOLD response reflects input and intracortical processing rather than pyramidal cell output activity.

The arrival of fMRI has triggered a continuous development of experimental design and image analysis. A typical block design for an BOLD-fMRI experiment requires the participant to perform a task during experimental 'blocks' of time interspersed with other blocks of time during which the participant is required to rest or perform a different task. Echo-planar gradient echo or spin echo brain images are acquired during the task and the resting periods. A statistical comparison between blocks generates activation maps that can be overlaid on anatomy. The block design has been widely used in BOLD-fMRI experiments, and shows excellent functional contrast-to-noise ratio. Alternatively, event-related designs with high-speed fMRI methods (Buckner et al. 1996) offer other advantages, such as temporal resolution that is closer to the underlying neuronal activity (Logothetis 2008). Another advantage is that effects of briefly presented, individual stimuli can be measured in an event-related design. What is common about the two forms of experimental design is the contrast of blocks or events against baselines and that different blocks and events can be used to contrast fMRI correlates from different tasks or stimuli, or to contrast effects of

task or stimuli against a baseline.

Data from event-related and block designs can be analysed in univariate and multivariate ways. Multivariate approaches (Cox and Savoy 2003; De Martino et al. 2008; Haxby et al. 2001) take advantage of the full spatial pattern of brain activity measured simultaneously at many voxels. The multivariate analysis approach is the basis for various related approaches including representational similarity analysis (Kriegeskorte et al. 2008), and decoding (Formisano et al. 2008; Haynes and Rees 2006). Such techniques can often detect small differences in multivariate activation patterns between tasks or conditions that would not be picked up by conventional univariate methods (Haynes and Rees 2006; Logothetis 2008). Additionally, in order to link fMRI signals with computational models of brain function, fMRI encoding and model based decoding techniques have been developed (Naselaris et al. 2011). In these ways, advanced data (image) analysis techniques can provide deeper insights from fMRI data. Nevertheless, insights from fMRI will still be limited by the quality of the original signal, therefore advances in data acquisition are critical.

BOLD at ultra-high field

In fMRI, Temporal signal-to-noise ratio (tSNR) is used to estimate the SNR of the time series, which fluctuates due to thermal and physiological noise sources. It is calculated by the division of the mean signal by its standard deviation (Triantafyllou et al. 2011). It is far more important than the SNR (reflects the level of a desired signal to the level of background noise in a static MRI image), which is also affected by data analysis, system stability and physiological noise (Jorge et al. 2013; Krüger and Glover 2001; Triantafyllou et al. 2006; Welvaert and Rosseel 2013). The relation between SNR and tSNR depends on the impact of thermal and physiological noise (De Martino et al. 2018). In the thermal noise dominated regime, which applies to the acquisition of high spatial resolution functional images, increases in SNR lead to increases in tSNR (De Martino et al. 2018). It has been shown that

net tSNR increases at ultra-high field strength, particularly at higher spatial resolutions (Triantafyllou et al. 2005). For example, increases in image SNR acquired from 7T acquisition with the resolution of 1 x 1 x 3 mm^3 produces higher tSNR, however, at the resolution of 3 mm isotropic only produces modest increases in tSNR (Triantafyllou et al. 2005).

Moving to UHF has considerable advantages for the BOLD contrast (Ugurbil 2016; Uğurbil et al. 2003). The BOLD contrast represents a combination of intravascular and extravascular signals. Extravascular signals around small vessels increases with the square of the magnetic field, while the signal around larger vessels increases more linearly: at UHF, intravascular signals decay faster than in the surrounding tissue due to the shortening of T_2/T_2^*. When the data is collected at a TE that approximately equals the grey matter T_2^*, then the intravascular signals will have almost decayed by the time of image acquisition (Uludağ and Blinder 2018; Uludağ et al. 2009). Thus, at UHF, BOLD contrast is based less on intravascular and more on extravascular contributions. The intravascular signals come partially from large draining veins and therefore show little or no signal specificity compared to the extravascular signal picked up from surrounding grey matter tissue (De Martino et al. 2018). A number of studies have confirmed the large relative increase in microvascular contributions at UHF (Kim and Ogawa 2012; Uludağ et al. 2009; Yacoub et al. 2001), and the consequently higher specificity of fMRI signal at UHF.

Despite the increased sensitivity towards signals from small vessels, the GE BOLD signal at UHF is still significantly influenced by large vessels. Consequently, researchers have observed an overall increase in BOLD contrast towards the cortical surface in laminar studies (De Martino et al. 2015; Huber et al. 2015; Koopmans et al. 2010; Polimeni et al. 2010; Siero et al. 2011). Although spin echo imaging techniques can reduce the effects from large vessels, due to implementation limitations and inherently lower SNR, GE-EPI remains the mainstream method for BOLD fMRI at UHF. In the current thesis we also utilised the GE-EPI

sequence to acquire the functional data.

Investigating cortical processing requires UHF-fMRI

The human cerebral cortex is a highly folded sheet of neurons, of which the thickness ranges from 1 to 4 mm, with an overall average of about 2.5 mm (Fischl and Dale 2000). It is formed by distinct layers with different cytoarchitecture and connectivity, which enable different functions. According to the canonical hierarchical connectivity model, feedforward signals from lower areas mainly terminate in the granular layer (Layer IV) and feedback signals from higher areas mainly terminate in the supra-granular (Layer I-III) and infra-granular layers (Layer V-VI) (Felleman and Van Essen 1991; Maunsell and Essen 1983; Rockland and Pandya 1979). In a cortical column, neurons with similar preference, such as orientation and ocular dominance, are grouped together vertically across cortical depth. The width of cortical columns varies from 200 μm to 600 μm (Hawkins et al. 2017; Horton and Adams 2005), or to 850 μm (Dumoulin et al. 2018). Therefore, it's important and necessary to reach submillimetre resolution in functional MRI at ultra-high field to explore cortical processing. Apart from the high spatial resolution at UHF imaging, microvasculature contributions to the BOLD signals also increase at UHF, which provide a higher spatial specificity to neuronal tissue and make it more feasible to show cortical depth/column dependent responses (Dumoulin et al. 2018).

1.3 Attention and UHF-fMRI

The first research line in the thesis had as a major aim to investigate neural mechanisms of attention, and in particular, of one of its major control structures (the Nucleus Basalis of Meynert). Understanding attention has been one of the main goals in philosophy and psychology, and later in more integrative fields such as cognitive psychology and cognitive neuroscience. The early interest in attention is clear in the following (more than a century old) quote of William James: 'Every-

one knows what attention is. It is taking possession of the mind, in clear and vivid form, of one out of what seems several simultaneously possible objects or trains of thought. Focalization, concentration of consciousness are of its essence. It implies a withdrawal from some things in order to deal effectively with others.' The development of theoretical frameworks in attention in the 1960s was dominated by the debate between early (Broadbent 1958) and late selection models (Deutsch and Deutsch 1963). Early selection models propose that stimuli are selected early in the sensory processing stream based on their features, before which their meaning is processed. Late selection models propose the opposite, namely, that selection takes place after the meaning of stimuli has been processed pre-attentively. Interestingly, early selection models may be considered more in line with modern concepts of bottom-up and exogenous attention, whereas late selection models may be more in line with modern concepts of top-down attention. Many neurophysiological studies in animals (Herrero et al. 2008; Ito and Gilbert 1999; McAdams and Reid 2005; Motter 1993; Roelfsema et al. 1998) have demonstrated strong evidence of the involvement of early visual areas in selective attention. An increase in firing rates in response to attended stimuli has been observed in sites along the visual pathway as early as area V1 and even LGN (McAlonan et al. 2008). Several landmark studies in the visual cortex from the group of Robert Desimone demonstrated that neuronal receptive fields (RFs) containing two stimuli 'contract' around the relevant stimulus. The recorded neurons, whose RFs were stimulated with two stimuli, showed responses to the relevant (attended) stimulus that became similar to the responses observed when that stimulus was presented alone in the RF (Moran and Desimone 1985; Reynolds et al. 1999). These findings were prevalent in various extrastriate visual areas, and certainly confirmed a contribution of early visual areas to attentional selection. Related observations have been reported in a multitude of fMRI studies (Kastner et al. 1998; Kastner et al. 2001; Kastner et al. 1999) and EEG studies (Gallotto et al. 2020; Schneider et al. 2012; Walter et al. 2014) in humans. The question remains however what factor induces neurons in the early visual cortex to increase their response rate and/or sensitivity to process

relevant stimuli. A number of high level areas in parietal and frontal lobes have been proposed as attentional control centres. These areas include the lateral intraparietal area (Bisley and Goldberg 2003; Bisley and Goldberg 2006; Goldberg et al. 2002; Goldberg et al. 2006, January), the frontal eye field in premotor cortex (Crowne 1983; Moore and Fallah 2004; Schafer and Moore 2007; Schall 2004; Thompson et al. 2005), and dorsal and ventral prefrontal cortex (Corbetta and Shulman 2002; Fox et al. 2006; Hamker 2005; Vossel et al. 2014). The influence from high-level cortical areas over attentional selection in lower-level areas has been shown to rely on feedback connections, and may involve neural synchronisation across areas (Briggs 2020; Hamker 1999; Harris and Thiele 2011; Ito and Gilbert 1999; Lamme et al. 1998). Attentional control also involves contributions from subcortical structures. Relevant cortical structures include the superior colliculus (in visual attention) (Krauzlis et al. 2013; Müller et al. 2005; Robinson and Kertzman 1995) and the pulvinar (Desimone et al. 1990; Fischer and Whitney 2012; Petersen et al. 1987; Saalmann et al. 2012; Zhou et al. 2016). Local deactivation in the pulvinar of the monkey causes spatial attention deficits (Desimone et al. 1990; Zhou et al. 2016) similar to neglect as observed after parietal lesions in human patients (Driver and Mattingley 1998; Pouget and Driver 2000).

Attentional control is also mediated by neuromodulatory systems, including the noradrenergic (Sara 2009), dopaminergic (Nieoullon 2002), and cholinergic systems (Thiele and Bellgrove 2018). In the present thesis, we were interested in the cholinergic modulation of attention. There is ample evidence that acetylcholine (ACh) is involved in mediating attentional modulation of neuronal processes. For example, during sustained attention cortical ACh release, measured by in-vivo-microdialysis, typically increases by 120–140% (Sarter et al. 2009). A number of psychophysical and neurophysiological studies (Herrero et al. 2008; Roberts et al. 2005; Roberts and Thiele 2008; Zinke et al. 2006) support the idea that increased cholinergic neuromodulation leads to a reduction of the influence of context on the neural responses related to target stimuli, and a concomitant reduction

of contextual effects on the perception of target stimuli. Moreover, in a striking demonstration of the importance of cholinergic mechanisms to attentional modulation, Herrero et al. (2008) measured attentional modulation of V1 neurons in control conditions and in the presence of cholinergic drugs applied to the recorded cells. The effect of attention was mimicked and enhanced by ACh, but suppressed by blockade of muscarinic cholinergic receptors. The major source of acetylcholine in the cortex is the nbM and electrical stimulation of the nbM has effects in the cortex that are similar to the effects of attention (Chen et al. 2012; Goard and Dan 2009; Liu et al. 2015). Thus, given the role of ACh in attention, this indicates that the nbM plays a major role in mediating attention, however it is an open question whether cholinergic innervation from the nbM to the cortex has sufficient spatial specificity to underlay the highly localised effects of selective attention.

Typically, it has been thought that the nbM supports global tonic levels of ACh in the cortex. However the possibility for a more spatially specific modulation is supported by anatomical evidence demonstrating that different subregions of nbM connect to cortical areas belonging to different sensory modalities in the cortex (Mesulam and Geula 1988). Tracing and stimulation studies indeed show that different subregions of the nbM project to different cortical regions. Notably, the posterior part of nbM (CH4p) projects to the temporal cortex, including auditory cortex, while the intermediate part (CH4id, CH4iv) projects to the lateral and posterior cortex including visual cortex (Liu et al. 2015). Some specificity of cholinergic modulation has also been demonstrated in microdialysis studies (Obermayer et al. 2017). Taken together, it seems that the nbM supports at least regionally specific cholinergic modulation of cortical processes, however whether this is achieved by a functional map within the nbM is unknown.

We were interested therefore in testing whether the specificity of selective attention is reflected in the activity of nbM, as measured with 7T fMRI. We aimed to test the specificity at two levels. First, we aimed

to assess between-modality specificity, that is, we hypothesised that auditory attention and visual attention tasks would activate separate subregions of nbM known to be connected to visual and auditory cortical domains. Second, we aimed to test whether within-modality attention (i.e. to different locations in the visual field) would reveal an even more fine-grain level of functional organisation within the modality specific subregion.

Assigning the term 'nucleus' to the nbM is somewhat misleading because rather than a nucleus, it is a cluster of neurons without a clear boundary and without a regular shape. It is located 13-14 mm from the olfactory tubercle towards the uncal hippocampus in the sagittal view, extending 13-14 mm antero-posteriorly and 16-18 mm medio-laterally within the substantia innominata(Mesulam and Geula 1988). Histological studies reported that the volume of nbM ranges from 58.6 - 156 mm^3 (Grinberg and Heinsen 2007; Halliday et al. 1993). Because of the limited anatomical size and the diffusive and open structure of the nbM, we opted for ultra-high field fMRI to test our hypotheses. UHF-fMRI has as a primary advantage that it permits high spatial resolution, better tissue contrast and BOLD contrast. In addition, UHF-fMRI increases SNR especially in the middle of the brain (see section 1.2.2), which adds to the advantages achieved by using UHF-fMRI to study the nbM. Therefore, the enhanced spatial resolution combined with enhanced anatomical and BOLD contrasts make UHF-fMRI particularly suited to study the nbM, both to parcellate it in subregions (Keuken et al. 2018) and to measure its functional responses. UHF-fMRI also interacts with the BOLD signal to give it greater specificity for neural activity at the expense of the non-specific contributions of larger veins. The larger reliance on neural signals achieved with UHF-fMRI could have contributed in distinguishing functional activity within the nbM elicited by different attentional tasks. We used a sequence that reached a spatial resolution of 1.25 mm isotropic in functional imaging through a customised 2D multiband GE-EPI sequence (multiband factor =2) (Moeller et al. 2010; Setsompop et al. 2012). For the anatomy, we acquired 0.65 mm isotropic using customised white-matter nulled

MPRAGE sequence (Saranathan et al. 2015) at 7T. This sequence has been used for imaging subcortical thalamic nuclei, thus it might also be effective to visualise the nbM. Based on the enhanced sensitivity for BOLD at UHF-fMRI in the context of block designs, we also had designed a block design alternating auditory and visual attention tasks. In our task (see Figure 1.1), participants would perform a detection task with attention directed to either visual (left or right) or auditory (high or low) stimuli. Attention would be shifted between modalities among blocks. In the auditory domain, a frequency shift of a narrow-band sound is embedded in a sequence of quintets. The location of the frequency shift Narrow-band sounds were centred around 4000 Hz and 500 Hz. The visual target is the flashed gabor at the centre of the cued (left or right) field.

The data acquisition sequences for UHF-fMRI structural and functional imaging in our planned nbM attention project were chosen to maximise our ability to segment the nbM and to potentially observe differential activity in different tasks. We also optimised the scanning protocols to better record the functional activity and visualise the structure of the nbM. Moreover, we optimised our experimental design to maximise sensitivity for signal from the nbM, for example, changing the length of stimulus block, testing the efficiency and validity to include a control condition. For each experimental design, we collected data from 2-3 participants (particularly for the last experimental design, we collected 12 functional runs in two scanning sessions) in the pilot studies. Unfortunately, we did not manage to come up with a convincing strategy to localise the nbM based on our structural images, let alone to segment potential subregions. A successful functional study to distinguish differential contributions of nbM to visual and auditory attention was therefore not feasible. We therefore were forced to call off our planned study.

That we had to take this decision was surprising in the face of a relatively extensive MRI literature claiming to successfully estimate the volume (and in some studies the volume loss) of the nbM (Cantero

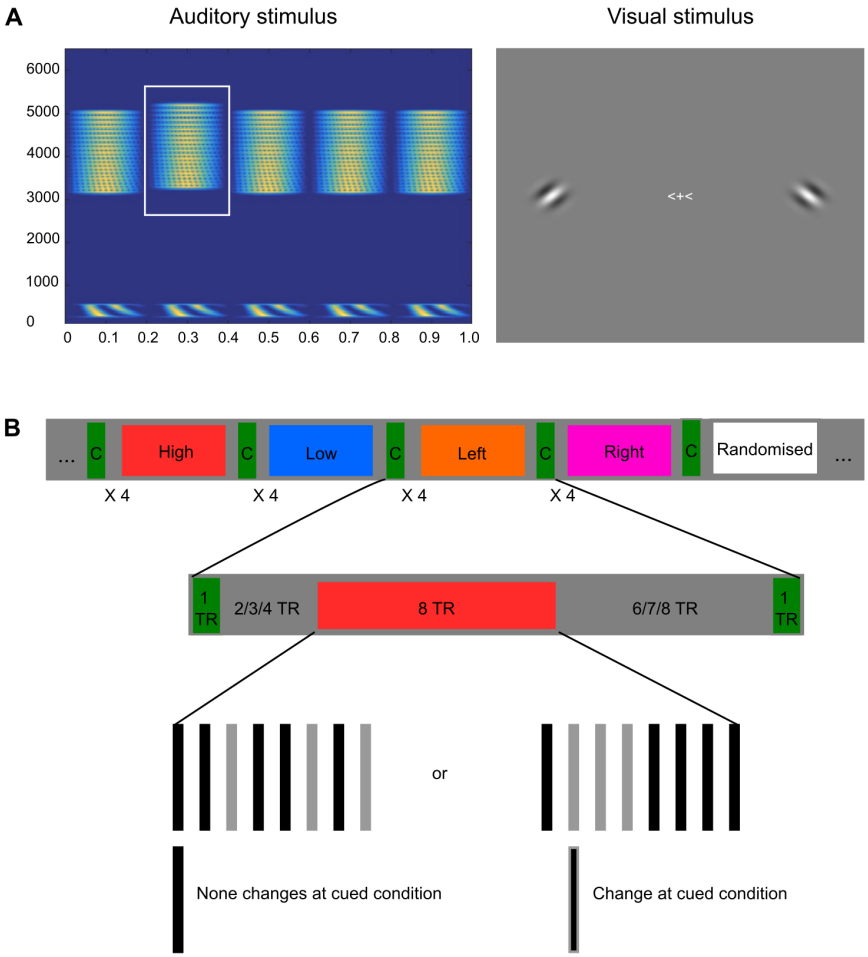
A
Auditory stimulus
Visual stimulus
6000
5000
4000
3000
2000
1000
0
0 0.1 0.2 0.3 0.4 0.5 0.6 0.7 0.8 0.9 1.0
<+<
B
...
C
High
C
Low
C
Left
C
Right
C
Randomised
...
X 4
X 4
X 4
X 4
1 TR
2/3/4 TR
8 TR
6/7/8 TR
1 TR
or
None changes at cued condition
Change at cued condition

Figure 1.1: (Previous page.) Experimental design for nbM attention specificity at 7T fMRI.
A: Stimulus and task. Subjects perform a detection task in the visual or auditory domain. The auditory streams contain bursts of narrow-band noise centred either at high or low frequencies (e.g. 4000 Hz vs. 500 Hz). The auditory target is a frequency-shift burst, which is marked by white rectangle frame. Prior to each scan session, the sound intensity of stimuli was adjusted individually to perceptually equalise the loudness of the stimuli. The visual stream contains serially presented Gabors in which each element has a randomly chosen orientation. The target is a flashed Gabor at the centre of the cued (left or right) field. The presentation of the sample at the start of the block indicates to which modality and to which frequency / location attention should be directed. Selective attention is directed to either high or low frequencies (auditory) or spatially left or right (visual). Auditory and visual stimulus streams are presented for 60 seconds at the same time in the silent gap after the acquisition of the 2D-GE-EPI sequence. Targets and distractors are presented pseudo-randomly (with replacement) keeping the hazard rate constant throughout the block.
B: Schematic of the stimulus presentation for an example task run. Repetition time (TR) = 2.4 s, Total acquisition (TA) = 13.04 mins. Cue (C) is presented for one TR before each block to indicate which modality should be attended to. For example, H+H represents an upcoming high frequency block, L+L represents an upcoming low frequency block, <+< represents an upcoming left block, and >+> represents an upcoming right block.

et al. 2020; Cantero et al. 2017; Grothe et al. 2012; Grothe et al. 2013; Grothe et al. 2014b; Schmitz et al. 2020; Teipel et al. 2011; Wolf et al. 2014; Yuan et al. 2019), and to have successfully studied the functional contribution of nbM to cognition (Markello et al. 2018; Nemy et al. 2020). We, therefore, decided to assess the methods used for localising the nbM in prior MRI studies. We found that the approaches taken often had severe limitations, which in a number of studies has led to ascribing specific cognitive abilities to the nbM based on weak evidence. Our work points to various avenues (or requirements) to improve (f)MRI research aiming to test functional contributions of small structures such

as the nbM in the future (Chapter 2). It may be possible to revisit our initial question in some years, when sufficient progress in (f)MRI methodology has been achieved.

1.4 Surface perception and UHF-fMRI

A second major goal of the thesis was to investigate surface perception. In our original concept of the thesis, this topic was tightly linked to the idea of cholinergic mechanisms of attention. Surface perception has long been known to depend on the context in which it is presented, thus the brightness and colour of a surface appears different depending on the brightness and colour of surrounding surfaces. Attention to the surface may modulate this process, as attention has been linked to contextual influences in various stimulus configurations. Moreover, it seems likely that ACh is the key mechanism by which this modulation is achieved: In the cortex, ACh acts as a neuromodulator, binding to nicotinic and muscarinic receptors, the location and action of which match the action of attention; as nicotinic receptors enhance bottom-up input whereas muscarinic receptors suppress lateral interactions (Disney et al. 2012). Thus, cholinergic mechanisms may contribute significantly to the enhanced neuronal responses to targets and the reduced impact of context or nearby distractors on neuronal responses. In our original project, we had envisaged experiments in which participants, for example, would detect a target patch of line texture that would deviate minimally from the orientation of a background texture, so that without attention the target patch would be experienced as integrated with the background. In such a task, cholinergic mechanisms engaged by attention may help to break the target free from its context (the background), so it is perceived (detected) better. Ideally, we would have observed enhanced activity in superficial (or deep) layers of early visual cortical areas together with increased activity in a segment of the nbM that in preceding work we would have established as involved in attention. However, because the first research line in the thesis did not develop according to plan, we decided to decouple the topic of contextual influences in sur-

face perception from the topic of cholinergic mechanisms. Thus, in the second project of the thesis, we decided to focus on a paradigm that, in a 3T study previous from our group, had been successfully used to modulate surface perception, namely, brightness induction. Our goal became to replicate the 3T correlate of brightness induction shown by Van de ven et al. (2012) at 7T, and to test by means of depth-resolved cortical fMRI activity whether surface brightness induction may rely on feedback.

Surface perception is a topic that has elicited strong debate in visual neuroscience. In particular, and similar to the debate in the domain of attention, the relative contributions of lower and higher level areas has been vigorously debated. According to high-level views, surface features are logically deduced from edge information. For example, based on the contrast polarity of the edges delineating a white square from a black background, it can be logically inferred that the inside of the square has to be white (in the absence of information about boundaries inside the square). Hence, instead of representing the brightness level in a literal way across the extent of the surface, the brightness is inferred. Dennett (1992) referred to these opposite views as filling-out surface features (logically assuming them without explicit representation) versus filling-in surface features (where surface features are explicitly coded across the extent of the surface).

The explicit representation of surfaces in the low-level visual cortex is supported by a number of neurophysiological studies. Studies by Gattass et al. (2005) and Komatsu et al. (2000) and Komatsu et al. (2002) demonstrated the explicit encoding of surfaces across the representation of the blind spot during monocular stimulation. In addition, several neurophysiological (Hung et al. 2007; Roe et al. 2005) and fMRI studies have shown correlates of surface filling-in in early visual cortical areas (Mendola et al. 2006; Sasaki and Watanabe 2004). In addition, in a study of surface perception using the Kanizsa square (Kok et al. 2016), enhanced activity was restricted to deep layers in the middle of the representation of the Kanizsa square in area V1, in line with possible

feedback contributions to surface perception. Marquardt et al. (2020) reported potentially feedback-related signals in the superficial layers in response to surface motion perception. These endeavours demonstrate the feasibility to isolate feedback and feedforward activities in vivo in humans.

The above overview suggests that the perception of surfaces may involve explicit representations of surface qualities in low-level visual areas, as well as higher level mechanisms that compute surface features based on the layout of contours in a visual scene. In addition, various studies have shown that the surface feature present or perceived throughout the extent of one surface can also influence the surface feature perceived in a neighbouring surface (Foster 2011; Haynes et al. 2004; Roe et al. 2005; Rossi and Paradiso 1999; Rossi et al. 1996; Sasaki and Watanabe 2004; Shimojo et al. 2001). For these observations, the same theoretical possibilities exist related to the roles of low and high-level areas in the visual system. Indeed, the contextual effects of surrounding surfaces on a central surface could result purely from computations on high-level areas, or alternatively, perceived contextual colour or brightness changes in a surface may be explicitly represented in low-level retinotopically organised visual areas. Moreover, specific layer distributions of activity in low-level areas during contextual changes in surface perception could be indicative of a role of feedback in enabling these contextual changes in surface perception. We investigated these questions in a typical brightness induction stimulus, in which the luminance in a large background (inducer) influenced the perceived brightness in an enclosed surface area (probing region). In particular, increasing the luminance in the inducer (background) decreased the brightness in the enclosed probing area, and vice versa. This occurs while the luminance in the enclosed probing area is kept constant. Neurophysiological studies have demonstrated convincing neural correlates of brightness induction in V1 (Rossi and Paradiso 1999; Rossi et al. 1996). In these studies, the spike rate of neurons with their RF inside a probing region of constant luminance, was modulated up or down in antiphase with the luminance variations in the surrounding inducers.

fMRI studies designed to replicate these findings have not consistently succeeded. For example, Cornelissen et al. (2006) reported a failure to find an fMRI correlate of brightness induction. Van de ven et al. (2012) however came to an opposite conclusion. They reported a correlate of brightness induction restricted to V2. Van de ven et al. (2012) used a stimulus that likely was more efficient in brightness induction, and in contrast to Cornelissen et al. (2006) they used a slow single-event design to separate the effects of luminance decreases and increases in the surface regions used to induce brightness changes in an enclosed region of constant luminance. Their data showed negative beta values in a probing region of constant luminance where brightness changes were perceived in antiphase to the inducer changes in the surrounding image regions. Although these findings were interesting, the study only reported beta values, which prevented an appreciation of the separate brightness induction effects in the probing region of luminance increases and decreases in inducers. In addition, the luminance changes varied between maximal luminance (above average grey background) and minimal luminance (below average grey background), which implied a possibility that only luminance changes occurring above or below the level of the grey background would drive the brightness induction effect. Considering these conflicting findings among various studies (Boyaci et al. 2007; Cornelissen et al. 2006; Perna et al. 2005; Van de ven et al. 2012), we revisited brightness induction using 7T fMRI at submillimetre resolution. In addition, we modified the slow single-event related experimental design of Van de ven et al. (2012) into a block design, and split the full extent of inducer luminance variations in half, with some events increasing luminance above the grey background, and other events decreasing the luminance below the grey background. With this design we hoped to replicate a fMRI brightness induction correlate in the early visual cortex. In addition, we expected that the advantages of 7T (higher spatial resolution and SNR) would allow us to study a depth-resolved signal, and to test whether the depth-resolved response would support a contribution of feedback (or lateral interactions). We anticipated that the use of a better experimental design to replicate a correlate of brightness induction already established in our group would

put us in an excellent position to test depth-resolved neural correlates of rightness induction in the low-level visual cortex.

1.5 Outline of the thesis

This thesis includes one methodological study and two empirical studies. The methodological study presented in Chapter 2 addresses the challenges of atlas-based volumetry for the human nucleus basalis of Meynert in neuroimaging studies, mainly in (f)MRI studies. We noticed large variability among the reported volumes not only from studies using various atlases but also from different studies using the same atlas and threshold. We implemented a method that examines the influence of spatial resolution on the variability of volume estimates by developing a novel nbM mask based on the normalised BigBrain dataset. We showed that the variance of the estimated nbM volume increased dramatically for voxel sizes above 1.3 mm isotropic but is quite stable at higher resolutions (0.1 - 1.3 mm isotropic). We concluded that applying any mask defined originally in histological space in one or more brains to MR images of other brains will almost certainly always be difficult. Furthermore, by exploring a high resolution ex-vivo structural MRI dataset obtained in our group, we revealed that quantitative T_2^* high-resolution MR measurements can be one of the ways forward to visualise nbM individually using MRI.

Chapter 3 reports on an fMRI study at 7T designed to shed light on the neural mechanisms in the early visual cortex contributing to brightness induction. Prior to the fMRI experiment, we had used psychophysics to devise a stimulus usable within the confines of the field-of-view in the scanner, which induced a consistent and strong brightness illusion, with increased brightness perception in the constant probing region upon an inducer luminance decrease, and decreased brightness perception in the constant probing region upon an inducer luminance increase. We found in the V1 representation of the inducer region a significant negative response, and of the probing region a non-significant trend towards a positive response during luminance decrements of the

inducer surfaces at the early (averaged across 3 TRs during positive-dominant BOLD periods) stage of the temporal response. The luminance increment condition, however, did not induce a response decrease in the cortical region corresponding to the probing region, and failed to induce any cortical response at all. It is possible that the pronounced difference in the response to the inducers during luminance increments and decrements was related to an asymmetry in the mechanisms of brightness induction. Indeed, the luminance increment in the inducer only gave a weak response, which was coupled to the absence of decreased brightness perception in the probing region.

These findings posed the question to what extent the observed fMRI signal changes were a correlate of brightness induction, and we therefore refrained from performing further, depth-resolved analysis. In addition, we also questioned whether average luminance changes in the display as a whole could have counteracted the weak effect of brightness induction (Salmela and Vanni 2013). In preparation of further fMRI investigations of brightness induction, we attempted to design stimuli in which brightness induction could be manipulated without overall luminance changes in the display. In a literature search with the goal to identify such stimuli, we discovered a paper by Anderson and Winawer (2005), which claimed to have discovered the hitherto largest brightness induction phenomenon ever reported. In a typical version of this stimulus, a scene is presented showing a full moon that is transparently visible through a layer of clouds (extending beyond the moon). When the overall luminance of the clouds is higher, the moon is perceived as darker, and vice versa. A remarkable aspect of this stimulus is that the brightness induction is destroyed simply by rotating the background of clouds around the moon, leaving the clouds overlapping with the moon in their original position. The resulting break in the transparent layer of clouds appears to destroy the illusion. Potentially, this stimulus has powerful advantages for fMRI studies, because brightness induction could be manipulated without altering the overall luminance in the display. Chapter 4 represents a parametrical study of the properties of this brightness induction stimulus, in order to replicate the reported ef-

fects, and to verify the effect of background rotation. Although we could replicate brightness induction, we found the illusion to be quite small, in contrast to the original report of Anderson and Winawer (2005) and did not fully replicate the reported rotation effect of completely nullifying the illusion. At present, it is therefore not clear whether the Anderson and Winawer brightness induction stimulus is a good tool to investigate neural correlates of brightness induction in fMRI experiments. Yet, we believe it is promising, and further psychophysics testing in the lab will be needed.

Chapter 5 summarises and discusses the findings of the methods chapter and the two empirical chapters. The findings are placed in the context of the literature, limitations of the studies are discussed, and avenues for further research are suggested.

2

Inconsistencies in atlas-based volumetric measures of the human nucleus basalis of Meynert: A need for high-resolution alternatives

---

Based on

Wang, Y., Zhan, M., Roebroeck, A., De Weerd, P., Kashyap S., Roberts, M.J. (2022). Inconsistencies in atlas-based volumetric measures of the human nucleus basalis of Meynert: A need for high-resolution alternatives. *NeuroImage*, 119421. DOI: 10.1016/j.neuroimage.2022.119421

2.1 Abstract

The nucleus basalis of Meynert (nbM) is the major source of cortical acetylcholine (ACh) and has been related to cognitive processes and to neurological disorders. However, spatially delineating the human nbM in MRI studies remains challenging. Due to the absence of a functional localiser for the human nbM, studies to date have localised it using nearby neuroanatomical landmarks or using probabilistic atlases. To understand the feasibility of MRI of the nbM we set our four goals; our first goal was to review current human nbM region-of-interest (ROI) selection protocols used in MRI studies, which we found have reported highly variable nbM volume estimates. Our next goal was to quantify and discuss the limitations of existing atlas-based volumetry of nbM. We found that the identified ROI volume depends heavily on the atlas used and on the probabilistic threshold set. In addition, we found large disparities even for data/studies using the same atlas and threshold. To test whether spatial resolution contributes to volume variability, as our third goal, we developed a novel nbM mask based on the normalized BigBrain dataset. We found that as long as the spatial resolution of the target data was 1.3 mm isotropic or above, our novel nbM mask offered realistic and stable volume estimates. Finally, as our last goal we tried to discern nbM using publicly available and novel high resolution structural MRI ex vivo MRI datasets. We find that, using an optimised 9.4T quantitative T_2^* ex vivo dataset, the nbM can be visualised using MRI. We conclude caution is needed when applying the current methods of mapping nbM, especially for high resolution MRI data. Direct imaging of the nbM appears feasible and would eliminate the problems we identify, although further development is required to allow such imaging using standard (f)MRI scanning.

2.2 Introduction

The structure of the nucleus basalis of Meynert (nbM), as well as its efferent and afferent connections and its neuromodulatory functions, have been widely studied in animals (Ballinger et al. 2016) and human (Grin-

berg and Heinsen 2007; Halliday et al. 1993; Heinsen et al. 2006; Liu et al. 2015; Mesulam et al. 1983; Teipel et al. 2005). The nbM' s neuromodulatory function is exerted by acetylcholine (ACh) and is highly relevant to cognitive domains ranging from perception and attention, to learning and memory formation. Moreover, cholinergic dysfunction has been associated with both cognitive dysfunction and psychiatric disease (Liu et al. 2015). In light of the nbM' s relevance to such a broad range of functions, the study of nbM structure and function directly in the human brain has garnered increasing interest. This has been attempted by a number of researchers using both structural (hereafter referred to as MRI) and functional magnetic resonance imaging (hereafter referred to with the prefix 'f' to MRI, fMRI). However, in our own hands as well as in the broader literature, it has been demonstrably difficult to accurately determine the nbM and its subdivisions using in vivo MRI, despite the feasibility of sub-millimetre spatial resolution. This is reflected in the large disparities of structural volume and location of the nbM amongst (f)MRI studies. Given that fMRI studies rely on accurate delineations of the nbM in structural MRI images, the interpretations of the nbM function following mapping of the relatively lower resolution functional data onto structural data in human fMRI research also raise questions.

The overarching goal of the present article is to first review literature available regarding imaging the human nbM, evaluate the different approaches that have been used in the literature to achieve estimates of the nbM' s volume, and to present the challenges in the different approaches used. In addition, we argue for the need for high-spatial resolution imaging to resolve structures like nbM, we suggest some avenues to address current challenges, and specifically highlight the promise of ultra-high field MRI in imaging the nbM directly. To introduce the topic, we describe the importance of the nbM and its role in modulating cognition based on existing human and animal studies (section 2.2.1). Then, we introduce the histological ground truth regarding the nbM' s volume (section 2.2.2) because accurate volumetric estimates of the nbM in neuroimaging studies are critically important. Finally, we

introduce the main methods with which histological/anatomical information is used to determine the nbM as a region of interest (ROI) in structural and functional MRI datasets (section 2.2.3).

2.2.1 The role of ACh and nbM in regulating brain function and cognition

Acetylcholine (ACh) acts as a neuromodulator in the brain. It has been related to cognitive processes including arousal (Semba 1991), attention (Klinkenberg et al. 2011), memory and learning (Hasselmo 2006) while its dysregulation has been linked to several neurological disorders (Liu et al. 2015; Rogers et al. 1985; Vogels et al. 1990). The main source of ACh in the brain is the basal forebrain complex, a collection of subcortical nuclei which provide the cholinergic input to cortical and subcortical areas (Hedreen et al. 1984). Classically, these cholinergic nuclei have been divided into 4 subregions: Ch1 referring to the medial septal nucleus; Ch2 and Ch3 respectively referring to the nucleus of vertical and horizontal limb of the diagonal band of Broca, and Ch4 referring to the nucleus basalis of Meynert (nbM). nbM in humans can be further divided into anteromedial (Ch4am) and anterolateral (Ch4al or nucleus subputaminalis), anterointermediate (Ch4ai), intermediodorsal (Ch4id), intermedioventral (Ch4iv), and posterior areas (Ch4p) (Heinsen et al. 2006; Mesulam and Geula 1988; Simić et al. 1999). Ch1 to 3 projects to subcortical areas, whereas Ch4 provides cortical cholinergic innervation through its widespread projections (Mesulam et al. 1983).

Work in rodents and monkeys has established the relevance of ACh in attention, learning and memory. Manipulation of ACh level in the basal forebrain (Gritton et al. 2016), in the sensory cortex (Herrero et al. 2008; Minces et al. 2017) and stimulation of the basal forebrain (Chen et al. 2015; Goard and Dan 2009; Kalmbach et al. 2012; Kim et al. 2016; Pinto et al. 2013; Rodriguez et al. 2004), yielded neurophysiological and behavioural data compatible with the attentional role of ACh. In addition, ACh has a well-established role in modulating experience-dependent synaptic changes, and hence in learning and

memory (Ang et al. 2021; Easton et al. 2012; Hasselmo 2006; Hasselmo 1999; Mitsushima et al. 2013; Obermayer et al. 2017; Picciotto et al. 2012). Moreover, cholinergic dysfunction has also been considered as a key factor in neurodegenerative diseases such as Alzheimer' s disease (AD) (Arendt et al. 1983; Hanna Al-Shaikh et al. 2020; McGeer et al. 1984; Nagai et al. 1983; Rinne et al. 2003; Sabri et al. 2015; Vogels et al. 1990; Whitehouse et al. 1981; Wu et al. 2010) and Parkinson's disease (Arendt et al. 1983; Bohnen et al. 2015; Bohnen et al. 2012; Chan-Palay 1988; Gaspar and Gray 1984; Hall et al. 2014; Klein et al. 2010; Kuhl et al. 1996; Müller et al. 2015; Nakano and Hirano 1984; Tagliavini et al. 1984; Whitehouse et al. 1983a; Zarow et al. 2003) and in neurodevelopmental disorders such as Schizophrenia (Carruthers et al. 2015).

With such significant roles in neuronal function, cognition and neurodegenerative diseases, the cholinergic pathway, and especially the nbM, is of particular interest to both clinical and fundamental neuroscience. To better translate findings from animal models to humans, and to directly test hypotheses in nbM function in humans, MRI can be considered a promising methodology. However, when we embarked on a survey of literature in preparation of an fMRI study of the nbM' s role in attentional modulation of visual and auditory processing, we were surprised by the broad range of volumes and locations ascribed to the nbM. This motivated us to review the anatomical literature on the nbM.

2.2.2 Histology of the nbM

Histological techniques allow direct visualisation of clusters of neurons belonging to the nbM. The visualised nbM following histological procedures represents the ground truth and can only be approximated by MRI but has thus far proved to be very challenging. Using histochemical and immunohistochemical labelling for choline acetyltransferase (ChAT) and acetylcholinesterase, Mesulan and collaborators (Mesulam and Geula 1988) identified various cholinergic neurons in the human

basal forebrain and introduced the nomenclature Ch1-Ch4 to describe four cholinergic cellular groups. Myelin-stain and Nissl-stain have both been used in studying nbM. The nbM appears brighter in the myelin-stained section (Figure 2.1 A) due to neuronal clusters. Nissl-stained (Figure 2.1 B) and silver-stained (Figure 2.1 C) sections of nbM reveal the nucleus as a large aggregate of darkly stained neurons scattered in the sub-pallidal area extending laterally up to the most caudal level of the medial mammillary nucleus and the central nucleus of the amygdala (Mesulam and Geula 1988). However, the nbM does not have restricted boundaries surrounded by fibre bundles or by distinct cellular groups. These features make it difficult to delineate precise boundaries of nbM, which may contribute to the variability in reported volumes within and between studies.

The volume of the nbM, based on histological methods, has been reported in two studies (Grinberg and Heinsen 2007; Halliday et al. 1993) using brain samples from subjects who died of non-neurodegenerative diseases. Halliday and colleagues (Halliday et al. 1993) reported the volume of bilateral nbM from 5 people aged 20-80 years. The volume bilaterally ranged from 76 to 156 mm^3 (Figure 2.2), with a mean volume of 130 mm^3. This is in close agreement to Grinberg and colleagues (Grinberg and Heinsen 2007) who reported the volume for nbM (Ch4am_al, Ch4i, Ch4p combined) to be 58.6 mm^3 (Figure 2.2) from the brain of a single 29-year-old man. Notably, those volumes were all estimated in the stitched 3D space following 2D sectioning and staining without post-mortem MRI scans to correct for shrinkage and distortion in 3D. Taken together these anatomical studies suggest that the bilateral volume of the nbM is in the range of 58.6 to 156 mm^3, with the mean volume of around 118 mm^3. The volume of nbM from these histological studies are informative and can be considered to give a fair estimation of the true volume, as the individual neurons were visible in the stained sections.

With the advent of MRI, there has been an increase in non-invasive studies of the nbM both at standard field strengths (1.5 and 3 T) and

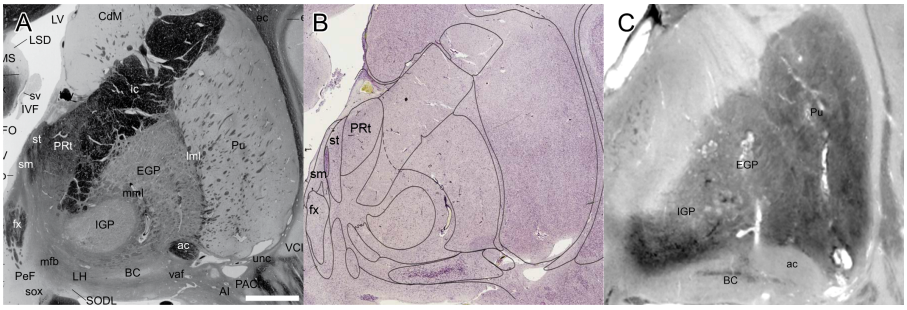

Figure 2.1: Histological sections where the NBM could be visually identified (coronal view, left hemisphere).
A: Myeloarchitectonic atlas from (Mai 2008) (Used with permission from Mai J, Paxinos G, Voss T: Atlas of the Human Brain, 3rd ed. San Diego: Elsevier Academic Press; 2008), plate 25, TAL y=4, from a 24-year-old male, where the NBM was marked as BC, a region with light myelination. Scale bar in **A** and **B**: 5 mm.
B: Nissl stains of the same brain in a section right next to **A**, from the same atlas, where the NBM cell bodies could be seen clearly. The labels in **A** and **B** were directly copied from the atlas.
C: A coronal slice from the BigBrain data (65-year-old male, silver stain) (Amunts et al. 2013), roughly corresponded to the same field of view in **A** and **B** (MNI space, slice 1331/2330, 100 μm isotropic resolution, zoomed %252 to match the scale bar in **A** and **B**). The labels were added by the authors, following the abbreviations **A** and **B**.
Abbreviations: BC: basal nucleus, compact part (nbM); ac: anterior commissure; IGP: internal globus pallidus; EGP: external globus pallidus; Pu: putamen. Fx: fornix.

more recently at ultra-high fields ($\geq$ 7 T). However, studying the nbM with MRI is challenging, especially in vivo and even more so with fMRI. This is because the nbM is diffusive and extensive with an 'open' structure in all three dimensions, unlike other nuclei in the sub-cortex (e.g., subthalamic nucleus, substantia nigra, red nucleus) which are contiguous and have 'regular' shapes (Alkemade et al. 2013; Pauli et al. 2018). Mesulam and Geula (1988) described the nbM' s location as being 13-14 mm from the olfactory tubercle towards the uncal hippocampus in the sagittal view, extending 13-14 mm antero-posteriorly and 16-18 mm medio-laterally within the substantia innominata (SI). Difficulties in localising the nbM can be overcome in studies using invasive procedures, such as electrophysiology, positron emission tomography (PET) or post-mortem histology, because they can use patterns of firing rates, a specific tracer or staining of neuronal bodies to target nbM respectively. This is different to MRI where localisation of the nbM ROI depends on first choosing the appropriate MRI contrast mechanism (T_1, T_2, T_2^* etc.) and/or a functional localiser to define it using fMRI, while ensuring a high-enough spatial resolution can be acquired to resolve the nbM. Since the nbM is made of isolated neuronal islands in SI, any inaccuracies of the nbM mask would likely include many surrounding non-nbM structures resulting in an overestimation of the nbM ROI and thus, affecting any further results. Any functional studies using such overestimated or displaced estimates of the nbM run the risk of drawing invalid inferences and conclusions. It is, therefore, important to carefully evaluate the methods that have been used for localisation, identify their apparent limitations, and to develop potential solutions to the problem of localising human nbM in MRI.

2.2.3 Methods to define the nbM using MRI

There are two broad methods that have been used to localise nbM and estimate its volume in literature. The first is based on its anatomical structure from histological sections and then transferred to a single T_1-weighted post-mortem MRI acquired on 1.5T (Teipel et al. 2005)

and 3T (Kilimann et al. 2014; Teipel et al. 2014a), which described the size, length and distribution of nbM in the basal forebrain relative to nearby anatomical landmarks such as Gpe, Gpi, AC. The second is based on the application of probabilistic atlases (Zaborszky et al. 2008). Both methods have been combined with fMRI using post-processing procedures that transform the anatomically determined nbM ROI into the space of the fMRI data.

Definition of nbM using a post-mortem brain with MRI scan at low resolution

Kilimann et al. (2014), Teipel et al. (2014a) and Teipel et al. (2005) identified the basal forebrain nuclei from the histological sections of the dehydrated brain and then registered these sections in MNI space. They accomplished this by carefully matching the histological sections (400 μm thick from Kilimann et al. (2014) and Teipel et al. (2014a), 440 μm thick from Teipel et al. (2005)) by means of visual inspection to the corresponding slices of the T_1-weighted MPRAGE sequence acquired at 3T of the fixed brain (Repetition time(TR) = 2500 ms, echo time (TE) = 4.81 ms, inversion time (TI) = 1100 ms, flip angle (FA) = 8° from Kilimann et al. (2014); TR = 2500 ms, TE = 4.81 ms, TI = 1100 ms, FA = 7° from Teipel et al. (2014a)) and 1.5T (TR = 1570 ms, TE = 3.93 ms from Teipel et al. (2005)) with spatial resolutions of 1 and 0.9 mm isotropic respectively. To the registration, Kilimann et al. (2014) and Teipel et al. (2014a) acquired in cranio post-mortem MRI scans using T_1 weighted Fast field echo sequence at 3T (Field of view = 240 mm, TR = 7 ms, TE = 3.2 ms, FA = 8°). The fixed MRI scans were first registered to in cranio MRI scans. The registration to an in cranio MRI scan of the same subject reduced the effect of shrinkage and distortion and improved the quality of the spatial projection from histology into MNI space (Ashburner 2007; Klein et al. 2009). Then, the post-mortem in cranio MRI scans was transferred to the MNI space. Using this approach, Kilimann et al. (2014) made a grey-matter ROI, automatically extracted the modulated grey-matter voxels within ROI for individual participants of the healthy control group, and reported

a volume of approximately 260 mm^3 for bilateral Ch4 (Ch4am_al + Ch4p estimated from Figure 3 in Kilimann et al. (2014) in their two healthy control groups of 180 adults. Grothe et al. (2014b) localised nbM based on a cytoarchitectonic map in MNI space, which was derived from combined histology and post-mortem MRI scan (Kilimann et al. 2014; Teipel et al. 2014a). They reported a volume (CH4p = 72.1 mm^3, CH4a-i = 95.5 mm^3) of approximately 167 mm^3 among their healthy control group of 22 adults. Wolf et al. (2014) used the same procedure as in Teipel et al. (2014a) and make a new ROI template. They suggested the nbM volume to be around 128.53 mm^3. Teipel et al. (2014a) and Teipel et al. (2005), however, did not directly report the volume of nbM. The volume of basal forebrain nuclei in Teipel et al. (2005) was reported to be 942 mm^3 on each side of the brain in the supplementary material of Grothe et al. (2012). Teipel et al. (2005) reported signal reduction of AD patients at bilateral lateral SI (Ch4al) with cluster extension of 450 and 134 voxels at left medial SI (Ch4i). However, we were unable to estimate the physical volumes of the nbM due to lack of reported information on the spatial resolution of their target MRI images. This post-mortem brain scan was also used by later studies (Grothe et al. 2012; Grothe et al. 2013; Teipel et al. 2011) to report a volume loss of right Ch4 in AD patients ranging from 566 to 836 voxels (reported as cluster size and cluster extension; the voxel size is not explicitly reported). Nevertheless, these volumes are substantially larger than the total volume of nbM as reported in histological studies (Grinberg and Heinsen 2007; Halliday et al. 1993), in which the volume of bilateral nbM did not surpass 156 mm^3, and are also substantially larger than the volumes reported by Grothe et al. (2014b) and Kilimann et al. (2014). In summary, based on the available literature, the histological 'ground truth' volumes are in the range 58.6 - 156 mm^3 whereas MRI studies have reported volumes that are not only inconsistent with each other but also in some cases inconsistent with the 'ground truth', ranging from 120 to 260 mm^3.

Definition of nbM using probabilistic atlases

Zaborszky et al. (2008) presented a stereotaxic probabilistic atlas of the basal forebrain from ten post-mortem brains of participants without neurological or psychiatric disorders. They acquired MRI of these brains at 1.5T using a 3D FLASH sequence (FA = 40°; TR = 40 ms; TE = 5 ms; voxel size = 1.17 mm [mediolateral] × 1 mm [rostrocaudal] × 1 mm [dorsoventral]) and reported the size of the nbM in cubic millimetres as the unit of volume. To delineate the magnocellular Ch compartments in each brain sample, Zaborszky et al. (2008) used a modified version of the Ch1–Ch4 nomenclature of Mesulam et al. (1983) in which Ch1 and Ch2 were grouped together, Ch3 was maintained as a division, and nbM (or CH4 in Mesulam' s nomenclature) was separated into two parts (Ch4 and Ch4p) rather than 6 subareas. The Ch4 subdivision was delineated in each participant by rostrally extending to the nucleus accumbens, ventrolateral to the bed nucleus of stria terminalis at the edge of the internal capsule/anterior commissure (AC), ventrally to the internal part of the globus pallidus, stretching between the lateral hypothalamus and the temporal aspect of the AC. Ch4p was defined as beginning caudally to the supraoptic (SO) nucleus at the level where the optic tract (OT) adjoins the internal capsule/cerebral peduncle and extending progressively laterally up to the most caudal level of the medial mammillary nucleus and the central nucleus of the amygdala. The resulting outlines of those two compartments were traced on 2D histological sections (1.2 mm apart) using their in-house software. To construct the histological 3D structure, they used the MRI scans of the fixed brain as a shape reference at a resolution of 1 mm isotropic. The reconstructed 3D structure was then transformed to MNI-Colin space. Based on the probabilistic map constructed from the delineated structures in the individual samples, they reported for a Ch4 volume of 85.03 ± 36.26 mm^3 and a Ch4p volume of 30.36 ± 10.84 mm^3 and 89.73 ± 36.65 mm^3 for Ch4 and 27.51 ± 16.72 mm^3 for Ch4p for the left and right hemispheres respectively. Thus, for comparison with other studies reviewed here, the total bilateral nbM volume was approximately 232.63 mm^3. Despite the lower resolution (1 mm isotropic compared to the

sub-millimetre resolutions feasible at 7T) and complex resampling and transformation steps that the data underwent, this probabilistic atlas provides a convenient estimation of position and size of nbM for those neuroimaging studies without access to post-mortem brains.

In summary, we find that the two principal methods (Kilimann et al. (2014) and Zaborszky et al. (2008), see review below) cited for (f)MRI indicated a mean bilateral nbM volume (in MRI space) of between 240 - 250 mm^3, which is inconsistent with nbM volume reported from the two histological studies (Grinberg and Heinsen 2007; Halliday et al. 1993) indicating that the bilateral nbM volume ranges from 58.6 to 156 mm^3. In principle, this clear discrepancy in volumes may be due to an underestimation in histology (due to tissue distortion and shrinkage during preparation and processing) or an overestimation by MRI. We consider it more likely that the volume is overestimated in MRI because histology has a higher spatial resolution and the delineation of the nbM is based on a more direct and specific method (staining). Furthermore, tissue shrinkage during histological procedures is generally in the order of 12%, although could be up to 68% (Mouritzen Dam 1979; Quester and Schröder 1997; Wehrl et al. 2015; Zaborszky et al. 2008), and is accounted for in the reports of the tissue volumes obtained in histological studies.

2.2.4 Objectives

The present work focuses on the structural delineation of the nbM using non-invasive MR imaging using MRI. Accurately delineating the nbM structure is a necessary prerequisite for valid fMRI studies to be feasible. The current literature shows large variability and, in many cases, large overestimations of the nbM volume indicating that the necessary condition of accurate volumetric estimation is often not satisfied. The overall goal of the present paper is to facilitate better (f)MRI research of the nbM by improving the precision of nbM volumetric estimates. To help reach that goal, we have formulated four objectives. First, we aimed to review prior MRI literature that has attempted to image the

nbM, to make an inventory of volumetric estimates and methods used to arrive at these estimates, and to reach insight into potential methodological shortcomings. Second, as probabilistic maps of the nbM are a major tool in estimating nbM volumes, we investigated the effect of thresholding and other parameter choices when employing probabilistic maps. Third, we investigated the effects of the spatial resolution of anatomical data as well as the effect of head position relative to nbM ROI and their impact on the nbM volumetric estimates. Fourth, we explored the potential for direct neuroimaging of the nbM using ultra-high field MRI at 9.4T.

2.3 Review of the volume of nbM from the literature

2.3.1 Goal 1

The present work was triggered by our own unsuccessful attempt to study the contributions of nbM to visual and auditory attention using fMRI. Despite using high-resolution functional (1.25 mm isotropic) and structural MRI (0.65 mm isotropic) at 7T, we called off our planned study as we were dissatisfied with determining a credible ROI for the nbM in vivo. We, therefore, investigated the methods used for localising nbM in prior MRI studies, their limitations, and potential avenues for improvement. This translated into our first objective to survey methods and previously reported volumes of the nbM in MRI studies, and to determine what could be the potential factors that have led to the high variability of volume estimates reported within healthy/control groups amongst published studies, as well as to the sizable overestimations in a subset of these studies. We addressed this objective while being cognizant of the natural variability of volumes that are due to the population demographic and due to ageing.

2.3.2 Methods

We surveyed the state-of-the-art of MRI studies with regard to scanning parameters, ROI definition and eventual nbM volume in a review of 37 studies published between 2010 and 2020. Papers were selected on the basis of a Web of Science search for neuroimaging studies that included terms Basal Forebrain, Nucleus Basalis or Cholinergic. We also included papers that referenced or were referenced in other included papers. The papers reviewed have been listed in Table S2.1. To compare the nbM volume between neuroimaging studies and histological studies, we collected nbM volumes in Table S2.1 from the healthy control group in the corresponding study.

Most studies used 1.5 T (14 of 37) or 3 T (22 of 37) scanners, whereas a minority used 7 T scanners (2 of 37) and one used a 0.3 T scanner. A spatial resolution of 1–1.5 mm isotropic was the most common (24 of 37), whereas 7 of 37 used larger voxels up to 3 mm isotropic and 8 of 37 used voxels smaller than 1.0 mm isotropic. All studies used a T_1-weighted structural scan as the participant-specific reference image typically from an MPRAGE sequence (Mugler and Brookeman 1991). The probabilistic atlas from Zaborszky et al. (2008) was the most common tool used for defining the nbM ROI and was reported to be used in 24 of 37 studies. The post-mortem MRI data from Kilimann et al. (2014) was used in 6 of 37 studies, and the post-mortem MRI data of Teipel et al. (2005) was used in 6 of 37 studies. The post-mortem MR data from Teipel et al. (2014a) was used twice. Some studies used more than one reference to localise nbM. An important aspect of using probabilistic atlases is the threshold selected for the localisation of the ROI and we found that only a minority of studies (7 of 24) report the probabilistic threshold they used. Of those that did, a threshold of 50% (or 0.5) was most common (5 of 7) with the remaining 2 studies using a more liberal 40% (or 0.4). Only three of the aforementioned papers reported both the probabilistic threshold used to extract nbM ROI and the estimated volume.

2.3.3 Findings

As shown in Table S2.1 (right hand column), the physical nbM volume in cubic millimetres was reported and/or could be estimated in only 7 of 37 studies (studies 1–7 in Table S2.1). The nbM volumes reported were 167 mm^3 (Table 2 from Grothe et al. (2014b)) and 128.53 mm^3 (Table 1 from Wolf et al. (2014)), 1377 mm^3 (estimated, p289, 'Regions of interest' from Markello et al. (2018)), 791 mm^3 (estimated based on Table 1 from Yuan et al. (2019)), 40–80 mm^3 (estimated based on Figure 1 from Teipel et al. (2016b)), 200–300 mm^3 (estimated based on Figure 2 from Fernández-Cabello et al. (2020)), and 290 mm^3 (Figure 2B from Schmitz et al. (2020)). The two highest nbM estimates (Markello et al. 2018; Yuan et al. 2019) were based on resampling the probability masks to lower resolution (with resolutions of 3.0 mm isotropic in functional space (Markello et al. 2018) and 1.5 mm isotropic in standard MNI space (Yuan et al. 2019). Two studies (studies 8–9 in Table S2.1) reported the size of nbM in terms of "mean voxel value" (not cubic millimetres). Gang et al. (2020) reported a mean voxel value of 0.31 calculated by scaling each voxel by the weighting contained within the probabilistic map and summing bilaterally. Schulz et al. (2018) reported the mean voxel value as 0.397 (after partial volume correction and do not report how this was calculated.

Six studies (studies 11–16 in Table S2.1) reported changes in volume of nbM or nbM subregions between groups in terms of cluster size (CS) or cluster extension (CE) (that is the number of contiguous voxels passing the height threshold, set at ≥ 5) and did not report absolute volumes. Note that the CS and CE do not have units and their conversion to cubic millimetres were not reported. To visualise the wide range of CS or CE, we listed these partial reports from the papers: the extent of atrophy between patients and the healthy control group were reported to be 312 in left Ch4 and 365 in right Ch4/Ch4p (Table 2 from the Grothe et al. (2010)), 566 in right Ch4al (Tabel 2 from Teipel et al. (2011)), 767 in left Ch4p and 836 in right CH4p (Table S4 from Grothe et al. (2012)), 156 in left Ch4 and 99 in right Ch4 (Table 1 from

Cantero et al. (2017)), 219 in right nbM (Table 3 from Nakaizumi et al. (2018)), 273 in left Ch4 and 181 in right Ch4 (Table 2 from Cantero et al. (2020)). While six studies (studies 17–22 in Table S2.1) reported the nbM volume, they did so by using metrics without a physical unit or a conversion to cubic millimetres (Barrett et al. 2018; Lammers et al. 2016; Nemy et al. 2020; Schmitz et al. 2018; Schmitz and Nathan Spreng 2016; Wang et al. 2019).

Five studies (studies 23–27 in Table S2.1) did not report the volume nor could the volume could not be estimated (Jacobs et al. 2018; Li et al. 2014; Teipel et al. 2014b; van Dalen et al. 2017; Wan et al. 2018). Okada et al. (2013) defined their nbM ROI based on the reported centre of gravity values from Zaborszky et al. (2008), although the exact steps deriving the final ROI was not clearly described.

For completeness we included an additional nine studies (28–37) in our review, but they did not separate the nbM from the larger surrounding regions (i.e., basal forebrain or SI). Two studies 27–28 in Table S2.1 reported the volume of the entire SI region, without separating the nbM. Gao et al. (2013) reported in cubic centimetres ($0.46 \pm 0.06\ cm^3$ or $460 \pm 60\ mm^3$, Table 1). George et al. (2011) reported the normalised volume (between 0.1–0.12 or 153–183.5 mm^3 as estimated by us based on Figure 2 and Table 1 from the paper). Likewise, studies 16 and 30–37 in Table S2.1 reported the volume of the entire basal forebrain, including the nbM, in cubic millimetres (Fritz et al. 2018; Grothe et al. 2012; Grothe et al. 2013; Grothe et al. 2014a; Lammers et al. 2018; Liu et al. 2018; Teipel et al. 2016a; Teipel et al. 2018; Zhang et al. 2011). The reported mean volume of basal forebrain also varies between studies, for instance, it is 481 mm^3 (Table 1 from Teipel et al. (2018)), 1020 mm^3 (Table 2 from Grothe et al. (2013)), 1884 mm^3 (supplementary information from Grothe et al. (2012)), 2201 mm^3 (Table 4 from Lammers et al. (2018)) and 5103 mm^3 (189 voxels was reported, estimate based on section 2.4 from Fritz et al. (2018)).

In summary, from MRI studies that either clearly reported or from which we were able to estimate nbM volumes in units of cubic millime-

tres, we found the total bilateral estimates (reported more often than unilateral) of the nbM to be in the range 40 mm^3 to 1377 mm^3. Population mean volumes ranged from 400–500 mm^3, or 300–400mm^3 when the minimum 40–80 mm^3 and maximum 1377 mm^3(which were outliers) were excluded. For volume losses of nbM reported in units of cluster size, we found highly variable ranges even for a unilateral nbM, such as from 156–872 in left nbM, 99–836 in right nbM. However, these clusters can be highly variable in size depending on the size of the voxel. If the resolution of all the studies were 1.0 mm isotropic, the mean atrophy of unilateral nbM from those studies would be 377 mm^3, which would suggest a much higher volume for the healthy bilateral nbM than those reported in histological studies and in the two widely referenced in MRI studies. Please note that we report inconsistencies in measured nbM volumes in literature. However, natural differences in tissue volumes between young and elderly groups or control and disease groups are expected. In addition to keeping this important caveat in mind, we only included volumes reported from the healthy controls for our analysis.

Overall, in 74% (20 out of 27) of the studies, we observed a distinct lack of the reporting nbM volume with meaningful physical units (such as cubic millimetres). This was especially true in those papers examining the correlation between nbM volume and development of certain diseases. We also noted the discrepancy amongst (f)MRI studies, and between histology and post-mortem MRI studies in the nbM volume reported.

In addition, crucial methodological details were also often missing in some of the reviewed papers. For example, 71% of studies that used the probabilistic atlas (Zaborszky et al. 2008) to define nbM ROI failed to report the probabilistic threshold used to extract nbM. For the subset of studies that had volume reports (or its estimates) as well as sufficient methodological information, we graphically displayed variations in nbM volume as a function of methods employed (histological studies, public toolboxes, PMP and MPM) in Figure 2.2. The figure illustrates the large variation in nbM volume estimates amongst studies

and methods.

The volumes obtained from histological studies (Grinberg and Heinsen 2007; Halliday et al. 1993) are shown Figure 2.2. The nbM volumes are of 156, 154, 134, 128 and 76 mm^3 (Halliday et al. 1993), 58.6 mm^3 (Grinberg and Heinsen 2007). These histological studies provide our reference (due to the absence of a 'ground truth') estimate of nbM volume and suggest the average nbM volume is around 118 ± 37 mm^3.

Next, the volume of the bilateral nbM was found to be 733 mm^3 from SPM anatomy toolbox version 2.2, 538 mm^3 from SPM anatomy toolbox version 3.0, 569 mm^3 in MNI-ICBM152 and 544 mm^3 in Julich-brain MNI-Colin27 space, indicated respectively with empty grey circles and solid grey circles in Figure 2.2. The mean volume across the SPM anatomy toolbox versions and MNI spaces was 596 ± 80 mm^3; approximately four times that of the mean volume reported by histology studies and twice that of the mean volume in the MRI studies referenced earlier.

2.4 Testing probablistic maps

2.4.1 Goal 2

The variability amongst volumetric estimates of the nbM reviewed in the previous section is quite remarkable. The smaller, more consistent, and more realistic volumes are yielded by histological analysis. MRI studies however reported or implied a large range of the nbM volumes, with the larger volumes being unrealistic given what we know about the nbM. Here, we hypothesised that one source of the variability in reported volumes in MRI studies is related to the different methods to localise nbM. In the present section, we aimed to test the effects of parameter choice, particularly the probabilistic threshold used in probabilistic maps, on the volumetric estimates of the nbM.

2.4.2 Methods

To investigate how nbM volume varies in standard MRI space when applying probabilistic maps, we extracted nbM using the SPM anatomy toolbox (Eickhoff et al. 2005a; Zaborszky et al. 2008) version 2.2 and 3.0, maximum probability maps (MPM, version 2.2) (Amunts et al. 2020) and cytoarchitectonic probabilistic maps (PMP, version 4.2) (Zaborszky et al. 2019) (Figure 2.2). Although those datasets all have the resolution of 1.0 mm isotropic, the dimensions of the volume files differed amongst each other, which will prevent applying the mask created from one atlas to an acquired dataset if the reference brain is not included. The MRI images from the SPM anatomy toolbox version 2.2 had a dimension size of 151×181×154, whereas SPM anatomy toolbox version 3.0 yielded a size of 193×229×193. MPM version 2.2 and PMP version 4.2 yielded a dimension size of 256×256×256. SPM nbM ROIs were extracted by the default functions in the anatomy toolbox. The functions are based on MPM maps that are already provided in the toolbox with 'L BF(Ch4)' and 'R BF(Ch4)' as the input parameters. Two important criteria for including voxels for the reference brain while generating MPM are: 1) the probabilities for any area are higher than 40%, 2) the sum of the probabilities for all areas are higher than 50% (Eickhoff et al. 2005b). Therefore, we assume the probabilistic threshold for a single ROI is 40%. However, the brains were registered to MNI-Colin27 space in version 2.2 and to Julich-brain in version 3.0. The MPM version 2.2 (Amunts et al. 2020) nbM ROI was in MNI-ICBM152 and MNI-Colin27 spaces, which were extracted by assigning to pixels whose intensity equalled 12 using a custom python script.

We also used public PMP version 4.2 (Zaborszky et al. 2019) to investigate the effects of thresholding on volume. By setting probabilistic thresholds ranging from 0.3 to 0.7 with increments of 0.1, we obtained nbM ROIs at each threshold and then calculated its volume (Figure 2.2) in both MNI-ICBM152 and MNI-Colin spaces. It is also important to note here that the PMP and MPM in the Julich brain atlas (Amunts and Zilles 2015) and in the SPM anatomy toolbox are an expansion of

work on the 10 post-mortem brains used in Zaborszky et al. (2008).

To approximate and evaluate the effects of thresholding probabilistic cytoarchitectonic maps on in vivo sub-millimetre resolution isotropic MRI images, we applied the map from SPM anatomy version 2.2 to our own dataset acquired at 7T. This dataset included whole brain anatomical scans at 0.8 mm isotropic from five participants acquired with a 3D-MP2RAGE (Marques et al. 2010) sequence with Fat Navigators (Gallichan et al. 2016) [TI1/TI2 = 800/2750 ms, FA1/FA2 = 4°/5°, TE = 1.95 ms, FOV = 256×256 mm2, matrix size = 300×300, slices = 256, Phase partial Fourier = 7/8, Slice partial Fourier = 7/8, FatNav resolution = 2 mm, FatNav FA = 3.0°, Train-FatNav delay = 20 ms]. The fat navigators were used to retrospectively correct for within scan head motion. Each dataset was bias-corrected in SPM12 (Ashburner and Friston 2005) and processed using Freesurfer recon-all (Fischl 2012). Each processed brain was then carefully registered to MNI-Colin27 space using antsAI and antsRegistrationSyN (Avants et al. 2011). To import the probabilistic maps into each participant's native space, the inverse of the transformation matrix was applied to probabilistic maps of nbM in MNI-Colin27 space using antsApplyTransforms. The effect of thresholding was then explored in the same range as mentioned above. nbM volumes were calculated using custom python code. The mean and standard error of the bilateral nbM volume from each participant was shown in Figure 2.2.

2.4.3 Findings

Probabilistic maps determine the probability for each voxel that it represents the nbM, that is, in the map developed by Zaborszky et al. (2008), a probability of 0.5 indicates that a voxel was found to be within the nbM in 5 out of the 10 brains investigated in that study. As we show earlier, the inclusion threshold used for obtaining the nbM ROI has not been widely reported in the literature, but necessarily influences the eventual volume. We tested the probabilistic map using thresholds from 0.3 to 0.7 to investigate volume changes of nbM based

on the nbM voxel distributions from Zaborszky et al. (2008), PMP version 4.2 (Zaborszky et al. 2019), and probabilistic maps (SPM anatomy toolbox version 2.2) registered to in vivo individual participant's space. In Figure 2.2, the volumes in MNI-Colin27 space decreased from 802 mm^3 at a threshold of 0.3 to 6 mm^3 at a threshold of 0.7. Likewise, the volumes in MNI-ICBM152 space decreased from 754 mm^3 at threshold of 0.3 to 0 mm^3 at a threshold of 0.7. When thresholds were set to 0.4 and 0.5, the two levels that have been reported in the literature, nbM volumes were 392 mm^3, 160 mm^3 in MNI-ICBM152 space, respectively and 432 mm^3, 193 mm^3 in MNI-Colin27 space, respectively. We also created nbM ROIs for our own 7T datasets at subject native space with the resolution of 0.8 mm isotropic based on PMP (SPM anatomy toolbox version 2.2) and thresholded the maps from 0.3 to 0.7. As in the public datasets, the volume decreased with increasing the threshold, as shown by the decreasing grey solid line. Error bars represent standard deviation of nbM volume amongst our five participants. The mean of nbM volume across participants were 300.3 mm^3 and 91.0 mm^3 when thresholds were 0.4 and 0.5, respectively.

In summary, nbM volume at 50% threshold seems to be most compatible to the volume from histological studies, although even this threshold results in considerable variation between datasets. However, only 5 out of 24 reviewed papers reported using probabilistic maps to delineate nbM having 50% as their chosen threshold. 2 of these 5 papers allowed us to estimate their reported volume of nbM, which are 200–300 mm^3 and 791 mm^3. 2 out of 24 use 40% as their threshold. It may be that studies, which didn't report a threshold to extract nbM ROI, used the default settings from the SPM anatomy toolbox. According to the procedures to calculate MPM (Eickhoff et al. 2005a), we could assume that these studies also use 40% as their threshold to extract nbM. The nbM volume with default threshold in SPM anatomy toolbox is around 596 mm^3, which overestimates nbM by about 505% compared to the volume provided by histological studies.

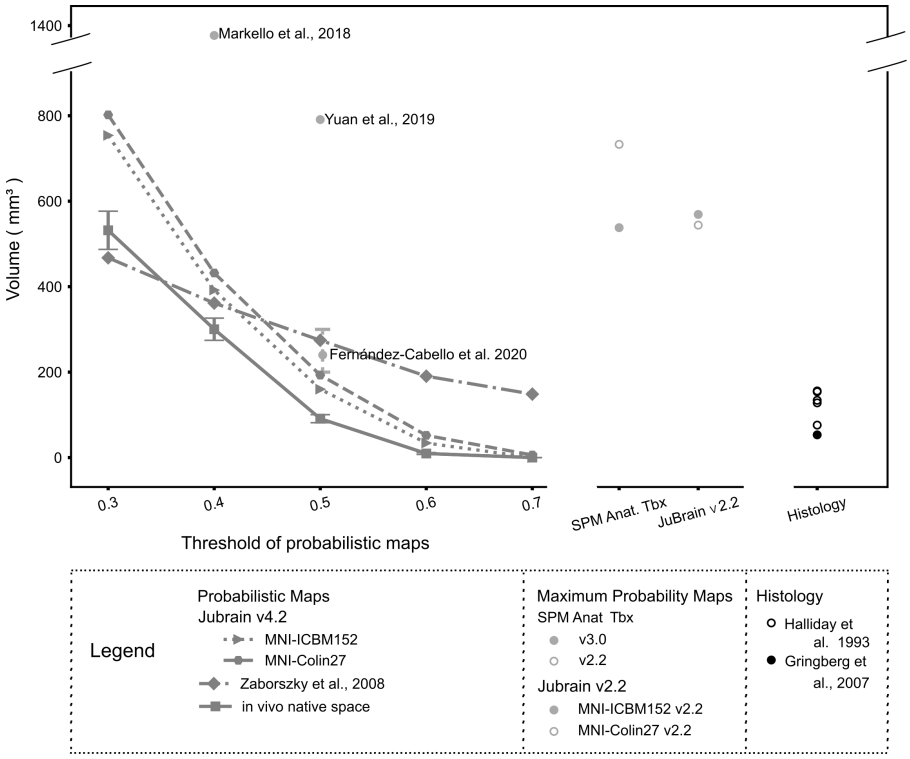

Figure 2.2: Summary of variations of nbM volume from different sources. nbM volume from histological studies represented by black circles. Each empty black circle represented a nbM volume from one subject from Halliday et al. (1993). Solid black circle indicated nbM volume from Grinberg and Heinsen (2007). The nbM volume estimation based on Julich-brain V2.2 in MNI-ICBM152 and MNI-Colin27 space were represented by solid and empty grey circle correspondingly. The nbM volume estimation based on SPM anatomy toolbox version 2.2 and version 3.0 were by empty and solid grey circle correspondingly. Grey dotted line with right-triangle markers and grey dashed line with hexagon markers: nbM volumes estimated based on PMP V4.2 (Zaborszky et al. 2019) at different thresholds in MNI-ICBM152 and MNI-Colin27 space. Grey dash-dotted line with diamond markers: nbM volume range reported from Zaborszky et al. (2008). Grey solid line: nbM volume when the PMP atlas (SPM anatomy toolbox version 2.2) was in native space across five participants at 0.8 mm isotropic resolution at different probabilistic thresholds.

2.5 Novel mask and simulating the effect of downsampling

2.5.1 Goal 3

While the threshold set in probabilistic maps is a clear determinant of estimated volume of the nbM, other factors may also play a role in the observed volume discrepancy. One factor that could play a role is the spatial resolution of the stitched and digitised version of the histological data on which the nbM ROI is based. Then, on the resolution of the subsequent transformation to the standard MRI space such as the MNI space. Unless nbM is readily visible in an individual MR image, extracting nbM ROI occurs in the standard MRI space. Thus, the transformation between a native space brain and a reference template brain can influence the estimated volume size, not only because of the individual differences of the size and location of nbM but also by its alignment with the template nbM. Therefore, we hypothesised that the head position in the head coil during acquisition and the slice angulation during data acquisition and the later transformation to the reference template may have an influence on volumetric estimate. That is, head position would determine the relationship between voxels in native space and voxels of the reference nbM ROI, and the difference in spatial resolution between the native space data and the reference space and its corresponding resampling would together influence the volume outcomes. For this, we specifically tested whether head position interacted with differences in spatial resolution of the image used to delineate nbM ROI, and whether this could lead to an overestimation or variability of volumetric estimates of the nbM. To test this idea, we first developed a new high-resolution nbM ROI using the publicly available ultra-high resolution BigBrain dataset.

2.5.2 Methods

It is important to reiterate that the nbM probabilistic maps are based on the combination of histological data and their corresponding 1.0 mm

isotropic post-mortem reference scans (Zaborszky et al. 2008). Even if the nbM neurons were originally identified in stitched high-resolution histological sections, their downsampling to 1.0 mm isotropic can lose many details. We explored several additional publicly available high-resolution ex vivo datasets (including MGH atlas (Edlow et al. 2019), Ding atlas (Ding et al. 2016)), we developed a novel ROI mask for the nbM based on the 100 μm isotropic BigBrain dataset (Amunts et al. 2013), the only dataset where the nbM could be visually discerned (Figure 2.3). This brain was extracted, embedded in paraffin and sectioned in 7404 coronal histological slices. The resulting BigBrain dataset offers a digitised reconstruction of stained cell bodies at 20 μm isotropic resolution in histological space. They provide volumes in MNI-ICBM152 and MNI-SYN24 stereotaxic space at different resolutions. We obtained the version at a 100 μm isotropic resolution in MNI-ICBM152 space, from the BigBrain3D Volume Data Release 2015 (https: //bigbrain.loris.ca). In this dataset, low intensity (dark) areas represent the location of neurons relative to the brighter surroundings. Due to the large size of the data and to allow feasible computation, we extracted a smaller volume of the data (dimension of 900×500×140 of the original dimension of 1970×2330×1890) that included the nbM and its surrounding structures. To delineate the nbM, we adhered to Mesulam's definitions (Mesulam and Geula 1988). We regarded nbM as one ROI rather than segregating it into 2 or 6 parts. To draw the boundaries separating nbM from surrounding structures, we used sharp, local drops of image intensity from regions considered to be within nbM to surrounding areas considered to be outside nbM, following the procedure of Zaborszky et al. (2008). To reduce the subjective influence on defining nbM, we used a semi-automatic segmentation method to delineate the border of the region in both hemispheres. We first drew a larger ROI mask that included all parts of nbM in each hemisphere and used AFNI's *3dSeg* (Vovk et al. 2011) to segment the contents of that mask into 3 clusters. We then thresholded the posterior probability maps from the segmented cluster 1 at 0.7 for both hemispheres and manually excluded areas outside of nbM slice by slice using ITK-SNAP (Yushkevich et al. 2006) by carefully inspecting the data all three

(coronal, sagittal and transverse) dimensions.

We next tested the robustness of estimating nbM volume with regard to spatial resampling using this novel BigBrain mask. Due to the diffuse and open shape of the nbM, the exact voxel location with respect to the 3D nbM structure can influence the eventual estimation of volume with spatial resampling. To investigate the impact of this effect in a population of subjects, we randomly simulated 180 head orientations across all spatial resolutions 1000 times. For each iteration, we simulated 6 head positions and downsampled each head orientation from 100 μm up to 3 mm in steps of 0.1 mm (30 steps) using zoom from sdimage in scipy with 'nearest' interpolation. For each resolution, we computed volume mean in cubic millimetres, and coefficient of variation of volume for left, right and bilateral nbM (Figure 2.4). We also estimated the number of voxels (Figure S2.1) in left and right nbM using custom python scripts.

2.5.3 Findings

Using the BigBrain dataset, we estimated the volume of the nbM to be 31.51 mm^3 (31,513 voxels) and 34.85 mm^3 (34,846 voxels) for the left and right hemispheres respectively, thereby, amounting to a total bilateral volume of 66.36 mm^3 (66,359 voxels). While this may seem small compared to other reports of the nbM volume, we do not believe this to be an underestimation for the following reasons. The BigBrain atlas gives us direct visibility of neuronal clusters to define the nbM instead of an MRI voxel signal proxy. We followed a similar procedure as Zaborszky et al. (2008) to avoid including too many non-nbM regions (see 2.5 Methods). Shrinkage and distortion due to histological processing was already partially corrected for in the original reconstruction of the BigBrain data that we used (Please see details in the section of supporting material 2 in Amunts et al. (2013); and in the section on Shrinkage Estimation in Wagstyl et al. (2020)). From our simulation analysis, we calculated the average volume and coefficient of variations of volumes (CVV) at each resolution (Figure 2.4). We

observed that the average volume [nbM (L): 29.46 ± 0.91 mm^3; nbM (R): 30.44 ± 0.56 mm^3; nbM (Bilateral): 59.90 ± 1.43 mm^3] was stable [CVV: nbM(L): 0.10 ± 0.04; nbM (R): 0.22 ± 0.01; nbM (Bilateral): 0.14 ± 0.01] across resolutions from 100 μm to 1.0 mm isotropic. For resolutions from 1.0 mm isotropic to 2.0 mm isotropic, the average volume decreased [nbM (L): 25.75 ± 2.92 mm^3; nbM (R): 27.87 ± 2.25 mm^3; nbM (Bilateral): 53.61 ± 4.28 mm^3] and became more variable [CVV: nbM(L): 0.34 ± 0.18; nbM (R): 0.37 ± 0.10; nbM (Bilateral): 0.26 ± 0.09]. For resolutions between 2.0 mm isotropic to 3.0 isotropic, the average volume was even smaller [nbM (L): 23.43 ± 6.62 mm^3; nbM (R): 26.91 ± 1.76 mm^3; nbM (Bilateral): 50.35 ± 6.93 mm^3] and yet more variable [CVV: nbM(L): 0.97 ± 0.31; nbM (R): 0.74 ± 0.12; nbM (Bilateral): 0.58 ± 0.14]. Thus, starting with nbM segmented based on one ultra-high-resolution dataset, the volume estimation was only reliable for resolutions higher than 1.3 mm isotropic, as variance was seen to increase with lower resolutions. Strikingly, at a resolution of 2.0 mm isotropic, volumes could be either very large or very small (Figure S2.1). We also counted the number of voxels inside the ROI (Figure S2.2) to compare with the studies that report numbers of voxels. The average number of voxels monotonically decreased with increasing spatial resolution. The number of voxels inside the nbM are up to 34,846 (Figure S2.2) when the resolution is below 0.5 mm isotropic, to compare the number clearly with much lower resolution such as 1.0 [Bilateral nbM: 57.09 ± 9.39 voxels], 2.0 [Bilateral nbM: 5.99 ± 2.43 voxels] and 3.0 mm isotropic [Bilateral nbM: 1.70 ± 1.29 voxels].

In summary, this analysis highlights the difficulty of applying a high-resolution nbM ROI in relatively low-resolution MRI datasets including those that are typically considered as high-resolution (0.8–1.0 mm). At even lower spatial resolutions, it becomes increasingly impactful whether individual voxels are counted as in or out of the nbM ROI, which depends on how the voxel grid aligns to the ROI mask being used. This effect may explain some variability in the volume between individuals and between studies. In the case of applying a (relatively) low resolution map to a scan with higher resolution (e.g., applying the

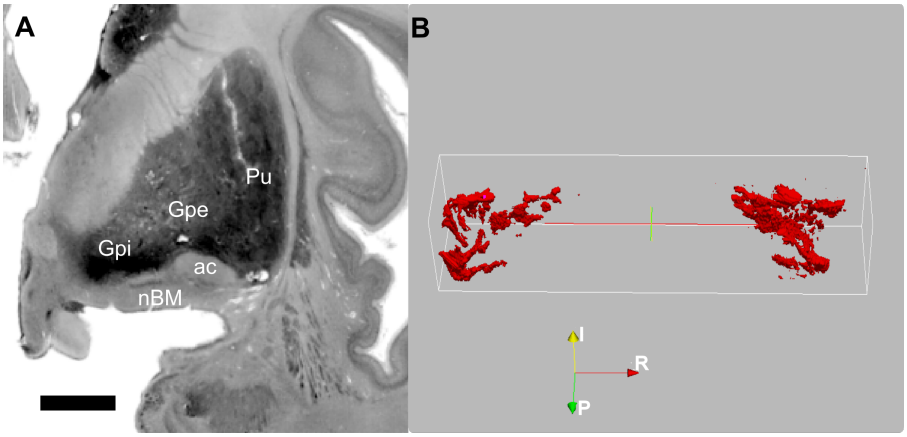

Figure 2.3: Semi-manual segmentation of nbM in the BigBrain dataset (Amunts et al. 2013).
A: The 1339th coronal slice along anterior to posterior direction from the released dataset at 100 μm isotropic. Zoom factor (width x height: 3.41 x 3.42). Scale bar: 5 mm.
B: 3D structure of the segmented nbM. R, I and P represent the right, inferior and posterior of the brain.

1 mm isotropic Zaborszky map to 0.7 mm isotropic data), the structural details from the high-resolution scan cannot be taken advantage of, since the map is limited in its ability to resolve at 1 mm. On the other hand, our novel nbM ROI contains the whole detailed diffuse structure of the nbM at the resolution of 0.1 mm isotropic in MNI space as provided by the BigBrain dataset, and its downsampling (e.g., 0.7 mm isotropic) would still retain more structural information than if the reference data was acquired using a much lower resolution of 1 mm isotropic. Thus, our map may be more appropriate for high resolution sub-millimetre studies, and is made publicly available along with the code (https://github.com/YawenWang1/nbM_review.git). Our analysis suggests that despite having been derived at a high resolution, the nbM map would become unreliable at spatial resolutions lower than 1.3 mm isotropic. Considering the higher variability of nbM volumes

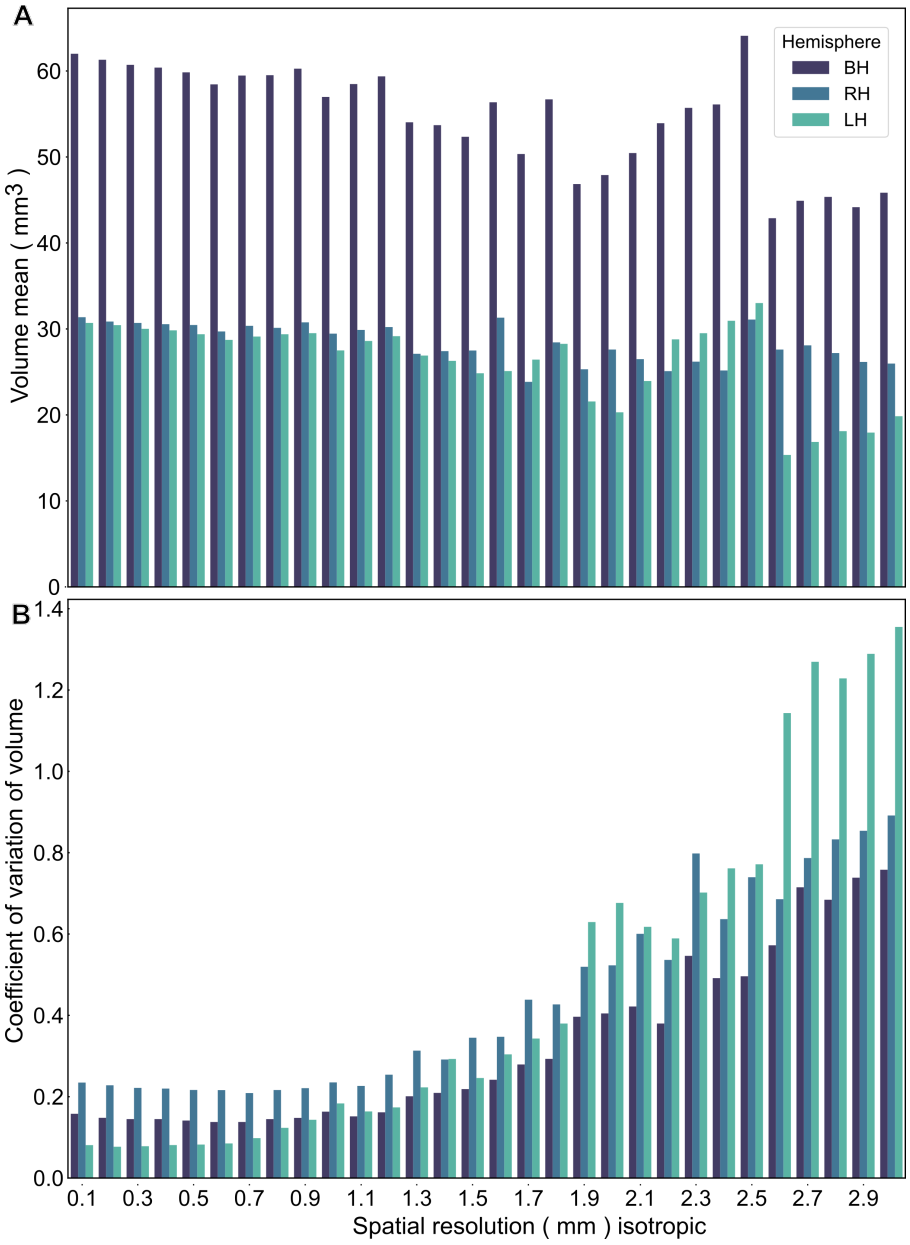
A
Hemisphere
BH
RH
LH
Volume mean (mm3)
0
10
20
30
40
50
60
B
Coefficient of variation of volume
0.0
0.2
0.4
0.6
0.8
1.0
1.2
1.4
0.1
0.3
0.5
0.7
0.9
1.1
1.3
1.5
1.7
1.9
2.1
2.3
2.5
2.7
2.9
Spatial resolution (mm) isotropic

Figure 2.4: (Previous page.) Volume mean estimates for the semi-automatically delineated nbM ROI mask using the 100 μm BigBrain data, downsampled at different spatial resolutions (**A**), and the corresponding coefficient of variation (**B**).
Abbreviations: BH: left and right hemisphere combined; RH: right hemisphere; LH: left hemisphere.

reported in studies that used the mask in fMRI space ($\sim$ 3 mm), the extent of overestimation of nbM is likely more severe than if the data were analysed in anatomical space ($\sim$ 1 mm). Taken together, our results emphasise the need for using high-spatial resolutions for fMRI studies of the nbM as well.

2.6 Direct imaging of the nbM from post-mortem brains using high resolution MRI

2.6.1 Goal 4

Transferring anatomical knowledge (anatomical markers or a histology-based ROI) into the reference frame of MRI data is subject to inherent flaws and challenges. Our fourth objective was, therefore, to examine the feasibility of directly imaging the nbM using the current state-of-the-art MRI techniques, since a direct delineation of the nbM in MRI images based on sufficient image contrast would circumvent some of the challenges with the currently used methods in literature. In this regard, we first explored publicly available high-resolution post-mortem MRI datasets (MGH brain (Edlow et al. 2019), and the Ding atlas (Ding et al. 2016)) to see if there is suitable image contrast to enable direct delineation of the nbM. Next, we used a novel ultra-high-resolution ex vivo dataset (Roebroeck et al. 2015, July) acquired using a human 9.4 T scanner (Scannexus B.V., Maastricht, The Netherlands). These explorations yielded some useful insights, based upon which we discuss potentially encouraging avenues towards in vivo structural MRI of the

human nbM.

2.6.2 Methods

First, we delved into the 100 μm isotropic MGH brain (Edlow et al. 2019) and the images from the 200 μm isotropic Ding atlas (Ding et al. 2016). Those two datasets were acquired with different imaging parameters, and both had very high spatial resolution. The MGH brain (Edlow et al. 2019) provides a good contrast between cortical and subcortical structures. The Ding atlas (Ding et al. 2016) provided MRI images with T_1, PD, and T_2^* weighted contrast and also, MRI images acquired at different flip angles (20°, 40°, 60°, 80°) resulting in T_1 and PD weighted contrasts (Sprawls Jr 2000, July).

As shown in Figure 2.1 A, nbM is visible in myelin-stained sections, where it shows as a light region embedded in the heavily myelinated SI. An increased T_2^* value indicates reductions of local myelination (Lee et al. 2017; Lee et al. 2012). Thus, we explored a quantitative T_2^* dataset acquired at 9.4T with a resolution of 200 μm isotropic using state-of-the-art image acquisition and reconstruction methods (Roebroeck et al. 2015, July). Importantly it also provided much higher dynamic range and contrast-to-noise ratio than the atlases mentioned above. We then used the semi-automatic segmentation method to draw nbM in both hemispheres. The qT_2^* images (Figure 2.5 A) were acquired at our institute using a Siemens Magnetom 9.4T human scanner using a head gradient set (AC84-mk2, maximum amplitude 80 mT/m, maximum slew rate 333T/m/s, inner diameter 36 cm) with a specialized 8-parallel transmitter/24-receiver head coil. The multi-echo data was acquired using a 3D gradient recalled echo pulse sequence with kt-points composite excitation pulse (matrix 676×844×704, FA = 15°, 2 avgs, TR = 32 ms, TE = 10 ms, RO-bw = 80 Hz/px, TA = 8h42m, full duty-cycle). Due to the large size of the dataset and to make the analysis computational feasible, we extracted a smaller volume covering nbM and its surrounding structures with the dimension of 90×578×590 from the original dimension of 810×768×704. To calculate the nbM

volume, we used a similar semi-automatic segmentation method to the one we used to delineate nbM in the BigBrain dataset (Section 2.5.2). The final nbM ROI of both hemispheres were manually adjusted by viewing it in 3D in ITK-SNAP (Yushkevich et al. 2006). We compared different extents of anisotropic diffusion denoising on the qT_2^* image with different parameters (AFNI's *3danisosmooth*) on the quality of segmentation of nbM in both hemispheres. By comparing the segmented masks, we settled on the following parameters to denoise the qT_2^* dataset by AFNI's *3danisosmooth* (Ding et al. 2005) with '-deltat' set to 0.1 and '-edgefrac' set to 0.8 and then used *3dSeg* to segment the left nbM. The cluster 2 was thresholded at 0.5 to get the initial nbM mask. For the right nbM, we found the denoising procedure did not impact the segmentation outcomes. Thus, we used the native qT_2^* for the right hemisphere dataset for *3dSeg* algorithm and extracted the values between 0.01 and 0.3 in cluster 2 as the initial nbM mask. The final masks for both hemispheres were manually adjusted by viewing it in 3D in ITK-SNAP (Yushkevich et al. 2006) and combined to obtain the bilateral nbM ROI.

2.6.3 Findings

The 100 μm isotropic synthesised FLASH25 volume from MGH (Edlow et al. 2019) provided high apparent contrast between cortical and subcortical structures (Figure S2.3). However, based on careful visual inspection, we did not find any contrast between regions of the SI that would enable image-based delineation of the nbM. The 200 μm isotropic dataset from Ding atlas (Ding et al. 2016) provided the possibility to explore imaging nbM under different flip angles, proton density, T_1, and T_2^* weighted contrasts (Figure S2.4). However, again, on careful visual inspection we did not find any contrast between regions of the SI to indicate the nbM in any image set.

Finally, we explored our in-house ex vivo quantitative T_2^* dataset acquired at 9.4T (unpublished data, Roebroeck et al. (2015, July)). T_2^* has a range of 16–40 ms at 7T scanner and decreases with higher mag-

netic field (Metere et al. 2017; Peters et al. 2007). The dynamic range of our qT_2^* dataset is 0–40 ms, which likely covers the whole range of T_2^* across tissues. The high image fidelity due to the optimised acquisition and reconstruction of this data in addition to access to its full dynamic range, allowed us to visually distinguish nbM as a bright region within the darker SI. Our semi-automatic segmentation of this 200um isotropic dataset resulted in a 36.26 mm^3 region (4533 voxels) of relatively high signal intensity on the left hemisphere and a 33.86 mm^3 (4233 voxels) area on the right (Figure 2.5) at similar positions of the nbM as indicated in the myelin-stained slice in Figure 2.1 A and landmarks based on (Mesulam et al. 1983), thereby further supporting our segmentation method. We show the normalised intensity of nbM and its surrounding regions (Figure 2.5 C) illustrating an appreciable difference in intensity profile in our demarcated region. Additionally, the total bilateral volume is well in line with what we expect from histological studies mentioned in the earlier sections. As far as we know, this is the first direct MRI-only image of the nbM, demonstrating the feasibility of imaging the human nbM albeit using a post-mortem brain. From this exercise, we can confidently conclude that using high-resolution, the appropriate contrast mechanism (in our experience, quantitative T_2^*) and high spatial fidelity imaging at ultra-high field shows the most promise for resolving nbM directly using MRI.

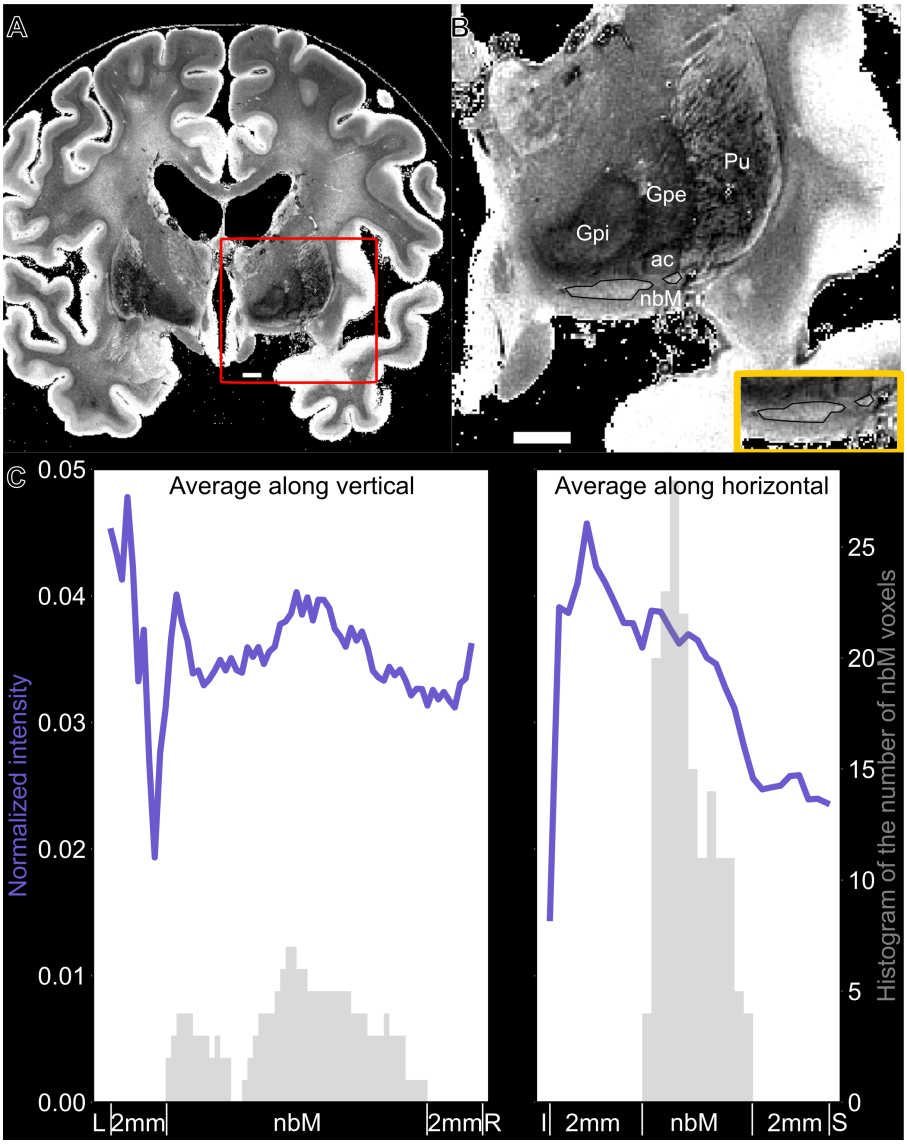
A
B
Pu
Gpe
Gpi
ac
nbM
C
Average along vertical
Average along horizontal
Normalized intensity
Histogram of the number of nbM voxels
0.05
0.04
0.03
0.02
0.01
0.00
25
20
15
10
5
0
L
2mm
nbM
2mm
R
I
2mm
nbM
2mm
S

Figure 2.5: (Previous page.) Post-mortem quantitative T_2^* MRI may allow the localisation of nbM.
A: The 396th coronal slice along anterior to posterior direction from a 200µm isotropic resolution quantitative T_2^* ex vivo dataset acquired at 9.4 T (unpublished data, Roebroeck et al. (2015, July)). Zoom factor (width x height: 0.87 x 0.87). Red box indicates the zoomed panel in B. Scale bar: 5 mm.
B: Zoomed view of basal ganglia and nbM in the same slice as A. The yellow inset is the cropped view of the nbM indicated by a black outline. Zoom factor (width x height: 2.55 x 2.55). Scale bar: 5 mm. Scale bar: 5 mm.
C: Normalized mean intensity of the zoomed panel across vertical (Left) and horizontal direction (Right). The purple line indicates the normalized mean intensity, whose Y axis on the left. Histograms of nbM voxels in both horizontal (Left) and vertical (Right) direction of the zoomed view were shown in grey.
Abbreviations: nbM: nucleus basalis of Meynert; ac: anterior commissure; Gpi: internal globus pallidus; GPe: external globus pallidus; Pu: putamen; L: left; R: right; I: inferior; S: superior.

2.7 Discussion

The nbM is the major source for cortical cholinergic input and has been implicated in many cognitive processes and neurodegenerative diseases. Accurately locating the nucleus is essential for in vivo neuroimaging studies of the nbM in humans. As the nbM is an open and diffusive structure lacking clear boundaries with surrounding regions, it has been challenging to visualise nbM in structural MRI images at commonly used resolutions such as 1 mm isotropic. On the other hand, the nbM can be clearly discerned in histologically treated slices of post-mortem brains. The primary strategy in MRI studies of the nbM to date has therefore been to transfer histological information about the shape and size of the nbM into the reference frame of the MRI data.

2.7.1 Review of the volume of nbM from the literature

In the present paper, we surveyed methods used and reported volumes of the nbM from previous MRI studies. We found 89% of the studies

used standard field strength (3T and below) scanners. Only 5% of the studies used high-field (7T) scanners. All the studies acquired T_1-weighted structural images as the base to extract nbM. 19% of the studies reported or implied nbM volume in cubic millimetres. 74% of the studies reported nbM volume in various metrics without describing the conversion between the metric and cubic millimetres. 65% of the studies used probabilistic maps to extract nbM and only 29% reported the probabilistic threshold used to extract nbM. Of those that did, 71% of the studies chose 50% (0.5) as the threshold with the remaining 29% of the studies using a more liberal 40% (0.4). When we compared estimates of the nbM derived directly from histological data to estimates of the nbM in MRI we found a wide range of nbM volumes reported or implied in the MRI literature to date, some of which seemed unrealistic when compared to the results of histological studies (Grinberg and Heinsen 2007; Halliday et al. 1993).

2.7.2 Testing probabilistic maps

One source of the variability could be variability in the probabilistic threshold authors had used to delineate nbM, which we found to be rarely reported yet was critical in determining the eventual size of the ROI. After exploring different publicly available toolboxes, PMPs, MPMs and a high resolution in vivo 7T dataset, we found in 1) using standard probabilistic maps (Zaborszky et al. 2008; Zaborszky et al. 2019) across a number of datasets, a threshold of 50% resulted in masks with volumes closer to the volumes estimated from histology. 2) Nevertheless, the 50% threshold still resulted in considerable variability, both in our analysis and in published work (Fernández-Cabello et al. 2020; Yuan et al. 2019). 3) The default settings of the SPM anatomy toolbox seemed to give a substantial overestimation.

2.7.3 Novel mask and simulating the effect of downsampling

An additional source of variability could arise from the process of downsampling high resolution histological data to match lower resolution (f)MRI data, which may be especially problematic for the defuse structure of the nbM. To understand how the apparent systematic overestimation of nbM in the majority of reviewed MRI studies could come about, we segmented nbM from the BigBrain, and applied this mask to 6000 head positions and downsampled from 0.1 mm to 3.0 mm isotropic. We did not find a systematic increase in the mean estimated volume at lower resolutions, however we found that the variance of bilateral nbM volume increased drastically for voxel sizes above 1.3 mm isotropic. For small voxel sizes i.e., spatial resolutions higher than 1.3 mm isotropic, the volume estimate was relatively stable [CVV: 0.26 ± 0.09]. Thus, one potential risk of volume estimation is downsampling of a high-resolution mask to match especially lower resolution MRI data. We therefore urge caution regarding volumetric measurements of nbM reported from (f)MRI especially at spatial resolutions lower than 1.3 mm isotropic. The novel high-resolution mask we created for this analysis may be useful for future studies, especially for (f)MRI studies with high resolution. We have therefore made our mask publically available.

2.7.4 Direct imaging of the nbM from post-mortem brains using high resolution MRI

Ultimately, applying any mask originally defined in histological space in one (or more) brain(s) to MR images of other brains will likely always be fraught with challenges. The likely best solution to this problem will be to delineate the nbM directly from the individual MRI datasets. To test the feasibility of using MRI to delinerate nbM directly, we inspected three ex vivo high resolution datasets with various contrasts. While nbM was not directly discernable in the Ding et al. (2016) 200 μm or MGH brain (Edlow et al. 2019) 100 μm datasets, we found that we could observe a region of bright voxels that likely corresponded to the nbM in an ultra-high resolution 200 um qT_2^* ex vivo dataset ac-

quired using an ultra-high field 9.4T human scanner. Even with such a high spatial resolution, one factor for being unable to visualise nbM in other datasets could be insufficient dynamic range of intensities in the MR image. For instance, the image intensity range for MGH dataset available for download is 0 to 53.57 signal units. While this intensity range may suffice for delineating grey matter from white matter, it could be insufficient to render the demarcation of small subcortical structures such as the nbM. Therefore, having the entire dynamic range of the acquisition available would be another step towards making these datasets more valuable to studies that go beyond the cortex. In other words, resolving small structures such as the nbM in MRI images requires the optimal contrast, ultra-high spatial resolutions and having enough dynamic range in the reconstructed image.

From our exploration of datasets (Ding atlas, MGH brain, qT_2^*) thus far, we can say that this is the first clear and direct visualisation of human nbM using MRI. Given the advent and availability of high-field (7T and 9.4T) MRI, it is now almost routinely possible to acquire sub-millimetre (functional) data. However, as we saw in the Ding and MGH datasets, increasing resolution alone is not enough to successfully segment nbM. From our exploration of existing datasets, it is all the more important to choose the right contrast, optimise acquisition and reconstruction parameters so as to be able to visualise nuclei of interest. While we emphasise the importance of ultra-high field and ultra-high resolution MR imaging for the human nbM using the illustrative example of the qT_2^* dataset, we strongly believe such optimised data acquisition and analysis would also help unravel the structure and properties of other subcortical nuclei and structures as well.

In our literature survey (Section 2.3), we observed a lack of reporting of the nbM volume with a physical unit in 30 studies, and inconsistencies of nbM volume amongst healthy control groups in 7 studies. Despite contributions of individual variability and effects of age differences, we suggest a major contributor to these inconsistencies could be the consequence of using various probabilistic thresholds

and resampling between the native space and atlas space. Using a low threshold and resampling to a lower resolution, especially in functional space, leads to a higher inflation of volume estimate. Although using the same probabilistic threshold (50%), by resampling to 1.5 mm functional space, Yuan et al. (2019) had a much higher estimate (791 mm^3) than Fernández-Cabello et al. (2020) (200–300 mm^3), who resampled to 1.5 mm anatomical space. Using 40% as threshold and resampling to 3.0 mm isotropic, Markello et al. (2018) defined nbM with the volume of 1377 mm^3. Currently there is a lack of a gold standard for nbM volume in the literature. The closest we can get is using ultra-high-resolution datasets such as the BigBrain dataset, and using ultra-high field quantitative MRI data using contrasts at a spatial scale that can enable clear, visible demarcation of the small yet highly relevant nuclei such as the nbM. With the increasing availability of the ultra-high field scanners (https://layerfmri.com/2018/01/04/high-field-mri-scanners/; Uğurbil 2014) and our own experience with 9.4T quantitative MRI, we are increasingly optimistic that regions and nuclei that were thus far challenging to image ('terra incognita') can be visualised and characterised in detail.

2.7.5 Outlook

nbM atrophy due to normal ageing. Estimates for neuronal loss in nbM due to normal ageing in early studies vary greatly from 23% to 50% (De Lacalle et al. 1991; Lowes-Hummel et al. 1989), even 70% (Bloom et al., 1997) to no neuronal loss at all (Bloom et al. 1997; Chui et al. 1984; Whitehouse et al. 1983b). The age of donors of BigBrain and Halliday et al. 's study ranges from 20 to 80 years old (Amunts et al. 2013; Halliday et al. 1993). Data from Halliday et al. (1993) and Zaborszky et al. (2008) also showed the negative correlation between nbM volumes and age. Except for one 50 years old female from Halliday et al., 1993 who has larger nbM volume (156 mm^3) than a 20 years old man (154 mm^3). Additionally, Bethlehem et al. (2022) revealed that the volume of grey matter, white matter and subcortical grey matter have different

developmental trajectories during the lifespan and start to decline after a certain age. Those suggest that volumetric measurement of brain structures would obtain the most consistent results from a population with a narrow age range, but that results should be applied with caution to populations outside that range. Alternatively, an nbM template generated from one donor may only be suitable for the population at a similar age range, or if there are many donors with a large age spectrum, it may be better to create multiple nbM templates corresponding to each age range. The confounding effects of age on nbM template construction can contribute to the variability of volumetry of hard to resolve structures such as the nbM. Therefore, large cohort studies at ultra-high field should make use of multiparametric imaging techniques at high-spatial resolutions to study small but important structures such as the nbM reliably across a wide age range.

Pursuit of various MR properties on nbM. Future studies may explore the MRI properties (proton density, relaxation times, Larmor resonance frequencies, magnetic susceptibility, magnetisation transfer (MT) rates and water diffusion characteristics) of nbM to understand which MRI contrast is most suitable to image this diffusive nucleus. Those parameters carry important information of local microstructure, especially cell membrane, myelin and iron (Beaulieu and Allen 1994; Filo et al. 2019; Langkammer et al. 2010; Möller et al. 2019; Palombo et al. 2020; Sagi et al. 2012; Stüber et al. 2014). Myelin sheath contains several tightly wrapped layers of oligodendrocyte cell membranes, with water residing in the axon and thin layers between adjoining myelin layers. Myelin is known as diamagnetic due to its phospholipid layers (Lonsdale and Bragg 1939). Between the adjacent myelin membrane layers, water protons frequently interact with non-aqueous components, which accelerate longitudinal and transverse relaxation and induce MT between water and macromolecular protons (Sled 2018). Myelin-water fraction (MWF) is also thought to be a correlative measure of myelin content (Laule et al. 2008; West et al. 2018). Myelination has been estimated in R_2^* and R_2 (the reciprocal of T_2^* and T_2) (Alonso-Ortiz et al. 2018; Du et al. 2007; Mackay et al.

1994; Prasloski et al. 2012; Whittall and MacKay 1989), T_1 (Bock et al. 2013; Labadie et al. 2014; Lutti et al. 2014; Oakden et al. 2017) and MT contrast (Schmierer et al. 2007). There is currently no single approach for relating MRI measures to myelin content that is decidedly better than others (Möller et al. 2019). But it has been suggested so far that using MWF, MT rate and quantitative MT to quantify myelin has the highest correspondence with myelin histology in human studies (van der Weijden et al. 2021). Iron is by far the most abundant paramagnetic ion in the brain (Möller et al. 2019) and involved in myelination, oxygen transport and neurotransmitter synthesis (Weiskopf et al. 2021). Much of the MRI-visible iron in tissue is located in ferritin and hemosiderin, associated with proteins that facilitate storage and transport (Schenck and Zimmerman 2004). Early studies found that iron colocalised with myelin in white matter (Connor et al. 1990; Levine 1991; Morris et al. 1992), and cortex (Fukunaga et al. 2010). Both R_2^* and quantitative susceptibility mapping was used to map iron. R_2^* signal decay occurs more profoundly in the regions with different susceptibility variations such as heterogeneous tissues or at boundaries (Bagnato et al. 2013). Research has reported granular, glial, fibrous, oligodendroglial, neuronal and vascular iron reactivity in SI using a pale iron staining with diaminobenzidine tetrahydrochloride (DAB) (Morris et al. 1992). nbM is scattered inside SI and surrounded by relatively dense myelin (Figure 2.1 A). Comparing nbM with the rest of SI, its open structure, magnocellular, isodendritic, heteromorphic, AChE-rich, and choline-acetyltransferase, might lead to differential MRI properties (e.g. $T_2(^*)$ from Figure 2.5 A, T_1, MT). Quantitative MRI (qMRI) goes beyond conventional MRI because it provides specific physical parameters related to the spins of underlying microstructure (Weiskopf et al. 2021). It has high repeatability across different vendors (Gracien et al. 2020; Weiskopf et al. 2013) and could avoid the MR contrast being cancelled out due to microstructures having opposite effects on the MRI properties. Following this reasoning, we have recently examined in vivo T_1 maps acquired by MP2RAGE (Marques et al. 2010) sequence at 7T with the resolution of 0.65 mm isotropic for four participants (additionally to the data reported above). In some datasets, we noticed a

bright area inside SI, which might indicate the location of nbM. Although the contrast was too weak and the signal too diffusive for us to reliably quantify, or to make strong claims about the locations of nbM, we found this data encouraging. It seems clear that, in addition to increasing the spatial resolution, future studies should take the effects of different MRI contrasts on nbM into consideration for localisation.

Utilise contrast agent and cholinergic nature of nbM. Alternatively, future studies may explore strategies for localising nbM based on its cholinergic nature. Luo et al. (2018) used a nanosensor composed of pH-sensitive Gadolinium contrast agents and ACh-catalysing enzymes to image in vivo ACh concentration by changing T_1 relaxation rate ($1/T_1$) on rats at 7T scanner. The mechanisms behind this method involved decreases of pH caused by hydrolysis of ACh, which lead to the increase of H ion, and R_1 lengthening using Gadolinium-based contrast agents. To image human nbM at higher resolution, one could also try MRI contrast agents to enlarge the difference of MRI imaging properties between nbM and surrounding regions.

Improve probabilistic atlas. While methods to directly image the nbM in vivo remain immature, the use of standardized maps will remain an important technique. One method to improve upon the currently available map may be to identify nbM in histology with specific immunohistochemistry targeted to AChE and ChAT rather than simply staining for cell bodies. Using this technique, Mesulam and Geula (1988) originally identified the various cholinergic neurons in the human basal forebrain and introduced the nomenclature Ch1-Ch4 to describe four cholinergic cellular groups. Secondly, a significant loss of detail may occur when transferring high resolution histology data to lower resolution MRI, especially when the nbM is not visible in MRI. Ex vivo MRI is the measurement closest to histology, which can offer 100 μm isotropic resolution (Edlow et al. 2019). Even though the resolution of ex vivo MRI is lower than histology (histology offers up to 1 μm/pixel (Ding et al. 2016)), it is higher than in vivo MRI, which is maximally around 500 μm isotropic resolution (Fracasso et al. 2016) or potentially

up to 250 μm if sophisticated acquisition approaches like prospective motion correction are available (Lüsebrink et al. 2017). Moreover, ex vivo MRI could also make use of stained samples to enhance contrasts amongst tissues as well as ultra-high field strength and longer scanning time to increase signal to noise ratio (SNR). Thus, by combining ex vivo histology with ex vivo ultra-high-resolution MRI, in which the contrast makes nbM visible, a highly accurate MRI map of nbM might be produced.

However, ex vivo MRI and histology also have its limitations. Fixation of the ex vivo sample could influence size estimation (Mouritzen Dam 1979) even before slicing, and MRI contrast (Dinse et al. 2015). Staining in histology is performed on 2D slices and operations during sample preparation, such as fixation, might both have impacts on 3D-reconstruction and morphological estimations of the regions. But having a post-mortem scan for an undistorted brain (such as in cranio scans) could reduce the distortion from histology.

Recently, deep learning-based approaches (Greve et al. 2021) have been developed that allow segmentation of the basal forebrain region. While they are capable of delineating the basal forebrain as a whole, they presently do not segment the structures within it. We hope future work can take this a step further to allow segmentation of subcompartments of the basal forebrain using segmentations derived from high-resolution data with the appropriate contrast.

In conclusion, for a structure that cannot currently be mapped at the individual level, it will be difficult to detect its structural or functional changes related to cognition or disease. Our review of the (f)MRI literature to date revealed inconsistencies between (f)MRI studies and with histology as well as inadequate reporting of methods and basic findings. Given this, we first would like to encourage future papers to report nbM volume with a physical unit, such as ml, or mm^3, to help readers to grasp its size and allow comparison between studies. Papers which use probabilistic maps for ROI should also report the threshold they chose and may wish to explore how robust their results are to changing

the threshold. Where volumes were reported, we noted the discrepancy in the reported nbM volume amongst (f)MRI studies and between some (f)MRI and histological studies. Current nbM atlases were based on post-mortem scans up to 3T with the resolution of close to 1.0 mm isotropic. Our analysis and review of the literature suggests that these methods add variability to the localisation of nbM, with consequent reduction to the statistical reliability of experiments. We suggest that the long-term solution to these problems should be to use direct imaging of the nbM for defining individual ROI. To this end, future studies could explore the MRI properties of nbM, such as its quantitative T_1, $T_2(^*)$, MT using qMRI under ultra-high field (7T or 9.4T) allowing up to 100 μm isotropic images. Our exploration of one such qT_2^* ex vivo dataset suggests that nbM is visible in this way. In the first instance, combining such high-resolution scans and histological sections, may yield a more accurate delineation of nbM to estimate its volume and provide novel atlases. Moreover, we are hopeful that, as technology advances, it will soon be possible to identify nbM in individual in vivo MRI which will allow study of its structural and functional contributions to human cognition and disease in unprecedented detail.

2.8 Supplementary Materials

Table S2.1: (Next page) Overview of the 37 studies included in the literature review on scanning parameters, ROI definition and eventual nbM volume.

A: Studies reported/implied nbm volume with a physical unit and 'mean voxel value'

Study number	Publication	Subjects (M/F)			Field Strength (Tesla)				Resolution (mm^3)			Method for nbM definition				Reported volume			nbM volume estimates (mm^3)
		Age	H	P	0.3	1.5	3	7	<1	1-1.5	>1.5	Zaborszky et al. 2008	Kilimman et al. 2014	Teipel et al. 2014b	Teipel et al. 2005	Structure	Value	Unit	
1	Grothe et al. 2014a	73.0-73.9[a]	14/8	7/4(DLB & AD)			✓			✓			✓	✓		CH4	Ch4a-i: 95.5; CH4p: 72.1	mm^3	167.6
2	Wolf et al. 2014	70.02[b]	18/25				✓		✓					✓		CH4	Ch4a-i: 70.36; CH4p: 58.17	mm^3	128.53
3	Teipel et al. 2016a	65.3-68.2[a]	16/15	30/32 (PPA)			✓		✓	✓			✓			CH4	Ch4am_al: 20-40; CH4p: 20-40	mm^3	40-80
4	Markello et al. 2018	22.6[b]	42/58				✓			✓	✓	40%				CH4	51	voxels	1377
5	Yuan et al. 2019	18-26[c]	10/11					✓	✓	✓		50%				CH4	73&40%; 52&100%	voxels & overlapped %	791
6	Fernández-Cabello et al. 2020	70-80[a]	108/118	79/42(MCI/AD); 29/38 (PREC); 134/85(PROD); 115/89 (AD)		✓	✓					50%				CH4	0.2-0.3	ml	200-300
7	Schmitz et al. 2020	68.5-76[a]	CN103/108(NTPY); 18/39 (PREC)				✓			✓		✓				NBM	around 0.29	mL (TIme1, NYTP)	290
8	Schulz et al. 2018	59.9-61.4[a]	110/57	200/104 (PD)		✓	✓			✓	✓	✓				NBM	0.397	Mean voxel value	
9	Gang et al. 2020	63.0-70.29[a]	7/6	24/32 (PD)		✓				✓		50%				NBM	0.31	Mean voxel value	

B: Studies reported/implied nbm volume in 'cluster size/extension' and other metrics

Study number	Publication	Subjects (M/F)			Field Strength (Tesla)				Resolution (mm^3)			Method for nbM definition				Reported volume			nbM volume estimates (mm^3)
		Age	H	P	0.3	1.5	3	7	<1	1-1.5	>1.5	Zaborszky et al. 2008	Kilimman et al. 2014	Teipel et al. 2014b	Teipel et al. 2005	Structure	Value	Unit	
10	Okada et al. 2013	62.2-64.7[a]	10/15	9/11 (AD)	✓				0.93 x 0.93 x 1.2			✓				NBM	R NBM: 103	CS/voxel: lower 18F-2FA-85380 binding in AD than in the healthy group	
11	Grothe et al. 2010	66.6-69.6[a]	12/16	20/13 (MCI)		✓				Matrix dimensions 256 × 192, 1.2 mm (thickness)		50%				CH4	RCh4: 365; L CH4: 312	CS/voxel: volume loss	
12	Teipel et al. 2011	67.0-76.1[a]	12/8	9/12 (AD); 9/7 (MCI)			✓		✓	0.9x0.9x5 mm^3	✓					CH4	RCh4al: 566	CS/voxel: volume loss	
13	Grothe et al. 2012	55.8 Y; 75.6-77.8[a]	75/136 [Y]; 25/70 [E]	9/19 (AD); 31/38 (very mild AD)		✓				✓					✓	BFCs/ CH4	BF:1884; R CH4al: 942; L CH4al: 872; L CH4p: 767; R CH4p: 836	mm^3/CS	
14	Cantero et al. 2017	66.9-70.4[a]	33/43	55/51 (MCI)			✓		✓			✓				CH4	LCh4: 156; RCH4: 99	CS/voxel: volume loss (mm^3)	
15	Nakaizumi et al. 2018	30.5 [Y]/ 63.9-71.3[a] [E]	5/5 [Y]; 3/7 [E]	7/13 (AD)		✓				Matrix dimensions 256 × 256, 1.2 mm (thickness)		✓				nbm	R nbM: 219	CS/voxel: binding	
16	Cantero et al. 2020	58.4-69.9[a]	10/23	9/24 (A+ amlyloidosis); 15/14(T+SNAPs);6/2(AT PREC AD); 5/12(AT PROD AD)			✓			✓		✓				Ch4	L Ch4: 273; R CH4: 181	CS/voxel: volume loss	
17	Nemy et al. 2020	55.6[b]	122/140				✓			✓	✓		✓			NBM	0.00025		
18	Lammers et al. 2016	33.5[b]	18/20				✓			✓		40%				CH4	L Ch4: 0.026 ± 0.027;	Correlation of volume with task performance	
19	Wang et al. 2019	76.9-77.81[a]	85/95	59/47 (AD)		✓				✓		✓				CH4	0.3097	adjusted for age, gender and intracranial volume	
20	Schmitz et al. 2016	74.5-75.6[a]	77/73	69/34 (MCI-NP); 52/32 (MCI-NP); 49/48 (AD)		✓				✓		50%				NBM	0.5-0.6		
21	Barrett et al. 2018	61.7[b]	101	423		✓				✓		✓				NBM	80-100	Mean value of Gray matter density	
22	Schmitz et al. 2018	67.0-75.1[c]	25/27 $CN_{NA\beta}$; 3/3 CN	53/27 ($MCI_{AA\beta}$); 3/3 (AD)								✓				NBM	0.01	GM degeneration (Time 1-Time 2)	

C: Studies didn't report nbM volume or the volume could not be estimated

Study number	Publication	Subjects (M/F)			Field Strength (Tesla)				Resolution (mm^3)			Method for nbM definition				Reported volume			nbM volume estimates (mm^3)
		Age	H	P	0.3	1.5	3	7	<1	1-1.5	>1.5	Zaborszky et al. 2008	Kilimman et al. 2014	Teipel et al. 2014b	Teipel et al. 2005	Structure	Value	Unit	
23	Teipel et al. 2014a	69.4-78.5[a]	91/88	121/148 (EMCI); 62/74 (LMCI); 36/50 (AD)			✓								✓	NBM		Reported AUC score between groups	
24	Li et al. 2014	18-53[c]	108/116				✓					✓				NBM		Connectivity between nbM and other regions	
25	Wan et al. 2018	70.18 [E]	212 [Y]; 22/18 [E]				✓			✓	✓	✓				NB		Functional connectivity and alpha reactivity	
26	van Dalen et al. 2017	79[b]	29/29	12/17			✓			✓	✓	Teipel et al. 2011				NbM		NbM cortical pathway	
27	Jacobs et al. 2018	44.12[b]	12/17					✓	✓	✓		✓				NBM		Age relationships with FC	

D: Studies reported substantia innomiata and basal forebrain 's volume

Study number	Publication	Subjects (M/F)			Field Strength (Tesla)				Resolution (mm^3)			Method for nbM definition				Reported volume			nbM volume estimates (mm^3)
		Age	H	P	0.3	1.5	3	7	<1	1-1.5	>1.5	Zaborszky et al. 2008	Kilimman et al. 2014	Teipel et al. 2014b	Teipel et al. 2005	Structure	Value	Unit	
28	George et al. 2011	76-78[a]	10/17	13/20 (aMCI); 6/13 (mild AD)		✓				✓		The Analyze software (Mayo Clinic Foundation, Rochester, MN)				SI	0.11-0.12	Normalized	153-183.5
29	Gao et al. 2013	76.0-78.2[a]	15/15	18/12 (AD); 12/18 (AD/SVD)		✓			✓	✓		Callen et al. 2001				SI	0.46	mm^3	
16	Grothe et al. 2012	55.8 Y; 75.6-77.8[a]	75/136 [Y]; 25/70 [E]	9/19 (AD); 31/38 (very mild AD)		✓				✓					✓	BFCs/ CH4	BF:1884; R CH4al: 942; L CH4al: 872; L CH4p: 767; R CH4p: 836	mm^3/CS	
30	Teipel et al. 2018	75.3[b]		68/56 (AD)		✓							✓			BF	BF: 481	mm^3	
31	Grothe et al. 2013	72.7-78.0[a]	20/49	4/9 (p-HE); 22/15(s-vmAD); 7/6(p-vmAD)		✓				✓					✓	BF	BF: 1020	mm^3	
32	Grothe et al. 2014b	73.1-76.2[a]	18/18 [-]	9/12 (CN+); 41/49 (EMCI-); 27/39(EMCI+);3/6 (LMCI-); 11/12 (LMCI+)			✓					✓			✓	BF	761	Estimated marginal means	
33	Lammers et al. 2018	65-87[c]	172/110 (The participants were divided into various group based on their cognitive performance)				✓			✓		✓				BF	2201	mm^3	
34	Fritz et al. 2019	19-85 [P]; 65-89 [V]	47/38 [P], 13/12 [V]				✓			✓	✓	✓	✓		✓	BF	5103	mm^3	
35	Zhang et al. 2011	77.8-79.2[a]	103/140	66/80(MCI); 49/32 (aMCI); 16/39 (naMCI)			✓			✓		✓			✓	BFA	Bilateral BFA: 0.633		
36	Teipel et al. 2016b	73.67-74.13[a]		48/54 (placebo); 54/59 (Donepezil) [MCI]		✓	✓						✓			BF		Predictor effects	
37	Liu et al. 2018	29.2[b]	251/275 (HCP data)				✓		✓	✓		✓						Normalized BOLD in nbM	
	Count				1	15	22	2	8	25	7	24	6	2	7				8

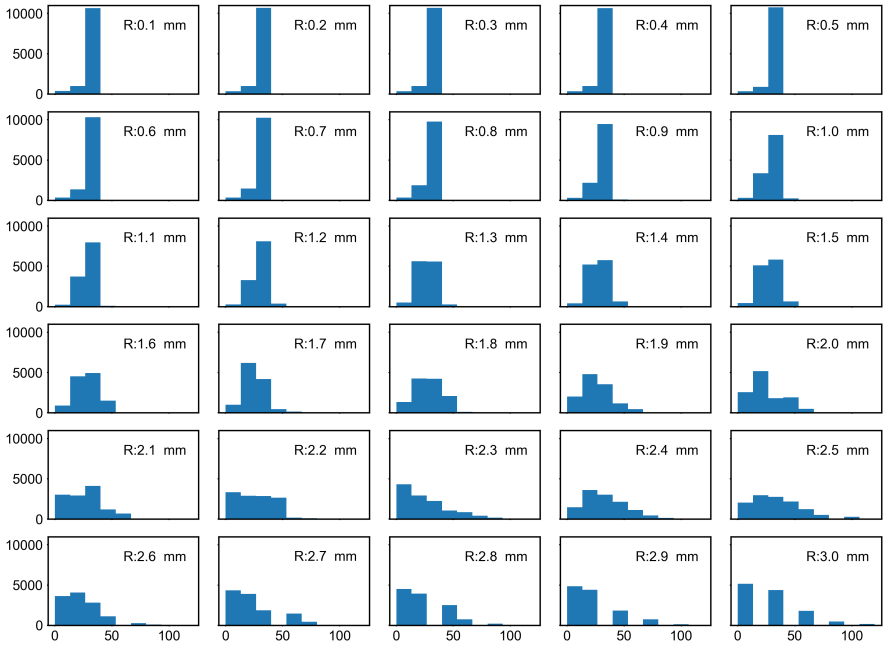

Figure S2.1: Histogram of bilateral nbM volume at each spatial resolution after the simulation.
X axis represents nbM volume estimation in cubic millimetres. Y axis represents the number of repetitions at each volume estimation. R represents spatial resolution. 'R: 0.1 mm' indicates the current resolution is 0.1 mm isotropic.

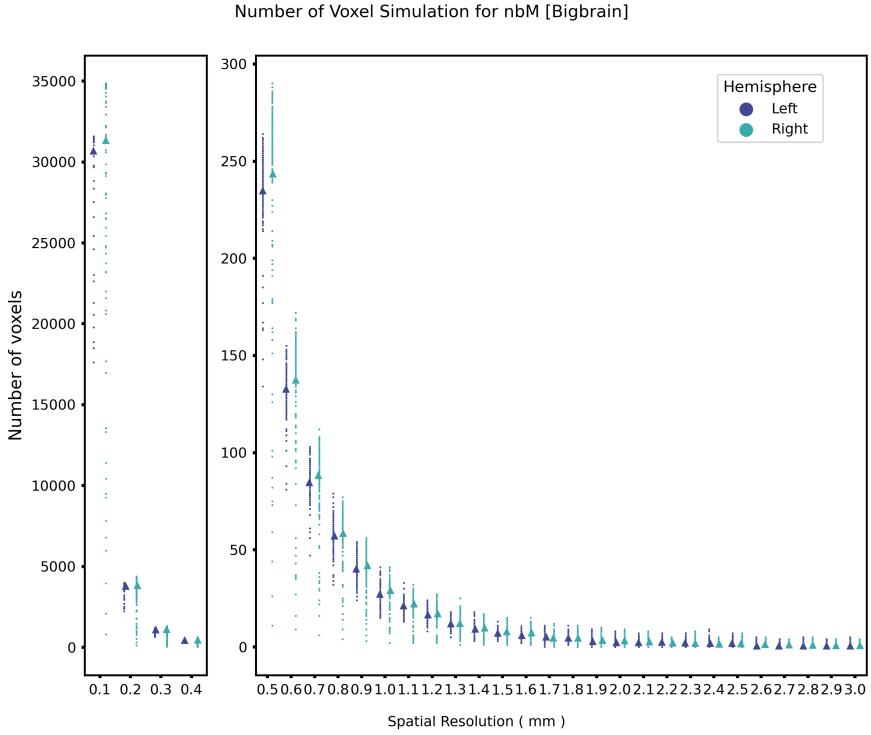

Figure S2.2: Number of voxels estimation for nbM from the BigBrain dataset (Amunts et al. 2013) (left-right panel).
Left Panel: Estimation of the number of voxels based on semi-manual drawn nbM on 100 μm BigBrain data across the resolution spectrum (100 μm to 400 μm).
Right Panel: Estimation of the number of voxels in resampled structural MRI data across the resolution spectrum (500 μm to 3.0 mm). Blue and green dot depicts the left and right nbM. Each dot represents one data point. Triangle is the mean of those data points. There are 6001 data points for each hemisphere at each threshold. The triangle represents the mean of the current column.

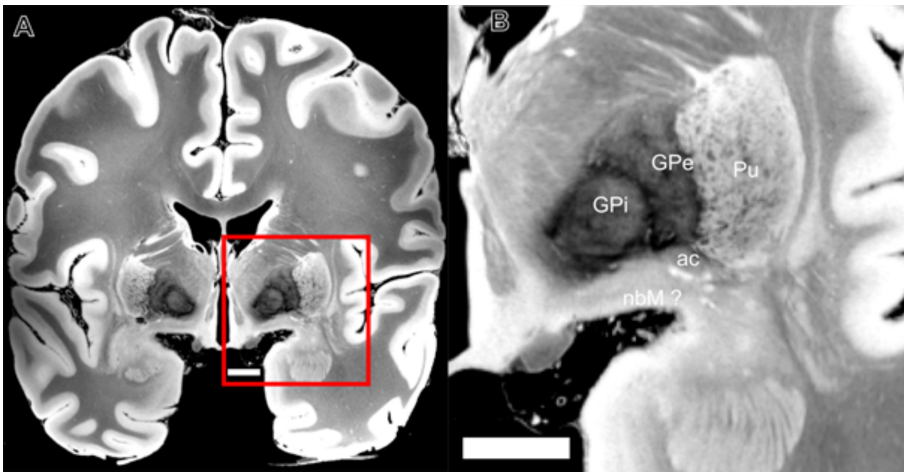

Figure S2.3: Visualisation of nbM from MGH brain.
A:The 889th coronal slice along anterior to posterior direction from a 100 μm isotropic resolution ex vivo dataset acquired at 7.0 T (Edlow et al. 2019). Zoom factor (width x height: 1.51 x 1.50). Red box indicates the zoomed panel in **B**. Scale bar: 5 mm.
B: Zoomed view of basal ganglia and nbM in the same slice as A. The label "nbM ?" indicates the likely location of the nbM but we cannot visualise it directly on the image due to lack of contrast. Zoom factor (width x height: 4.91 x 4.91). Scale bar: 5 mm.
B: Zoomed view of basal ganglia and nbM in the same slice as A. The label "nbM ?" indicates the likely location of the nbM but we cannot visualise it directly on the image due to lack of contrast. Zoom factor (width x height: 4.91 x 4.91). Scale bar: 5 mm.
Abbreviations: nbM: nucleus basalis of Meynert; ac: anterior commissure; Gpi: internal globus pallidus; GPe: external globus pallidus; Pu: putamen.

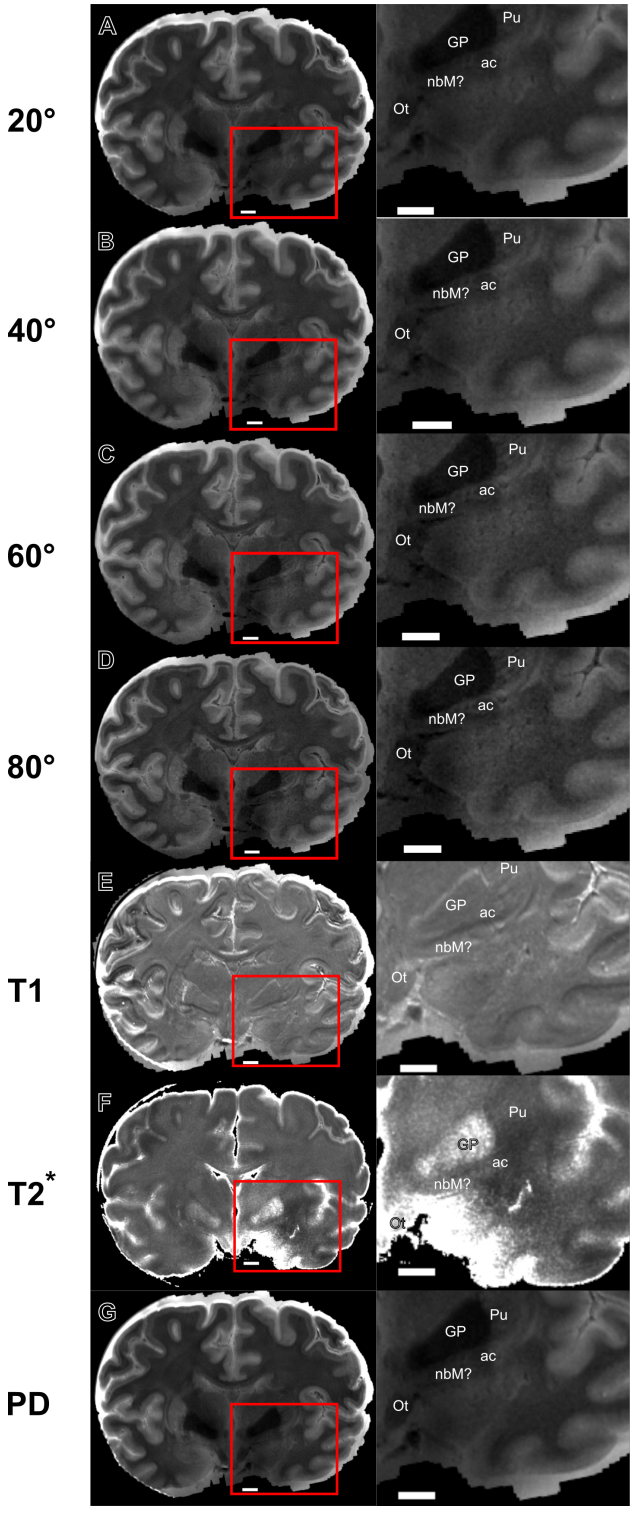
A
B
C
D
E
F
G
20°
40°
60°
80°
T1
T2*
PD
Pu
GP
ac
nbM?
Ot

Figure S2.4: (Previous page.) Visualisation of nbM from the Ding atlas.
Left Panel:The 178th coronal slice along anterior to posterior direction from a 200 μm isotropic resolution ex vivo dataset acquired at 7.0 T (Ding et al. 2016) with four flip angles (A: 20°, B: 40°, C: 60°, D: 80°, E: T_1 weighted, F: T_2^* weighted, G: PD weighted). Zoom factor (width x height: 1.01 x 1.01). Red box indicates the zoomed panel in the right panel. Scale bar: 5 mm.
Right panel: Zoomed view of basal ganglia and nbM in the same slice as A. The label "nbM ?" indicates the likely location of the nbM but we cannot visualise it directly on the image due to lack of contrast visuals. Zoom factor (width x height: 2.49 x 2.41). Scale bar: 5 mm.
Abbreviations: nbM: nucleus basalis of Meynert; ac: anterior commissure; Gpi: internal globus pallidus; GPe: external globus pallidus; Pu: putamen.

3

Cortical responses to illusory surface brightness perception at 7T fMRI

Based on
Wang, Y., Kashyap S., Zhan, M., Roberts, M.J., De Weerd, P. (in preparation). Cortical responses to illusory surface brightness perception at 7T fMRI.

3.1 Abstract

The perception of brightness is not only influenced by the luminance of the surface but also by contextual interactions with nearby surfaces. In the visual illusion of brightness induction, increased luminance in a surrounding stimulus induces an illusory decrease in brightness of a physically constant centre stimulus and vice versa. Several electrophysiological studies in animals and fMRI studies in humans have shown neural signals in early visual cortex representations of the physically constant centre in accordance with induced brightness changes. Other studies however failed to find correlates of brightness induction. In view of these contradictory results, we here re-investigated brightness induction using ultra-high field fMRI (7T). In the case we would confirm a correlate of brightness induction, we also aimed to test the hypothesis that the effect would be strongest in superficial or deep layers, in line with feedback contributions or lateral interactions. We first designed a stimulus adapted to the limited field of view of the 7T scanner stimulus display, but that nevertheless permitted brightness induction, using psychophysics to optimise the size and base luminance of the constant probing region. 7T fMRI measurements were performed with 11 participants, of which 7 passed inclusion criteria. Because of the asymmetric tSNR of the 7T fMRI dataset, our analysis focused on the left hemisphere which showed the better data quality. Nevertheless, we did not observe significant fMRI temporal response in the V1, V2, or V3 representations of the probing region that could be related to brightness induction. In the V1 and V2 representation of the inducer, we found that decreases in inducer luminance led to decreased signal, but luminance increases did not lead to signal increases. The V3 representations of the probing region, edge, and inducers did not reveal any fMRI responses. For further analysis, we grouped the temporal response into positive-dominant BOLD (Early), post-stimulus undershoot (Late) and recovery periods (End). Inducer luminance decrements induced a significant negative response in the inducer representations and a non-significant trend towards a positive Early BOLD response in the V1 representation of the probing region. Inducer luminance increments

brought about no response changes in the probing region. We found stronger Late responses in the inducer and probing region than in the edge representation, which might indicate additional, delayed cortical processing in these regions. In conclusion, despite some data trends worth following up with further improved experimental and stimulus designs, our current findings did not indicate a clear correlate of brightness induction in the human early visual cortex.

3.2 Introduction

The perception of surfaces is fundamental to visual behaviour, yet the neural mechanisms of surface perception are poorly understood. Early neurophysiological studies have emphasised that retinal ganglion cells (Kuffler 1953) as well as neurons in the early visual cortex respond strongly to local contrast but only weakly, or not at all, to uniform surfaces (Albrecht and Hamilton 1982; Hubel and Wiesel 1962). These contrast-related mechanisms appear insufficient to encode homogeneous stimulus surfaces. To date, it is not fully established whether or not there is a signal related to surface perception in the early visual cortex. In the present study, we investigated the neural mechanisms of surface perception with the brightness induction paradigm, in which luminance changes in one direction in a surrounding region (the inducer) , induce perceived brightness changes in the opposite direction in the enclosed centre region of constant luminance (the probing region). Using ultra-high field (UHF) fMRI at 7T, we sought out to confirm previous observations at 3T (Van de ven et al. 2012) that showed brightness-related responses in retinotopic representations of the probing region. In addition, we aimed to assess whether there was a cortical depth-resolved pattern of activity in order to gain insight into the mechanisms of brightness-related responses. We hypothesised brightness-related responses to be strongest in deep and/or superficial layers, in line with potential contributions of lateral interactions and feedback.

The role of early visual cortex in the processing of surface perception has long been a topic of debate. Several neurophysiological studies

in cats (Hung et al. 2001; Hung et al. 2007; MacEvoy et al. 1998; Rossi and Paradiso 1999; Rossi et al. 1996) and monkeys (Kinoshita and Komatsu 2001; Lamme 1995; Lamme et al. 1999; Roe et al. 2005; Weerd et al. 1995), as well as optical imaging studies in monkeys (Lu and Roe 2007) and neuroimaging studies in humans (Boyaci et al. 2007; Haynes et al. 2004; Kok et al. 2016; Koopmans et al. 2010; Marquardt et al. 2020; McCourt and Foxe 2004; Pereverzeva and Murray 2008; Sasaki and Watanabe 2004; Van de ven et al. 2012) have reported retinotopic signals in early visual cortex related to the processing of surface texture, colour and brightness. However, several other studies have reported no contribution of early visual cortex to the processing of surfaces (Cornelissen et al. 2006; Friedman et al. 2003; Perna et al. 2005). It is not clear why some studies report neural signals related to surface perception, and why others do not.

Nevertheless, it is clear that the early visual system (retinal ganglion cells, LGN cells, V1) emphasises the processing of local contrasts and boundaries (Field et al. 1993; Grossberg and Mingolla 1985; Tadmor and Tolhurst 2000), and that the bottom-up signal from retina to V1 is poorly suited to represent homogeneous surfaces. This is due to the antagonistic organisation of receptive fields of neurons in the feedforward processing stream from retina to V1 layer 4C. In line with the idea that the early visual system is not suited to represent the subjective visual qualities of surfaces, symbolic theories (Dennett 1991; Komatsu 2006) have suggested that the subjective experience of surface properties results from logical operations computed in higher order cortical areas, based on an interpretation of the local contrast polarities computed in early areas. These theories do not support the existence of a correlation of surface perception with activity in low-level visual areas. However, there are at least two categories of alternative views that do entail surface-related activity in the low-level visual cortex. On the one hand, as suggested by the well-established horizontal connectivity in the early visual cortex (Schwabe et al. 2006), a form of lateral interaction in the visual cortex may play a role in surface perception. For example, computational views (Grossberg 1987a; Grossberg 1987b;

Keil et al. 2005) suggest that different modules in low-level visual cortex V1 and V2 encode boundaries in a boundary-system and represent surfaces in a surface-system, whereby boundary contrast initiates an analog 'diffusion-like' fast process of neural activity spreading, responsible for the 'filled-in' percept of surfaces. In addition, lateral inhibition theories state that the surrounding surfaces have an impact on the perceived brightness of the target area because neurons corresponding to both the background and the target area interact with each other (Dixon et al. 2014). On the other hand, it is plausible that feedback operations play a role in mediating any potential signals in the low-level visual cortex in response to surfaces. Computations in high-level areas interpreting visual scenes as a whole, may send feedback that causes neurons in low-level areas to respond to the subjective experience of visual surfaces (Kafaligonul et al. 2015; Kirchberger et al. 2019, August; Lamme and Roelfsema 2000).

In the domain of surface brightness perception, several extracellular recording studies in animals have reported that V1 neurons with receptive fields corresponding to the interiors of achromatic constant luminance surfaces, exhibit responses consistent with human brightness constancy (MacEvoy et al. 1998), brightness induction (Kinoshita and Komatsu 2001; Rossi and Paradiso 1999; Rossi et al. 1996), the Craik–O Brien–Cornsweet (COC) illusion (Hung et al. 2001), White' s Effect (McCourt and Foxe 2004) and surface completion of the blind spot (Komatsu et al. 2000; Komatsu et al. 2002). Furthermore, additional neurophysiological studies have demonstrated that neurons in the thin stripes of V2 carry signals related to the perception of surface brightness in the COC illusion (Hung et al. 2007; Roe et al. 2005), in line with the proposed existence of a specific module for surface feature spreading in V2 (Grossberg 1987a; Grossberg 1987b). These studies support the idea that there are responses related to surface brightness perception at the earliest stages of cortical processing, in V1 or V2.

The findings from human neuroimaging studies on the topic are more diverse. Boyaci et al. (2007) found cortical activity in V1-V3 asso-

ciated with brightness perception using the COC illusion with 3T fMRI. Another study, using the same illusion but with a different experimental setup in a 1.5T fMRI study (Perna et al. 2005), only found relevant signals to brightness in high order areas (caudal region of the intraparietal sulcus and lateral occipital sulcus). Boucard et al. (2005) and Cornelissen et al. (2006) used a similar paradigm to study brightness filling-in. Neither Boucard et al. (2005) nor Cornelissen et al. (2006) observed a retinotopic correlation of changes in perceived brightness. Van de ven et al. (2012), using 3T fMRI and an induced brightness paradigm with cyclical increases and decreases of the inducer luminance (Rossi and Paradiso 1999; Rossi et al. 1996), showed an antiphase BOLD response in the V2 representations of the probing region and the surrounding inducers. Thus, the response in V2 voxels representing the physically constant probing region appeared to follow its perceived brightness changes. A similar trend was observed in V1, which however did not reach statistical significance.

At 1.5T and 3T, the specific choices of size and eccentricity of the probing region and inducers to overcome limitations in spatial resolution may have played a role in the diverging results among previous fMRI studies of surface brightness perception. Specifically, at 1.5T and 3T, a difficult compromise has to be sought related to the size of the probing region: for the purpose of separating fMRI signals from probing and inducer regions, the probing region should be as large as possible, whereas from the perspective of maximising the illusion, the probing region should be as small as possible. A non-optimal compromise between these opposite constraints could result in the signals representing the inducers overwhelming the signal representing the probing region, thus masking any correlation between activity related to brightness induction and surface brightness perception. Thus, a suboptimal compromise related to the size of the probing region could explain an absence of fMRI signals related to brightness induction. In contrast, 7T fMRI permits better spatial resolution, which we reasoned would allow a better isolation of signal from the probing region to robustly test for a signal related to brightness induction.

While the existence of a signal in the early visual cortex related to surface perception remains controversial, it should be noted that, even if such a signal were established, major questions about its mechanisms would remain unanswered. 7T fMRI also provides opportunities to tackle those questions. A large body of literature has shown that feedforward connections target predominantly layer IV of visual cortical areas, whereas feedback connections target superficial and deep layers, while avoiding layer IV (Callaway 2004; Dumoulin et al. 2017; Felleman and Van Essen 1991). Horizontal connections are largely confined to superficial layers (Hess et al. 1996; McGuire et al. 1991; Schwabe et al. 2006). 7T fMRI studies offer the spatial resolution to assess functional effects separately in a layer-dependent manner. If the hypothesis is correct that perceived brightness is not given in the feedforward stream, but involves lateral spreading and/or feedback, then the strongest correlation of brightness induction is expected in superficial or deep layers of early visual cortex, especially in V1.

Hence, in the present 7T fMRI study, our goals were first to replicate prior studies showing a correlation of brightness induction. Secondly, we aimed to measure a layer-specific pattern that would support contributions of either feedback or lateral interactions. Using a stimulus optimised for the 7T scanner, our experimental design included separate up- and down regulations of inducer luminance to put us in the best position to observe the opposite signal changes in the probing region that would indicate a correlation of brightness induction. Hence, we expected to observe signal changes in the probing region representation limited to superficial or deep layers opposite in direction to the luminance changes in the inducers.

3.3 Methods

3.3.1 Psychophysics

We first aimed to find a stimulus that produced a robust brightness illusion and could be shown on the limited display size in the 7T scan-

ner.

Participants

Twelve healthy participants (age range: 20-30 years old) with normal or corrected-to-normal vision participated in the study and had given written informed consent. Participants from the behavioural study did not join the fMRI experiment later. The study was approved by the Ethics Review Committee for Psychology and Neuroscience (ERCPN) (176_02_07_2006_V2_A1) at Maastricht University and all procedures followed the principles expressed in the Declaration of Helsinki.

Experimental Design and stimuli

We used a psychophysical experiment to optimise the size, location and shape of the probing region and the surrounding inducers to maximise the brightness illusion. The stimuli were created and presented using Psychopy version 1.82.01 (Peirce 2007; Peirce 2009), and displayed on a 19″ Samsung SyncMaster 940BF LCD monitor with the resolution of 1280 x 1024 and 60 Hz of nominal refresh rate (Samsung, Seoul, South Korea). To match the visual angles of the screen in the scanner, the stimulus size was reduced to 960 x 600 pixels (16.6° x 10°, 26.7 cm x 17.8 cm). The area outside this region was covered by cardboard sheets. The viewing distance was 64 cm and the light in the room was off during the experiment.

During the experiment, participants were asked to fixate on a small fixation cross. Following the presentation of a uniform grey screen in the 16.6 x 10 deg area of interest, the luminance in the inducing area either changed from grey to white (192.9 cd/m^2, luminance increase, or Lum. Inc.) or to black (2.1 cd/m^2, luminance decrease, or Lum. Dec.) in a sinusoidal fashion within one second. Figure 3.1 shows a luminance increase of the inducer. Following the completion of the luminance increment (or decrement) stimulus exposure continued for 2s. Following these 2s, the inducer area was replaced with Gaussian noise (same mean

luminance as the probing region), to mask potential after-effects, and to define the area of the probing region. Participants then had to adjust the luminance in the probing region to match the brightness experienced in the preceding part of the trial during brightness induction (details in Figure 3.1 legend).

To explore the strength of the brightness illusion as a function of stimulus size, shape and location, we tested twelve configurations. They included four rectangles with the same width (12°) but 4 different heights of 3°, 4°, 5°, and 6° located in the centre of the screen, as well as four squares with side lengths of 3°, 4°, 5°, and 6° located either at 4° to the left or to the right of the fixation cross. For each rectangular probing region, participants completed 20 trials. For each of the four sizes of squares, participants completed 10 trials on the left and on the right.

We also manipulated the base luminance level of the probing region and stimulus areas as a whole. Seven participants (S1-S7) were exposed to a low base luminance level (30, 30, 30; Psychopy RGB value, 27.5 cd/m^2). Five participants (S8-S12) were exposed to a high basic luminance level (80, 80, 80; Psychopy RGB value, 69.16 cd/m^2). Due to technical reasons, condition 12 (side length 6°, represented on 4° right of the fixation) was not included in the analysis. A two-way repeated-measures ANOVA was performed to the low and high base luminance dataset separately (see Figure 3.11), with within-subject factors, Luminance (Lum. Inc., Lum. Dec.), Conditions (From 1 to 11). To compare the effect of different base luminance levels on perceived luminance, we performed a three-way repeated-measures ANOVA with FDR correction on the combined dataset (low and high base luminance), with within-subject factors, Luminance (Lum. Inc., Lum. Dec.), Conditions (From 1 to 11) and Base (Low, High).

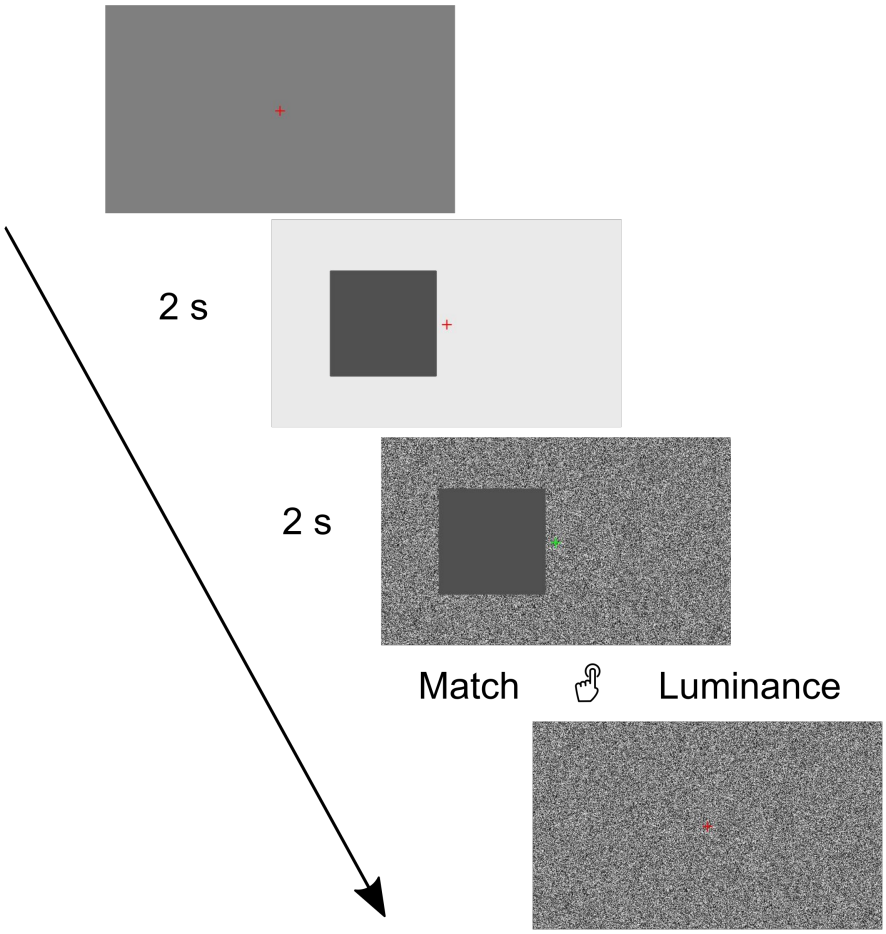

Figure 3.1: Stimulus presentation for an example trial in the luminance increasing condition with a square probe (6 degrees side length) presented on the left. 1) Each trial started with 1 s of red fixation on a grey screen. 2) The luminance of the inducing area then changed from grey to white (or black) within one second, and then the white (or black) and stayed constant for 2 s. 3) The inducing area was replaced by a gaussian texture (sigma=0.28) mask and the fixation spot changed to green. Participants were asked to match the brightness of the probing region at stage 3 to the brightness of the probing region at stage 2 by pressing '1' to increase, '2' to decrease the luminance, '3' to accept the match. 4) Once they accepted the match, the next trial started.

3.3.2 fMRI experiment

Participants

Eleven healthy participants (20 - 35 years old, mean 28.4 ± 4.3 SD years) with normal or corrected-to-normal vision participated in the study after having given written informed consent. The study was approved by the Ethics Review Committee for Psychology and Neuroscience (ERCPN) (176_02_07_2006_V2_A1) at Maastricht University and all procedures followed the principles expressed in the Declaration of Helsinki.

Experimental design

Visual stimuli were created and presented using Psychopy (version 1.82.01), and were projected onto a translucent screen behind the head coil (Panasonic projector PT-EZ570; Newark, NJ, USA; size=28 cm x 17.5 cm, resolution 1920 x 1200; nominal refresh rate: 60 Hz). The projection intensity was calibrated based on luminance measurements taken with a Minolta photometer. Participants viewed the screen on a mirror mounted to the head coil (viewing distance = 99 cm). To maintain participants' alertness and gaze centre, participants performed a colour change detection task at fixation (see below). Button responses were recorded using an MR-compatible button box (Current Designs, 8-button response device, HHSC-2 × 4-C; Philadelphia, USA).

For every participant, we collected three runs of population receptive field (pRF) (227 volume per run), and six runs of the brightness induction experiment (258 volumes per run).

Retinotopic mapping: pRF runs allowed us to delineate visual areas (V1, V2, V3) and project the stimuli configuration on the cortical surface. pRF mapping was performed following the framework outlined by (Dumoulin and Wandell 2008) and using the PyPRF 2.0 (https://github.com/ingo-m/pyprf) implementation. The stimuli were

bars containing black and white checkerboard patterns (see Figure 3.2). The bars had a width of 1.24° visual angle. The spatial frequency of the checkerboard pattern within the bar stimulus was 1.2 cycles/deg. The luminance of the black and white sectors within the bar stimulus was 6.9 cd/m^2 and 771.7 cd/m^2. The polarity of the chequerboard pattern was reversed at a frequency of 4 Hz. There were 14 possible bar positions along the width of the display screen and along the diagonals, and 9 possible bar positions along the height of the screen. Each bar position was presented for 2.604 s and repeated four times. Each run took 9.85 mins. During the pRF mapping run, participants were instructed to fixate on the central dot (0.04°, RGB value [40, 233, 208]), surrounded by a thin fixation grid (0.09°, RGB value [249, 133, 0]), and report colour changes of the fixation spot from green to orange by pressing button 1. Targets were presented randomly for 0.3 s, with a mean inter-trial interval of 15 s.

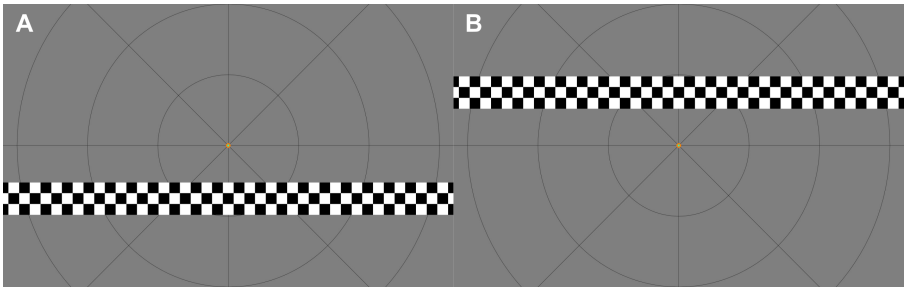

Figure 3.2: Examples of pRF stimuli with mapping stimulus below (**A**) and above (**B**) fixation. Circular grid was not shown to the participant.

Brightness Induction (BI) main experiment: Following results from our psychophysics measurements, the size of the probing region had the width of 12° and the height of 5°. The size of the display was 16.6° x 10.38° (width x height). The region beyond the probing region was inducer. The probing region was always grey (78.98 cd/m^2) and every stimulus block started from a whole-field grey surface. Stimulus onset and duration were locked to the TR. During a stimulus block, the luminance of the inducing region changed from grey to its maxi-

mum (Lum. inc, 771.7 cd/m^2.) or minimum (Lum. dec, 6.9 cd/m^2) in a sinusoidal fashion within one second. The maximum or minimum luminance was then maintained for 11.02 seconds. In the last second of each stimulus block, the inducing region returned to its baseline in a sinusoidal fashion. To induce a stronger illusion and avoid changes of perception due to environmental light sources, all lights in the scanning room and console area were switched off.

Each run included 6 repetitions of the luminance increment and decrement conditions presented in pseudo-random order. Stimulus blocks (13.02 s) were followed by baseline (fixation-only) blocks of either 15 TRs or 14 TRs (39.06 s, 36.46 s). We also included 52.08 s of baseline period at the beginning of each run and 5.20 s at the end. The total duration of one run was 11.20 mins. Participants reported when the fixation dot changed from green to orange by pressing button 1. Colour changes were presented for 0.8 s with a mean inter-trial interval of 17 s (jittered $\pm$ 11 s) between changes. No target colour change was shown during the first and last 70 s of each run. The timing of target colour changes was interspersed with the stimulus events in a way that the predicted haemodynamic responses to the targets and to the stimulus block had minimal correlation. To achieve this, we first defined an event vector representing stimulus blocks and an event vector representing pseudo-randomly timed target events, both convolved with the haemodynamic response function (represented by a gamma function). Then the correlation between the two vectors was calculated. If the correlation coefficient was above the threshold of 0.001, a new pseudo-random design matrix of target events was created and the procedure was repeated, until the correlation coefficient fell between the threshold and zero. This procedure was performed separately for each run.

Data acquisition

All data were acquired with a Siemens Magnetom 7T scanner using the 1-Tx/32-Rx commercial head coil (Nova Medical, Wilmington, MA,

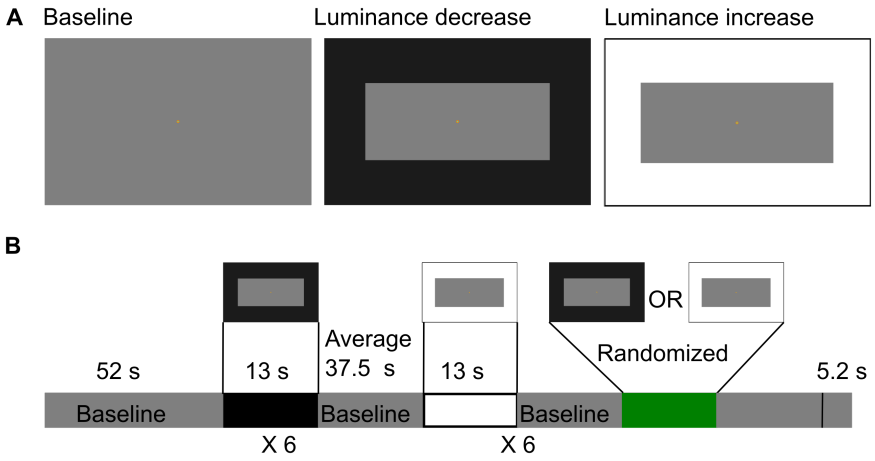

Figure 3.3: Experimental design.
A: experimental conditions. The two stimulus conditions consisted of a luminance decrease (followed by a return to grey) and luminance increase (followed by a return to grey). The centre grey rectangle (probing region) had a size of 12° x 5° (width x height), where the luminance was constant. The luminance of the surrounding frame (inducing area) changed at the beginning and end 1 s of the block. A central fixation spot was presented throughout the experiment. Stimuli were presented in blocks of 13 s, followed by jittered baseline periods. The two stimulus conditions were pseudo-randomised within the run and across the 6 runs.
B: Schematic of the stimulus presentation for an example task run.

USA). The acquisition was performed in two sessions. Opposite phase encoding data [5 volumes] were acquired after each EPI run for within-session run-wise distortion correction. For every participant, we collected 3-4 runs of pRF (227 volumes per run) to delineate visual fields in the visual cortex and to project areas from the visual field to the cortex. We also collected 6 runs of the brightness induction experiment (main experiment).

Session 1: pRF

pRF mapping data were acquired using gradient-echo (GE) 3D-EPI (Poser et al. 2010) sequence (Figure 3.4) [1.0mm iso, GRAPPA=3, Repetition Time (TR)=2.604 s, Flip angle (FA)=15°, Echo Time (TE)=25 ms, field of view (FOV)=150 mm, Phase encoding direction (PE)=R≫L, coronal slices=52, Bandwidth (BW)=1282Hz/Px, partial-Fourierslice=6/8, partial-Fourierphase=6/8, echo-spacing=0.88ms, RF. lines PE=78, EPI factor=150].

Session 2: Brightness illusion (BI) main experiment

Anatomy: for n=5 participants, whole brain anatomy was acquired using a 0.8 mm isotropic 3D-MP2RAGE sequence (Marques et al. 2010) [Sagittal slices=224, TI1/TI2=800/2750 ms, FA1/FA2=4°/5°, TR=6.0s, TE=1.95 ms, FOV=256x256 mm^2, matrix size=320x320, slices=224, partial-Fourierphase=7/8, partial-Fourierslice=off, echo-spacing=5.8 ms, RF. lines PE=32, PE=A≫P, BW=250 Hz/Px], for n=6 participants, the whole brain anatomy was acquired using a 3D-MP2RAGE with Fat Navigators (Gallichan et al. 2016) sequence [0.8 mm isotropic, TI1/TI2=800/2750 ms, FA1/FA2=4°/5°, TE=1.95 ms, FOV=256x256 mm^2, PE=A≫P, BW=180 Hz/Px, matrix size=300x300, slices=256, partial-Fourierphase=7/8, partial -Fourierslice=7/8, echo-spacing=6.9 ms, RF. lines PE=30, FatNav resolution=2 mm, FatNav FA= 3.0°, Train-FatNav delay=20 ms], which allowed retrospective correction of within-scan head motion.

fMRI: 6 runs of fMRI data were acquired using a GE 3D-EPI (Poser et al. 2010) sequence [0.8 mm isotropic, GRAPPA=3, TR=2.604 s, FA=15°, TE=25ms, FOV=150, PE=R≫L, coronal slices=52, BW=1108Hz/Px, partial-Fourierslice=6/8, partial-Fourierphase=6/8, echo-spacing=1.01 ms, RF. lines PE=78, EPI factor=188], covering the early visual cortex (Figure 3.4).

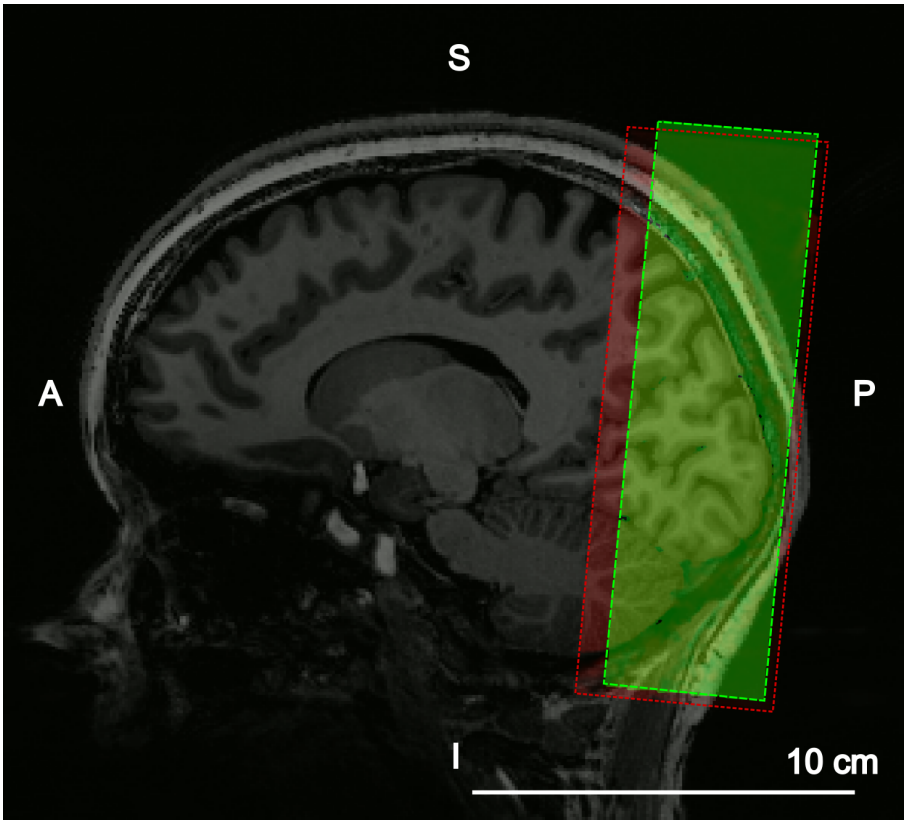

Figure 3.4: Coverage of 3D GE-EPI data in the pRF session (red shade) and the BI-fMRI session (green shade). Scale bar: 10 cm.
Abbreviations: A: anterior, P: posterior, S: superior, I: inferior.

Data processing

All the DICOM data were transformed to NIfTI following the BIDS specification (Gorgolewski et al. 2016). See Figure 3.5 for a scheme of the preprocessing and analysis pipeline.

Anatomical (see Figure 3.6): the anatomical data were bias-corrected in SPM12 (Ashburner and Friston 2005). The second inversion (INV2) of the MP2RAGE was fitted to FSL BET v2.1 (Smith 2002) to create a brain mask and also for automated segmentation in SPM12 (Ashburner and Friston 2005). The non-brain tissue segments from SPM12 were combined with the brain mask created from FSL BET to mask out the large vessels and non-brain tissue. The brain mask was applied to the T_1 image of the MP2RAGE. The UNI image of the MP2RAGE was bias-corrected in SPM12 and then the combined brain mask was applied before fitting it to Freesurfer v7.1.0 (*recon-all*) (Fischl 2012) together with the skull-stripped T_1 image. The segmentation and surface reconstruction were completed in the native resolution and the segmentation in the occipital lobe was manually corrected in ITK-SNAP v3.8.0 (Yushkevich et al. 2006).

Preprocessing- fMRI (pRF & BI): 4D EPI data from every run was disassembled into 3D volumes. Motion and distortion correction were performed using ANTs (Avants et al. 2009). Specifically, we extracted the first five volumes of the first run for the whole session using *fslroi* to create a template image. Each volume in the five volumes were then aligned to the first volume using *antsRegistration*. The template [fMRI-template] was generated by calculating the mean of those aligned five volumes using *AverageImages*. Motion within run and across runs were estimated by iteratively registering each volume to this template using *antsRegistration*. To estimate distortion, we first created a template for opposite [oppo-template] phase encoding runs using the method above. Distortion between the oppo-template and the fMRI-template image was estimated using *antsMultivariateTemplateConstruction2* with *SyN* transformation (Avants et al. 2009). The

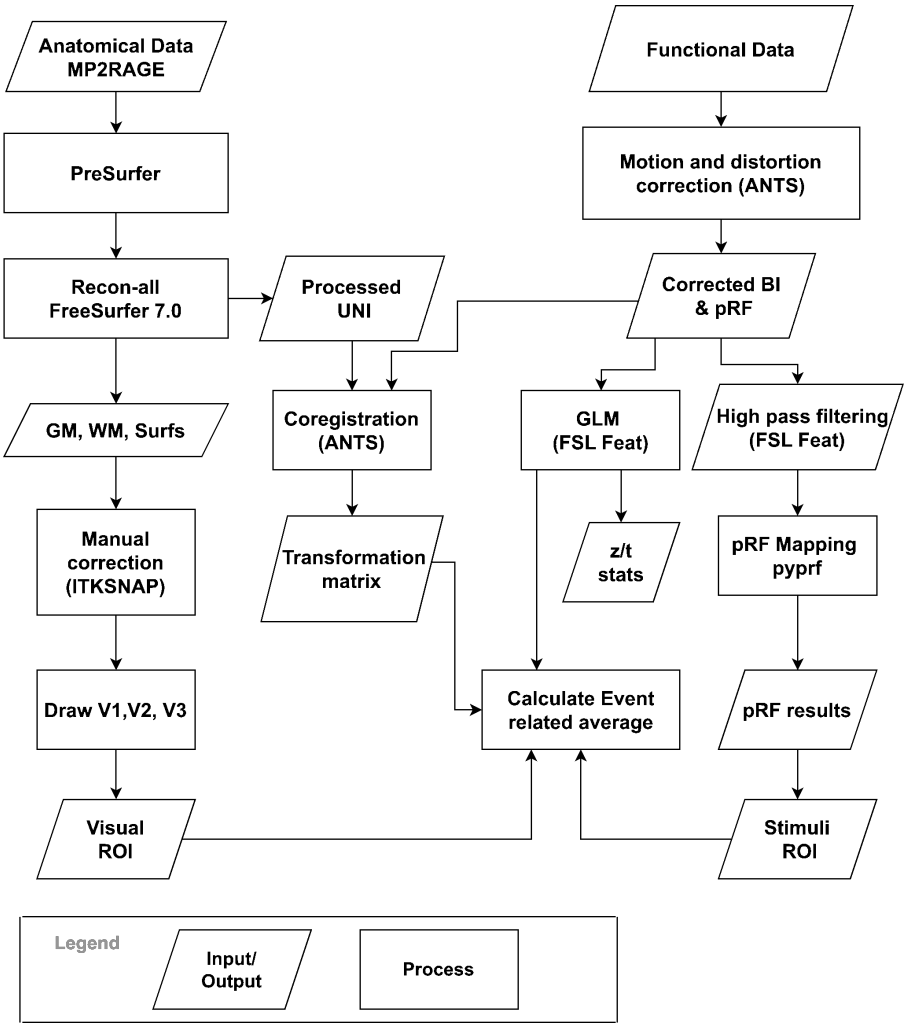

Figure 3.5: Overview of processing pipeline for structural and functional images. Rhombic shapes represent input or output. Slanted Rectangular shapes represent processing steps.

functional data were then motion- and distortion-corrected by combin-

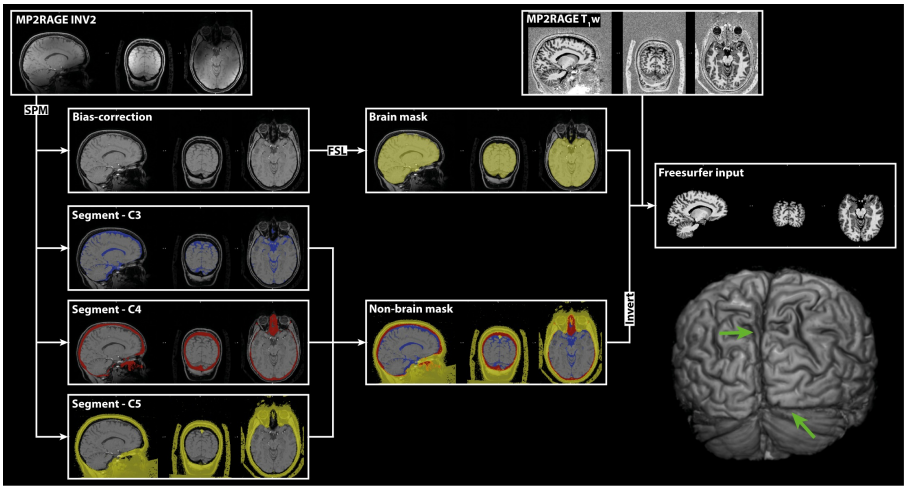

Figure 3.6: Anatomical data pre-processing workflow for MP2RAGE data for input to Freesurfer' s recon-all (https://github.com/srikash/presurfer) (Kashyap et al. 2021b) The 3D rendering of the anatomical image in the bottom right panel shows the intact GM surface at the occipital lobe. Green arrows indicated locations of the (resected) sagittal and transverse sinuses.

ing the motion and distortion transformations in a single resampling step using *antsApplyTransforms* and a *BSpline[4]* interpolation. These motion and distortion corrected 3D volumes were finally reassembled into a 4D dataset. High pass temporal filtering (Gaussian-weighted least-squares straight line fitting, with sigma = 50.0s for BI EPI and 22.5s for pRF EPI) was applied to the 4D dataset using FEAT (FMRI Expert Analysis Tool) Version 6.00, part of FSL (FMRIB's Software Library, www.fmrib.ox.ac.uk/fsl). Temporal signal to noise ratio (tSNR) maps were derived from the high pass filtered dataset.

Across-session coregistration: The motion and distortion corrected fMRI template (pRF- and BI-template) was aligned to the anatomy after being processed by *recon-all* (anat template) and to each other. The initial transformation matrix of these three pairs of registration was guided visually in ITK-SNAP and estimated

using a rigid transformation. This initial transformation was used as initial-moving-transform to obtain a fine-tuning transformation matrix using *antsRegistration*. The fine-tuned transformation matrix was then applied using *antsApplyTransforms* to transform the data from one space (e.g. pRF, fMRI) to another (e.g. anatomy).

Session-2 (BI fMRI): fMRI data processing was carried out using FEAT (FMRI Expert Analysis Tool) Version 6.00. Registration to high resolution 'structural' and 'standard space' [fMRI-template] images was carried out using FLIRT (Jenkinson et al. 2002; Jenkinson and Smith 2001). A general linear model (GLM) was fitted with separate predictors for the two stimulus conditions (Luminance increase, decrease) for the target events of the fixation task. Time-series statistical analysis was carried out using FILM (FMRIB's Improved Linear Model, first-level GLM analysis) with local autocorrelation correction (Woolrich et al. 2001).

Regions of interest definition

Population receptive mapping was performed on the preprocessed 4D data using publicly available python code (Marquardt et al. 2018) and standard scientific python packages (Cython, Matplotlib, Scipy, Numpy) (Behnel et al. 2011; Harris et al. 2020; Hunter 2007; Virtanen et al. 2020). We projected the pRF outputs (eccentricity and polar angles) to an inflated surface in Freeview (Fischl 2012). On this inflated representation, we manually drew borders of V1, V2 and V3, identified from polar angle maps. We used $R^2 > 0.10$ as an inclusion criterion so that only those locations with a reasonable fit were included. ROIs passing this criterion were subdivided into three distinct retinotopic regions (see Figure 3.7), corresponding to the centre of the probing region, its edges, and a part of the inducer.

Stimulus ROIs were defined in visual-field space. See Figure 3.8 B, the central ROI (probing region) was defined as a rectangle with a height of 2° and a width of 6°, centred on the fixation dot. A circular sector with a diameter of 0.75° was omitted in order to avoid the influence of

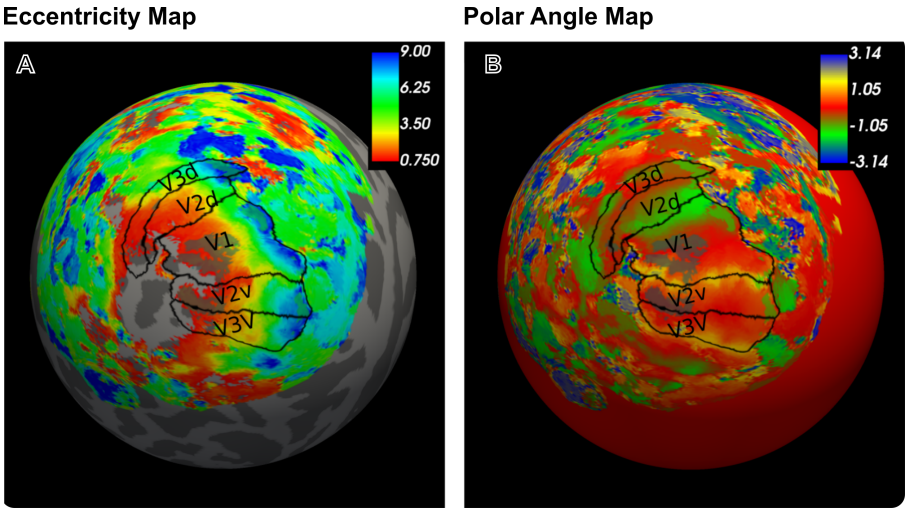

Figure 3.7: Visual eccentricity and polar angle (colour bars) maps from pRF mapping used for delineation of visual fields. The pRF properties were shown on the left hemisphere of a representative participant. The hemisphere reconstruction was morphed into a sphere for better visualisation. Colored areas indicate a pRF fit of $R^2 > 0.10$. Dark-grey colour indicates sulci and light-grey colour indicates gyri. Borders between visual areas V1, V2 and V3 (black outlines) were defined by the polar angle map with yellow and green colours indicating the upper and lower vertical meridians respectively. 9° of eccentricity (blue) correspond to the outer edge of our pRF mapping and so marks the edge of identified visual areas.

the fixation dot (diameter = 0.09°). The probing region had an area of 17.3 cm^2. The edge ROI was constructed along the edge of the probing region and the inducing area with a width of 1°, covering a total area of 57.8 cm^2. The background (inducer) ROI was a frame of 16.6° x 10.38°, of which the inner edges were removed from the outer edges of the edge frame by 14° x 7°. It had an area of 98.6 cm^2.

The pRF of a voxel has a given size in the visual field and the shape of 2D Gaussian. To decide whether a voxel belonged to the cortical representation of a stimulus ROI, we set a criterion on how much

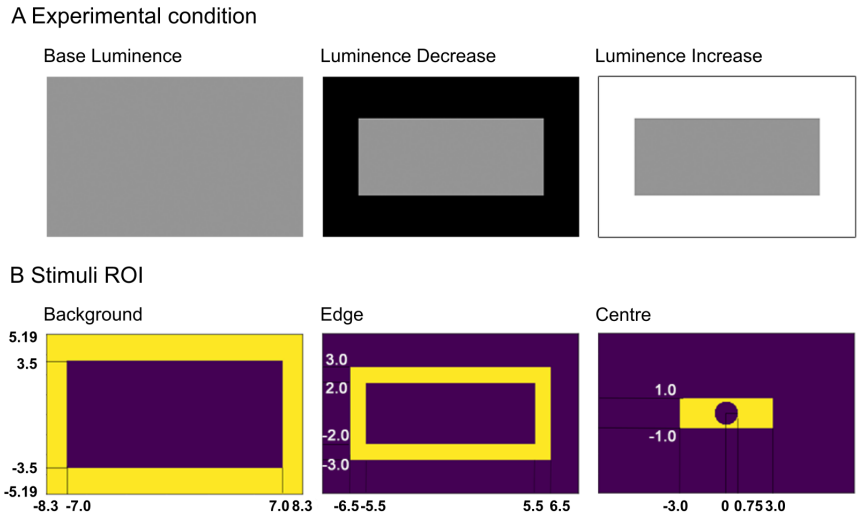

Figure 3.8: Stimulus conditions (**A**), and stimulus ROI defined according to the shape of the stimulus (**B**). Numbers are in degrees of visual angle.

overlap there had to be between the pRF and the stimulus ROI. If the pRF of a voxel overlapped by more than the criterion with the stimulus ROI, the voxel was considered to be part of the cortical representation of the stimulus ROI. We compared three overlap criterions (50%, 75% and 90%, see Figure 3.9), and summarised the number of voxels in each ROI per criterion (Table 3.1). Table 3.1 shows how cortical magnification is reflected in our defined ROIs (also in Figure 3.10) by the decrease of number of voxels in each ROI from centre to background, even though the area in visual-field space increased. Figure 3.10 shows how the number of voxels also decreased between V1, V2 and V3 in each ROI. To have enough voxels to work on in each stimuli ROIs, we chose 75% overlap for the centre and background ROIs, and 50% overlapping for the edge ROI.

Because the pRF maps from S4, S7, S10 could not be used, further analysis was focused on the remaining eight participants. S6 was not

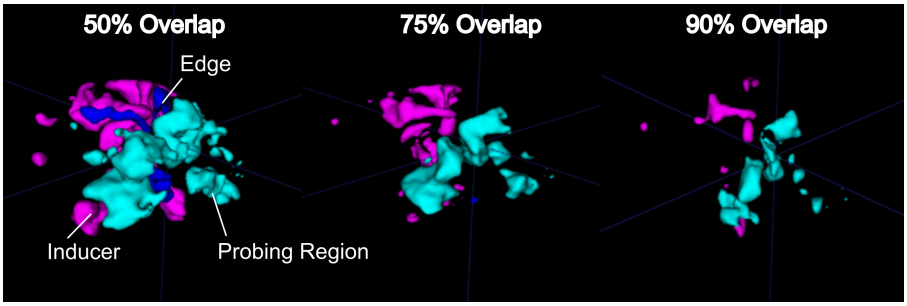

Figure 3.9: Comparison among three overlapping ratios.

Table 3.1: Number of Voxels per stimulus ROIs (summation of all visual areas) with various overlapping ratios from one participant.

Num. Voxel / ROI	50% Overlap	75% Overlap	90% Overlap
Probing region	10566	4436	1809
Edge	1535	67	9
Inducer	11017	3218	838

included in event-related analysis since the edge ROIs of this participant in V1 and V2 did not show the canonical BOLD hemodynamic response, thus, for that analysis only seven participants were included. As pRF maps from S5 could only be used on the left hemisphere, group time courses were generated from 13 hemispheres.

Temporal response pattern

To investigate the temporal dynamics of the luminance increment and decrement conditions, we extracted event-related average time courses corresponding to the inducer ROI, probing region ROI, and edge of the stimulus that fell in V1, V2 and V3. The percent signal change for each luminance condition per participant in each ROI was calculated per epoch, which started 2 TRs before the stimulus onset and ended 16 TRs after the stimulus onset. Each epoch was

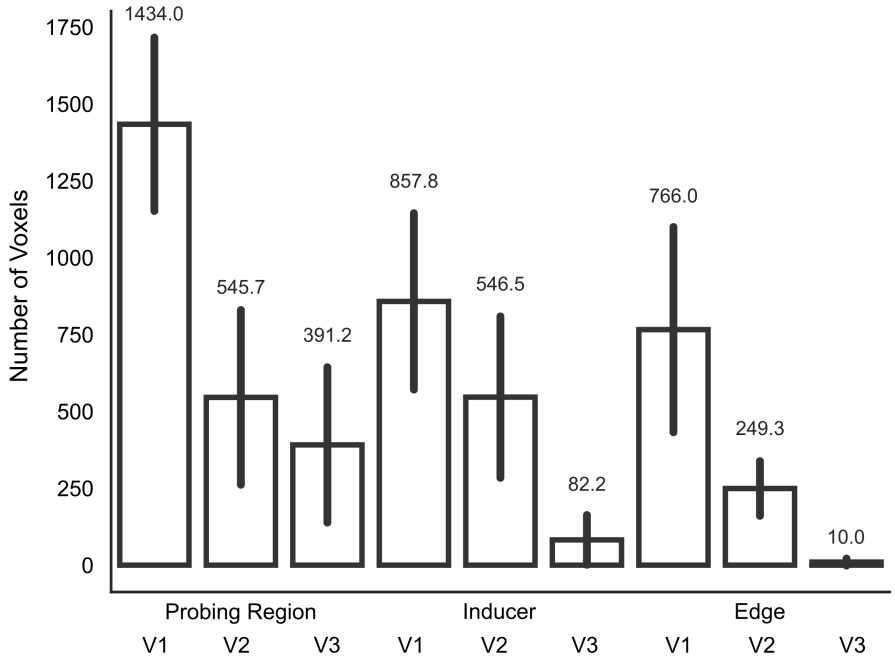

Figure 3.10: Number of Voxels in all the ROIs across 6 participants (12 hemispheres, participant S5 not included here). Error bar represents standard deviation.

normalised by its own baseline, which was the mean activity of the first 3 TRs of the epoch (-2 to 0 TRs before stimulus onset). The epochs per condition were then averaged across voxels, trials and runs. To compare the BOLD response with its baseline, paired t-test with FDR correction was performed on the dataset at each TR.

We also tested the effect of three different sizes of probing ROI on the temporal response, because we observed strong cortical responses outside of the defined ROIs (Figure 3.12 D, E, and F). The widths of the three probing region ROI were 8° visual angle (Large), 6° visual angle (Medium), 4° visual angle (Small) for a constant height of 2° visual

angle.

3.4 Results

3.4.1 Psychophysics: how does the inducer luminance influence perceived brightness in the probing region?

Figure 3.11 A and B show group-averaged changes in perceived brightness (units are in psychopy colors [-1 to 1]) in the probing region as a function of various configurations and locations on the basis of low (Figure 3.11 A) and high (Figure 3.11 B) base luminance. In both base luminance settings, participants perceived the probing region as brighter when the luminance of the inducers was decreased, as indicated by setting a luminance increment (positive value in Figure 3.11) to match their brightness impression in the probing region. Conversely, participants perceived the probing region as darker when the luminance of the inducers was increased, indicated by a decreased luminance setting (negative values in Figure 3.11) to match the brightness impression in the probing region. This pattern of results agrees with previous studies (Rossi and Paradiso 1999; Rossi, Rittenhouse, and Paradiso 1996; Van de Ven et al. 2012). We observed that with low base luminance, brightness induction was stronger for inducer luminance decrements (Figure 3.11 C). However, with high base luminance, the illusion had similar strength for both luminance increments and decrements in the inducers. (Figure 3.11 D). A two-way repeated-measures ANOVA was performed to the low and high base luminance dataset separately (see Figure 3.11), with within-subject factors, Luminance (Lum. Inc, Lum. Dec.) and Conditions (From 1 to 11). The main effect of luminance in the two base luminance settings was statistically significant and large in both low ($F(1, 150) = 165.94$, $p < .001$, Eta2 (partial) = 0.53) and high ($F(1, 88) = 181.39$, $p < .001$, Eta2 (partial) = 0.67) luminance base settings. The strength of the illusion was not significantly affected by shape, size or location of the probing region ($p > 0.90$). These data patterns were also reflected in the single-subject data (see Figure S3.1).

The latter results did not conform to our expectation that larger stimulus areas (or larger cortical representations) would reduce the strength of brightness induction. To examine the effects of changing base luminance, we performed a three-way repeated-measures ANOVA with FDR correction on the combined dataset (low and high base luminance), with within-subject factors, Base (Low, High) Luminance (Lum. Inc., Lum. Dec.) and Conditions (From 1 to 11). We found a significant main effect of Luminance ($F(1, 256) = 363.06$, $p < .001$, Eta2 (partial) = 0.59) and interaction between Luminance and Base ($F(1, 256) = 4.34$, $p = 0.038$, Eta2 (partial) = 0.02). The perceived luminance in luminance increments was significantly increased using high base luminance ($t(256) = 4.20$, $p = 0.00021$)).

These results informed the design of the stimulus to be used in the fMRI experiment. Because size seemed to be irrelevant in the set of stimuli used, we chose to maximise the probing region, while keeping a sufficiently large inducer region, and we chose the higher baseline luminance for the probing region to enhance chances for neural correlates of brightness induction for both inducer luminance increments and decrements (stimulus 3 in Figure 3.11 B, Width 12°, Height 5°).

3.4.2 fMRI: how does the inducer luminance influence the BOLD response of the three ROIs?

The experimental stimuli caused different bilateral activation maps in the visual cortex (Figure 3.12 A and B). These activation maps were projected to a spherical surface (Figure 3.12 D and E). The data of a representative participant showed a negative BOLD response in the inducer ROI compared to baseline for luminance increments (blue colours, Figure 3.12 D), and a yet stronger negative BOLD response ROI for the luminance decrements (blue colours Figure 3.12 E and red in F). The edge induced strong positive BOLD response in both luminance conditions (red colours, Figure 3.12 D and E). In the probing ROI, it was difficult to see a clear trend in the data (Figure 3.12 D, E and F).

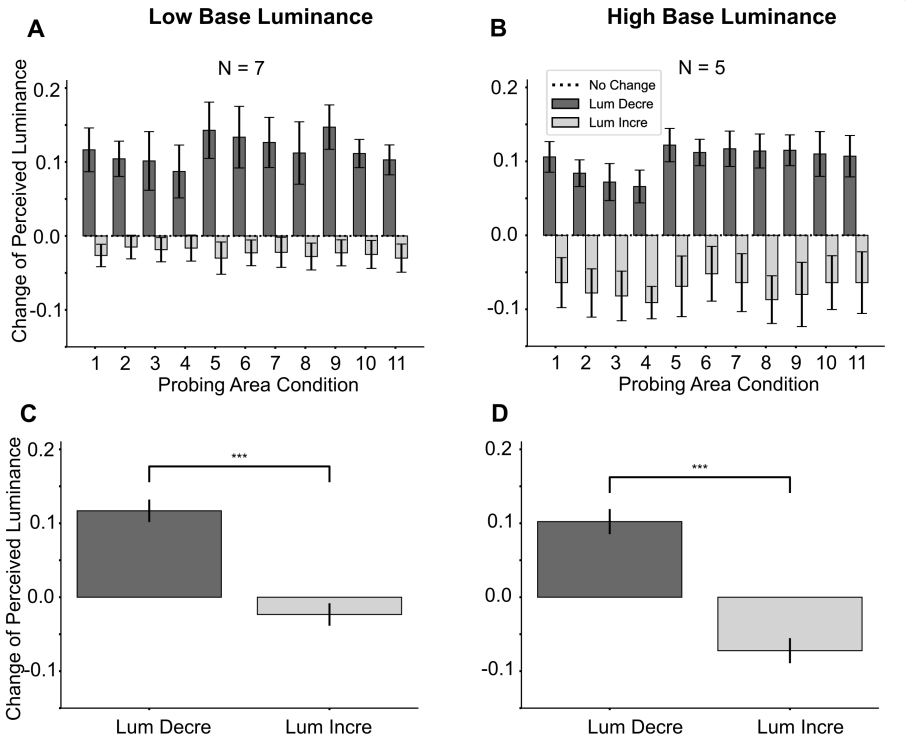

To get a better view of the data, we performed an event-related analysis and followed up with additional statistical testing on grouped time periods of interest, identified from the model HRF. We first performed this analysis combining both hemispheres (13 hemispheres, S5 right hemisphere excluded). The results, fully described in supplementary material S5.1, showed only weak effects which we reasoned may indicate poor signal-to-noise ratio (SNR) in the data. Since the coil used has a known property of better SNR on the left hemisphere (Kashyap et al. 2021a; Marquardt et al. 2018; Vu et al. 2015), we next tested whether this was also true in our dataset. Our main analysis was then performed only on the highest-quality data to give the best representa-

Figure 3.11: (Previous page.) Overview of psychophysics results.
A: Mean change of perceived luminance for low base luminance across seven participants (low base luminance). Numbers on the x axis represent different configurations of the probing region. 1-4: rectangular shape with the width of 12 degrees, various heights (3°, 4°, 5°, 6°, respectively). 5-8: square shape with various side length (3°, 4°, 5°, 6°, respectively), which were presented on 4 ° left of the fixation. 9-11: square shape with various side length (3°, 4°, 5°, respectively), which were presented on 4° right of the fixation. Due to technical reasons, condition 12 (side length 6°, represented on 4° right of the fixation) was not included in the analysis. Error bars represented standard errors. **B**: Mean change of perceived luminance for high base luminance across five participants (high base luminance). Same conventions as in (**A**). **C**: Mean of change of perceived luminance in two luminance conditions for low base luminance across seven participants. Error bars represent 95% confidence intervals. **D**: Mean of change of perceived luminance in two luminance conditions for high base luminance across five participants. Same conventions as in (**C**).

tion of the underlying effects.

Asymmetric tSNR between two hemispheres

Coil-dependent asymmetry of B1 at 7T has been previously observed in B1-sensitive sequences such as diffusion (Vu et al. 2015), ASL (Kashyap et al. 2021a) and GE-EPI BOLD (Marquardt et al. 2018). In our experiment, low tSNR could mask any (differential) response to brightness changes in the probe and inducer regions. Therefore, we tested whether these hemispheric differences were also present in our datasets (motion, distortion corrected and high-pass filtered dataset) in the visual cortex (averaged across V1, V2 and V3). We performed a paired t-test for each run with Benjamini/Hochberg correction among 7 subjects on the tSNR between the two hemispheres. For all 6 runs, we found a significantly higher tSNR in the left hemisphere (Figure 3.13A) consistent with observations in previous studies (Kashyap et al. 2021a; Marquardt et al. 2018; Vu et al. 2015). We next inspected the tSNR per voxel, com-

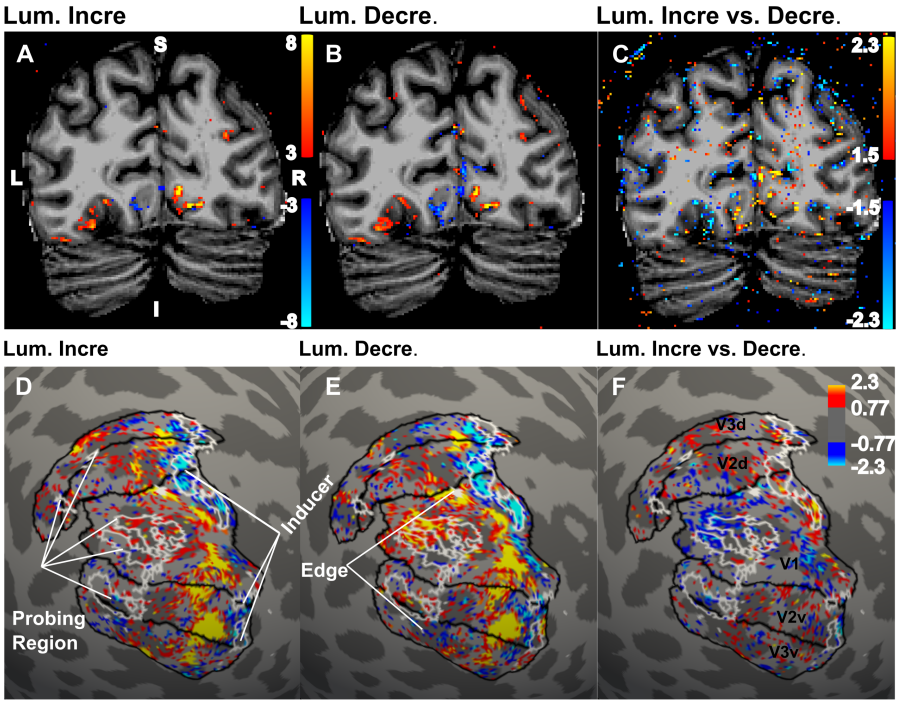

Figure 3.12: The visual stimuli induced positive and negative fMRI BOLD responses in the visual cortex relative to baseline, in a representative participant. The z-scores (**A** and **B**, $p < 0.001$ uncorrected, **C**, $0.06 > p > 0.01$ uncorrected) are shown for the GLM contrasts, each luminance condition against baseline (in **A** and **B**) and contrast (**A** vs. **B**) between two luminance conditions (in **C**), overlaid on the anatomical image (A, **B** and **C**), and projected onto the surface on the left hemisphere (**D**, **E** and **F**, $0.15 > p > 0.01$ uncorrected).
Abbreviations: L: Left; R: Right; S: Superior; I: Inferior.

bined across runs and subjects. We observed a bimodal distribution of tSNR in both hemispheres (Figure 3.13 B), however, the right hemisphere showed the highest density of voxels with low tSNR. Since the stimulus used in the BI experiment was symmetrical along the vertical meridian, it was unlikely to have introduced these differences. In addi-

tion, our experimental design and post-processing was common to the two hemispheres, and therefore was unlikely to have caused the tSNR difference between hemispheres. This supports the idea of a hardware-dependent signal difference, with less reliable data recorded from the right hemisphere. Accordingly, we excluded the right hemisphere from further analysis, and present only data from the left hemisphere in the main text. Analysis of both hemispheres combined are shown in supplementary material 3.6.1.

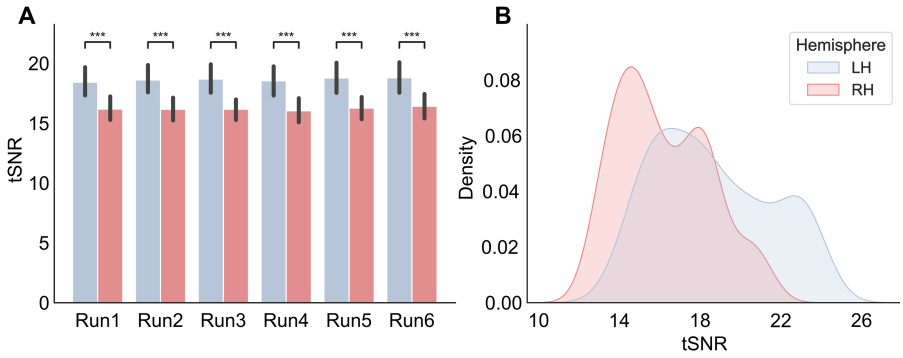

Figure 3.13: Comparison of tSNR between two hemispheres among 7 subjects (14 hemispheres) on the high pass filtered of motion, distortion corrected dataset. **A** shows the mean of tSNR in the visual cortex across functional runs in the left and right hemisphere. **B** shows the distribution of tSNR in each hemisphere. *: $p < 0.05$; **: $p < 0.01$; ***: $p < 0.001$.

Temporal response change from baseline in retinotopic regions

The temporal response from V1, V2 and V3 of the left hemisphere to the two luminance conditions were investigated by extracting event-related time courses, separately for the retinotopic ROIs corresponding to the inducer, edge and probing regions (Figure 3.14), as defined in Methods. We observed various temporal responses in the different ROIs for the two conditions, but these responses were not in agreement with our hypotheses.

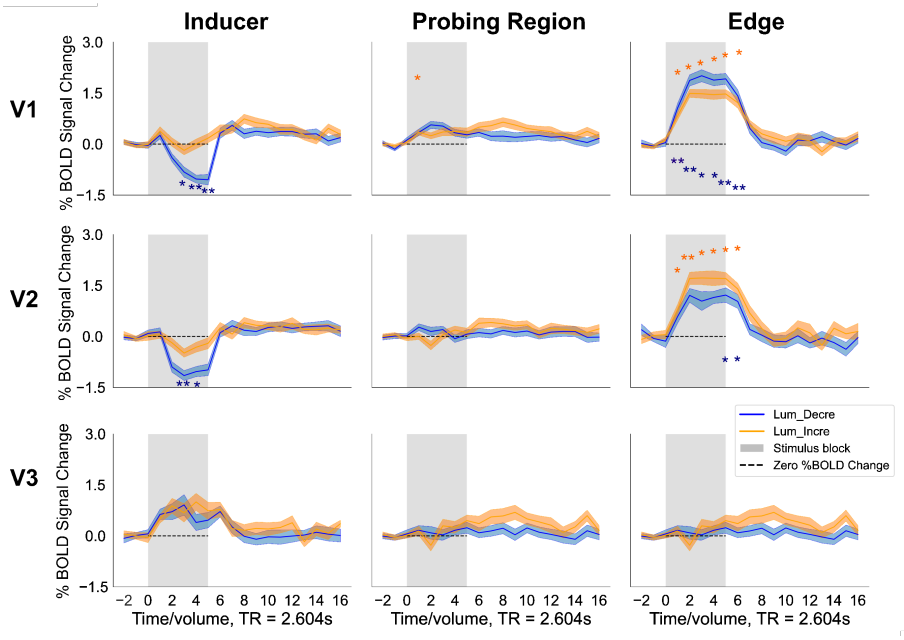

Figure 3.14: Event related averages for all the ROIs on the left hemisphere across 7 participants. Orange * indicated a significant % BOLD signal change compared to its baseline for luminance increment condition. Blue * indicated a significant % BOLD signal change compared to its baseline for luminance decrement condition. *: $p < 0.05$; **: $p < 0.01$.

We had hypothesised that fMRI signal changes from baseline in the probing region would be opposite to the changes associated with the inducers. This hypothesis was not confirmed in the time courses shown in Figure 3.14. Instead, in the probing region, the luminance decrements and increments of the inducers did not lead to noticeable responses compared to baseline. Indeed, we found no significant (paired t-test with FDR correction) change in response from baseline in the probing region ROI of V1, V2 or V3, except at 1 TR after stimulus onset where we observed a positive response ($p = 0.023$) in V1 for the luminance increment condition. Additionally, in V1 there appeared to be a late

sustained response increase in the probing region in the luminance increment condition, although it did not reach significance (7 TRs after stimulus onset: $p = 0.081$; 8 TRs: $p = 0.059$, 10 TRs: $p = 0.054$). This response went in the opposite direction of the hypothesised correlation for brightness induction. Likewise, the response in the inducers was limited to a signal decrease in the inducer luminance decrement condition (V1; 3-5 TRs after stimulus onset, $p < 0.05$. V2; 3-4 TRs after stimulus onset, $p < 0.05$), but without the expected signal increase in response to inducer luminance increments.

Time course analysis did show significant positive BOLD responses elicited in the edge ROIs in V1 and V2 for both luminance increments (1-6 TRs after stimulus onset in V1 and V2, $p < 0.05$) and decrements (1-6 TRs after stimulus onset in V1, 5-6 TRs after stimulus onset in V2, $p < 0.05$). These responses were in line with a response to a contrast edge in the pRF, irrespective of the polarity of the luminance difference of the edge.

Statistical testing of time course components

For further analysis, including comparisons between the conditions, we defined three windows for statistical analysis, based on the predicted BOLD responses to the inducers (Figure 3.15) calculated by convolving double-gamma haemodynamic response function (HRF) from FSL-FEAT with the design matrix of each luminance condition. This analysis allowed reducing the dimensionality of the data and boosting SNR by grouping time points that best represented the main features of the response. We identified three main components; an Early positive response, a Late negative response and a final End response. We took the Early response as the average of percent BOLD signal change from 3-5 TRs after stimulus onset, corresponding to the positive dominant BOLD period. The Late response was the average from 8-10 TRs after stimulus onset, corresponding to post-stimulus undershoot period. The End response was the average from 12-14 TRs after stimulus onset, corresponding to the post-stimulus recovery period.

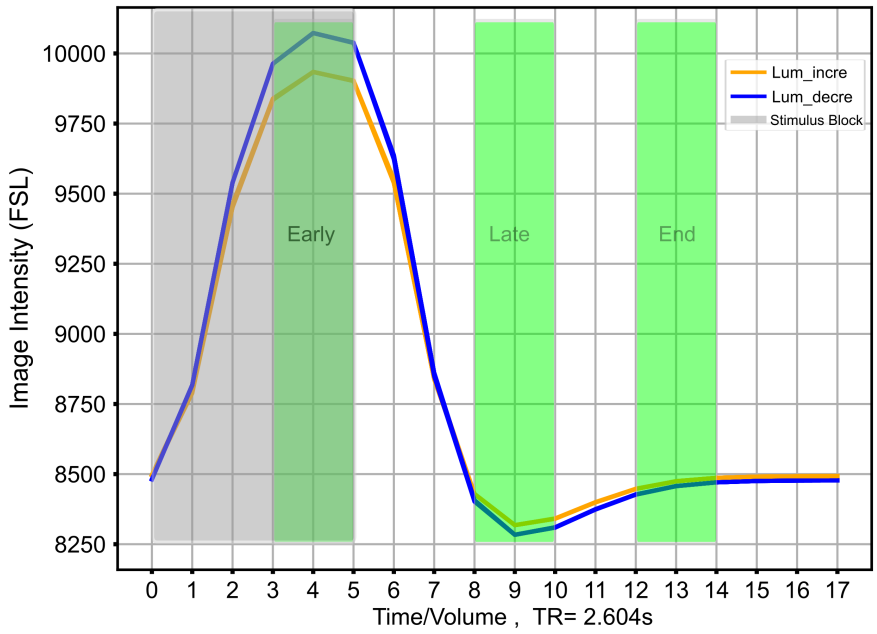

Figure 3.15: An example of predicted BOLD responses for two luminance conditions in the inducers. The three windows chosen for the analysis are shown in green.

We tested fMRI signals on luminance changes in all retinotopic areas using a three-way repeated-measure ANOVA, performed separately on the Early, Late, End responses using the data shown in the Figure 3.14, with within-subject factors including Condition (Lum. Inc., Lum. Dec.), Visual Area (V1, V2, V3) and Stimulus ROI (Inducer, probing region, Edge). Post-hoc paired t-tests (Benjamini-Hochberg correction) were performed to estimate relationships with each other.

In the Early response (Figure 3.16 A & C), we observed significant main effects of Condition ($F(1, 102) = 8.58$, $p = 0.004$, Eta2 (partial) $= 0.08$) and Stimulus ROI ($F(2, 102) = 68.33$, $p < .001$, Eta2 (partial) $= 0.57$). There were also significant interactions between Condition

and Stimulus ROI (F (2, 102) = 3.95, p = 0.022, Eta2 (partial) = 0.07) and between Visual Area and Stimulus ROI (F (4, 102) = 30.03, p < .001, Eta2 (partial) = 0.54). Post-hoc tests showed significantly different cortical responses to luminance changes between the inducer and the probing regions in both V1 (t (13) = -5.69, p = 0.00012) and V2 (t (13) = -5.38, p = 0.00017) (Figure 3.16 A). However, post-hoc tests showed that this was only significant for the luminance decrement condition (t (20) = -2.78, p = 0.014, Figure 3.16 C). Luminance increments did not induce significantly different BOLD signal changes in the inducer and probing regions, indicated by no significantly different responses between the two ROIs (Figure 3.16 C). The opposite sign of BOLD signal change (Figure 3.16 C) in the inducer and probing region for inducer luminance decrements, might indicate a neural correlate for brightness induction. However, further tests showed that while there was a significantly negative early response in the inducer (comparison with baseline, p = 0.014), there was no significant response in the probing region (p = 0.371), which was consistent with our observation of the temporal response (Figure 3.14).

In the edge ROI, contrast due to a luminance change induced a strong positive Early BOLD signal change in V1 and V2 (see Figure 3.16 A). We found significantly higher BOLD signal change for the edge ROI compared to the inducer ROI (V1: t (13) = 8.17, p = 7.08e-6; V2: t (13) = 11.6, p = 2.46e-7, both luminance conditions combined), and for the edge ROI compared to the probing ROI in (V1: t (13) = 7.76, p = 8.32e-6; V2: t (13) = 7.15, p = 1.51e-5, luminance conditions combined). Moreover, we found similar patterns in the edge ROI for each luminance condition (Figure 3.16 C, visual areas combined). Both luminance increment and decrement induced stronger BOLD response in the edge ROI than in the inducer (Lum Decre: t (20) = 4.10, p = 0.00011, Lum Incre: t (20) = 3.41, p = 0.00045) and probing ROI (Lum Decre: t (20) = 4.72, p = 0.00039, Lum Incre: t (20) = 4.97, p = 0.00039).

In the Late response (Figure 3.16 B & D), we only observed sig-

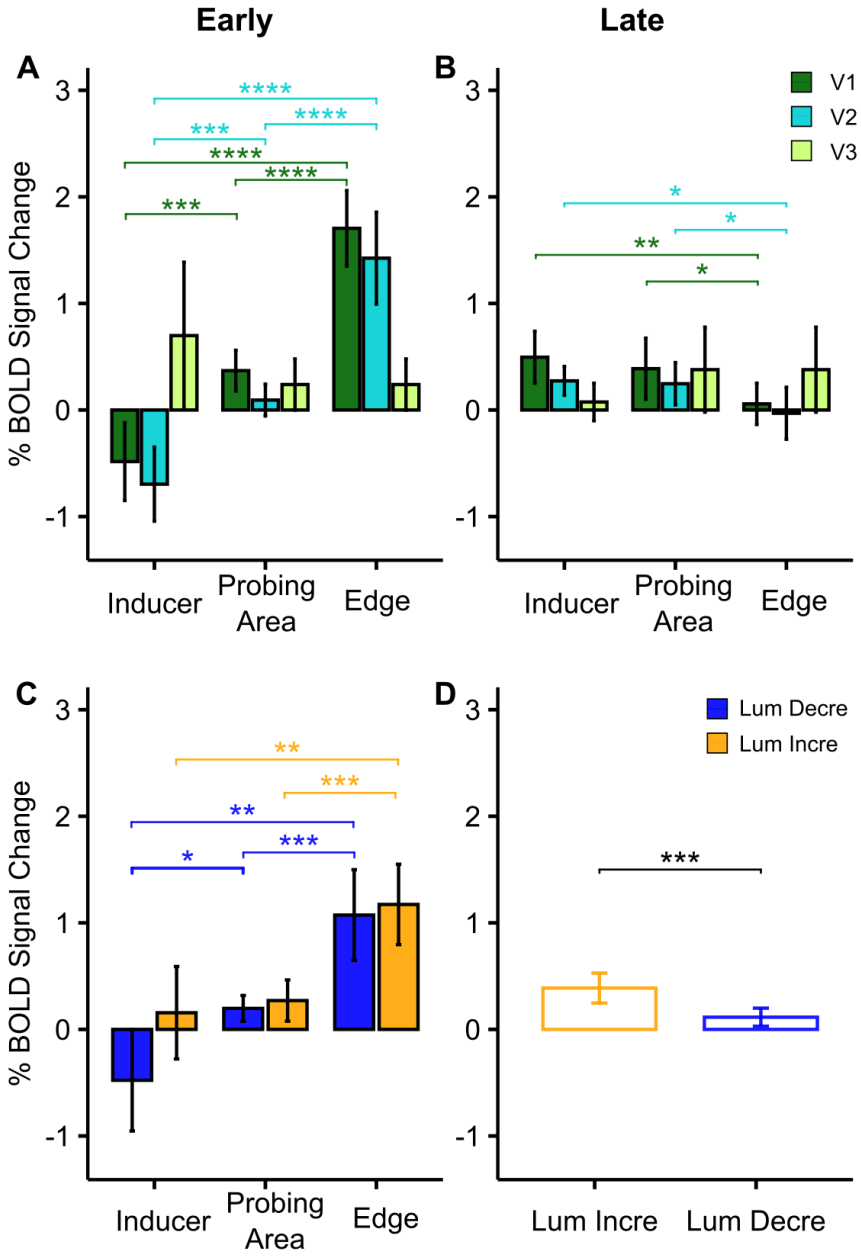
Early
Late
A
B
C
D
% BOLD Signal Change
V1
V2
V3
Lum Decre
Lum Incre
Inducer
Probing Area
Edge
Lum Incre
Lum Decre

Figure 3.16: (Previous page.) Significant ANOVA results in all retinotopic regions in the left hemispheres (N=7). A: Significant interaction between Stimulus ROI (Inducer, probing region, Edge) and Visual Area (V1, V2, V3) in the Early response (response combined over luminance up and down conditions). B: Significant interaction between Stimulus ROI and Visual Area in the Late response (response combined over luminance up and down conditions). C: Significant interaction between Stimulus ROI and Condition (Luminance decrement, Luminance increment) in the Early response (responses combined over V1, V2 and V3). D: Significant main effect of Condition in the Late response, combined over regions and areas. *: $p < 0.05$; **: $p < 0.01$; ***: $p < 0.001$; ****: $p < 0.0001$.

nificant main effects of Condition ($F(1, 102) = 14.44$, $p < .001$, Eta2 (partial) = 0.12, Figure 3.16 D) and significant interactions between Visual Area and Stimulus ROI ($F(4, 102) = 3.36$, $p = 0.012$, Eta2 (partial) = 0.12 Figure 3.16 B). In line with the interaction effect, in both V1 and V2, we observed stronger BOLD responses in the inducer (V1: $t(13) = 4.24$, $p = 0.0077$; V2: $t(13) = 3.15$, $p = 0.032$) and probing regions (V1: $t(13) = 2.53$, $p = 0.050$; V2: $t(13) = 2.81$, $p = 0.040$) than in the edge ROI. The main effect of Condition indicated a stronger BOLD signal change for luminance increment than luminance decrement ($t(63) = 3.76$, $p = 0.00038$). Since the polarity of the response did not differ between ROIs, or between luminance conditions, we conclude that there was no correlate of brightness perception in the late response.

In the End responses, we observed a significant main effect of Stimulus ROI ($F(2, 102) = 3.50$, $p = 0.034$, Eta2 (partial) = 0.06). However, post-hoc analysis did not reveal any pairs of stimulus ROIs with significantly different BOLD responses. There were no other main effects or interactions that could indicate a correlate of brightness perception.

Effects of different sizes of probing region

In view of the results in Figure 3.14 and 3.16, we reasoned that it was possible that the signal from the probing region was somehow interfered with by the signal from the inducers. That is, a hypothetical positive response in the probe region during inducer luminance decrease may have been masked by the strong negative responses observed in the inducer region. Likewise, hypothetical negative and positive responses respectively in the probing and inducer regions may have cancelled each other out during inducer luminance increase. To investigate this possibility, we analysed the event-related responses in the probing region with ROIs that were smaller than the ROI used in our standard analysis. On the other hand, it was possible that we did not sample enough of the probing region to detect a signal related to brightness induction. We therefore also tested an ROI that was larger than that used in our standard analysis. Figure **??** shows that the data from the different ROI sizes were very similar. We performed paired t-tests between each luminance condition and its own baseline with FDR correction separately for the data in the three ROI sizes. In this event-related analysis, we included all the time points rather than use the grouped time windows. We only observed significant BOLD responses to luminance increment in the small probing region at 1 TR ($p = 0.027$) and at 8 TRs ($p = 0.044$) after stimulus onset.

To further investigate effects of the size of the probing region on the BOLD response, a three-way repeated-measures ANOVA was performed on the Early, Late and End responses separately from the data shown in the Figure 3.17, with within-subject factors including Condition (Lum. Inc., Lum. Dec.), probing region (V1, V2, V3) and ROI size (Large, Medium, Small). Post-hoc paired t-tests were performed to estimate the relationship between each other. We found a significant main effect of Condition in the Early ($F(1, 102) = 41.85$, $p < .001$, Eta2 (partial) $= 0.29$) and Late ($F(1, 102) = 41.85$, $p < .001$, Eta2 (partial) $= 0.29$) response whereby BOLD signal change to luminance decrement was smaller than in response to luminance increment in both the Early (t

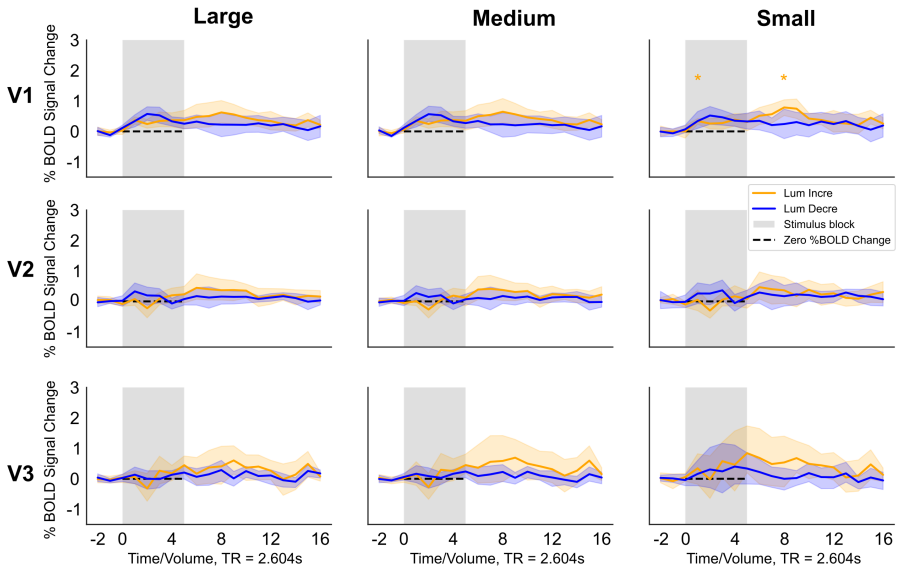

Figure 3.17: Overview of event related averages in probing region ROI with different ROI size across 7 participants on the left hemisphere. Solid lines: mean, shading: standard error. The height of all probing region ROIs are 2°. Large ROI: 8° x 2°. Middle ROI: 6° x 2°. Small ROI: 4° x 2°.

(62) = -6.07, p = 8.33e-08, Figure 3.18 A) and Late (t (62) = -4.96, p = 5.86e-06, Figure 3.18 B) responses. No significant main effects or interactions were observed in the End response. Importantly, no significant interactions were observed in any of the three responses with the size of the probing region. Thus, this analysis does not support the notion that our choice of ROI size for the probe region influenced the pattern of results we observed in the main analysis.

Statistical testing on luminance decrement dataset

Our analysis thus far had indicated that inducer luminance decrements may have been more successful in producing luminance and brightness related responses than the inducer luminance increments. This was

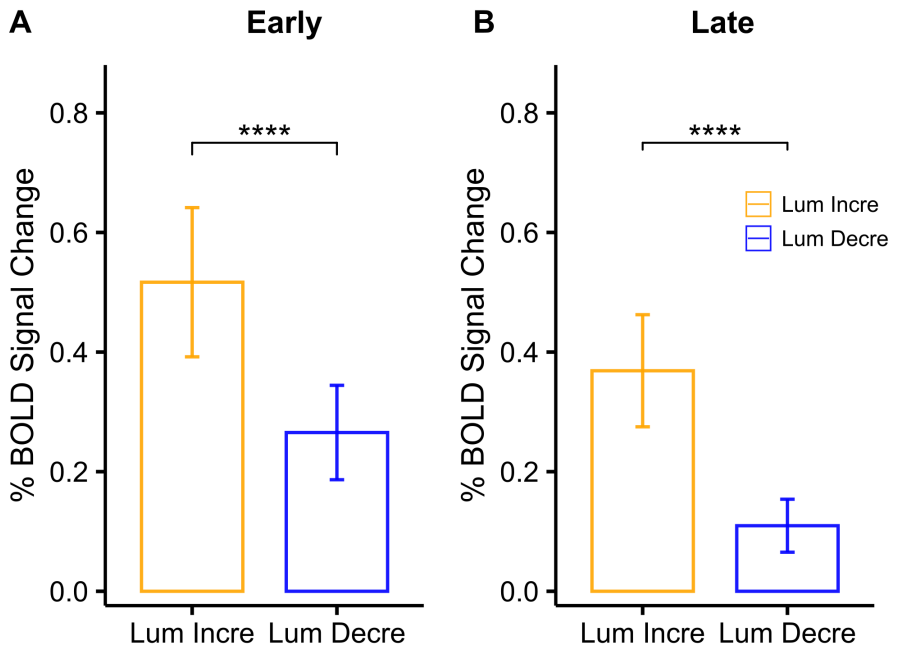

Figure 3.18: Significant ANOVA results in all sizes of the probing region for the two luminance conditions on the left hemispheres (N=7). Error bars represent 95% confidence intervals. ****: $p < 0.0001$.

evident in Figure 3.14, where only the luminance decrement condition led to a response in the inducer ROI, and in Figure 3.16, where the luminance decrement condition was associated with a significant difference between the (negative) response in the inducer ROI and the (trend towards significantly positive) response in the probe ROI. To further investigate the luminance decrement condition in isolation, we performed a two-way repeated measures ANOVA, separately for the Early, Late and End responses using the luminance decrement condition only, with within-subject factors including Visual Area (V1, V2, V3) and Stimulus ROI (Inducer, probing region, edge). Post-hoc paired t-tests (Benjamini-Hochberg correction) were performed to estimate re-

lationships between the factors.

In the Early response, we found significant main effects of Visual Area ($F(2, 48) = 3.29$, $p = 0.046$, Eta2 (partial) = 0.12) and Stimulus ROI ($F(2, 48) = 48.74$, $p < .001$, Eta2 (partial) = 0.67), and a significant interaction between Visual Area and Stimulus ROI ($F(4, 48) = 21.07$, $p < .001$, Eta2 (partial) = 0.64). Post-hoc paired t-tests (Figure 3.19 A) in the inducer luminance decrement condition showed that the positive-trending response in the probing region and the negative-trending response in the inducer was significantly different (inducer < probing region: V1, $t(6) = -16.27$, $p = 2.74e-05$; V2, $t(6) = -5.79$, $p = 1.60e-03$). This data pattern was in line with a correlate of perceptual brightness, with a lower response related to the physically dark inducer than to the perceptually bright probe. However, post-hoc tests failed to show a significant response change (compared to baseline) in the probing region (V1: $p = 0.12$; V2: $p = 0.75$; V3: $p = 0.562$). The observed data trends therefore may be suggestive, but are insufficient to support a correlates of brightness induction in the early visual cortex. The negative responses relative to baseline in the V1 and V2 inducer ROIs, and the positive response in V3, were significant (V1: $p = 7.18e-05$; V2: $p = 2.21e-05$; V3: $p = 0.0137$).

As in previous analysis, the strongest BOLD signal differences were observed in the edge ROI in both V1 (inducer < edge: $t(6) = -9.85$, $p = 2.52e-04$; probing region < edge: $t(6) = -6.14$, $p = 1.60e-03$) and V2 (inducer < edge: $t(6) = -7.85$, $p = 6.00e-04$; probing region < edge: $t(6) = -4.12$, $p = 8.00e-03$). In the Late response, there were no significant main effects and no significant interactions. In the End response, we found significant main effects of Visual Area ($F(2, 48) = 3.44$, $p = 0.040$, Eta2 (partial) = 0.13) and Stimulus ROI ($F(2, 48) = 3.66$, $p = 0.033$, Eta2 (partial) = 0.13) but no significant interactions. A post-hoc paired t-test (Figure 3.19 B) showed a higher BOLD signal change in the inducer than in the edge in V2 ($t(6) = 5.10$, $p = 0.016$).

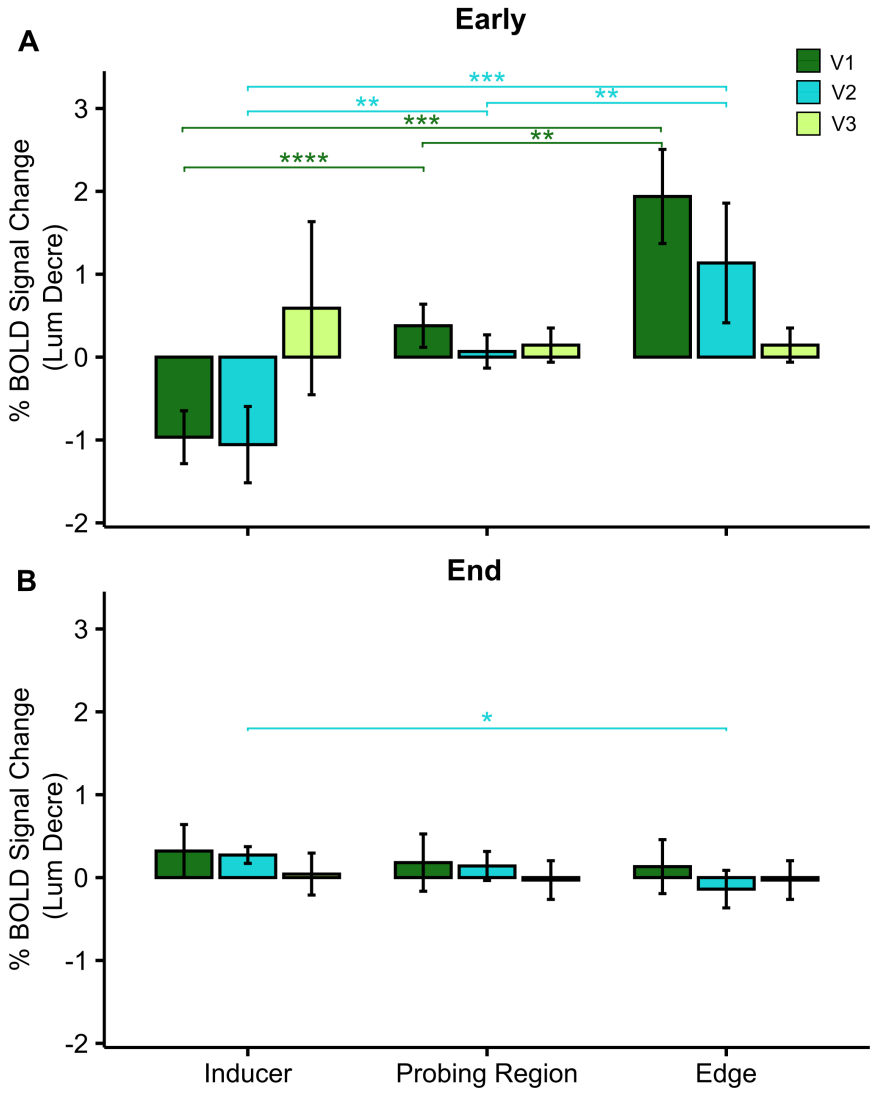

Figure 3.19: Significant ANOVA results in luminance decrement in all retinotopic regions on the left hemispheres (N=7). **A**: Significant interaction between Stimulus ROI (Inducer, probing region, Edge) and Visual Area (V1, V2, V3) in the Early response. **B**: BOLD signal change in the End response (No significant main effects and interactions). *: $p < 0.05$; **: $p < 0.01$; ***: $p < 0.001$; ****: $p < 0.0001$.

3.5 Discussion

3.5.1 Temporal response in the early visual cortex

In this study, we investigated the processing of a brightness illusion in the early visual cortex using high-resolution fMRI at 7T. We extracted event-related fMRI signals in retinotopic areas while participants viewed brightness changes evoked by changing luminance in the inducers. Early visual cortex (V1 and V2, but not V3) responded most strongly to contrast edges, produced by both luminance increments and decrements of the inducer, which was shown by strong positive BOLD responses at the edge representation. Areas of early visual cortex representing the inducer also responded strongly to luminance decrement, which was shown by a strong negative BOLD response, however, luminance increments of the inducer failed to induce a BOLD response in the corresponding cortex. In the representation of the probing region there were no noticeable BOLD responses to brightness changes in early visual cortex, except for in V1 at one time point in the time course analysis (1 TR after stimulus onset) for the luminance increment condition. This result does not replicate the findings of several previous studies that did report a correlate of brightness induction in either V1 (Boyaci et al. 2007; Kinoshita and Komatsu 2001; Pereverzeva and Murray 2008; Rossi and Paradiso 1999; Rossi et al. 1996) or V2 (Hung et al. 2007; Roe et al. 2005; Van de ven et al. 2012). Instead, our fMRI study represents an additional instance of a negative result from an experimental design that had aimed to assess neural correlates of brightness induction in early visual cortex of humans (see also Cornelissen et al. (2006) and Perna et al. (2005)). Taken together our results do not support a robust response that correlates to changes in brightness or luminance in the early visual cortex. That is, if a brightness induction response does occur in line with previous studies (Boyaci et al. 2007; Hung et al. 2007; Kinoshita and Komatsu 2001; Pereverzeva and Murray 2008; Roe et al. 2005; Rossi and Paradiso 1999; Rossi et al. 1996; Van de ven et al. 2012), it does not appear to be sufficiently robust to be statistically significant in our experiment. However, our null finding cannot be

taken as support for symbolic theories of brightness perception and it is possible that methodological differences between our study and studies that have reported a brightness correlate, explain the inconsistency.

In our experimental design, each luminance condition followed a long rest period to allow signal changes from the previous stimulation block to return to baseline. Earlier studies (Cornelissen et al. 2006; Pereverzeva and Murray 2008; Van de ven et al. 2012) presented both luminance conditions in one stimulus block with no break between. By doing so, they effectively increase the luminance/brightness amplitude difference between conditions, albeit at the cost that it becomes difficult to disentangle whether the cortical response they observe was driven by luminance increment or decrement. From our results, luminance decrement induced much stronger cortical response. This asymmetry, in which 'darkness induction' greatly surpasses 'brightness induction' , has been previously observed in White' s effect (Blakeslee and McCourt 1999; McCourt and Foxe 2004) and so the lack of the expected responses we observed to inducer luminance changes makes the absence of a correlation of brightness induction in the probing region not surprising. Thus, we suggest that future investigations of cortical correlates of brightness induction should take advantage of the full luminance amplitude sweep rather than separating up and down components as we have here. Further adaptations to this design, such as alternating between cycles starting with the dark sweep and cycles starting with the light sweep, could still allow investigation into the relative contributions of the dark and light phases.

We have observed multiple temporal patterns in the various retinotopic regions for each luminance condition. This implies that the underlying hemodynamic response function in the regions we examined may be different from the model we used. Our study and earlier fMRI studies (Cornelissen et al. 2006; Pereverzeva and Murray 2008; Perna et al. 2005; Van de ven et al. 2012) used a GLM model to estimate brain activations. However, GLM often assumes a canonical double gamma HRF to convolve with the stimuli' s design matrix. Using inappropriate

HRF models could lead to inaccurate parameter estimation (beta coefficient). To avoid such inaccuracy, we only used GLM estimations for descriptive analysis (Figure 3.12), while the estimated % BOLD signal change used in our main analysis was independent of GLM estimates. Future studies should consider using a set of sine waves with different frequencies or FIR (finite-impulse-response) filters to estimate the HRF for each condition in each ROI (Henson 2004).

3.5.2 Cortical response to brightness induction on grouped time course segments

For statistical analysis of cortical responses to luminance changes in all retinotopic areas, we grouped the time courses into three segments (Early, Late and End), which corresponded to the positive dominant BOLD period, post-stimulus undershoot period, and post-stimulus recovery period respectively. Here we found that only during the luminance decrement condition, the Early BOLD response in the V1 representation of the probing and inducer regions were of opposite sign. Notably, only the negative responses in the inducer ROI during inducer luminance decrements were significant with respect to the baseline, whereas there were no significant responses related to inducer luminance increments. This may explain the observation of a potentially brightness induction-related response only in the inducer luminance decrement condition.

To investigate whether these findings could be explained by signal mixing between the probe ROI and the regions beyond, we tested varying the size of the probing region ROI. We found that the ROI size did not influence the magnitude of cortical responses in the probing region. It is in fact striking that varying the size did not influence the observed response. Given these findings, it may be possible to use smaller stimuli presented away from fixation and still record a specific response representing the probe. Such a stimulus would be more similar to that used in previous studies (Van de ven et al. 2012) and may give more promising results.

3.5.3 Effects of data quality on the results

We used the 7T 32Rx/1Tx commercial head coil (Nova Medical), which has an inherent asymmetry observable in B1 maps. While this is expected to more strongly influence B1-sensitive sequences such as diffusion (Vu et al. 2015) and ASL (Kashyap et al. 2021a)), this can also affect GE-BOLD studies (Markello et al. (2018), present study from Figure 3.13 & Figure S3.2). The statistically significant hemispheric differences in data quality we found cannot be corrected post-hoc. Therefore, we only included the left hemisphere from all subjects for the main analysis reported here. Future studies can consider using dielectric pads or pTx technology during acquisition to mitigate this issue.

For completeness, we also presented the same analyses on data that included both hemispheres. There are some observable differences when we analysed the results from the combined dataset as reported in the supplementary materials. Both sets of analyses identified that the strongest positive BOLD responses were found in the V1 and V2 edge ROIs and that there was a strong negative BOLD response for luminance decrement was observed in V1 and V2 inducer ROIs (Figure 3.14 & Figure S3.3). Both sets of analysis also found that the size of the probing region chosen did not influence the overall BOLD response. These similarities indicate that the hemispheric asymmetry in tSNR we encountered was not so large as to obscure the most major features of the data. Thus, our results indicate that tSNR hemispheric asymmetry should not influence studies where a strong response is expected. An important feature where the two analyses diverged in our study, however, was in the cortical response from the inducer and probe ROIs from the luminance decrement conditions. The left hemisphere-only analysis suggested a significant difference between the negative response associated with the dark inducer ROI and the positive response associated with the perceptually bright probe ROI (Figure 3.16 C), but this was absent in the combined-hemispheres analysis (Figure S3.4 C). This feature was weakly in line with our original hypothesis, although the support is not strong, given that the response to the probing region

was not significantly different from baseline by itself. In addition, there were several other patterns that diverged between the left-only and full dataset analysis, especially for the luminance increment condition and cortical response in the Late and End period, for example, whether a response reached significance compared to baseline, or the presence of one or more main effects or interaction effects.

Taken together, these results underline the importance of data quality when investigating weak phenomena, such as brightness induction, using 7T fMRI. Future studies may take advantage of the better quality data in the left hemisphere due to B1+ asymmetry by placing experimental stimuli exclusively in the right visual field. Not that B1+ asymmetry is unlikely to have been a factor in previous studies on brightness induction carried out at lower field strengths such as (Boucard et al. 2005; Boyaci et al. 2007; Cornelissen et al. 2006; Haynes et al. 2004; Van de ven et al. 2012) on brightness induction.

3.5.4 Limitations and Outlook

A major drawback in our study may have been that we did not control fixation using an eye-tracker in the scanner. We did not use an eye-tracking system, because the setup was time-consuming (up to an hour), and we therefore opted for maximising data collection during the time slots we had. In our study, participants did perform a fixation task, in which they pressed a button as soon as they detected a colour change of the fixation dot. Those target events happened only every 17 s jittered by 11 s during the brightness induction experiment. Although this task ensured a minimum of engagement, it cannot be considered a task that required accurate fixation. Hence, regular fixation breaks could have compromised the data. In addition, a major feature in our results, that luminance increments in the inducer did not lead to fMRI response increases, may have been due to disturbance from reflected light inside the bore. Scattering light from the bright inducers may have led to increased luminance of the probe region, which would counteract any induced decrease in perceived brightness (Sten-

backa and Vanni 2007). Future studies may attempt to reduce these reflections inside the bore or reduce the change in overall luminance of the stimulus between conditions. Alternatively, the null result from the luminance increment condition may indicate an unoptimized base luminance in the scanner environment, despite our intent to replicate stimuli used in the behavioural setup in the scanner. Our behavioural results and Pereverzeva and Murray (2008) showed that base luminance affected the strength of the brightness illusion. Future studies may wish to assess participants' perception of the stimulus during the scanning, although this has inherent methodological (time constraint) and theoretical (allocation of attention) difficulties.

A previous study from our group was successful in detecting a signal related to brightness induction (Van de ven et al. 2012). A comparison with Van de ven et al. (2012)'s study reveals several relevant differences in the experimental setting. First, their annular stimulus was much larger and included a probing region with a width of 6° (area: 226.08°), which was additionally presented away from the fixation. This was much bigger than what was used in the current study (12° x 5°) due to the limitation of the scanner bore. Other human 3T fMRI studies on the similar topic have also used much larger stimuli than ours (10° x 10° from Boyaci et al. (2007); a diameter of 7° from Cornelissen et al. (2006); a diameter of 9° from Pereverzeva and Murray (2008)), thus the use of a smaller stimulus might have been a limitation in the present study. Previous studies have chosen to use a larger stimulus (in part) to limit spatial spreading of signals between probing and inducing regions, as large probing regions reduce the effects of fMRI spatial signal spread ((De Weerd et al. 1997; Sereno et al. 1995) cited in Van de ven et al. (2012)) especially at lower field strength. In comparison, at 7T a recent estimate suggested a spread of approximately 0.83-1.78 mm (Fracasso et al. 2021), or 2.34 ± 0.20 mm (Shmuel et al. 2007) at half-width-at-half-maximum in the visual cortex, thus mixing of signals between probing, edge and inducer representations is unlikely to explain our null findings. Indeed, our analysis of changing ROI size suggests that the use of an even smaller stimulus (representation) would be feasible as,

even at the largest ROI the response from the edge did not seem to influence the probing region. On the other hand, the smaller stimulus used in our study effectively restricted the probe ROI to central vision (especially in the vertical), whereas a larger stimulus, even presented centrally, covers substantial portions of peripheral vision. In the case of Van de ven et al. (2012) their probe stimulus was entirely restricted to peripheral vision. Likewise, animal studies tend to record from neurons in the periphery/parafovea. Thus, it may be that the limitation of our stimulus was more related to its central position than its small size per se.

A second feature in the study of Van de ven et al. (2012) was the annular design of the brightness induction stimulus. This has a particular advantage in assessing psychophysical performance. Because of the constant eccentricity along the annulus that constituted the probing region in their study, psychophysical performance could be linked with that eccentricity. In our stimulus, we do not know on what part of the stimulus participants made their judgments of induced brightness, and it cannot be excluded that the illusion was generated mostly in the peripheral parts of the stimulus, whereas the probe ROI mostly represented central vision. Note that, in our psychophysics measurements we only compared the perception of small probe stimuli presented peripherally with rectangle stimuli presented centrally. We did not include a small central probe condition. In addition, in Van de ven et al. (2012), the fixation spot was placed in an inner inducer area, making the consequences of smaller fixation errors less consequential than in our stimulus, where a high-contrast fixation spot was placed in the middle of the probing region. Given these considerations, it would be interesting to parametrically vary the position of a relatively small probe stimulus in a future study.

Third, we used a block design with long baseline periods leading to long function runs (11.2 minutes) whereas Van de ven et al. (2012) used shorter functional runs (7.6 mins). The length of the runs in our study may have interfered with proper fixation. Although Van de ven

et al. (2012) also did not use eye-tracking in the scanner, maintaining fixation for 7.6 minutes may have been a more realistic target than doing so for 11.2 minutes. Given the length of our runs, the absence of eye tracking may have been especially deleterious for data quality in our experiment.

Fourth, we acquired the EPI data with the resolution of 0.8 mm^3 acquired by 7T scanners, whereas Van de ven et al. (2012) used a resolution of 2 mm^3 acquired with a 3T scanner. We used 7T fMRI because the ultimate goal of our study was to develop a layer-resolved approach to brightness induction. However, the BOLD signal scales with voxel volume at higher fields; thus we traded off the gain in signal from B_0 for smaller voxels (albeit with an increase in thermal noise), thereby reducing signal to noise, which may have prevented us from detecting the small signal related to brightness induction (Barth and Poser 2011). In our analysis, we did not use spatial smoothing as this is not recommended for laminar fMRI data. However, to see if the paradigm was eliciting effects of interest, smoothing within the grey matter (Blazejewska et al. 2016; Blazejewska et al. 2019; Huber et al. 2017) can be done, which can help in increasing signal to noise. A re-analysis of the data using smoothing may be a useful avenue for further analysis. Another consideration is that compared to 3T, there were more B_1 inhomogeneities in 7T. As we did not correct the B1 field, which may have resulted in poor SNR and uneven contrast (Vaughan et al. 2001). Future research could use dielectric pads or acquire SA2RAGE to correct B_1 maps (Eggenschwiler et al. 2012). A reservation with respect to the idea of further analysis of the current data however is that also the responses from the inducers were not as expected, and the specific issues with experimental and stimulus design that may have caused this will obviously not be resolved by an additional smoothing step in data analysis. Additionally, this experiment was designed for a layer fMRI study. Due to the lack of noticeable BOLD response in the probing region and lack of layer patterns from the activation map after smoothing within the layers, we did not further perform layer related analysis.

In hindsight, prior to moving from 3T to 7T, it would have been better to first perform the study at 3T using the stimulus we planned to use at 7T to first observe the main effects of interest. Only later, we would then have moved to a laminar study. However, the resources and time were lacking. To better replicate and test the observations from Van de ven et al. (2012), a similar experimental setup may also contribute to make better comparisons.

Last but not least, we may need to look into various parameters in fMRI studies to investigate the brightness induction. Beta coefficients (Van de ven et al. 2012) and BOLD signal change (Boyaci et al. 2007; Cornelissen et al. 2006; Perna et al. 2005; Sasaki and Watanabe 2004) often were chosen to be an indicator. However, the methods to estimate these two will influence the results. Estimation of beta coefficients is often based on the GLM model. The selection of HRF models will affect the final results.

In conclusion, the current study showed several interesting features, especially with regard to the difference between luminance increment and luminance decrement conditions which our paradigm allowed us to separate. Nevertheless, we did not observe clear indications of the expected response correlate of brightness perception. We have discussed several factors which may have contributed to this conclusion.

3.6 Supplementary Materials

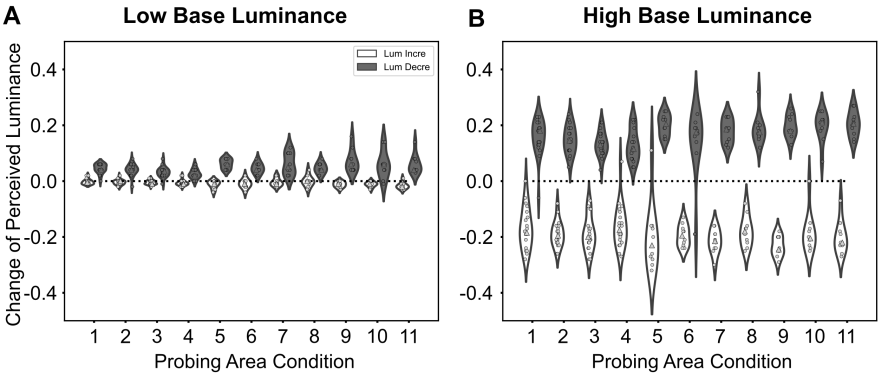

Figure S3.1: Psychophysics results from a single subject at low (**A**) and high (**B**) base luminance. Each dot represents a perceived luminance per trial per probing region condition. Each triangle represents the current condition. Numbers on the X axis represent different probing region conditions. Rectangular: Width: 12°, Height: 3°, 4°, 5°, 6°, respectively. Square L: Location: four degrees left from the fixation, Side length: 3°, 4°, 5°, 6° , respectively. Square R: Location: four degrees right from the fixation, Side length: 3°, 4°, 5°, 6°.

3.6.1 Analysis on the data from 13 hemispheres

Given the previous 3T fMRI experiments (Boucard et al. 2005; Boyaci et al. 2007; Cornelissen et al. 2006; Haynes et al. 2004; Van de ven et al. 2012) used data from both hemispheres, we performed the same analyses reported as in the main text, but combining data from both right and left hemispheres. These results must be considered in context of Sections 3.4.2 and 3.5.3.

Temporal response in retinotopic regions

We extracted the temporal response to the two luminance conditions, separately for the retinotopic ROIs corresponding to the inducer, edge

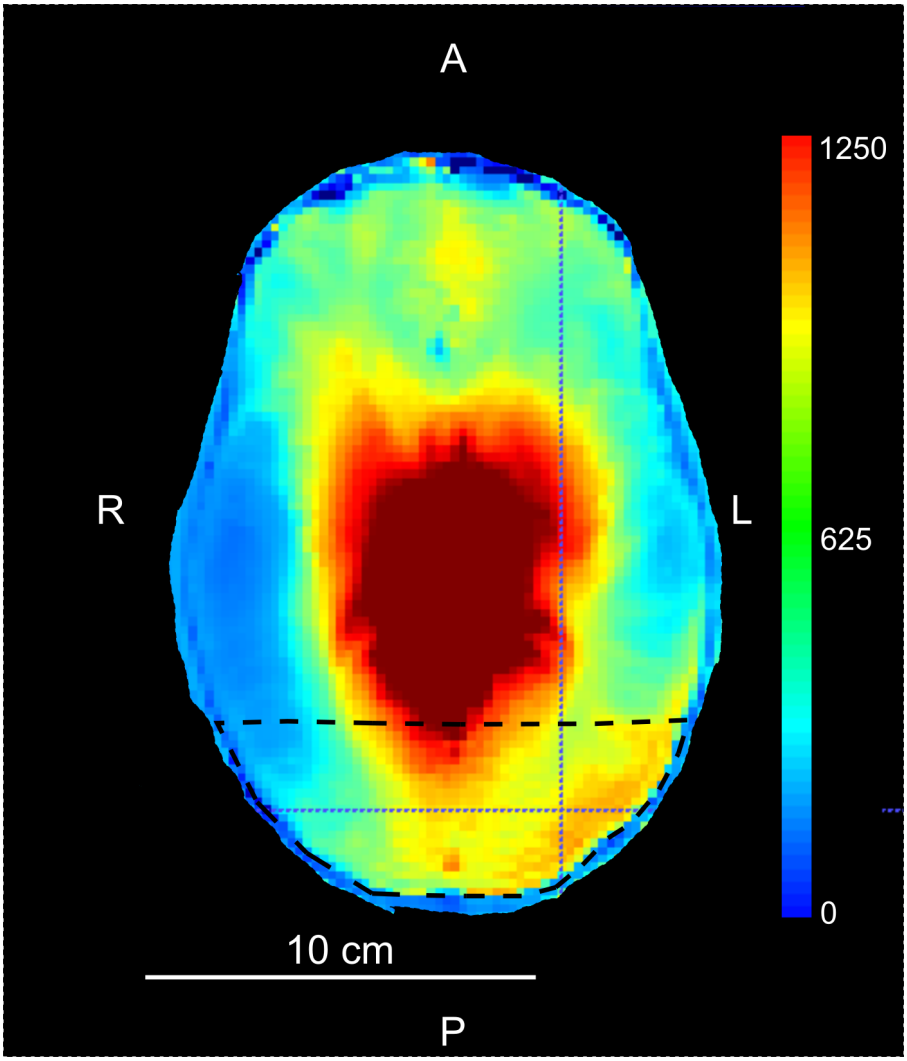

Figure S3.2: Illustration of the B1 map acquired from the SA2RAGE sequence (Eggenschwiler et al. 2012) at 7T scanner. The dashed line represents the field of view of a functional slice.

and probing regions (Figure S3.3), by the method defined in section 3.3.2. We had hypothesised that fMRI signal changes in the probing region would be opposite to the activity changes (and the luminance changes) associated with the inducers. This hypothesis was not confirmed in the time courses either from Figure 3.14 or Figure S3.3. Instead, similar to the results from Figure 3.14, in the probing region, the luminance decrements and increments of the inducers did not lead to noticeable responses compared to baseline, which therefore also could not be related to brightness induction. This was true in V1, V2 and V3. In V1 and V2 there appeared to be a very late somewhat sustained response increase in the probing region in the luminance increment condition (7-8, and 10-12 TRs after stimulus onset, $p < 0.086$). This response however went in the opposite direction of the hypothesised correlation for brightness induction. Likewise, the response in the inducers (limited to V1 and V2) was limited to an fMRI signal decrease in the inducer luminance decrement condition, but without the expected fMRI signal increase in response to inducer luminance increments. The only result in line with expectations was the positive BOLD response elicited at the edge by the contrast changes due to luminance increments and decrements. These qualitative observations were confirmed by paired-t tests with FDR correction (see Figure S3.3).

In the background ROIs, paired-samples t-test with FDR correction confirmed a pronounced negative BOLD response in both V1 (1, 3-5 TRs after stimulus onset, $p < 0.009$) and V2 (3-5 TRs after stimulus onset, $p < 0.03$) for the luminance decrease condition. The luminance increase condition did not cause a response increase in the inducer ROI, in either V1 or V2. There were no significant responses to inducer luminance changes in V3. The responses to the edge were also limited to V1 and V2. In V1, the positive responses in the edge ROI were significant during both inducer luminance increments and decrements, whereas in V2, only the response to the luminance increment was consistently statistically significant.

Comparing the temporal responses shown here and that from the

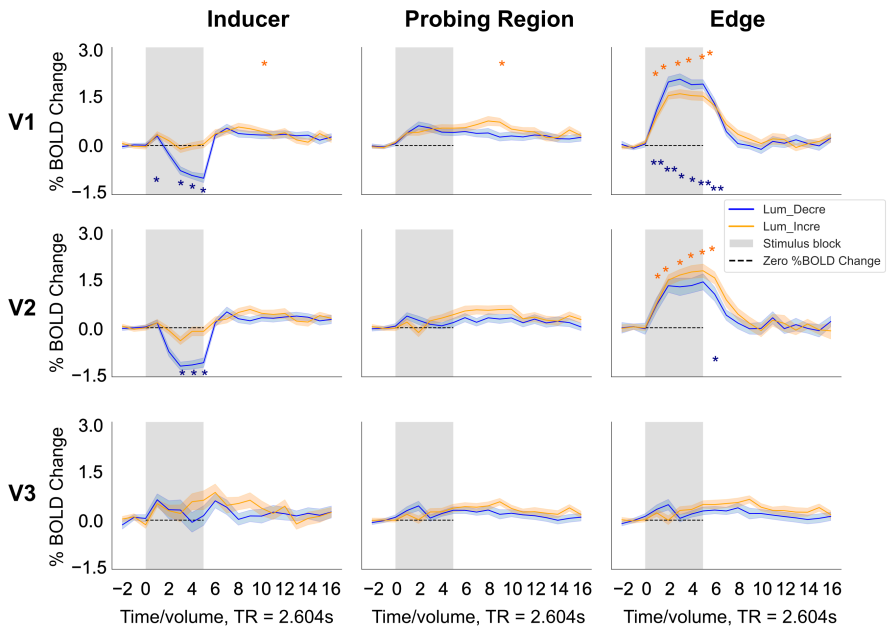

Figure S3.3: Event related averages for all the ROIs across 7 participants (13 hemispheres, see section 3.3.2 Experimental Design). Orange * indicated a significant % BOLD signal change compared to its baseline for luminance increment condition. Blue * indicated a significant % BOLD signal change compared to its baseline for luminance decrement condition. *: $p < 0.05$; **: $p < 0.01$; ***: $p < 0.001$.

left hemisphere shown in the main text (Figure 3.14 & Figure S3.3), both dataset confirmed that the strongest positive BOLD responses were found in V1 and V2 edge ROI, a strong negative BOLD response for luminance decrement was observed in V1 and V2 inducer, no response were found in the probing region and luminance increment was not a successful condition. The differences were which time point had a significant BOLD response and how significant it was.

Statistical testing on grouped time course segments

To test fMRI signals on luminance changes in all retinotopic areas, a three-way repeated-measure ANOVA was performed on the Early, Late, End responses to the data shown in the Figure S3.2, with within-subject factors including Condition (Lum. Inc., Lum. Dec.), Visual Area (V1, V2, V3) and Stimulus ROI (Inducer, probing region, Edge). Post-hoc paired t-test (Benjamini-Hochberg correction) was performed to estimate relationship among each other. In the Early response (Figure S3.4 A & C), we found significant main effects of Condition ($F(1, 85) = 8.81$, $p = 0.004$, Eta2 (partial) = 0.09) and Stimulus ROI ($F(2, 85) = 43.68$, $p < .001$, Eta2 (partial) = 0.51), and a significant interaction between Visual Area and Stimulus ROI ($F(4, 85) = 13.57$, $p < .001$, Eta2 (partial) = 0.39). In V1 and V2, BOLD responses were observed stronger in the edge ROI than inducer (V1: $t(11) = -7.61$, $p = 0.000066$; V2: $t(11) = -7.25$, $p = 0.000066$) and probing region (V1: $t(11) = -5.44$, $p = 0.00041$; V2: $t(11) = -4.99$, $p = 0.00064$). BOLD responses in the inducer and probing region showed an opposite sign (V1: $t(11) = -5.92$, $p = 0.00027$; V2: $t(11) = -4.53$, $P = 0.0011$). A small positive fMRI signal was observed in the probing region and a negative BOLD response was observed in the inducer (Figure S3.4 A). Decreasing luminance in the inducer caused smaller positive fMRI signals than increase of luminance ($t(53) = -4.29$, $p = 7.6e\text{-}05$) in the early response (Figure S3.4 C), however note that the expected reversal of response polarity reversing the inducer luminance was not shown.

In the Late response (see Figure S3.4 B & D), we also found sig-

nificant main effects of Condition (F (1, 85) = 20.38, p < .001, Eta2 (partial) = 0.19) and Stimulus ROI (F (2, 85) = 6.37, p = 0.003, Eta2 (partial) = 0.13) but no significant interactions. BOLD responses in the inducer (t (35) = 2.65, p = 0.018) and probing region (t (35) = 4.37, p = 0.003) were stronger than in the edge ROI (Figure S3.4 B). And decreasing luminance in the inducer also caused smaller positive fMRI signals than increase of luminance in visual cortex (t (53) = -4.92, p = 8.76e-06) in the Late response (Figure S3.4 D). In the End response, we found a significant main effect of Stimulus ROI (F (2, 85) = 3.98, p = 0.022, Eta2 (partial) = 0.09) but post-hoc testing showed that BOLD responses were not significantly stronger in any one of the ROIs.

Comparing the results with those from the left hemisphere (Figure 3.16 & Figure S3.4), both datasets showed a converse relationship in BOLD response between the cortical representation of the inducer and probing region in the Early response (Figure 3.16 A & Figure S3.4 A), however in the full dataset the relationship was not influenced by the luminance condition. Data from the left hemisphere revealed that the relationship was driven by luminance decrement (Figure 3.14 C). However, data from 13 hemispheres showed a stronger BOLD response to luminance increment than luminance decrement (Figure S3.4 C). Combining the previous time courses, this smaller BOLD response to luminance decrement was actually the cause of averaging across visual areas, especially due to the strong negative BOLD observed in V1 and V2. Hence the statistical results from data from left hemispheres represented the data better. As in the Late response (Figure 3.16 B & D & Figure S3.4 B & D), we observed significant main effects of Condition and Stimulus ROI in both datasets. In contrast, when we only focused on the left hemisphere, we observed significant interactions between Visual Area and Stimulus ROI in the Late response. The interaction revealed a significantly higher BOLD signal change in the inducer and probing region than it in the edge at the Late response period. This is indicative of an extra, or longer lasting, cortical processing (e.g. horizontal activity and feedback signal from higher region) in response to surface interiors as compared to contrast edges.

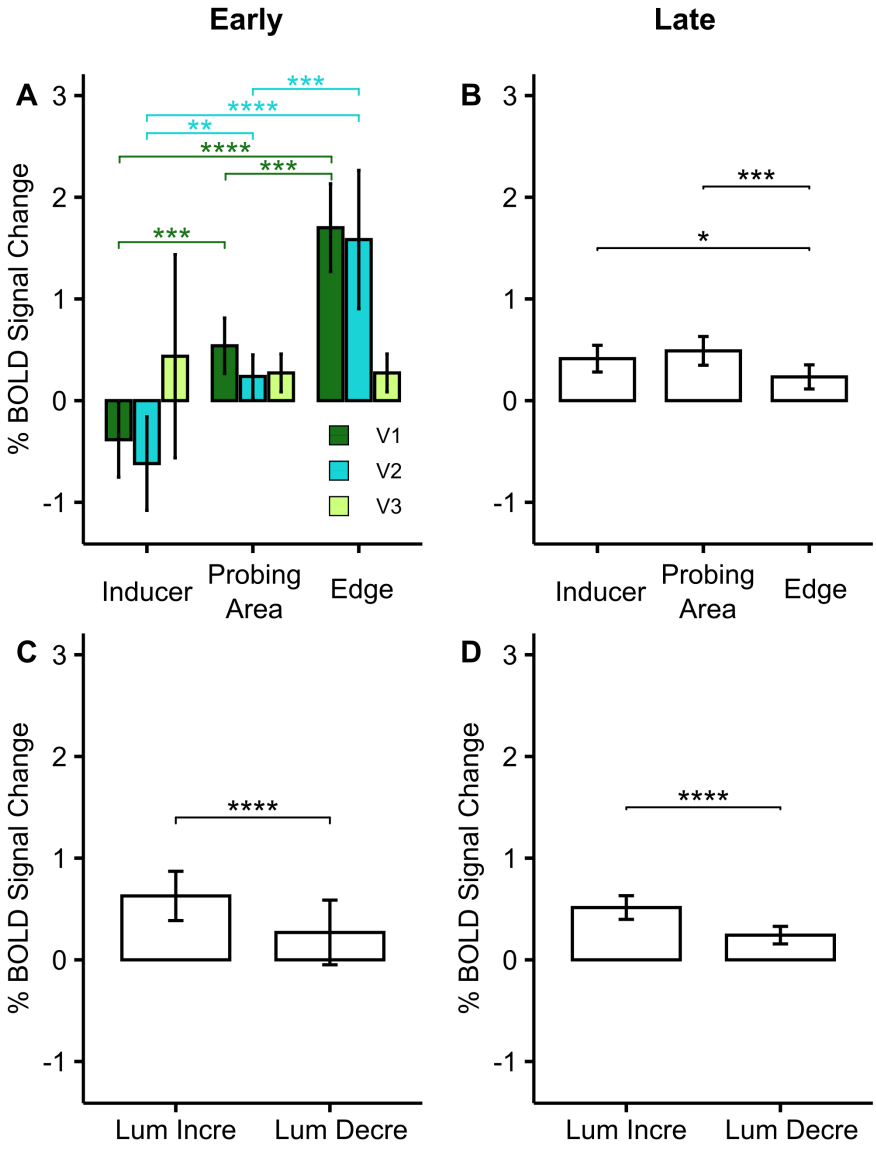
Early
Late
A
B
C
D
% BOLD Signal Change
3
2
1
0
-1
***
****
**
****
***
***
V1
V2
V3
Inducer
Probing Area
Edge
***
*
****
****
Lum Incre
Lum Decre

Figure S3.4: (Previous Page.) Significant ANOVA results in all retinotopic areas across 13 hemispheres. **A**: Significant interaction between Stimulus ROI (Inducer, probing region, Edge) and Visual Area (V1, V2, V3) in the Early response (response combined over luminance up and down conditions). **B**: Significant main effect of Stimulus ROI in the Late response (response combined over two luminance conditions and three visual areas). **C**: Significant main effect of Condition (Luminance decrement, Luminance increment) in the Early response (response combined over 9 retinotopic areas). **D**: Significant main effect of Condition in the Late response (response combined over 9 retinotopic areas). *: $p < 0.05$; **: $p < 0.01$; ***: $p < 0.001$; ****: $p < 0.0001$.

Effects of different sizes of probing region

We extracted temporal responses for the two luminance conditions in three sizes of probing regions. Figure S3.5 shows that the data among the different probing region ROI sizes were very similar. We performed paired t-tests between the luminance increase and decrease conditions with FDR correction separately for the data in the three ROI sizes. We did not find any significant differences in data trends that could be related to brightness induction. A three-way repeated-measures ANOVA was performed on the Early, Late and End responses separately from the data shown in the Figure S3.5, with within-subject factors including Condition (Lum. Inc., Lum. Dec.), probing region (V1, V2, V3) and ROI size (Large, Medium, Small). Post-hoc paired t-test was performed to estimate relationship between each other. We found a significant main effect of Condition in the Early ($F(1, 102) = 6.31$, $p = 0.014$, Eta2 (partial) = 0.06), Late ($F(1, 102) = 38.40$, $p < .001$, Eta2 (partial) = 0.27) and End ($F(1, 102) = 8.25$, $p = 0.005$, Eta2 (partial) = 0.07) responses. No significant interactions were observed. BOLD signal change to luminance decrement was smaller than it to luminance increment in Early ($t(62) = -2.16$, $p = 0.035$), Late ($t(62) = -4.91$, $p = 6.87e\text{-}6$) and End ($t(62) = -2.42$, $p = 0.018$) responses (Figure S3.6). However, changing the size of the probing region did not induce significant BOLD response changes in Early, Late and End responses. This result was consistent with that from the left hemisphere-only data.

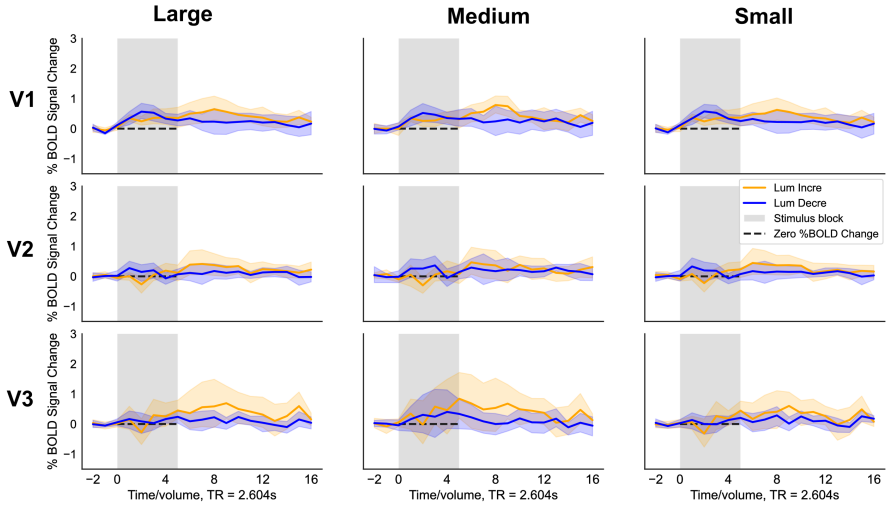

Figure S3.5: Overview of event related averages in probing region ROI with different ROI size across 13 hemispheres. Solid lines: mean, shading: standard error. The height of all probing region ROIs are 2°. Large ROI: 8° x 2°. Medium ROI: 6° x 2°. Small ROI: 4° x 2°.

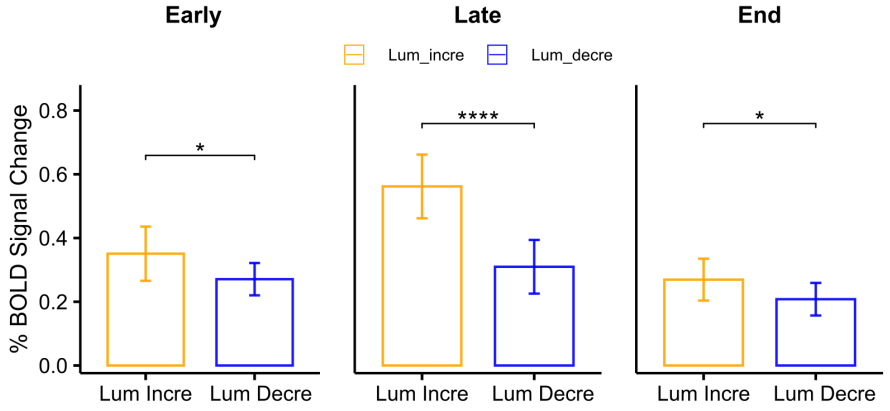

Figure S3.6: Early, Late and End BOLD responses in all sizes of Probing region for the two luminance conditions from 13 hemispheres. Error bars represent 95% confidence intervals. *: $p < 0.05$; ****: $p < 0.0001$.

Statistical testing of luminance decrement only dataset

A two-way repeated measures ANOVA, performed on the Early, Late and End response using the luminance decrement dataset, with within-subject factors including Visual Area (V1, V2, V3) and Stimulus ROI (Inducer, probing region, edge). Post-hoc paired t-tests (Benjamini-Hochberg correction) were performed to estimate relationships with each other.

In the Early response (Figure S3.7 A), we found a significant main effect of Stimulus ROI ($F(2, 40) = 24.79$, $p < .001$; Eta2 (partial) $= 0.55$) and interaction between Visual Area and Stimulus ROI ($F(4, 40) = 6.79$, $p < .001$; Eta2 (partial) $= 0.40$). Post-hoc paired t-tests showed an antiphase relationship in V1 and V2, whereby BOLD signal change in the probing region was positive while that in the inducers were negative (V1: $t(5) = -8.45$, $p = 0.00020$; V2: $t(5) = -6.1$, $p = 0.00053$). The strongest positive BOLD signals change were observed in the edge in both V1 (inducer < edge: $t(5) = -8.00$, $p = 0.00020$; probing region < edge: $t(5) = -3.92$, $p = 0.0178$) and V2 (inducer < edge: $t(5) = -4.40$, $p = 0.014$; probing region < edge: $t(5) = -2.90$, $p = 0.045$). In both the Late and End response, we only found a significant main effect of Stimulus ROI (Late: $F(2, 40) = 3.29$, $p = 0.047$, Eta2 (partial) $= 0.14$); End: $F(2, 40) = 4.47$, $p = 0.018$, Eta2 (partial) $= 0.18$) and no significant interaction. Post-hoc paired t-test showed that BOLD signal change in the Late response was not significantly higher in any of the Stimulus ROI. However, we observed higher BOLD signal change in the inducer ($t(17) = 3.23$, $p = 0.015$) and probing region ($t(17) = 2.61$, $p = 0.027$) than in the edge in the End (Figure S3.7 B).

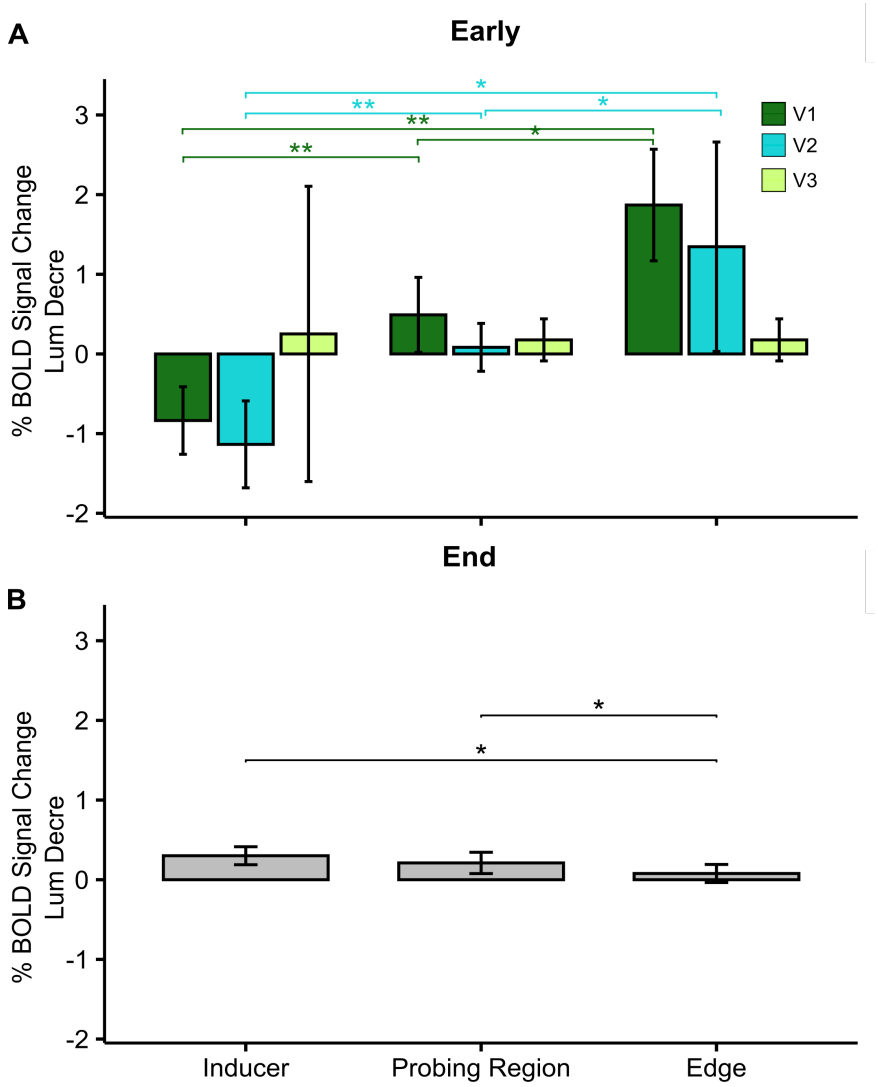

Figure S3.7: Significant ANOVA results for luminance decrement condition in all retinotopic regions on the 13 hemispheres (N=7). **A**: Significant interaction between Stimulus ROI (Inducer, probing region, Edge) and Visual Area (V1, V2, V3) in the Early response. **B**: Significant main effect of Stimulus ROI in the End response. Error bars represent 95% confidence intervals. *: $p < 0.05$; **: $p < 0.01$.

4

Developing a novel stimulus for brightness illusion using online psychophysics

Based on
Wang, Y., Maiocchi C., Kazan C., De Weerd, P., Roberts, M.J.(in preparation). Developing a novel stimulus for brightness illusion using online psychophysics.

4.1 Abstract

The current study reports on a parametric study of a strong lightness illusion first reported by Anderson and Winawer (2005). The aim of our study was to develop the illusion for use in future neuroimaging investigations of the cortical processing of the surface perception. Anderson and Winawer (2005)'s experimental stimulus elicits an illusion in which identical figures (disks of texture) appear either lighter or darker depending on the background. This illusion is destroyed in a control stimulus, in which the surround is rotated relative to the disk. This rotation breaks the geometric and layered representation of the stimulus, which is suggested to mediate the illusion. Importantly, the overall luminance of the entire stimulus is constant between the experimental and control stimuli. This makes Anderson and Winawer (2005) stimulus interesting for neuroimaging experiments on surface perception. In pilot experiments, we tested how the illusion depends on the texture contrast gain (indicating the level of contrast between dark and light patches in the textures) and the spatial frequency content of the stimuli. We found stronger illusion effects with higher gain and medium spatial frequency. In addition, spatial frequency strongly affected the extent to which background rotation influenced the strength of the lightness illusion. Rotation had the strongest effect at low spatial frequency. Next, in online experiments, we investigated the dependency on "pedestal width" by modulating the distance between the border of the target and a limited region of the background. This novel approach showed an effective perceptual effect was induced by only manipulating luminance close to the target border, rather than in the entire background, thereby reducing the overall luminance difference between conditions where the target is perceived as light or dark. Despite these interesting parametric effects, the measured effect of the illusion was very small, in contrast to original observations by Anderson and Winawer (2005). In an additional online experiment we tested whether larger effects could be measured using either a staircase method or an adjustment method, in contrast to the method of constant stimuli we used in the first experiments. For both methods, effect sizes remained small. Taken together,

we conclude that while the stimulus is promising, future testing in the psychophysics lab will be needed before bringing the stimulus to neuroimaging experiments.

4.2 Introduction

Surface perception provides the scaffold for all visual experience. The physical appearance of a surface is determined by the reflectance of the surface, the amount of light falling onto the surface and the transparency of the medium between the surface and the viewer (Anderson and Winawer 2005; Kingdom 2011; Salmela and Vanni 2013). Correspondingly, the perceived features of the surface are lightness (perceived reflectance) and brightness (perceived luminance) (Gilchrist 2007; Salmela and Vanni 2013). With simple visual stimuli, such as a grey square surrounded by another shade of grey, both brightness and lightness indicate the same perception (Salmela and Vanni 2013). If the stimulus consists of information of transparency and depth, brightness and lightness may become disengaged because extra information is accessible to separate between luminance changes due to material or illumination (Adelson 1993; Anderson 1999). In the natural environment, our visual system is able to dissociate variations due to illumination (a change in environment) from changes in reflectance (a change in object), an effect known as brightness constancy, however the neuronal mechanisms of this process is not yet fully understood.

Early visual cortex is known to respond strongly to edge contrast but is thought to respond poorly to the uniform surfaces (De Valois and De Valois 1988; Hubel and Wiesel 1968; Tucker and Fitzpatrick 2006). These contrast-related mechanisms appear insufficient to encode homogeneous stimulus surfaces. To date, although the underlying neural mechanism of surface perception has been studied for decades using lightness and brightness paradigms and a range of stimuli (Anderson and Winawer 2005; Cornelissen et al. 2006; Cox and Maier 2015; Friedman et al. 2003; Grossberg and Hong 2006; Roe et al. 2005; Rossi

et al. 1996; Ruff et al. 2018; Vinke and Ling 2020; Yang et al. 2022), the role of early visual cortex on the processing of surface perception is still under debate.

In Chapter 3, we investigated the neural mechanisms of surface perception with the brightness induction paradigm in which luminance changes of a surrounding region (the inducer) in one direction, induced the opposite perceived brightness changes in the enclosed centre region of constant luminance (the probing region). Even though participants verbally reported seeing the brightness illusion for both conditions, the luminance increment condition failed to induce a cortical response in early cortical areas corresponding to the inducer and probing area, while the luminance decrement condition induced only a weak response in the area corresponding to the probing region. In addition to the weakness of the responses, another major challenge in measuring brightness responses with fMRI is dissociating responses caused by perceptual change in brightness from responses caused by changes in the (mean) luminance and local contrast of the stimulus (Salmela and Vanni 2013). Stenbacka and Vanni (2007) reported that blood oxygen level-dependent (BOLD) response to luminance in early visual areas may be partially confounded by the scattering of light in the eye. The modulation of probe brightness in Chapter 3 was induced by changing the surrounding region, which necessarily produces different mean luminance during the different stimulation blocks and the fixation block. To address these two issues, the current study aimed to set up and optimise an experimental stimulus that not only can induce a stronger illusion than the simultaneous contrast illusion, but can also manipulate perceived brightness/lightness without altering the mean physical luminance of the display. With such an optimised experimental stimulus, future studies will be able to further explore the underlying neural mechanisms of surface perception using neuroimaging techniques such as EEG and fMRI.

Illusions have been used in many studies to investigate the neural mechanisms of surface perception, and several theories of surface perception have been proposed. The illusions that have been used, and

the theories that have been proposed, may offer insights into the development of potential new experimental stimuli. Theories of brightness perception may be organised according to the levels of the visual system where the critical processing is proposed. To explain brightness perception and related illusions, low-level theories focus on lateral inhibition, in which the response of a neuron is inhibited by neighbouring neurons. Lateral inhibition has been observed in the retina, the LGN and the cortex (Hartline et al. 1956; Isaacson and Scanziani 2011; Soranzo and Gilchrist 2019), and renders neurons more sensitive to spatially varying stimuli than spatially uniform stimuli. This mechanism was used to explain the simultaneous contrast illusion (Figure 4.1 A), in which the same square appears lighter on dark surrounds than light surrounds. However, for White' s illusion (Figure 4.1 B) and the Craik-O'Brien-Cornsweet effect (Figure 4.1 C), despite the two illusions containing various edge and contrast cues, brightness computation based on lateral inhibition would predict percepts opposite to what is observed. Thus, low level theories based on lateral inhibition, do not account well for brightness perception.

Mid-level theories assume that lightness and brightness perception is achieved as part of a holistic processing of the entire scene, including multiple possible cues. Accordingly, it has been demonstrated that the lightness of a target surface is influenced by changing the perceived depth with no change in the retinal image (Adelson 1993; Gilchrist 1977; Gilchrist 1980), or by changing a reflectance boundary (Gilchrist and Jacobsen 1983). One leading mid-level theory is the layer theory, which proposes that the retinal image is cognitively separated into two complementary overlapping layers, one made from the integration of all the reflectance edges and representing the underlying surface reflectances, and another with all the illumination edges and representing variation in incident light and overlapping transparency (Gilchrist 2007; Gilchrist 2015; Kingdom 2011). As a test of the layer theory, Anderson and Winawer (2005) designed a novel stimulus that effectively added a more explicit transparent layer to the standard simultaneous contrast stimulus (Figure 4.2 A). Thus, rather than a homologous grey stimuli

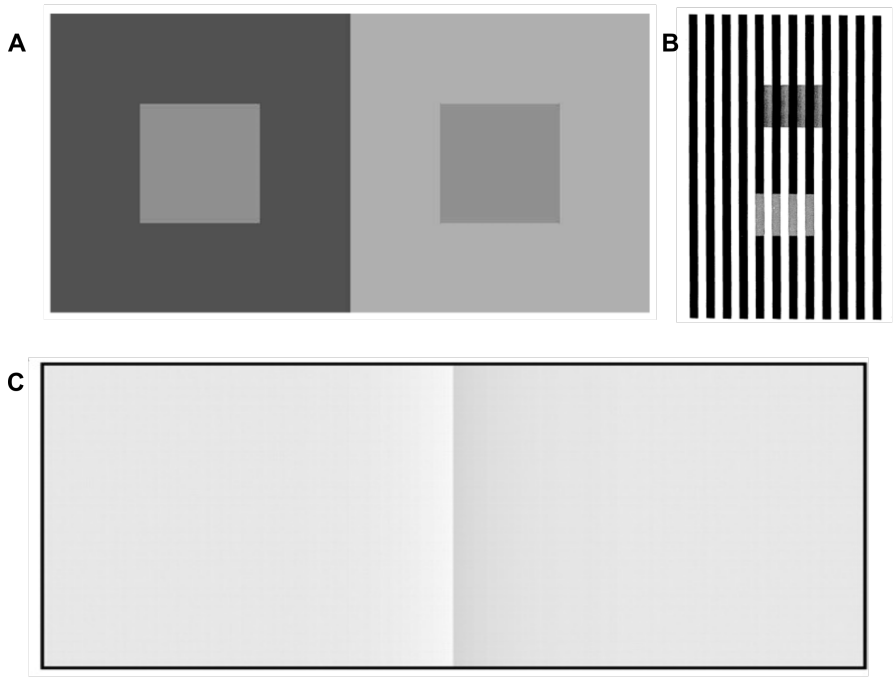

Figure 4.1: Classic lightness illusions used in previous studies. **A**: Simultaneous contrast effect. Grey surfaces on both sides were physically identical. Grey surface on the darker surrounding surface appeared brighter, while the surface on the brighter surrounding surface appeared darker. **B**: White effect. Both of the grey targets had the same colour and opacity. Grey targets on the white bars appear darker, while the targets on the black bars appear brighter. **C**: Cornsweet or Craik–O'Brien–Cornsweet illusion (Roe et al. 2005). The luminance of the two rectangles was the same, except for a narrow region at their common border, which had higher luminance in the left and lower luminance in the right.

(in which the inducer region is increased or decreased in luminance) they used a low-pass filtered random texture, with pixels spanning the range from white to black. Increasing or decreasing the mean luminance of the inducer region in these images had a dramatic effect on the perceived brightness of the probe region, especially when the contrast of the texture in the probe region was increased. For the dark inducer, the probe region appeared as a white surface seen through a veil of partially transparent dark clouds. For the light inducer, the identical probe region appeared black, seen through light clouds. In both cases the perceived brightness of the probe approximated either the darkest pixel in the probe region when the inducer was light, or the brightest pixel when the inducer was dark. This perception is in line with a layer interpretation, as in both cases, the most extreme pixel in the probe appears to represent an unobscured view of a distant homogeneous surface, while the remaining pixels appear to be a combination of the surface and a light or dark semi-transparent layer. According to the layer theory, the transparent texture layer is discounted when interpreting the brightness of the surface, hence it is perceived as either white or black depending on the perception of the transparent texture. Whether the transparent texture is perceived as bright or dark, thus whether light or dark pixels are discounted from the probe region, depends on its luminance in the inducer region. However, this segmentation of the probe surface from the overlaying texture is only possible when the texture in the probe region is contiguous with the texture over the inducer region. Following this logic, Anderson and Winawer (2005) showed that the illusion was effectively abolished by rotating the texture in the inducer, which removed both the geometric conditions and the luminance relationships needed to induce the perception of transparency. In follow-up studies they (Anderson and Winawer 2008) showed that the illusion could also be reduced by segregating the texture in the probe region from the texture in the inducer using a narrow grey ring around the probe, which also abolished the perception of transparency without rotating the entire background.

The stimulus advanced by Anderson and Winawer (2005) has been

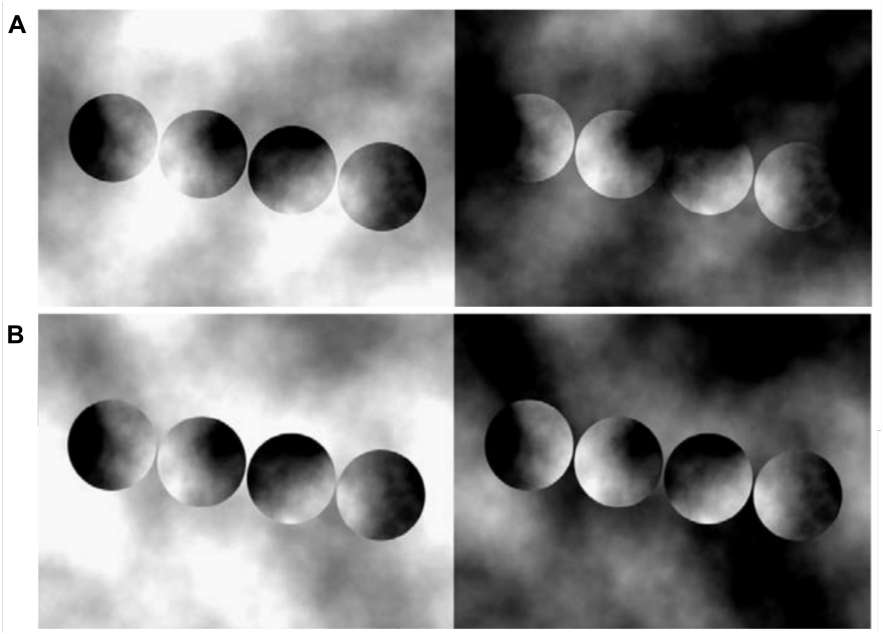

Figure 4.2: Anderson and Winawer illusion (Anderson and Winawer 2005). **A**: The textured disks on the dark and light surrounds were identical. The disk and the surround were spatially identical to the seed image but differed in the range of luminance values. The disk on the dark surround appeared brighter, whereas the disk on the light surround appeared darker. **B**: the same objects as in the upper row, except that the surround was rotated by 90°. This rotation destroys both the geometric and luminance conditions needed to evoke a perception of transparency, and also destroys the lightness illusion.

used in a number of psychophysical studies, some of which have called into question the precise interpretation of the underlying mechanism (Albert 2007; Anderson and Winawer 2008; Poiriehr 2009). Nevertheless, there appears to be a consensus that the A&W illusion is consistent and powerful, and hence can be used to uncover fundamental general mechanisms of surface perception. For our purpose, seeking an appropriate stimulus for future neuroimaging studies, the stimulus is interesting because of the very large illusion effect and the possibility of abolishing the illusion with minimal changes to the stimulus. However, the stimulus is not yet ideal because, although the control stimuli for A&W illusion can be generated by rotation, which keeps the mean luminance for the illusory stimuli and control stimuli the same for each background setting, it still shares in common with the simultaneous contrast illusion the large change in background luminance between dark and light settings. In a neuroimaging study, a different mean luminance could induce BOLD response to luminance in early visual areas because of light scattering, which may make it difficult to dissociate cortical response to probe brightness. One solution to this problem could be to reduce the area over which luminance in the inducer is modulated. A common theme of both low-level and mid-level theories of lightness perception is that contrast at the surface edge, not across large distances, is critical for the perception of the surface. This idea is well demonstrated in the Crack-O'brien-Cornsweet illusion, where the brightness of an entire surface is influenced by local changes in luminance on either side of the surface edge. Given this, we set out to test whether we could replicate the powerful illusion documented in Anderson and Winawer (2005), but with minimal changes to background luminance.

In the current study, we aimed to set up an experimental stimulus that can induce a strong brightness illusion and, as a novel addition to the original A&W stimulus, manipulate the perception of the probe without altering the mean luminance of the overall stimulus. Since we are interested in the shift of perception due to the change of luminance in the surrounding areas, we will use the term 'brightness' even though some researchers may argue that 'lightness' is more correct. In our

experiments, we tested the effects of the stimulus contrast (luminance range from dark elements to lighter elements in the stimulus texture), the spatial frequency content of the texture and the distance from the probe border where the background luminance was modulated. While the stimulus contrast has been investigated in previous studies, to our knowledge, no study has systematically explored the effects of the texture spatial frequency or of pedestal width. In addition to designing an effective stimulus, defining the properties of the stimulus could give insights into the mechanism. For example, if the full illusion can be replicated by only manipulating luminance at the target boundaries (i.e. a narrow pedestal), it will emphasise the role of low-level visual areas (those characterised by small receptive fields) on the processing of the illusion since the lightness perception would mainly determined by the luminance properties at the edge. The more the illusion relies on information far from the boundaries, the more global the underlying mechanism must be, implying processing at higher levels of the visual hierarchy.

4.3 Method

4.3.1 Participants

The study was approved by the Ethics Review Committee for Psychology and Neuroscience (ERCPN) (176_02_07_2006_V2_A1) at Maastricht University and all procedures followed the principles expressed in the Declaration of Helsinki. Only participants with normal or corrected normal vision were included. In all experiments, participants were provided with informed consent and debriefing information at the end of the measurements. Participants were informed that they could terminate their participant at any time for any reason. Age, sex and other personal information were not collected or considered for the analysis.

4.3.2 Experiment Design

In the current study we aimed to optimise A&W stimuli and develop a reliable behavioural paradigm for induced brightness perception. Given Coronavirus restrictions, all measurements were performed either by a small number of participants running the measurement on their own computer, or using online psychophysics in Inquisit 6 (https://www.millisecond.com). Our experiments used all three classical psychophysical methods, the method of adjustment, the method of limits (staircases) and the method of constant stimuli. The experimental set-up for each experiment was summarised in Table 1.

Standard stimulus design: Our standard stimuli were concentric circles. The outer ring we refer to as 'background' the inner circle as 'probe' or as 'test' (Figure 4.3). The probe region was used to probe the participants' perception of brightness, therefore the mean luminance value of the probe region was always constant with a mean luminance value of 0, on a scale of -1 to 1 (as in Chapter 3). The background around the probe functioned as an inducer, therefore the luminance of the probes' s background was altered by adding or subtracting a luminance either to the entire background region (Figure 4.3 A) or in a narrow 'pedestal' region close to the border of the probe (Figure 4.3 B). The function of the test region (Figure 4.3 C) was to test the luminance point of subjective equality (PSE) of the probe, therefore the mean luminance of the test region varied, trial-to-trial and participants compared it to the probe. The mean luminance of the test background was constant, with a mean luminance of 0 (mid level grey).

Adjustment to COVID-19 Measures: All experiments were adapted to the COVID-19 measures and were performed online outside standard conditions of the laboratories. All participants performed the experiments with their personal computers in domestic conditions. The exact calibration of the luminance values of the display and the standard visual distance could not be monitored. Stimulus dimensions were reported in centimetres and not in visual degrees. Stimulus size was

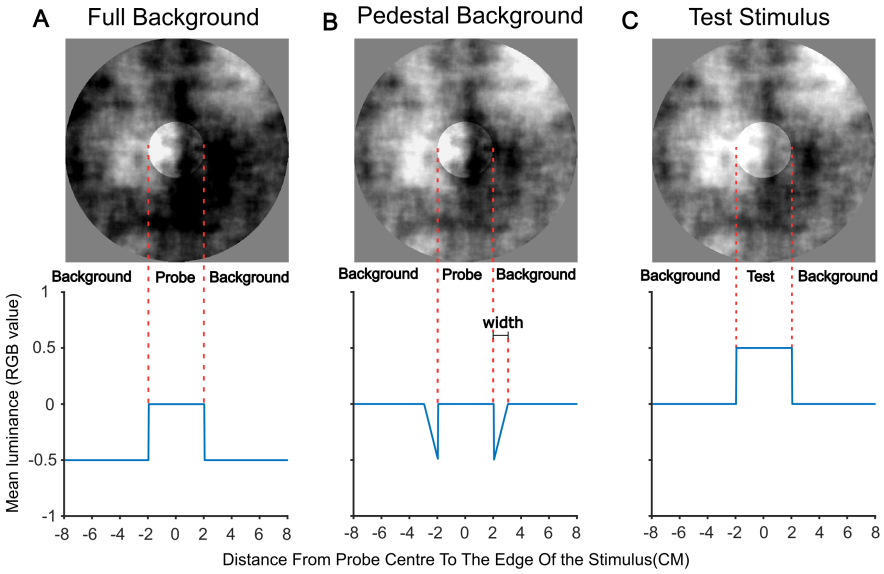

Figure 4.3: Stimuli design. **A**: Full background experimental stimulus, similar to stimuli used in Anderson and Winawer (2005). **Upper plot**: example stimulus. **Lower plot**: mean RGB value across the horizontal axis of the stimuli. In this example the luminance of the background has been lowered by 0.5 RGB, making the probe region appear bright. **B**: Novel pedestal background stimulus. Mean luminance of the background within the width of the pedestal has been lowered. The amount that luminance is lowered reduces linearly with distance from the border of the probe. **C**: Test stimulus. Here, the luminance of the test region is raised to approximately match the perceived brightness of the probe in **A** and **B**. The mean luminance of the background is not changed from the standard 0, the standard grey level.

calibrated to different screen sizes using a size calibration task: Before starting the experiments, participants were asked to match a blue box on the left bottom of their displays with a credit card / bank card, using the up/down and left/right arrows on the keyboard. Once the matching was completed, participants were directed to another verification, showing a blue rectangle measuring 5 x 10 cm to test that the scaling factor was appropriate. Experimental stimuli were scaled according to this calibration task and measured 2 cm and 8 cm, unless otherwise stated, which correspond to the inner and the outer disks respectively. We did not measure screen-viewing distance, therefore all measurements are kept in terms of cm. Assuming a typical viewing distance of about 50 cm, 1 cm of stimulus equates to slightly larger than 1 degree of visual angle. Since we also were not able to measure screen brightness, we report luminance in terms of the RGB value with -1 indicating the minimum and 1 indicating the maximum screen brightness.

Table 4.1: Summary of all experiments.

Location	Experiment	Number of Participants	Method	Condition				
				Target Texture gain	Texture spatial frequency Filter	Rotation	Target Background lum. offset	Pedestal radius (cm)
Home PC	Texture Gain	3	MOA	0.5, 1, 2, 3	2	0°; 90°	±0.2 ±0.4	Full
(Pilot)	Spatial Frequency	3		2	1, 1.5, 2, 2.5, 3, 3.5		±0.4	
Online inquisit	Pedestal width	37(23a)	MOC	2	2		±0.5,	Full, 1cm, 2cm
		16(15a)		1			±0.38	
		48(43a)	MOS	1	2		±0.5	Full, 2cm
			MOA					

Method of adjustment (MOA): MOA has been widely used to investigate the A&W illusion (Anderson and Winawer 2005; Anderson and Winawer 2008; Poiriehr 2009). In the current Chapter, we applied the method of adjustment in the pilot study (Section 4.3.2.1) and later

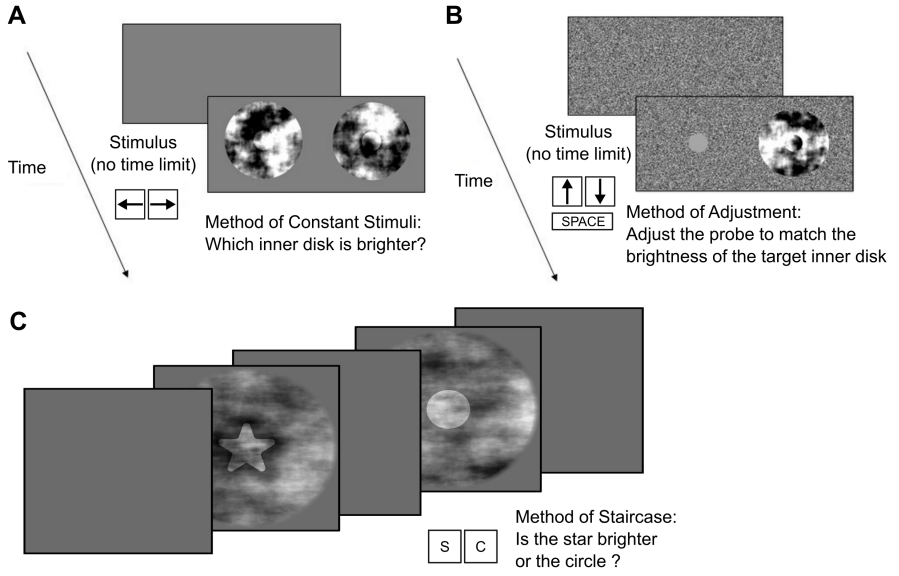

Figure 4.4: An example trial for method of constant stimuli (**A**), method of adjustment (**B**) in the pilot study, and method of staircase (**C**).

online experiment (Section 4.3.2.3). In pilot studies, the adjustment was implemented by increasing or decreasing the luminance of an untextured test stimulus that had the same shape and size as the probe (Figure 4.4 B). On each trial, the test started at one of three levels of luminance (-0.3 0 or 0.3). Each condition was repeated 10 times for both light and dark backgrounds, leading to a total of 60 trials per condition (combining 3 starting levels and 2 background levels). In our final online study we also used a method of adjustment design, but the test stimulus was textured and presented separately (in time) from the probe (Figure 4.13 B). The test alway had an initial mean luminance of 0.5 and each condition was presented only 6 times (for both light and dark backgrounds). In both experiments, the PSE on each trial was taken as the final luminance level that the participant set for the test patch before accepting the match.

Method of constant stimuli (MOC): An alternative method that is more reliable than the MOA, is the method of constant stimuli. This method also has the advantage of showing the full psychometric function, in which the slope of the function can indicate the reliability of the measurement. Such a measure of reliability is particularly relevant for online measurements. In the MOC experiment, the probe and test stimuli were presented on the left and right of the screen. Participants were asked to indicate which of the inner circles was perceived as brighter compared to the other one, by pressing the left or the right arrow key (Figure 4.4 A). Notably, the location of the probe and the test were randomised on each trial, making it difficult for participants to know which of the stimuli was the experimental stimulus. The perceived brightness of the probe was estimated by calculating the proportion of trials in which the participant chose the test as the brighter stimulus for each level and fitting a psychometric function to the data (Figure 4.5). To estimate the strength of the illusion, data from light and dark backgrounds were combined (after flipping data from the light background in both X and Y axes), separately for non-rotated and rotated conditions (Figure 4.5 C). The perceived brightness was then calculated as the point of subjective equality (PSE), taken as the point at which the fitted function crossed 50%. At this point, the participant was equally likely to perceive the probe or test as brighter.

Method of staircases (MOS): Although the method of adjustment is easy to perform, it produces unreliable results within participants and inconsistent results among them, because this method is sensitive to (changes in) criteria that participants use to match the target. This may be especially problematic when investigating the A&W illusion as the targets are not homogeneous. Furthermore, participants are aware of which stimulus is the experimental stimulus and which is the probe, which makes the measurement more vulnerable to participant' s bias, especially, for a study with small sample size and in which participants are authors. For example, in Anderson and Winawer (2005)' s study, two out of three participants were authors and in Boyaci et al. (2007)' s study, three out of five participants were authors. Some of

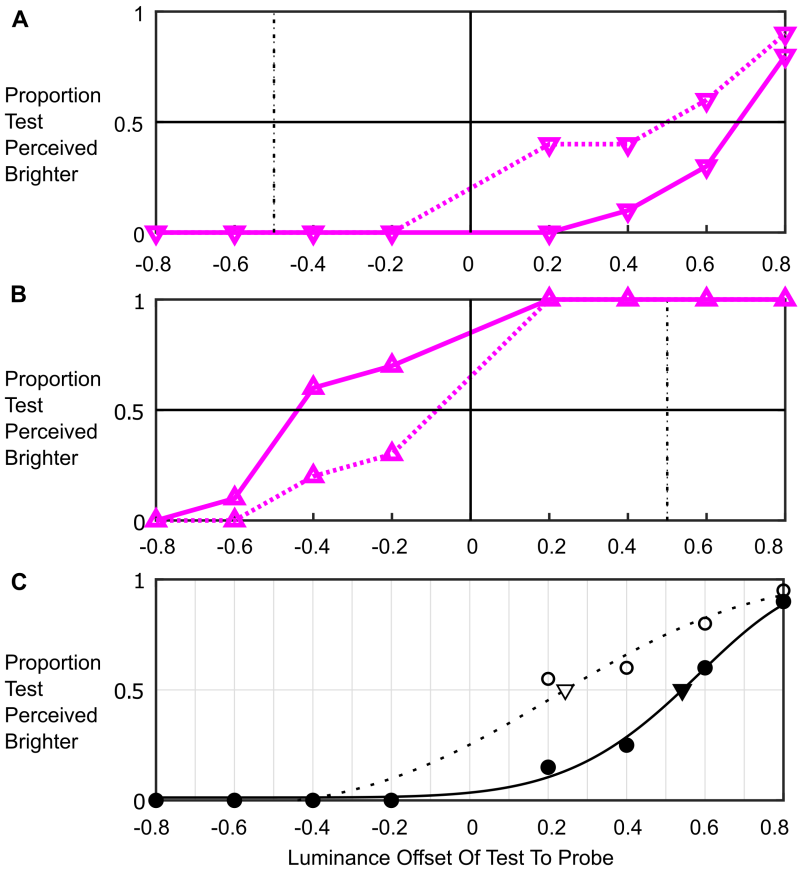

Figure 4.5: Psychometric fitting in the method of constant stimuli from a representative participant. The proportion of trials that the participant perceived the test stimulus as brighter than the probe is plotted as a function of the luminance offset of test to probe **A** for the dark probe backgrounds and **B** for light probe backgrounds. Black dashed vertical line indicates probe background luminance. Solid line indicates probe luminance If there is no illusory effect, the proportion should be 1 for all positive test luminance and be 0 for all negative test luminance. Data from both dark and light backgrounds are combined to fit the psychometric function (shown in **C**) and estimate the size of A&W illusion separately for non-rotated and rotated conditions. Non-rotated data was shown in the solid line, and rotated data was shown in the dotted line. Circles in **C** represent the data points and triangles in **C** represent the PSE value.

these limitations are addressed in the method of constant stimuli, however this method is also problematic since it is rather time consuming and repetitive. In an online experiment, participants may withdraw attention from the task over the course of the session. A faster method is the staircase method. During a staircase experiment, each staircase starts with a large, and easy to judge difference between test and probe. As the staircase progresses, the perceived difference between test and probe is reduced. Thus, if the participant responds that the test is perceived as darker than the probe on one trial, a brighter test is presented on the next trial. This is repeated until the participant's response reverses, indicating that the test was now perceived as brighter than the probe. Such a one-up-one-down staircase (Figure 4.6) will stabilise at the point where probe and test are equally likely (50% of trials) to be perceived as brighter. The point of subjective equality can be calculated by averaging the values of the last 15 (out of 20) reversal points. The staircase method is faster, and can be more accurate, than the method of constant stimuli since most trials are spent close to the PSE, and most trials far from the PSE are eliminated. In addition, by starting at an easily perceived level, the staircase method resolves the issue of participants using inconsistent criterias to compare brightness and also increases the engagement of participants to the experiment. Both the MOS and MOA have advantages, however are somewhat complex to write in INQUISIT. In the third online study we compared MOS and MOA. We recruited naive participants for this experiment to avoid the bias which may be present for experienced participants.

Pilot study: method of adjustment

The goal of these experiments was to maximise the A&W illusion by manipulating the texture gain and spatial frequency in texture patches. A small number of participants (N=3) performed this experiment with MOA. An inner disk surrounded by a bigger circle was presented on the right of the screen. The participant adjusted the luminance of a grey homogeneous patch on the left to match the perceived brightness of the probe on the right (Figure 4.4 A). The two disks had the same shape

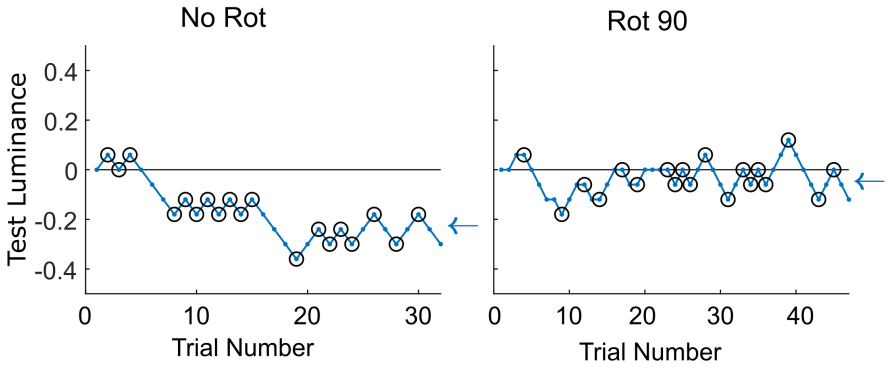

Figure 4.6: Example data in the 1-up 1-down staircase from a representative participant. **Left panel**: perceived luminance for non-rotated test on a full light background is plotted along the number of trials. Each circle represents a reversal point. PSE is estimated by averaging the luminance of the test in the last 15 reversal points. PSE for the staircase is represented by the arrow. **Right panel**: PSE for rotated probe on a full light background plotted along the number of trials. The rest information is the same as the **Left panel**.

and size. The luminance of the background was a gaussian texture of mean luminance of 0, that did not change across the trials.

Texture Contrast Gain

The texture contrast gain indicates the variation between light and dark patches in the textures. The value indicates the term by which the texture pattern is multiplied by. At a gain of 1 pixels are uniformly distributed between 0 and 1. At higher gain, a higher proportion of the image is set to either 0 or 1, as 0 to 1 is the maximum range of the image. For this pilot experiment, we set four levels of texture gain (0.5, 1, 2, 3), with four background luminance offsets (-0.4, -0.2, 0.2, 0.4), indicating the amount that is added to background pixels, and two rotation conditions (0°, 90°) indicating whether the background were rotated or not. The spatial frequency filter width used to create the texture patterns was set as 2.5 and there were 60 trials per condition.

Three participants were tested for the experiment, who were familiar with the design and the purpose of the experiment. Since the measurements were conducted in lockdown, stimulus size and luminance were not controlled.

Results

Figure 4.7 A shows the group (n=3) mean perceived brightness (PSE) at each texture gain in four conditions, with results pooled over positive and negative background luminances. Figures below show example images at each stimulus setting, each using the same random seed. The illusion was consistently weaker in the rotated conditions (Red), and appeared stronger for higher gain values. This pattern was confirmed in a three-way repeated measures ANOVA, with within-factors including Gain (0.5, 1, 2, 3), Rotation (Non-rotated, Rotated) and Background offset (0.2, 0.4), which indicated a significant effect of texture gain ($F(1, 39) = 6.47$, $p = 0.015$, Eta2 (partial) = 0.14) and a trend to a significant effect of rotation ($F(1, 39) = 3.05$, $p = 0.088$, Eta2 (partial) = 0.07). The background offset had no effect ($F(1, 39) = 0.72$, $p = 0.401$, Eta2 (partial) = 0.02). No significant interactions were observed. Post-hoc paired-samples t-tests (Benjamini-Hochberg correction) showed (Figure 4.7 B) significantly lower PSEs for non-rotated stimuli with a texture contrast gain at 0.5 (Mean: 0.24; $t(5) = -3.85$, $p = 0.048$) and 1 (Mean: 0.23; $t(5) = -4.14$, $p = 0.048$) than it at 3 (Mean: 0.28). It also showed a significantly lower PSE for non-rotated stimuli with a texture contrast gain at 1 (Mean: 0.23) than at 2 (Mean: 0.28; $t(5) = -4.24$, $p = 0.048$). These results must be regarded with caution given the small sample size, nevertheless it seems that texture contrast gain has an important impact on the size of the effect. We choose to use a texture gain of 2 for the next experiments, since this gave both a large effect and a relatively large rotation effect.

Spatial Frequency

The texture stimuli are created by low-pass filtering spatial white noise. The filter width determines the balance between local (high

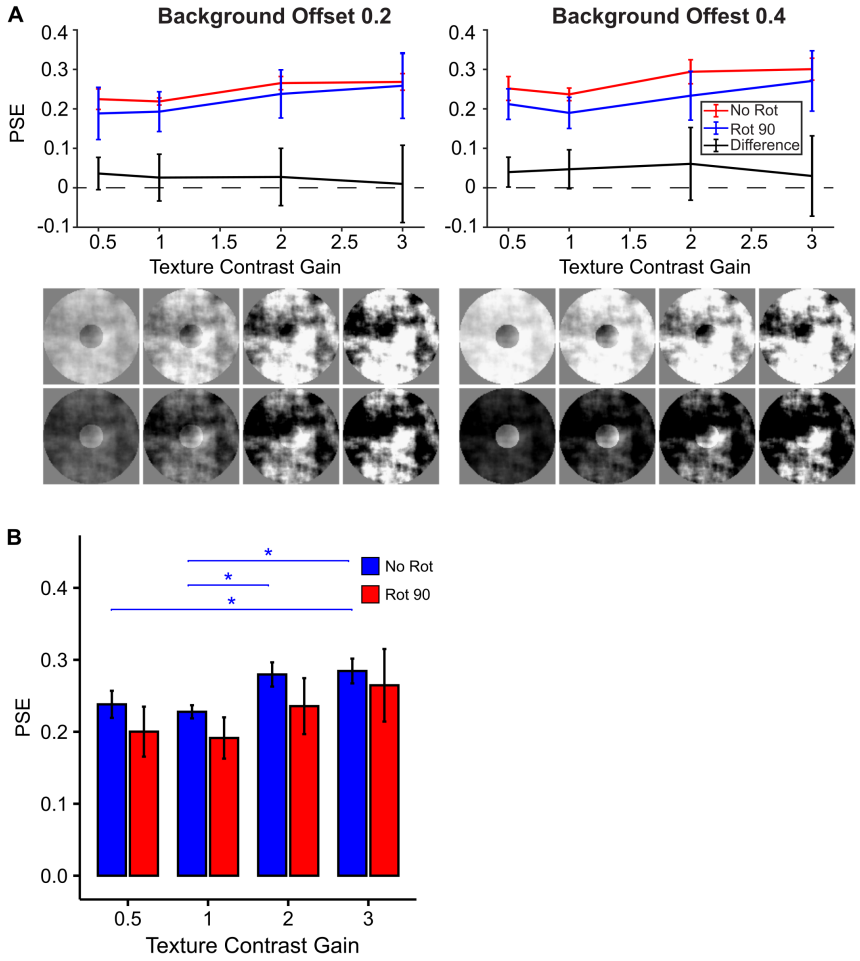

Figure 4.7: Psychophysic results for texture contrast gain experiments. **A** Left panel: Group averaged A&W illusion effect for 0.2 background luminance offset across texture contrast gains for rotated (blue) and non-rotated (red) stimuli. The effect of rotation (computed as the illusion magnitude for non-rotated stimuli minus illusion magnitude for rotated stimuli) is shown in black. Error bars show standard error (N=3). Examples of corresponding stimuli are shown below for dark (upper row) and light (lower) stimuli. Right panel: Same as **A** for 0.4 background offset. **B** Significant three–way repeated measures ANOVA results. The illusory effect (PSE) was averaged from all background offset. Error bars represent standard error. Blue * represents the significance within non-rotated stimuli. *: $p < 0.05$.

spatial frequency content) and global (low spatial frequency content) structure present in the final image. In the next pilot measurements we manipulated the filter width used to create the textures. The exponent of the filter width was set to 1, 1.5, 2, 2.5, 3 and 3.5, with higher values indicated into a stronger suppression of high spatial frequencies and an enhancement of low spatial frequencies (Figure 4.8 A). Thus, low filter width textures appear similar to white noise, while high filter width textures have a smoother appearance (Figure 4.8 C). In this pilot experiment we tested the effect of changing the filter width on the magnitude of the illusion. Considering the previous experiment, the texture gain was set at 2 and the background luminance offset was set to $\pm$ 0.4. The design of the experiment was the same as the texture gain experiment and the same three participants were tested.

Results

Figure 4.9 shows the group-averaged A&W illusion effects across 6 spatial frequency filter widths. For both rotated (blue) and non-rotated (red) conditions, the illusion became smaller with increasing spatial frequency filter width; however non-rotated conditions were somewhat less affected. The rotation effect (black) first increased with filter width from 1 to 2 cycles per 32 pixels (equivelant to 1cm), then reached a plateau at 3 cycles per 32 pixels, and decreased at 3.5 cycles per 32 pixels. A two-way repeated measure ANOVA was performed to evaluate the rotation effects and the impact of different levels of spatial frequency filter width on the illusion, with within-factors including Rotation (Non-rotated, Rotated), Spatial Frequency Width (1, 1.5, 2, 2.5, 3 and 3.5). We observed significant main effects of Rotation $F(1, 31) = 10.48$, $p = 0.003$, Eta2 (partial) = 0.25 and Spatial frequency filter width ($F(1, 31) = 34.52$, $p < .001$, Eta2 (partial) = 0.53). The interaction between the Rotation and Spatial frequency filter width was close to significant ($F(1, 31) = 3.60$, $p = 0.067$, Eta2 (partial) = 0.10). Post-hoc paired-samples t-tests (Benjamini-Hochberg correction) showed a significantly higher PSE ($t(19) = 2.60$, $p = 0.0187$) for non-rotated stimuli (Mean: 0.24) than rotated stimuli (Mean: 0.19). It also showed several significant

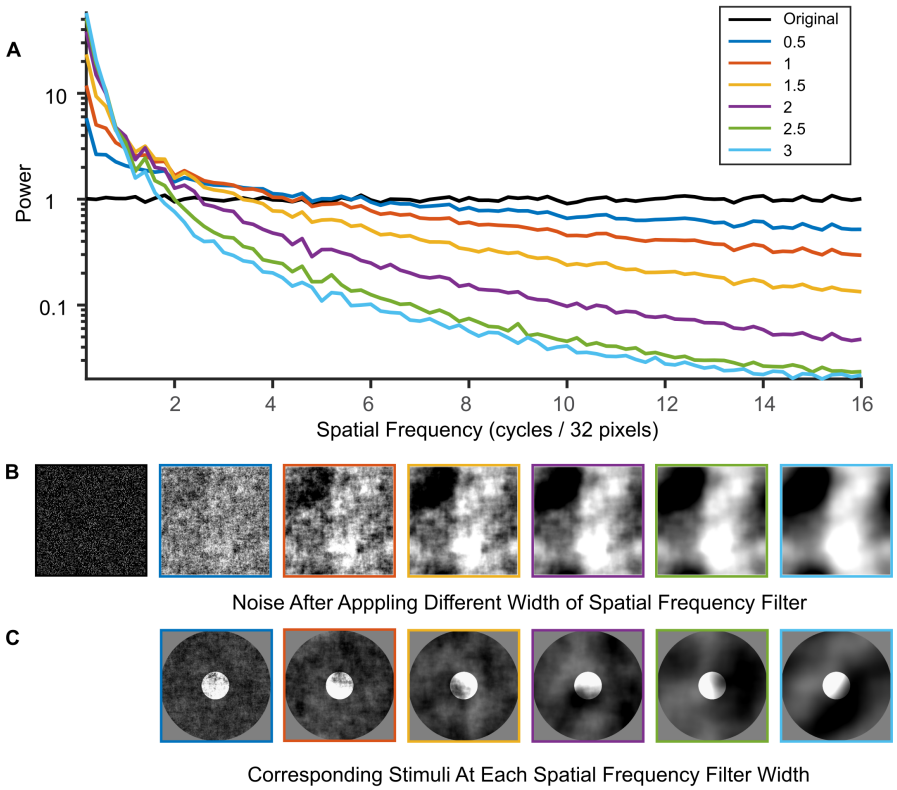

Figure 4.8: Spatial frequency modulation. **A**: Demonstration of spatial frequency signals under different filter widths. Back line represents spatial white noise where high and low spatial frequency signals are evenly distributed. Non-black lines show the output of different spatial filter widths, where the higher the filter width, the more suppression for the high spatial frequency signals. **B**: The noise image is shown in grey scale images after applying the spatial frequency filter. The coloured frames correspond to the same information as in **A**). **C**: Example stimuli generated from different spatial frequency filter widths. The coloured frames correspond to the same information as in **A**). In the experimental stimuli, 32 pixels corresponded to 1cm on the screen.

differences in the illusory effect among different spatial frequency filter

widths (Figure 4.9 B Right). The illusion was stronger for filter widths 1 (Mean: 0.30), 1.5 (Mean: 0.26) and 2 (Mean: 0.22) cycles per 32 pixels. Although these results must be regarded with caution given the small sample size, considering illusion and rotation effect together, a spatial frequency filter width of 2 seemed optimal.

Summary: Pilot experiments

The purpose of these two experiments was to maximise A&W illusion and rotation effect, by manipulating texture gain and spatial frequency parameters. The stimuli used in the current study were modified texture stimuli which were similar to the one used in the original study (Anderson and Winawer 2005). The first pilot experiment showed that a non-rotated stimulus with texture gain of 2 induced the strongest A&W illusion effect as well as the largest rotation effect. Increasing texture gain further to 3 did not increase the illusion effect. A previous study had shown that the increased illusion with increased gain is driven by the gain at the target location (Anderson and Winawer 2005). We did not investigate this observation here since we did not adjust gain separately for the target and the background regions. Rotation reduced the A&W illusion but did not reach significance ($p = 0.088$). Results from the spatial frequency manipulation in the second pilot experiment showed that the size of A&W illusion significantly dropped by the increase of spatial frequency filter width and by rotation. The interaction between the filter width and rotation almost reached significance ($p = 0.067$). Using a spatial frequency filter width of 2 induced a significantly stronger A&W illusion than using higher spatial width, but the illusory effect did not significantly differ from using lower spatial filter width. Additionally, rotating stimuli with a spatial frequency filter width of 2 reduced the illusion by a reasonable amount. Given the findings from our pilot measurements we expected that a texture gain of 2 and a spatial frequency filter width of 2 would give a strong illusion effect and large rotation effect. We tested this prediction in our first online experiment. Since we were interested in creating useful stimuli for future neuroimaging studies, in which luminance in a control stimulus could

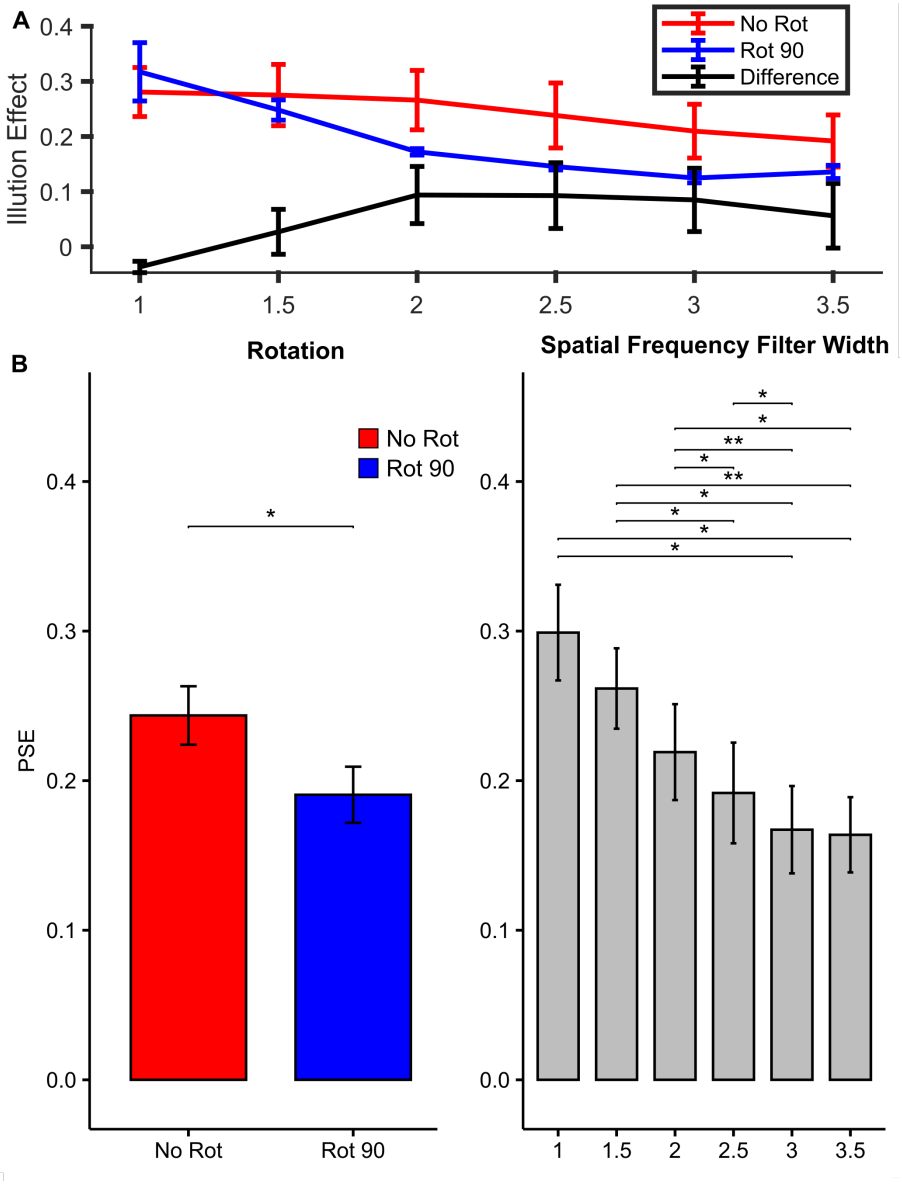
A
Illution Effect
0.4
0.3
0.2
0.1
0
No Rot
Rot 90
Difference
1
1.5
2
2.5
3
3.5
Rotation
Spatial Frequency Filter Width
B
PSE
0.4
0.3
0.2
0.1
0.0
No Rot
Rot 90
*
*
*
**
*
**
*
*
*
No Rot
Rot 90
1
1.5
2
2.5
3
3.5

Figure 4.9: (Previous page.) Psychophysic results for texture contrast gain experiments. **A**: Group averaged A&W illusion effect across spatial frequency (N=3). Red solid line: non-rotated conditions. Blue solid line: rotated conditions. Black solid line: difference between non-rotated and rotated conditions. Error bars show standard error (N=3). Illusion effect refers to the mean absolute point of subject equality (dark and light backgrounds combined), 60 MOA trials per condition. Insets show example textures at respective filter widths. **B**: Significant results for two-way repeated measures ANOVA, with within-factors including Rotation (Non-rotated, Rotated), Spatial Frequency Width (1, 1.5, 2, 2.5, 3 and 3.5). Left Panel in **B**: a significant main effect of Rotation. The illusion was averaged across all levels of spatial frequency filter width. Right panel in **B**: a significant main effect of spatial frequency filter width. The illusion was averaged across rotated and non-rotated conditions. *: $p < 0.05$; **: $p < 0.01$.

be compared to perceived brightness in an experimental stimulus, we used textured test stimuli rather than homogeneous grey. In addition, we tested the magnitude of the A&W illusion as a function of pedestal size.

Pedestal width experiments - method of constant stimuli

This experiment aimed to investigate whether A&W illusion can be induced just by changing the luminance in the background just outside the edge of the probe rather than by changing the luminance in the whole background. The restricted annular region of the background surrounding the probe to which the luminance manipulation is applied is called the pedestal (PD) region, of which the width can be manipulated (Figure 4.3 B). This will give insight into the level of processing at which the luminance comparison (probe to background) occurs since higher cortical areas are characterised by larger receptive fields (Bruce et al. 1981; Desimone et al. 1984; Tsao and Livingstone 2008). A greater dependency of perceived brightness on luminance in the background far from the probe edge would imply a higher-level process. Furthermore, an effective brightness illusion with minimum background luminance ma-

nipulation could be a useful tool for future neuroimaging studies since it would reduce or remove the confounding effect of display luminance and stimulus brightness.

Accordingly, we measured A&W illusion magnitude as a function of two main factors in this experiment. First, we compared the effect of changing the luminance of the full background with changing the background only up to only a few centimetres away from the target edge. Specifically, we used three levels of pedestal widths (PW): 1 cm, 2 cm, full background (Figure 4.10, 2-4 columns). A 'True Luminance' condition was included in which the mean luminance of the probe was set to +0.5 and -0.5 (Figure 4.10 first column). This extra condition allowed us to confirm that our method could reliably measure the participant' s perceived luminance of the probe. Each condition was tested using a non-rotated (0°) and rotated (90°) background. Hence the experiment used a 8 (levels of the luminance of the test) x 2 (levels of the luminance of probe background) x 2 (Rotated, Non-rotated) x 4 (True, Full, 1cm, 2cm) design, in which brightness perception was measured using the method of constant stimuli. Each condition was repeated 10 times. Before starting the measurements, there were 25 practice trials using true luminance targets in which feedback was given in the form of green (correct) and red (error) dots at the end of the trial. It took each participant 1305 trials to complete the whole experiment.

Two versions of the same experiment were run. In the first version,we used a texture contrast gain of 2, and in the second version we used a gain of 1, more in line with the stimuli used in the original study (Anderson and Winawer 2005).

Thirty-seven participants participated in the first experiment, of which twenty-three of them provided reliable data to perform further analysis. Sixteen participants attended the second width experiment, of which fifteen were included in the final analysis. The selection criteria were based on the fit quality of the psychometric functional that needed to explain more than 75% of the variance of the fitted data. The analysis was the same for both experiments. General linear model with

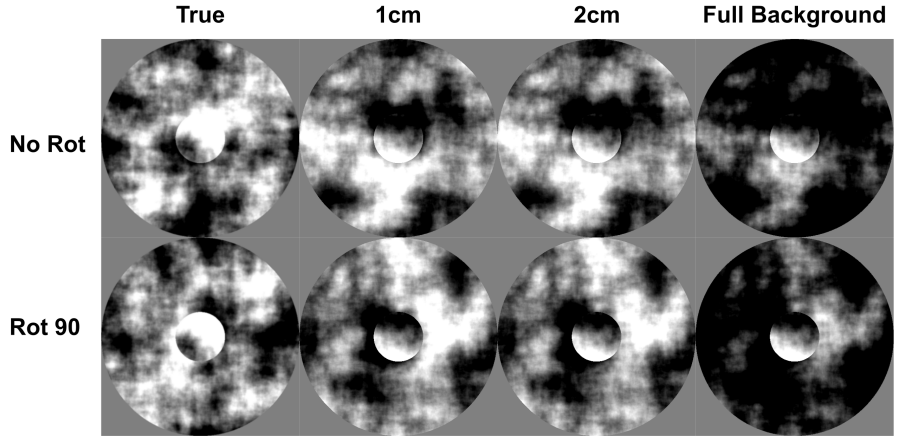

Figure 4.10: Example of stimuli. The upper panel shows one true condition and three conditions with non-rotated backgrounds in the pedestal experiments. Two sets of pedestal width are demonstrated, which are 1 cm on the left, 2 cm on the middle. On the right is the full background modulation. In the lower panel, the same conditions with a 90° rotation of the backgrounds.

Benjamini-Hochbergt correction was used for comparing the shift of PSE from 0. A two-way repeated measures ANOVA was performed to the data, with within-subject factors, Rotation (Rotated, Non-rotated) and PW (1cm, 2cm, Full background). Paired-samples t-test with Benjamini-Hochberg corrections were used for post-hoc testing.

Results

Figure 4.11 shows the group-averaged PSE in the first (left panel, Figure 4.11 A & 4.11 C) and second (right panel, Figure 4.11 B & 4.11 D) versions of the experiment. The PSE was plotted for the true luminance condition and the three different pedestal width conditions. Note that the use of the PSE as determined with the method of constant stimuli is based on data from both positive and negative differences of background luminance compared to the target (Section 4.3.2 Method of constant stimuli).

In the experiment using a texture contrast gain of 2 (Figure 4.11 A), the mean PSE for the true condition was close to 0.5 for both conditions matching the true luminance of the stimulus. This demonstrated the reliability of measuring the perceived lightness of the stimuli. For the illusory conditions, the mean PSE was greater than 0, indicating a shift in the perception of the target luminance. We performed a general linear model with Benjamini-Hochbergt correction to examine the perception shift from zero as a function of pedestal width condition (Figure 4.11 C). Non-rotated conditions (Blue) induced significant shifts of perceived brightness (stars Figure 4.11 C). Rotating the background by 90° (Red) destroyed the illusion in the full background condition, but only reduced the illusion in the PW conditions of 2cm and 1cm. The difference (yellow) between the non-rotated and rotated conditions were significant for the full background ($p = 0.0012$) and 2cm ($p = 0.029$) conditions.

In the second version of the experiment using a texture gain of 1 (Figure 4.11 D), modulating luminance of the full background failed to induce A&W illusion. Non-rotated stimuli only on the conditions of 2cm significantly induced the shift of perceived luminance ($p = 0.044$). The difference between the non-rotated and rotated conditions were not significant in any of the PW conditions.

To examine the effect of pedestal width and rotation on the A&W illusion, we performed two-ways repeated measures ANOVA, with within-subject factors, Rotation (Non-rotated, Rotated) and PW (1cm, 2cm, Full background). We observed a significant main effect of Rotation in the first version of the experiment ($F(1, 131) = 5.00$, $p = 0.027$, Eta2 (partial) = 0.04), and the second version of the experiment ($F(1, 83) = 4.17$, $p = 0.044$, Eta2 (partial) = 0.05). There was no significant main effect of PW and no significant interaction between PW and rotation in both experiments. Post hoc paired-samples t-tests (Figure 4.12, Left) revealed that rotation significantly reduced the brightness illusion in all three PW conditions in the first experiment (Full: $t (22) = 3.21$, $p = 0.012$; 2cm: $t (22) = 2.21$, $p = 0.037$; 1cm:

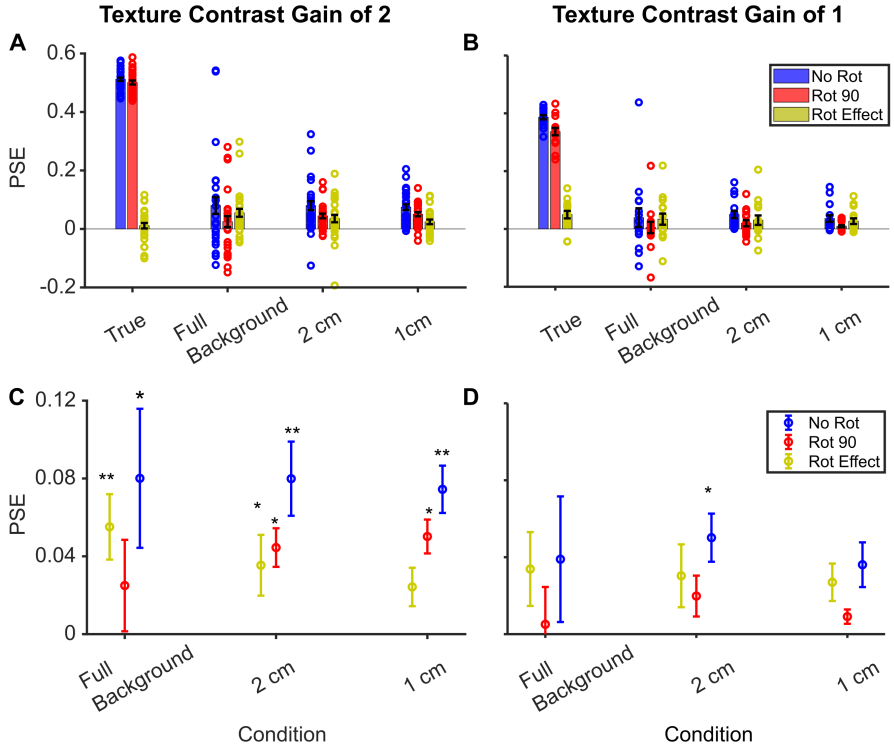

Figure 4.11: Group averaged results for two pedestal width experiments. **Left panel**: the first experiment that use a texture contrast gain of 2 (N=23). **Right Panel**: the second experiment that used a texture contrast gain of 1 (N=15). In **A** and **B**, bars represent mean PSE in each condition for non-rotated (blue) and rotated (red) targets, and the difference (yellow). Circles represent data from individual participants. Bars represent standard error in **C** and **D**. Significance notes represent a significant shift of brightness from zero. *** $p < 0.001$, ** $p < 0.01$, * $p < 0.05$.

t (22) = 2.40, p = 0.037). Although the overall illusion is stronger in the non-rotated stimuli than in the rotated stimuli in the second experiment (t (44) = 3.33, p = 0.002), we did not observe the rotation effect in any of the PW conditions (Figure4.12, Right).

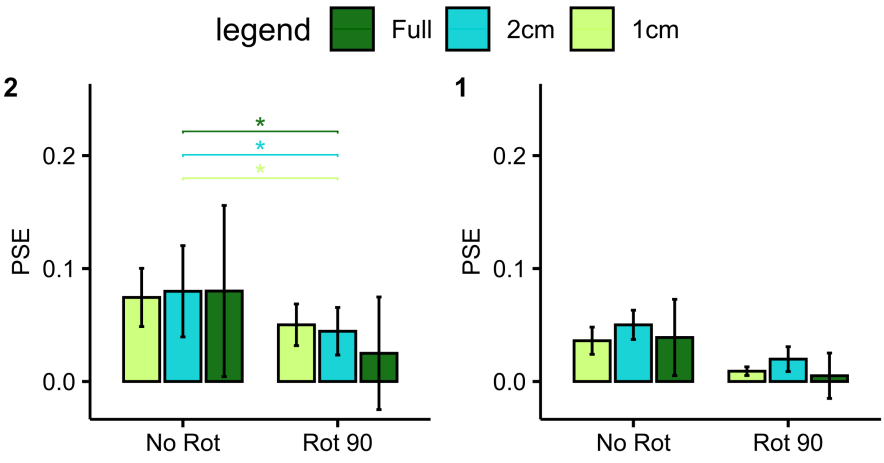

Figure 4.12: ANOVA results for pedestal width experiment using method of constant stimuli. Error bars represent standard error.*: $p < 0.05$.

Summary: method of constant stimuli

The purpose of the pedestal width experiment was to investigate potential differences between manipulations of luminance at the edges of the target and adjustment of whole background luminance. We did not find a significant difference among a full background, 2cm and 1cm modulation. Hence, perceived luminance in the A&W illusion did not depend on pedestal width. This result showed that the A&W illusion depends primarily on the background luminance close to the edges of the probe, and not far from the edge, since the size of the illusion was the same for both pedestal widths, and for the full background condition.

The results of the true luminance condition showed that an on-

line experiment was effective to measure the perceived luminance of the participants. The true luminance changes of the target were equally distinguishable in both non-rotated and rotated displays (see Figure 4.11 A & B). This was a crucial and reassuring observation given the lack of standardised conditions in which the experiment was administered (no supervision and minimal explanation of the task). Rotating significantly reduced the perceived luminance in both texture contrast gain settings. But the interaction between rotation and pedestal width is significant only when the texture contrast gain was set to 2.

Compared with the spatial frequency and texture gain pilot experiments, the size of A&W illusion on the pedestal experiments was reduced. Possibly the largest difference between two measurements was that, in the pilot experiments we used an isolated homogeneous grey patch as the test stimulus, whereas in the online experiment we used a textured patch surrounded by textured background. Previous studies using the A&W stimulus have typically used homogeneous patches as test stimuli. If participants perceive the experimental stimulus as a distant bright or dark surface obscured by overlaid light or dark clouds, in line with the layer theory interpretation, a homogeneous test stimulus is useful to test the perception of the probe when the clouds are discounted. However, such a test stimulus would not be an appropriate control stimulus for contrasting differences in brightness in the probe with differences in luminance in the test. Thus, we choose to keep the test and probe as similar as possible while varying only the mean luminance of the test. Alternatively, the difference in the size of the effect between the pilot study and the current measurement may be due to the different methods used to assess the strength of the A&W illusion. In the pilot study, we used the method of adjustment to assess the illusion strength, which was used frequently in previous experiments. In the pedestal width experiment, we used the method of constant stimuli. Finally, another alternative explanation is that the participants in the pilot experiments were aware of the illusion and the experimental design. This could have biassed the responses towards greater illusion strength. This potential bias might have been absent in the naive par-

ticipants who participated in the online experiments with the method of constant stimuli, which might have led to a decrease of illusion strength. Taking account of these differences, we planned an additional online experiment in which we contrasted the method of adjustment with a third method, staircase method. We again used naive participants and textured test stimuli.

Comparison between the method of adjustment and staircase

In a next experiment, we followed up on the idea that the test method used could be related to the relatively small illusion magnitudes measured in the previous experiment. Therefore, instead of using the method of constant stimuli, we here assessed illusion strength with the method of staircase and the method of adjustment. These methods also offer the opportunity to separately estimate the perceived brightness of the dark and light background conditions, which were otherwise combined in the method of constant stimuli. The measurements were conducted online via Inquisit, in line with COVID restrictions.

As in previous measurements, the participant compared a test stimulus with a probe stimulus, however here the test and probe were presented separately. In the MOS (Figure 4.13 A), the order of the test and probe presentation was randomised and the participant responded which stimulus presented was perceived as lighter. To further simplify the task, the target and probe had different shapes. The test was circular, while the probe was star-shaped (giving the probe a large contour). The participant thus responded whether the circle or star was perceived as brighter using the C and S keys. The mean RGB value of the probe was adjusted by 0.06 with each button press and the staircase continued until 20 reversals had been recorded. The PSE was calculated as the mean RGB value of the last 15 reversal points, corresponding to a position where the participant was equally likely to respond that the probe was darker or lighter than the target. Two staircases were collected for each experimental condition, with the test starting RGB

luminance value set to 0. The sessions started with a training block in which participants performed the staircase with a true dark and true light probe and were given feedback (red / green dot presented after the response).

In the method of adjustment (Figure 4.13 B), the test (circle) was always presented after the probe (star) and the participant used the up and down arrows to adjust the test to match the perceived brightness of the probe. The participant used the space bar to accept the match and could also use the right arrow to see the test and probe again. The PSE was calculated from 6 repetitions of the MOA per experimental condition. The two methods were separated into two blocks. Within each block, different conditions were randomised. The block of method of adjustment was presented after the method of staircase block.

Forty-eight participants participated in the experiment. Participants for whom the PSE was less than half the true value for the true stimuli, for both bright and dark targets, were excluded from the analysis, thereby we excluded 5 participants, leaving 43 for analysis. The experiment used a 2 x 2 x 2 x 2 experimental design, with the factors background (Light, Dark), target rotation (Not rotated, Rotated), pedestal width (Full, Narrow), and testing method (MOA, MOS). One-sample t-tests were used for comparing the shift of PSE with real luminance change. To estimate the impact of each stimulus condition on the A&W illusion, we performed a four-way repeated measures ANOVA, with within-subject factors including Pedestal width (Full, Narrow), Background (Light, Dark), Rotation (Non-rotated, Rotated) and Method (MOA, MOS). Post-hoc paired t-tests (Benjamini-Hochberg correction) were performed to estimate relationships among each other. For further analysis, three-way repeated measures ANOVA was performed separately on data from dark and light background, with within-factors including Pedestal width (Full, Narrow), Rotation (Non-rotated, Rotated) and Method (MOA, MOS). To further test the stability of the A&W illusion across test methods, we calculated R^2 and the associated P values using linear regression between each participant' s

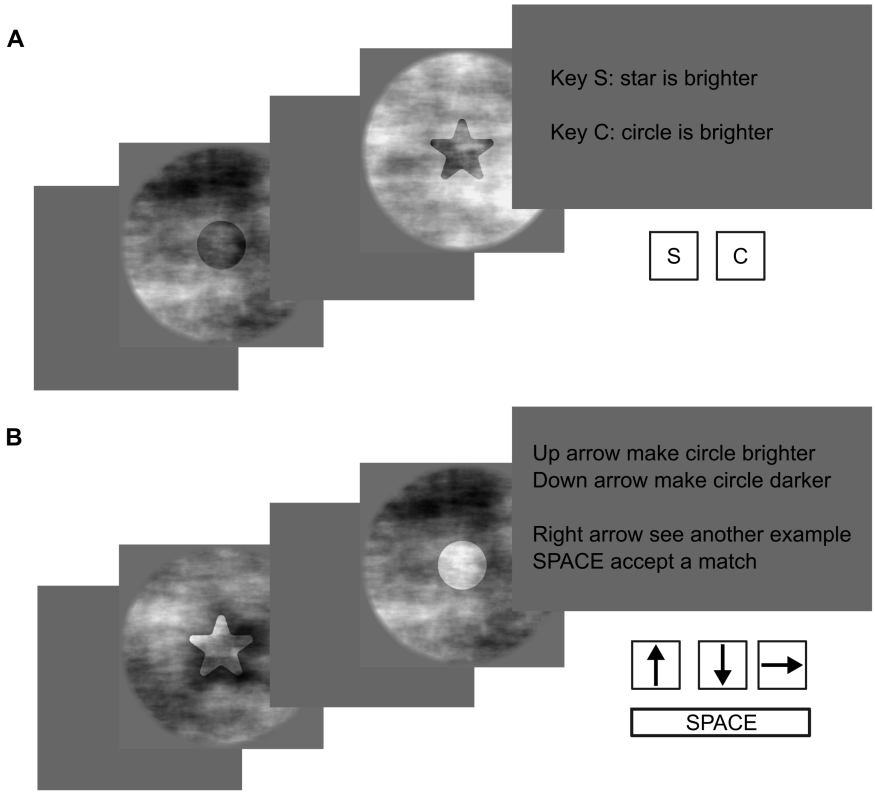

Figure 4.13: Second online paradigm. **A**: Staircase method trial, here showing a test-first example and target with full bright background. **B**: Method of adjustment trial.

PSE estimated by the two methods. We performed this analysis only for the dark (perceived) stimulus conditions, where the illusion was generally higher than for the light stimulus conditions.

Results

For all experimental conditions, PSE was measured using both MOS and MOA. Figure 4.14 shows the group averaged PSE for each condition (combined MOA and MOS, bars) and individual PSE (dots) in the online experiment. The Leftmost pair of bars show PSE measured during the practice block. Here the luminance of the probe was set to $\pm$ 0.275 (horizontal dashed lines). The mean PSE indicated that participants tended to overestimate the brightness of bright targets on the dark background (Mean = 0.33, SD = 0.04, t-test $\neq$ 0.275, t (42) = 7.9, $p < 0.001$) but underestimate dark stimuli on the light background (Mean = -0.23, SD = 0.04, t-test $\neq$ -0.275, t (42) = 7.3, $p < 0.001$).

A four-way repeated measures ANOVA was performed on data from 8 experimental conditions to examine the effects of testing methods on the A&W illusion. We found a significant main effect for Background ($F(1, 630) = 363.03$, $p < .001$, Eta2 (partial) = 0.37), significant interactions between Rotation and Background ($F(1, 630) = 22.06$, $p < .001$, Eta2 (partial) = 0.03), between Pedestal Width and Background ($F(1, 630) = 6.16$, $p = 0.013$, Eta2 (partial) = 9.68e-03), and among Rotation, Method and Background ($F(1, 630) = 5.17$, $p = 0.023$, Eta2 (partial) = 8.13e-03). To further investigate the relationship among each other, we ran paired-sample t-tests (Benjamini-Hochberg correction) for comparisons of interest. We found that modulation of the luminance in the full light background induced significantly smaller PSE than modulation of the luminance in the narrow light background (t (171) = -3.42, $p = 0.0018$). We also found that the influence of MOA and MOS was only significant for a rotated probe on a light background (Figure 4.15, upper panel right, t (85) = -2.80, $p = 0.026$). Using the method of adjustment, rotation significantly reduced the brightness illusion only with the probe appearing on the dark background (Figure4.15, middle panel left, t (85) = 3.46, $p = 0.0011$). However, with the method of

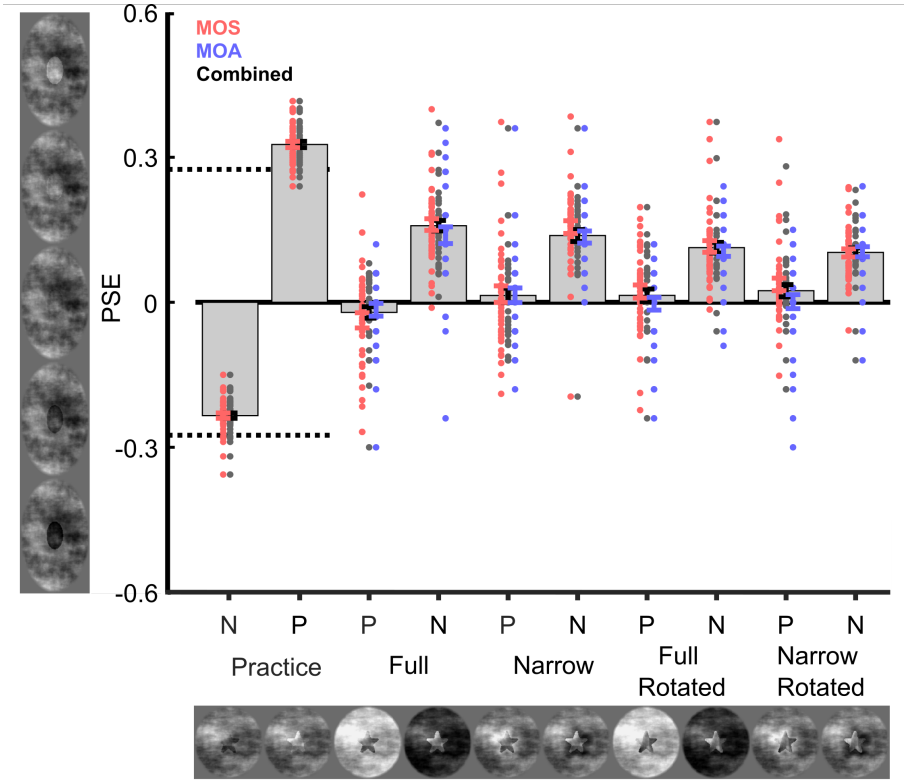

Figure 4.14: Data for online experiment to compare test methods. The barplot indicates the mean point of subjective equality (PSE) between the method of adjustment and staircase. The dots represent each data point from each testing method, which are distinguished by colour (Red: method of staircase; blue: method of adjustment; black: average of methods). In practice trials, probe luminance was modulated, in other conditions the probe-background was modulated. P / N indicates positive and negative luminance change from 0. Full indicates the modulation of luminance in the whole background. Narrow indicates the modulation of luminance only in the narrow pedestal region that is close to the border of the probe. Black dotted line represents the actual change of luminance.
Abbreviation: MOS: method of staircase; MOA: method of adjustment.

staircase, rotation had shown significant impacts on the illusion with the probes appearing on both backgrounds, but the impact was opposite (Figure 4.15, middle panel right, Dark: t (85) = 6.20, p =7.84e-8; Light: t (85) = -3.58, p = 0.0014). Probe on a dark background induced much stronger illusion than it on a light background in both Rotation conditions and in both testing methods (Figure 4.15, lower panel, all p < 0.001).

We also explored the data from the dark and light background separately due to the asymmetric illusory effects. We performed three-way repeated measures ANOVA separately on these datasets. For the dark background, we found significant main effects of Rotation (F(1, 294) = 36.04, p < .001, Eta2 (partial) = 0.11) and Method (F(1, 294) = 4.27, p = 0.040, Eta2 (partial) = 0.01) and no significant interactions. Post-hoc paired t-test showed a trend that MOA was not as effective as MOS to induce brightness illusion on non-rotated probes (Figure 4.16, dark background, t (85) = -2.09, p = 0.0784). It also showed the non-rotated probe induced a significantly stronger illusion than the rotated probe (t (171) = 6.66, p = 3.52e-10). For the light background, we found significant main effects of Rotation (F(1, 294) = 5.85, p = 0.016, Eta2 (partial) = 0.02) and Pedestal width (F(1, 294) = 9.93, p = 0.002, Eta2 (partial) = 0.03), and also significant interactions between Rotation and Method (F(1, 294) = 6.06, p = 0.014, Eta2 (partial) = 0.02), and between Rotation and Pedestal width (F(1, 294) = 4.00, p = 0.046, Eta2 (partial) = 0.01). Post-hoc paired t-tests showed a significantly higher PSE for rotated probes measured by MOS than MOA (Figure 4.16, light background, t (85) = -2.80, p = 0.013), and a significantly lower PSE for changing the luminance in the whole background than in the narrow band of the background for non-rotated probes (Figure 4.16 light background, t (85) = -3.68, p = 0.00082). If the target on the light background successfully induced the lightness illusion, the target is perceived darker, where the value of PSE should be negative. From our data, the PSE for the full background conditions is negative but is positive for the narrow band conditions. Although the PSE was significantly higher for narrow band conditions, it did not

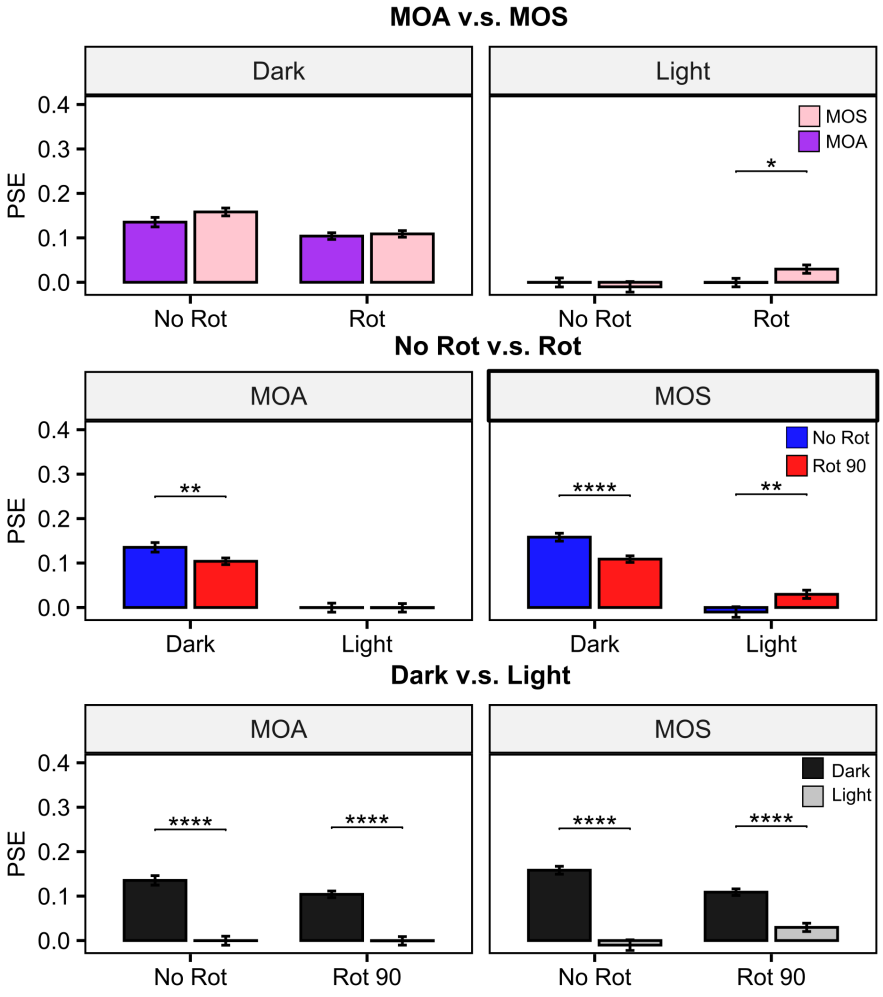

Figure 4.15: Significant results from four-way repeated measures ANOVA. It shows the significant interaction among Method (Method of adjustment (MOA), and staircase (MOS)), Rotation (Non-rotated, Rotated), and Background (Dark, Light). Upper panel shows the impact of Background and Rotation on the Method. Middle panel shows the impact of Method and Background on Rotation. Lower panel shows the impact of Method and Rotation on Background. Error bars represent standard error. *: $p < 0.05$; **: $p < 0.01$; ***: $p < 0.001$; ****: $p < 0.0001$.
Abbreviation: MOS: method of staircase; MOA: method of adjustment.

convey meaningful information about these two conditions. And it revealed that light background conditions failed to induce the lightness illusion.

Given the large spread of PSE across participants we further tested whether the illusion indicated by both methods was correlated per participant. This analysis was only focused on the data collected from dark backgrounds. Combining across the four conditions of interest, we found a significant correlation in PSE measured for the two methods ($R^2 = 0.15$, $p < 0.001$). Interestingly, when looking at individual conditions the correlation was only present for the narrow stimuli (Non-rotated: $R^2 = 0.26$, $p = 0.0005$; Rotated: $R^2 = 0.2$, $p = 0.0022$) but not for the full-background stimuli (Non-rotated: $R^2 = 0.08$, $p = 0.07$, Rotated: $R^2 = 0.05$, $p = 0.15$).

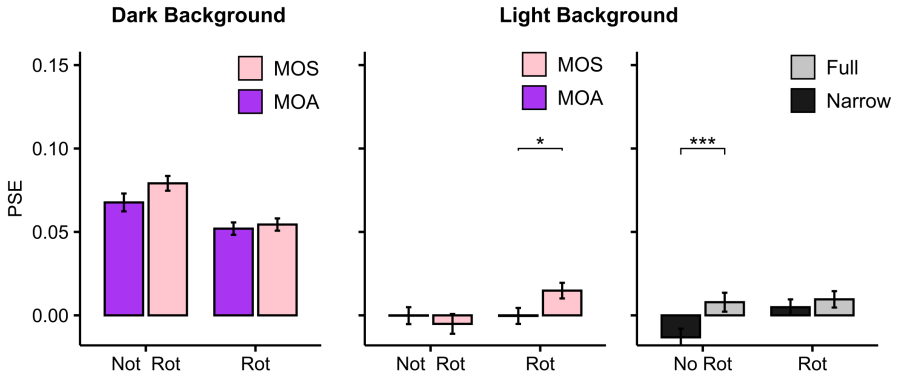

Figure 4.16: Results from three-way repeated measures ANOVA. Error bars represent standard error. *: $p < 0.05$; **: $p < 0.01$; ***: $p < 0.001$; ****: $p < 0.0001$.
Abbreviation: MOS: method of staircase; MOA: method of adjustment.

Summary

In previous experiments we found that the A&W brightness illusion appears weak when tested online using naive participants. To test whether this result may be due to the method of constant stimuli used

in our previous experiments, we here repeated the measurements using the method of staircase and adjustment, which have been more widely used in previous literature. The results again indicated a weak illusion effect. Moreover, PSE measured with the method of staircase tends to be slightly higher.

In addition, the illusion was present only for probes that were surrounded by dark backgrounds, whereas the illusion was effectively absent for stimuli with light backgrounds. This was consistent with our findings in Chapter 3 and also with previous studies (Taylor et al. 2018; Xing et al. 2014; Yang et al. 2022). For the stimuli presented on the dark background, rotating significantly reduced the illusion but did not destroy it. Interestingly, and in line with our previous measurements, our novel narrow pedestal stimulus effectively induced the illusion but with a slightly smaller size as the full background stimulus. This suggests that the A&W illusion may not be fully reduced to luminance manipulations close to the target, as the preceding experiment in this chapter may have suggested (see section 4.3.2).

4.4 Discussion

The main goal of the current chapter was to investigate a class of stimuli that has been reported to yield a powerful surface brightness/lightness illusion. A more powerful brightness illusion than was used in Chapter 3 and previous studies (Poiriehr 2009) might be more effective in driving surface related neuronal activity and produce stronger fMRI responses than were observed in Chapter 3. The stimulus introduced by Anderson and Winawer (2005) was hailed to be the strongest brightness/lightness illusion yet reported (Poiriehr 2009). Furthermore, this stimulus could be a powerful tool for neuroimaging experiments since the brightness illusion can be destroyed by simply rotating the background, without changing the overall mean luminance of the stimulus (for example, the control stimuli from Van de ven et al. (2012) is black, which the contrast and the mean luminance is very different from the grey test stimuli). While test and control stimuli have the same luminance, the original

stimuli differ substantially between dark-appearing and light-appearing target conditions. We aimed to reduce this difference by spatially varying the amount of luminance added or subtracted to the background, such that only a small region of the background differed between light- and dark-appearing target conditions. Our experiments coincided with the start of the 2020 to 2022 COVID pandemic, thus we were obliged to resort to online psychophysics measurements. While suboptimal, this gave us the opportunity to explore the possibilities that online psychophysics offers.

The strong brightness illusory effect and the rotation effect of the Anderson and Winawer stimulus (Anderson and Winawer 2005) are the two essential features that we are looking for in our test stimuli. By fine tuning texture contrast gain and spatial frequency filter width on three experienced participants using the method of adjustment, we acquired a relatively large illusory effect and nearly effective rotation effect. Using the optimised parameters, we performed an online experiment with naive participants using the method of constant stimuli to investigate whether the illusion can be induced by only changing the luminance of the background just outside of the edge of the probe rather than by changing the luminance of the whole background. The brightness illusion was successfully generated for all the non-rotated stimuli but the illusory size was small. Additionally, the illusion was significantly reduced by rotation in all pedestal width conditions (2cm, 1cm, Full) but only destroyed when the luminance was changed in the whole background. One of our assumptions for the small illusory size is that it was caused by the difference between our stimuli and original stimuli. Therefore, we applied a different texture contrast gain to create stimuli more similar to the original ones. However, with these stimuli, non-rotated stimuli only at the pedestal width condition of 2cm induced the brightness perception and there was no rotation effect. We next examined whether the small illusory size could be caused by the test method, because both our pilot study and Anderson and Winawer (2005) utilised the method of adjustment and acquired relatively strong illusion. Therefore, we assessed illusion strength with the method of

adjustment and the staircase method. Although there was no significant difference between these two methods, there was a trend that the staircase method was a bit more effective to estimate the A&W illusion. Meantime, we observed that only a probe on the dark background successfully induced the A&W illusion. Targets on the light background failed to induce the brightness illusion, which is in line with our observation in Chapter 3 and previous studies (Taylor et al. 2018; Xing et al. 2014; Yang et al. 2022). Furthermore, the rotation again only reduced the lightness illusion but did not destroy it.

Taken together, our online experiments showed a weak illusion and only a semi-effective rotation effect of Anderson and Winawer illusion. For further investigations, we would like to evaluate the factors that led to these unsatisfactory results by comparing experimental setups between our study and original research. First, the experiment of Anderson and Winawer (2005) was executed in a much controlled environment, such as fixed eye-to-screen distance, using a calibrated and linearized professional monitor. In contrast, we were not able to correct the luminance value on participants' screen or monitor the eye-to-screen distance (although methods to estimate viewing distance in online experiments have since been developed (Li et al. 2020)). Second, we could not control the environment's luminosity, which might have affected the illusory size (Zavagno et al. 2018). In a standard psychophysical laboratory, environmental light is much easier to control. Although they did not mention whether the experiment was performed in a dark environment, we assume it was because this is a common setup for luminance related experiments. Third, due to the storage limits for the uploaded materials, the number of conditions were also limited and the quality of the images was somewhat reduced. The limited number of conditions reduced the precision of our measurements, for example requiring participants to choose between a set of pre-prepared stimuli in the method of adjustment measurements, rather than precisely controlling the stimulus. Last but not least, most of the experiments took around 1 hour, and we cannot know how engaged the participants were in the experiment. In the original study, two of three participants were the authors,

which would highly engage in the study. Our pilot online study has the closest setup with the original study (Anderson and Winawer 2005). We also had three participants who were involved in the research performed the experiments using the method of adjustment. Here we found the largest illusions effect and confirmed that the rotated surround largely reduced the illusion. The illusory effect and rotation effect from the pilot study were larger than the later online experiments with the same settings. This pattern might suggest that an amount of (unintentional) participant bias may contribute to large reported effects.

Beyond the environmental and people factors, there are two main differences in stimulus setting between our later online experiments and the original study. First, our target was static but the target from Anderson and Winawer' s stimuli was presented in motion. Studies have shown that motion influences the perception of lightness/brightness (Ashida and Scott-Samuel 2014; Morikawa and Papathomas 2002). Using a brightness induction paradigm, Morikawa and Papathomas (2002) observed a reduced brightness induction due to the moving of the inducer. When elements with luminance gradients move across uniform backgrounds, they appear lighter or darker. Using this lightness illusion, Ashida and Scott-Samuel (2014) found that the perception of lightness is not only influenced by motion but also by the direction of motion of the inducer patterns. Additionally, apparent motion also affects the perception of brightness. In a luminance induced apparent motion paradigm, Nagai et al. (2011) observed more difficulties for participants to correctly associate luminance wedges when the motion perception is strong. Anstis (2006) reported that the White' s effect influences the strength of the motion signals. Second, we rotated the target instead of the surround in the later online experiments. The rotation in both designs breaks the perception of transparency but may have different levels of impact on the illusion. Finally, Anderson and Winawer state that the illusion is more compelling when multiple target surfaces are presented in a single test image (Anderson and Winawer 2008). Indeed, the example images that they show all contain multiple targets, although the stimuli used in their measurement contained only

one moving target.

A common feature of non-static presentation, rotating the surround or presenting multiple targets is the involvement of cortical processing of global features, requiring neurons with larger RFs that encompass the entire stimulus. In contrast, our investigation of the effects of a narrow pedestal width on the A&W illusion were designed to tap the involvement of neurons with small RFs, sensitive only to local contrast at the target surface edge, responsible for the detection of luminance contrast at the target boundaries, supporting edge extraction and assignment of edge polarity (Clay Reid and Shapley 1988; Land and McCann 1971; Rudd and Zemach 2007). Our stimulus excluded mechanisms that compare luminance over large distances (beyond the width of the pedestal). A notable feature of our data was that the size of the illusion was not statistically different for the full and narrow pedestal versions. This indicates that, for our stimuli, even in the full background stimuli the perception of surface brightness was mediated largely by edge-detection neurons. These neurons would be insensitive to global features, including the rotation of the target/background (Altmann et al. 2003; Gallant et al. 2000; Kastner et al. 2000; Tanaka 1996). Lack of the cortical processing of these global features could be one of the reasons why we only acquired small illusory effects and less effective rotation effects, for example, larger illusory effects in the pilot studies (rotating the surround) than in the later experiments (rotating the target).

The strength of only modulating a narrow pedestal width is that it reduces the influence to the mean luminance of the entire display. It facilitates the decoupling of cortical response to changes in brightness to luminance and contrast. Different studies used different methods to tackle this problem. Salmela and Vanni (2013) used second-order stimuli that include both decrement and increment of luminance to keep the local contrast and mean luminance constant. Perna et al. (2005) compared cortical responses to a brightness illusion (Craik-O' Brien Cornsweet illusion) to a stimulus with identical local energy but no brightness

illusion. Boucard et al. (2005) and Cornelissen et al. (2006) compared responses to induced brightness with responses to real luminance modulation. There have also been studies that compared responses to the brightness illusion with responses to different control stimuli that do not induce change in perceived brightness (Boyaci et al. 2007; Pereverzeva and Murray 2008; Van de ven et al. 2012), nonetheless the contrast and mean luminance of the control stimuli are different from the illusory stimuli in these studies. In the current chapter, modulating the luminance of a narrow pedestal width in the background and the rotation effect, may provide an effective and powerful control stimulus with the same contrast and mean luminance if follow up experiments in the lab can indicate a larger effect.

Online experiment is a new tool for psychophysics research. It provides easy access to a demographically and culturally diverse participant population, and was a helpful alternative during the pandemic when the labs were all closed. It also has high statistical power due to the large sample size (Birnnbaum 2000). It has been used in language studies (Keuleers et al. 2015; Lenzner et al. 2010), social studies (Beenen et al. 2004, November; Darley et al. 2010; Parigi et al. 2017; Sweeney et al. 2014), vision studies (Li et al. 2020; Rajananda et al. 2018; Semmelmann and Weigelt 2017) and others (Kauffman et al. 2011; Verheyen and Göritz 2009; Zampetakis and Melas 2021). But it also has disadvantages, such as multiple submissions from same participants, lack of experimental control, potential dropout during the experiment (Birnnbaum 2000) and storage limits for the uploaded materials. Additionally, most of our experiments took around 1 hour, and we cannot know how engaged the participants were in the experiment. Therefore, for experiments requiring restricted experimental control, such as our experiments (Calibration of the luminance value of the monitor, fixed eye-to-screen distance, dark environment), an online experiment might not be optimal. Although the online experiments provided some insights into the factors that influence the size of the illusion, the conclusions reached are also limited by inherent shortcomings of online experimentation. Therefore, it will be necessary to replicate these experiments

in the psychophysics laboratory. After setting up a stable experimental paradigm for A&W illusion in the psychophysics laboratory, we can transform the paradigm to make it available to neuroimaging studies to study the underlying neural mechanisms.

A valid experiment should possess both internal validity (results are only due to the manipulated independent variables) and external validity (can be generalised to groups, environments and contexts outside of the experimental settings) (Onwuegbuzie 2000, November). Studies including the current chapter used Anderson and Winawer ' s stimuli all replicate the brightness illusion, which has shown the internal validity of this stimulus (Albert 2007; Anderson and Winawer 2005; Anderson and Winawer 2008; Poiriehr 2009; Poirier et al. 2012). Our online experiments are the first to test this illusion in a natural environment (natural lights, multiple locations, none-calibrated monitors, and not-controlled eye-to-screen distance). The illusory effect was not as strong as the one that was tested in the psychophysics lab. Therefore, the external validity of this stimulus may be limited. Alternatively, the internal validity of our online measurements may be limited. The ultimate goal for the efforts in the professional laboratory is to understand how our brain enables cognition. In real-life, we don' t have a highly controlled environment but we can still perceive the change in the brightness due to the change in the surroundings. Although the results from our online experiments are sub-optimal, it still provides some insights on the direction of future experimental design.

5

General Discussion

5.1 Overview

Functional magnetic resonance imaging at ultra-high field (UHF) strength provides new opportunities for investigating (sub)-cortical processing of cognition. The goal of this thesis was to take advantage of the current state of the art to investigate fundamental questions, and understand what we can do to push it further. We first studied the localisation of the nucleus basalis of Meinhert (nbM) in neuroimaging studies (Chapter 2). Although we found that the nbM could be visualised in the quantitative T_2^* dataset acquired at 9.4 T with 200 μm isotropic resolution, this contrast and resolution is not yet readily available for normal in vivo scanning. However, as technology keeps evolving, we are optimistic that visualisation of nbM in vivo will be possible in the (near) future. We then performed high-field high-resolution fMRI experiments to investigate the neural mechanisms of surface perception in the early visual cortex, using a classic brightness induction paradigm (Chapter 3). We found little evidence of a correlate of surface brightness in the early visual cortex and discussed several avenues for future projects. One possible avenue will be to use a more powerful and further optimised brightness illusion. In Chapter 4, we parametrically investigated the properties of a textured brightness induction stimulus. Our experiments were limited by COVID restrictions, nevertheless our results indicated that some brightness illusion can be induced using a stimulus with minimum luminance difference between bright and dark conditions. A finding that currently limits the potential of the textured brightness induction stimulus is the fact that the magnitude of brightness induction is small. In the current Chapter, we first summarise the main findings of each empirical chapter, then discuss the limitations of each study, and finally identify potential avenues for future research.

5.2 Volumetric investigation of human nucleus basalis of Meynert

5.2.1 Summary

Understanding the neuronal basis of attention is one of the main goals in the field of cognitive neuroscience. Various studies have shown that the cholinergic system is a key mechanism for mediating attentional control (Klinkenberg et al. 2011; Thiele and Bellgrove 2018). The main source of cortical acetylcholine (ACh) is the nucleus basalis of Meynert (nbM) (Mesulam and Geula 1988; Mesulam et al. 1983). However, to date relatively little fMRI research has focused on the nbM, in part because of the difficulty of imaging the structure. Our first intention was to explore the functional specificity of the nbM in attention using 7T fMRI. Despite the feasibility of sub-millimetre spatial resolution at 7T, it has been difficult to directly visualise nbM and its subregions in vivo, which is reflected in the large variations in structural volume and location of the nbM observed across (f)MRI studies to date. This is due to the fact that the nbM is small, diffusive and extensive, with an 'open' structure in all three dimensions, in contrast to other subcortical nuclei (e.g. the red nucleus) which are compact and have 'regular' shapes (Liu et al. 2015; Pauli et al. 2018). In Chapter 2, we attempted to understand the feasibility of MRI to study the nbM in four steps. First, we reviewed current human nbM region-of-interest (ROI) selection protocols used in MRI studies and found highly variable nbM volume estimates. Then, we investigated the sources of the variability in reported nbM volumes, especially for the atlas based nbM estimates. We found that nbM estimates not only depend heavily on the atlas used and on the probabilistic threshold set, but also vary substantially between datasets using the same atlas and threshold. In order to test whether spatial resolution influences volume variability, we developed a novel nbM mask based on the normalised BigBrain dataset. The mean estimated nbM volume was quite stable at higher resolutions (0.1 - 1.3 mm isotropic), but the variance of the estimated nbM volume increased dramatically for voxel sizes above 1.3 mm isotropic. Our conclusion was that ap-

plying any mask defined originally in histological space in one or more brains to MR images of other brains will almost certainly always be difficult. The likely best solution will be to identify the nbM individually in structural scans. To investigate this possibility, we explored publicly available and novel high-resolution MRI ex vivo datasets with multiple MR contrasts. We found that the nbM could be visualised in the quantitative T_2^* dataset acquired at 9.4 T with 200 μm isotropic resolution. This demonstrates that it is technically possible to directly image the nbM, however only at a contrast and resolution that is not yet readily available for standard in vivo scanning.

5.2.2 The need for MRI atlases of human subcortical brain structures

The human subcortex contains approximately 455 unique, small structures, but only about 7% of these structures are currently represented in standard human brain MRI atlases (Alkemade et al. 2013; Forstmann et al. 2017). Although UHF imaging provides higher SNR and better CNR (as elaborated in the Chapter 1), in vivo imaging of subcortical structures is still challenging due to their deep location in the brain and, especially in the case of the nbM, their structural complexity. However, for any target structure of interest, it is necessary to have an anatomical reference in neuroimaging research, in order to, for example, estimate morphological and volumetric differences between groups, assess their structural or functional connectivity, or measure event-related activity in these structures (Casamitjana and Iglesias 2022; Leergaard and Bjaalie 2022; Shih et al. 2008). For a structure not visible on in vivo structural images and without an effective functional localiser, an atlas is essential for localisation and segmentation.

5.2.3 Limitations of the current nbM atlas

The most commonly used atlases for the nbM were created either from a single post-mortem T_1-weighted brain (Kilimann et al. 2014; Teipel et al. 2014a; Teipel et al. 2005) or from ten post-mortem T_1-weighted

brains (Zaborszky et al. 2008). These post-mortem scans were acquired at standard field strength (1.5 T and 3T) with a relative low resolution (around 1 mm isotropic) (Kilimann et al. 2014; Teipel et al. 2014a; Teipel et al. 2005; Zaborszky et al. 2008). Although the nbM neurons were identified in high-resolution histological sections they were downsampling to 1.0 mm isotropic, leading to a loss of many details. In Chapter 2, we created a nbM template at 100 μm isotropic resolution based on the BigBrain dataset. Although much details are included, it still shares in common with the previous nbM atlases that the accuracy of volumetric measurement is much reduced when the nbM ROI is applied to a dataset with lower resolution (e.g. above 1.3 mm isotropic). There are also other disadvantages of using atlases based on one, or few, subject(s), not the least of which is the bias towards the chosen subject(s). This becomes especially problematic for brain areas with less consistent anatomy across subjects because topological changes cannot be modelled by deformation (Casamitjana and Iglesias 2022). Histological studies have shown the existence of variability of nbM between populations and across the age range (Halliday et al. 1993; Zaborszky et al. 2008). Thus, building an nbM atlas from a single subject, or indeed from multiple subjects with similar age, may not accurately reflect the variability.

5.2.4 Building a future nbM atlas

With the development of UHF imaging, many atlases for subcortical structures have been created using in vivo and ex vivo MRI. Some of them collected multiple MR contrasts (T_1w, T_2w acquired hippocampus atlas from Winterburn et al. (2013); T_1w, R_1, R_2 , T_1, T_2 , QSM acquired for basal ganglia atlas from Alkemade et al. (2020)) with submillimetre resolution in vivo. To date, this kind of exploration has been lacking in nbM research and in most nbM neuroimaging studies, which acquired only T_1 weighted structural images. Although high-resolution imaging makes it easier to visualise fine structures, it may not be enough to image certain subcortical structures. Whole brain anatomy is com-

monly acquired by a T_1 weighted sequence (MPRAGE or MP2RAGE) (Marques et al. 2010; Mugler III and Brookeman 1990; Van de Moortele et al. 2009). The MP2RAGE sequence usually produces images with superior white matter contrast, while MPRAGE images enable better delineation of the grey matter/cerebral spinal fluid boundary (Schneider 2019). Moreover, different MR contrasts carry important information of local microstructure, especially cell membrane, myelin and iron (Beaulieu and Allen 1994; Filo et al. 2019; Palombo et al. 2020; Stüber et al. 2014). Thus, the sequence that is best to visualise subcortical nuclei depends on the anatomical structure of the specific region. For example, the subthalamic nucleus is more visible on a T_2^* weighted scans than T_1 weighted scans (Forstmann et al. 2014). To our knowledge, it is not yet known what contrast works best to image the nbM and to separate it from the surrounding region, known as the substantia innominata. In histology, a pale iron staining with diaminobenzidine tetrahydrochloride reveals granular, glial, fibrous, oligodendroglial, neuronal, and vascular iron reactivity (Morris et al. 1992). The nbM itself is dispersed within substantia innominata and surrounded by dense myelin. We reasoned that, when compared to the rest of substantia innominata, the nbM' s open structure, magnocellular, isodendritic, heteromorphic, AChE-rich, and choline-acetyltransferase, may result in differential MRI properties (e.g. $T_2(^*)$, T_1, Magnetic transfer). Moreover, compared to the weighted images, quantitative measurements provides specific physical parameters related to the spins of the underlying microstructure (Weiskopf et al. 2021), avoids the MR contrast being cancelled out due to microstructures having opposite effects on the MRI properties, and gives higher reliability across vendors (Gracien et al. 2020; Weiskopf et al. 2013). In line with this thinking, when we inspected 200 μm isotropic resolution ex vivo quantitative T_2 images we indeed found a bright region inside the dark substantia innominata that seemed to correspond to the nbM. If correct, this would be, to our knowledge, the first ever MRI image in which the human nbM is identified. By contrast, in weighted datasets with even higher resolution (100 μm isotropic) (Ding et al. 2016; Edlow et al. 2019), the nbM was not visibly distinct from the substantia innominata. We also examined our own T_1 maps acquired

in vivo by MP2RAGE (Marques et al. 2010) at 0.65 mm isotropic from four participants. We observed a bright area inside the substantia innominata in each participant, which might point to the location of nbM. However, the contrast was too weak and the signal was too diffuse for us to reliably quantify or make strong claims about the individual location or size of nbM. Despite this, we found this data encouraging. It seems that the current state of technology allows nbM to be imaged at the most extreme and cutting edge method (9.4T, ex vivo) or 'nearly' imaged using methods that are more feasible for regular studies. As technology keeps evolving, we are hopeful that visualisation of nbM in vivo will be possible in the (near) future. Future research should consider the effects of different MR contrasts on nbM for visualisation. Until it becomes feasible to individually image nbM in every participant, an MRI-based atlas will be beneficial. Considering the variability of nbM across the lifespan, large cohort studies at ultra-high fields may use multiparametric imaging techniques at high spatial resolutions either in vivo or ex vivo across a wide age range. Once we have these high-quality dataset, we can combine human-expert labelling, machine learning, and deep learning algorithms to construct a novel nbM template (Casamitjana and Iglesias 2022).

5.3 Investigation on neuronal correlates of surface perception

5.3.1 Summary

In Chapter 2, we concluded that MRI investigation of the function of the nbM is still beyond the scope of current technology, although it may be on the horizon. Our second goal was to investigate the cortical mechanisms of surface perception with the intention to leverage laminar functional scans to compare feed-forwared and feedback models of surface perception.

There has been an ongoing debate about the role of the early visual cortex in the processing of surface properties. The receptive field prop-

erties of neurons in the retina and in early cortical areas are well suited to represent local contrast edges, but are less well suited to represent homogeneous patches. Thus, it is clear that surface boundaries can be represented, but less clear how surface interiors may be represented. In the domain of surface brightness perception, conclusions from various studies have also not been consistent. Some animal studies support the idea that neurons in V1 (Kinoshita and Komatsu 2001; Komatsu et al. 2000; Komatsu et al. 2002; MacEvoy et al. 1998; McCourt and Foxe 2004; Rossi and Paradiso 1999; Rossi et al. 1996), or V2 (Hung et al. 2007; Roe et al. 2005) respond to changes in in the perceived brightness of surfaces. The findings of human neuroimaging studies on the subject are more varied. Boucard et al. (2005) and Cornelissen et al. (2006) did not observe an fMRI correlate of brightness induction. Boyaci et al. (2007) found a correlate of brightness induction restricted in V1-V3 while Van de ven et al. (2012) reported a correlate of brightness induction restricted to V2. However, Perna et al. (2005) only found relevant signals to brightness in higher order areas. Considering these conflicting findings among various studies, we revisited the question of surface brightness perception in Chapter 3 using a luminance induction paradigm at 7T fMRI with submillimetre resolution. 7T scanning could be important to this discussion given the possibility for higher resolution and higher SNR. Moreover, robust responses to surface features in this dataset would not only allow us to support or refute previous findings, but would also allow us to make layer-specific estimates of the signal, which might indicate source of the modulation (feedback, feedforward or horizontal).

We used a stimulus where a grey central rectangle probe was surrounded by either a black or white inducer. In offline psychophysics, we found a robust influence of the inducer luminance on the perceived brightness of the probe. In the scanner, we used a block design with separate conditions for black and white inducers with long fixation periods before and after. To estimate the cortical response, we calculated temporal response in BOLD signal change for two luminance conditions in 9 ROIs: 3 stimulus areas (inducer, probing region and edge) x 3 visual

areas (V1, V2, V3). Across spatial ROIs we observed strong cortical responses in V1 and V2 corresponding to the area with luminance change (inducer) and luminance induced contrast (edge). The cortical response to luminance changes in inducer representations were found only for luminance decrement. We also grouped the response temporally into positive-dominant BOLD (Early), post-stimulus undershoot (Late) and recovery periods (End). In the Early response, we observed opposite signs of BOLD signal change for luminance decrement in cortical areas (V1, V2, V3 combined) corresponding to the inducers and probing region representations (averaged over V1, V2 and V3). Especially, it induced a non-significant trend towards a positive BOLD response in the V1 representation of the probing region, paired with a significant negative response in the inducer representations. In the Late response, we also found stronger BOLD signals in the inducer and probing region than in the edge, which might indicate additional cortical processing in these regions. Our results only provide very weak or suggestive evidence for the idea that the early visual cortex is involved in the processing of surface brightness in the brightness induction paradigm we used.

The lack of solid evidence for a correlate of brightness induction may be due to various issues, including a lack of statistical power, which may have been insufficient to draw the small cortical response in the probing region out of the noise. In addition, there were strong asymmetries in the cortical responses to the inducer up- and down-luminance manipulations, which may underlie the asymmetry in the trends in brightness induction responses.

5.3.2 Limitations and outlooks

Our experimental design was inspired by the experimental paradigm from Van de ven et al. (2012). They utilised a paradigm that was likely more efficient for brightness induction than the slow single-event design from Cornelissen et al. (2006). However, due to the limited stimulus display size in the 7T scanner, we used a smaller rectangle stimulus. One advantage of the annular design from Van de ven et al. (2012) was

that the psychophysical performance could be linked with eccentricity whereas in our stimulus, we did not know which part of the stimulus participants used to make their judgement of induced brightness, so it cannot be ruled out that the illusion was generated mostly in the peripheral parts of the stimulus. However, there may also be a benefit of using a rectangle stimulus at 7T fMRI visual experiments according to a recent study (Kurzawski et al. 2022) which showed a higher BOLD response along the representation of the horizontal meridian than the vertical meridian at 7T fMRI. A further limitation of our study was that the fixation task in our experiments was not very engaging and could not be considered as a task that requires continuous accurate fixation. Thus, regular fixation breaks could have compromised the data. Moreover, to obtain a BOLD response with a complete HRF shape, we included a relatively long fixation block in between the stimulus blocks. This prolongs the duration of scanning time and can cause fatigue in participants, which further influences the quality of the data. In addition, although we ensured in psychophysical experiments that the up and down luminance inducer manipulations led to comparably sized (opposite) brightness induction in the probing region, this was not reflected in our fMRI data. Moreover, we found that there was a corresponding asymmetry in the responses to the inducers themselves. Furthermore, the mean luminance of each stimulus block was different due to the luminance change in the inducers. This mean luminance change may induce cortical response in the probing region and so cancel the responses to illusory surface changes. Last but not least, it could be that the simultaneous contrast illusion used in Chapter 3 was not strong enough to induce a large cortical response. In retrospect, it would have been better to first conduct the study with supra-millimetre resolution at 3T or 7T using the stimulus we planned to use at 7T to first observe the main effects of interest. Only later, we would then have moved to a laminar study. Lastly, given the small effects, it can be argued our study was underpowered. At the same time, at the completion of the analysis of the data collected, it became clear that a larger set of participants would not have solved the various issues with the stimulus and the experimental design that we have identified here.

In addition to limitations to the experimental design and stimulus, there may also be room for improvement of the scanning protocol. In 7T scanning, we trade off the increased SNR for higher resolution (along with an increase in thermal noise). Moreover, the BOLD signal scales with voxel volume at higher fields, thus going to sub-millimetre resolution may have prevented us from detecting the small signal related to brightness induction (Barth and Poser 2011). Another factor to consider is that 7T had more B1 inhomogeneities and lack of correcting inhomogeneity in the B1 field may result in a low SNR and uneven contrast (Vaughan et al. 2001). Future studies could use dielectric pads or acquire SA2RAGE (Eggenschwiler et al. 2012) to correct the B1 field. A recent advancement is to apply multi-echo imaging (acquiring multiple images with different echo times) in resting-state, task-based fMRI and diffusion MRI (Eichner et al. 2020; Heunis et al. 2021). By combining multiple images from different echo times, it has shown improved SNR, tSNR, functional contrast, functional connectivity, percent signal change (between task and baseline), increased spatial resolution and better control over distortion in multi-echo imaging than single-echo imaging (Chen and Wyrwicz 1999; Cohen et al. 2021; Heunis et al. 2021; Kundu et al. 2017; Poser and Norris 2009; Posse et al. 1999). Since T_2^* is short at UHF, multi-echo BOLD could be challenging at 7T. By comparing single echo and multiecho gradient-echo EPI for task fMRI at 3T, (Fazal et al. 2022) reported significantly higher statistics and more active voxels for multiecho acquisition in the motor, subcortical and medial frontal cortex. A long T_2^* at 3T could also be feasible to acquire high-resolution fMRI data. However, the study suggested multiecho could be a preferred protocol in task fMRI at resolution of above 2 mm isotropic. A recent work from Kashyap et al. 2022 (unpublished) achieved high-resolution (1.5 mm isotropic) using multi-echo fMRI at 3T combined with NORDIC PCA-based denoising (Moeller et al. 2021) techniques. Hence, a multi-echo BOLD fMRI with 1.5 mm isotropic at 3T could be a good start for any new study into the cortical processing of surface brightness. For further investigation at 7T, future research can consider the 2D sequential multi-echo passband sequence from Liang et al. (2022), which has shown submillimetre

in-plane acquisition without tSNR penalty.

BOLD-fMRI has been considered as an indirect measurement for neuronal activity with limited spatial and especially temporal resolution (Logothetis 2008). Studies have shown that BOLD signals correlates with cortical local field potential (LFP, integration of population post-synaptic potentials and integrative soma-dendritic process) (Logothetis 2008). Recently, Toi et al. (2022) were able to directly image neuronal activity with millisecond precision on mouse at 9.4T fMRI by using a two-dimensional fast line-scan approach. This is game-changing for noninvasive neuroimaging BOLD-fMRI. With the advantages of whole brain noninvasive neuroimaging and direct measurement of neuronal activity, it provides great potential for BOLD-fMRI in the future research. It is also easier to compare and correlate results between fMRI and electrophysiology studies. With such technical development, it will soon benefit the investigation of small cortical responses such those that are expected in response to brightness induction.

5.4 Developing a novel stimulus to manipulate perceived brightness without modulating luminance

5.4.1 Summary

The central finding of Chapter 3 was of weak or absent response to changing perceived surface properties. In addition, another challenge in Chapter 3 was dissociating responses caused by perceptual change in brightness from responses caused by changes in the (mean) luminance of the stimulus. In order to meet these challenges with a new stimulus, in Chapter 4, we used online psychophysics experiments to investigate the characteristics of Anderson and Winawer ' s brightness illusion stimulus, which has been reported to be the strongest brightness illusion ever described (Poiriehr 2009). In this illusion, identical textured probe surfaces appear as either black or white surfaces behind a veil of light or dark clouds, depending on the mean brightness of the textured veil.

In addition to the magnitude of the brightness induction, described as dramatic, a powerful control stimulus can be created by rotating the surround. In this manipulation, the illusion can be eliminated by breaking the geometric alignment of the texture in the probe with the texture in the surround. Thus, different perceptions can be induced, without a change to the overall luminance of the stimulus or the exact arrangement in the probe region.

In order to maximise the brightness illusion, we first parametrically investigated the properties of this stimulus in small pilot measurements. Based on these measurements we selected a spatial frequency filter and texture contrast level for use in the main experiments. Since these experiments coincided with the start of the 2020 to 2022 COVID pandemic, we conducted them using online psychophysics. Our main interest in these experiments was investigating the possibility to reduce the difference of mean luminance between the dark and light probe conditions. Thus, we investigated whether the illusion could be induced by changing the luminance in the inducer only in the region just outside the edge of the probe rather than by changing the luminance in the whole background, thereby minimising the overall luminance difference between light and dark appearing stimulus conditions. In the online experiments, using our optimised stimulus settings, we found an equal level of illusory perception for both the full background 'standard' stimulus and our novel 'narrow pedestal' stimulus. However, the measured illusory effect was small for both stimuli and neither of the control conditions did not fully replicate the reported rotation effect of completely nullifying the illusion. In follow up online experiments, we tested whether larger effect sizes (for both perceived brightness and of rotation) could be obtained with different stimulus parameters or behavioural paradigms but we found again small effects in all of our tests.

5.4.2 Limitations and outlooks

The weaker effects that we observed compared to previous literature (Anderson and Winawer 2005) could be due to the less controlled environmental setup of online experiments (non-calibrated monitors, no control of eye-to-screen distance, natural lights environment and so on) and the different stimulus setup (static presentation and rotating target) in our study compared to previous reports. Thus, we concluded that further psychophysics testing would be needed in the lab. Nevertheless, this work allowed us to explore the stimulus properties and learn to make appealing stimuli, which at least subjectively appear to yield strong brightness illusions.

Since the end of COVID restrictions it has been possible to make use of the labs. A recent study from our group was conducted to investigate cortical responses to luminance and brightness with EEG using the similar stimulus setting as our online experiments. Participants performed the behavioural experiments in the psychophysics laboratory and reported strong illusory effects, with a mean PSE of 0.24, compared to $\sim$0.1 in online measurements. Moreover, in an oddball detection task participants were unable to discriminate between probes defined by luminance and probes defined by brightness. Following our online experiments, and subsequent confirmation in the lab, the control stimuli were untextured grey patches rather than rotated texture patches. For these stimuli, participants could readily identify oddballs with otherwise identical settings to the textured stimuli. Using EEG, this study compared the steady-state-ERP for alternating luminance (with no change in brightness), alternating brightness (with no change in luminance) and alternating luminance and brightness. Interestingly, the response to alternating brightness with or without alternating luminance was not statistically different in occipital electrodes. In contrast, frontal electrodes showed higher response when the change in brightness was induced by the illusion than when it was induced by changing luminance, which could indicate a potential involvement of higher-order processing when viewing brightness illusions.

For future experiments, the untextured grey patches will not be an ideal control stimulus. The difference between a brightness induction condition and its ideal control stimulus should only be the presence or absence of the brightness illusion. But homogeneous patches and textured patches have different bottom-up input to the cortex. Therefore, future investigations should explore whether the rotation effect of Anderson and Winawer stimulus (for both original full background luminance manipulation and our novel setup) can be replicated in the psychophysics laboratory. If the rotation effect is compelling, it will provide a powerful control stimulus that has no luminance difference with the illusory condition and has a similar bottom up input to the cortex. With the strong illusory effect and powerful control stimulus, it will be beneficial to induce stronger cortical responses and further investigate the underlying neuronal mechanisms. To reduce the fatigue of participants during the long scanning, future studies may also consider slightly more engaging fixation tasks and acquiring multiple shorter functional runs. From our experience described in Chapter 3, we would suggest adopting a paradigm similar to Van de ven et al. (2012)' s study, in which the probe stimulus was presented away from fixation. The texture stimulus presents an additional factor that must be carefully controlled to avoid introducing a confound. Thus, the regions of dark and light texture should be carefully arranged and counterbalanced across conditions. An additional interesting feature that we observed in both Chapters 3 and 4 was the asymmetric response to luminance decrement and increment. Similar results have also been reported elsewhere (Haynes et al. 2004; Taylor et al. 2018; Xing et al. 2014; Yang et al. 2022). Our behavioural results in Chapter 3 and Pereverzeva and Murray (2008) both showed that base luminance affected the strength of the brightness illusion. This could imply that luminance changes in one of the two directions are primarily responsible for brightness induction. It is also possible that the psychophysics performed outside the scanner is less likely to be valid inside the scanner due to the use of different displays. To reduce the asymmetry in a future neuroimaging experiment, a staircase phase could be added to determine a proper base luminance for each participant so that the illusory effect from both luminance con-

ditions can be equally strong. Particularly, this can be arranged during the acquisition of structural images to save the scanning time. If participants cannot remain still while performing the staircase experiment, it should be arranged before the beginning of the scan while participants lie in the scanner.

5.5 Concluding remarks

This thesis set out to make use of cutting edge fMRI methods to address current questions in cognitive neuroscience. Overall it seems that our ambition was beyond what is currently feasible. This was especially so in Chapter 2, where we showed that accurately imaging the nbM is not yet feasible. This has important implications for interpreting the current literature of (f)MRI in the nbM. While this literature shows interesting trends, it is likely that a substantial contribution of the signal that is ascribed to the nbM (on the basis of atlas, or probabilistic map) in fact represented tissue outside of the nbM. We advocated a more cautious approach of using advanced contrasts, adapted to the region of interest, to individually identify the nbM on structural scans. While the technology to do this is not yet readily available, we are optimistic for future projects. In Chapter 3 we addressed what we thought was a more tractable problem in the cortex. While we anticipated being able to replicate findings from a previous 3T experiment at 7T, while acquiring higher spatial resolution and SNR, we found that the response was weak or absent. We suggest several possible avenues for future projects to investigate surface perception in the early visual cortex, including adapting the scanning protocol and making use of novel stimuli, such as those described in Chapter 4.

In summary, our projects aimed to explore brain function using functional neuroimaging at UHF. UHF presents great opportunities to tackle the fundamental questions in the field. However, high-resolution/sub-millimetre neuroimaging at UHF is still a young and rapidly developing field, where in order to enable investigating cognitive neuroscience questions, there are more technical challenges to be

addressed than just maximising high spatial resolution. For example, tailoring MR contrast to the region of interest may be essential to visualise the structure of interest. In addition, having a valid and reliable anatomical reference is a crucial basis for later structural and functional analysis. Experimental paradigm, environment settings, data measurement, analysis, and quality control all affect the final conclusion. Learning from negative findings (Taragin 2019) is important during the scientific process, as it helps us to improve the experimental design and analysis, to avoid subjective bias, and to inspire new hypotheses.

Summary

This thesis contains three empirical studies, which describe our journey of trying to investigate the neuronal mechanism of attention and surface perception using functional magnetic resonance imaging at ultra-high field (UHF). The cholinergic system has an essential role in mediating attentional control. Thus, our interest was drawn to the source of cortical acetylcholine; the nucleus basalis of Meynert (nbM). The initial plan was to test for functional specialisation within the nbM, first by comparing activation patterns during auditory and visual attention, using 7T fMRI. However, this plan was abandoned after collecting datasets from 8 participants (half of them had two scanning sessions) due to difficulties in accurately defining the region of interest for the nbM in those datasets using the existing atlases. As a result, the project turned to an examination of the methods and limitations of previous MRI studies that attempted to localise the nbM, as well as potential ways to improve upon them. The findings in Chapter 2 showed that the reported volume of the nbM varied greatly depending not only on the atlas and threshold used, but also among datasets using the same atlas and threshold. To test the effect of spatial resolution on volume variability, we created a novel mask based on the BigBrain dataset. It was found that the variance of the estimated nbM volume increased dramatically for voxel sizes above 1.3 mm isotropic but not for datasets with higher resolutions (0.1 - 1.3 mm isotropic). It will likely always be challenging to apply a mask that was defined originally in histological space from one (or more) brain(s) to MR images of other brains. One potential solution to this issue could be to directly delineate the nbM from each individual MRI dataset. To evaluate this possibility, we explored publicly available and novel high-resolution MRI ex vivo datasets. We found that the nbM could be visualised in the quantitative T_2^* dataset acquired at 9.4 T with 200 μm isotropic resolution. As technology continues to advance, we are increasingly optimistic that we

will be able to visualise the nbM and investigate its function in vivo in the (near) future.

Given that our work in Chapter 2 suggested that accurate fMRI measures in the nbM were not (yet) feasible, we next addressed what we considered to be a more tractable problem in the cortex. Specifically, we used 7T fMRI to investigate the role of the early visual cortex in surface perception. Previous work at 3T in our group had shown a significant fMRI signal in V2, and a trending signal in V1, related to perceived surface brightness. Re-examining these findings at 7T could clarify the pattern in V1, and crucially could allow us to make statements about the laminar organisation of the response. In Chapter 3, we used a brightness induction paradigm with uniform surfaces, wherein decreasing luminance in a surrounding stimulus (inducer) induces an illusory increase in brightness of a physically constant centre stimulus (probing region). Increasing the luminance of the inducer induces a perception of decreased brightness of the probe. We grouped the temporal response into positive-dominant BOLD (Early), post-stimulus undershoot (Late) and recovery periods (End). For the Early response, we found that luminance decrement of the inducer induced a significant negative response in the inducer representations and a non-significant trend towards a positive BOLD response in the V1 representation of the probing region. In the Late response, we found stronger BOLD signals in the inducer and probing representations than in the edge representation, which might indicate additional cortical processing in these regions. However, while these effects were interesting, the overall pattern in this study was of weak or absent responses for the probing region. Furthermore, we found no response in the inducer representation in the luminance increment condition. Thus, we did not find clear evidence supporting a neural mechanism of brightness induction in the early visual cortex.

In addition to the weak response, another challenge in Chapter 3 was dissociating responses caused by perceptual change in brightness from responses caused by changes in the (mean) luminance of the stim-

ulus, since these two factors are necessarily confounded in the simultaneous contrast illusion. Modulation of luminance in the inducer in Chapter 3 creates different mean luminance during the different stimulation blocks and compared to the fixation periods, which may lead to responses in the cortical representation of the probing region through scattering of light around the MRI bore and in the eye. In order to meet these challenges with a new stimulus, in Chapter 4, we used online psychophysics experiments to investigate the characteristics of Anderson and Winawer' s brightness illusion stimulus. In this illusion, identical textured probe surfaces appear either as either black or white surfaces behind a veil of respectively either light or dark clouds, depending on the mean brightness of the textured surrounding region. In addition, this illusion can be nullified by breaking the geometric alignment of the texture in the probe with the texture in the surround. This means that the illusion can be manipulated without a change in the luminance properties of the stimulus. Given these features, and the fact that Anderson and Winawer described the induction illusion in their stimulus as very powerful, we considered that their stimulus could be a useful tool for future fMRI research, and we wished to investigate it further. In our own version of the Anderson & Winawer stimulus, we found that the illusory perception could also be induced by only manipulating the luminance of a small region of the inducer near to the probing region' s border, thus minimising the overall luminance difference between light and dark appearing probe conditions. However, the measured illusory effect was small for both the full-background manipulation (as used by Anderson and Winawer) and our novel narrow inducer manipulation. We tested whether larger effect sizes could be obtained with different stimulus parameters or behavioural paradigms in a series of online experiments. Nonetheless, all of our tests showed small illusory effect sizes, hence we could not replicate the large effects reported by Anderson and Winawer in online experiments. We believe nevertheless that Anderson and Winawer' s stimulus is promising, and that larger effect size may be obtained in further psychophysics testing in the lab.

In summary, the studies in the present thesis aimed to explore brain

function using functional neuroimaging at UHF. The work indicates what the boundaries are of what is possible in contemporary UHF-fMRI, and how important it is to optimise experimental and stimulus design to make maximal use of the current possibilities. At the same time, there are indications in the reported data that, with ongoing and further developments of the technology, a deeper understanding of the neural mechanisms of attention and of surface perception will be achieved.

Samenvatting

Dit proefschrift bevat drie empirische studies, die onze reis beschrijven door het onderzoek dat we deden over de neuronale mechanismen van aandacht en oppervlakte perceptie. Voor dit onderzoek maakten we gebruik van psychofysica en van functionele magnetische resonantie beeldvorming met ultrahoog veld (UHF). Het cholinerge systeem speelt een essentiële rol bij het mediëren van aandachtscontrole. Zo werd onze interesse getrokken naar de bron van corticale acetylcholine; de nucleus basalis van Meynert (nbM). Het eerste plan was om voor functionele specialisatie binnen de nbM te testen door activatiepatronen tijdens auditieve en visuele aandacht te vergelijken met behulp van 7T fMRI.Dit plan werd echter opgegeven na het verzamelen van datasets van 8 deelnemers (de helft van hen had al twee scansessies) vanwege moeilijkheden bij het nauwkeurig definiëren van nbM anatomische locatie in die datasets met behulp van de bestaande atlassen. Als gevolg hiervan besloten we om een onderzoek uit te voeren naar de methodes en beperkingen van eerdere MRI-onderzoeken die rapporteerden de nbM gelokaliseerd te hebben, en naar mogelijke manieren om nbM lokalisatie te verbeteren. De bevindingen in Hoofdstuk 2 toonden aan dat het gerapporteerde volume van de nbM sterk varieerde, niet alleen afhankelijk van de gebruikte atlas en drempelwaarde, maar ook tussen datasets die dezelfde atlas en drempelwaarde gebruikten. Om het effect van spatiële resolutie op volume variabiliteit te testen, hebben we een nieuw masker gemaakt op basis van de BigBrain-dataset. Het bleek dat de variantie van het geschatte nbM-volume dramatisch toenam voor voxelgroottes groter dan 1,3 mm isotroop, maar niet voor datasets met hogere resoluties (0,1 - 1,3 mm isotroop). Het zal waarschijnlijk altijd een uitdaging blijven om een masker toe te passen dat oorspronkelijk in de histologische ruimte van één (of meer) hersenen werd gedefinieerd op MR-beelden van andere hersenen. Een mogelijke oplossing voor dit probleem zou kunnen zijn om de nbM direct af te bakenen in elke in-

dividuele MRI-dataset. Om deze mogelijkheid te evalueren, hebben we openbaar beschikbare en nieuwe hoge resolutie MRI ex vivo datasets onderzocht. We ontdekten dat de nbM kon worden gevisualiseerd in de kwantitatieve T_2^*-dataset verkregen bij 9,4 T met een isotrope resolutie van 200 μm. Naarmate de technologie zich verder ontwikkelt, zijn we steeds optimistischer dat we in de (nabije) toekomst de nbM kunnen visualiseren en de functie ervan in vivo kunnen onderzoeken.

Gezien het feit dat ons werk in Hoofdstuk 2 suggereerde dat nauwkeurige fMRI-metingen in de nbM (nog) niet haalbaar waren, hebben we ons vervolgens gericht op een vraagstelling waarvan we verwachtten dat die wel met 7T fMRI kon beantwoord worden. In deze studie was het ons doel om 7T fMRI te gebruiken om de rol van lagere visuele corticale gebieden in oppervlakte perceptie te onderzoeken. Eerder 3T werk van onze groep had een significant fMRI-signaal in V2 en een data trend in V1 aangetoond gerelateerd aan waargenomen veranderingen in helderheid van een oppervlak geïnduceerd door luminantie-veranderingen in nabije oppervlakken. We hadden meer bepaald als doel om de V2 data te repliceren, de data trend in V1 nader te onderzoeken, en uitspraken te doen over de laminaire organisatie van de respons. In Hoofdstuk 3 gebruikten we een helderheid inductie paradigma met uniforme oppervlakken, waarbij afnemende luminantie in een omringende stimulus (inducer) een illusoire toename in helderheid van een fysiek constante centrum stimulus (probing region) induceert. Het verhogen van de luminantie van de inducer induceert een perceptie van verminderde helderheid van de probing region. We hebben de temporele responsen gegroepeerd in een positief-dominante BOLD respons (Vroeg), een negatieve post-stimulus BOLD response(Laat) en een herstelperiode (Einde). Voor de vroege respons vonden we dat een afname van luminantie van de inductor een significant negatieve respons veroorzaakte in de representaties van de inductor en een niet-significante trend naar een positieve BOLD-respons in de V1-representatie van het onderzoeksgebied. Bij de Late respons vonden we sterkere BOLD-signalen in de inductor- en onderzoeksrepresentaties dan in de

rand representatie, wat aangeeft dat er additionele cortexverwerking plaatsvindt in deze gebieden. Maar hoewel deze effecten interessant waren, was het algehele patroon in deze studie van zwakke of afwezige responsen voor het onderzoeksgebied. Bovendien vonden we geen respons in de representatie van de inductor in de luminantie toename conditie. Dus vonden we geen duidelijk bewijs voor een neurale mechanisme van helderheids-inductie in de vroege visuele cortex.

Naast de zwakke respons was een andere uitdaging in Hoofdstuk 3 het onderscheiden van responsen verband houdend met inductie in de probing region, en responsen verband houdend met veranderingen in de (gemiddelde) luminantie van de stimulus als geheel, omdat deze twee factoren noodzakelijk samenhangen in de simultane contrastillusie. De modulatie van luminantie in de inducer leidt tot een verandering in de gemiddelde luminantie van de stimulus als geheel tijdens de verschillende stimulatie-blokken en in vergelijking met de fixatieperiodes. Dat kan leiden tot fMRI responsen op de luminantieverandering in de inductiegebienden van de stimulus in de corticale representatie van de probing region door verstrooiing van licht in de scanner en in het oog. Om deze uitdagingen in de toekomst het hoofd te bieden, hebben we in hoofdstuk 4 online psychofysische experimenten uitgevoerd om de kenmerken van de helderheidsillusie-stimulus van Anderson en Winawer te onderzoeken. In deze illusie worden oppervlakken aangeboden die versluierd zijn achter witte of donkere wolken. Het centrale oppervlak (de probing region) wordt als lichter of donkerder ervaren afhankelijk van de gemiddelde luminantie van het gestructureerde omringende gebied. Deze illusie wordt teniet gedaan door de geometrische uitlijning van de textuur in de probing region met de textuur in het omliggende oppervlak te verbreken. Dat betekent dat de illusie kan gemanipuleerd worden onafhankelijk van de luminantie in de verschillende delen van de stimulus. Gezien deze stimuluskenmerken waren we van mening dat de stimulus van Anderson en Winawer een krachtig hulpmiddel zou kunnen zijn voor toekomstig onderzoek, en we wilden dit verder onderzoeken. Met onze eigen versie van Anderson en Winawer' s stimulus, ontdekten we dat de illusoire helderheid verandering in de probing region ook

kan worden geïnduceerd door alleen de luminantie van een klein gebied van de inducer rondom de probing region te manipuleren. Dit biedt additionele perspectieven om manipulaties van helderheid inductie uit te voeren met minimale luminantie veranderingen in de stimulus. Het gemeten illusoire effect in onze studie was echter klein voor zowel inductie via luminantie manipulaties van de volledige achtergrond, als voor luminantie manipulaties beperkt tot de onmiddellijke omgeving van de probing region. In een reeks online experimenten hebben we getest of grotere effecten konden worden bereikt met verschillende stimulus parameters of gedrags paradigma's. Ondanks onze inspanningen vonden we in alle experimenten slechts kleine illusoire effecten. Wij beschouwen Winawer en Anderson's stimulus nog steeds als een veelbelovende stimulus voor toekomstig fMRI onderzoek. Het online onderzoek suggereert wel dat de psychofysische experimenten in een gecontroleerde laboratoriumomgeving moeten gedaan worden om de oorspronkelijk gerapporteerde grootte van de illusie de repliceren.

Samenvattend waren de studies in deze thesis gericht op het onderzoeken van de hersenfunctie met behulp van functionele neuroimaging bij UHF. Het werk geeft aan wat de grenzen zijn van het mogelijke in hedendaagse UHF-fMRI studies, en hoe belangrijk het is om het experimentele en stimulus ontwerp te optimaliseren om het maximale gebruik te maken van de huidige mogelijkheden. Tegelijkertijd zijn er aanwijzingen in de gerapporteerde gegevens dat, met voortgaande en verdere ontwikkelingen van de technologie, een dieper begrip van de neurale mechanismen van aandacht en oppervlakte beleving zal worden bereikt.

Valorisation

The practice of science may be restricted to certain groups of people, but the knowledge produced should belong to the public. The work presented in this thesis contains methodological development of atlas-based volumetry of the human nucleus basalis of Meynert (nbM) in neuroimaging studies, hypothesis testing on surface brightness perception in the early visual cortex using 7T fMRI, and experimental development of potential brightness illusion stimuli for future neuroimaging research. All of these efforts aim to answer some open questions in modern neuroscience. The findings may be mostly of interest to those members of the scientific community who share similar interests in the topic, and will have the most straightforward application for their own research. Individuals from the general public with a keen interest in the topics we cover may also be interested in our research, especially as the projects that are initiated in this thesis continue to develop in the future.

It has been well established that cellular loss of the nbM correlates with cognitive decline in dementing disorders such as Alzheimer's disease and is also a feature of Parkinson's disease. However, investigating the nbM with neuroimaging is challenging since the nbM is not visible in in vivo neuroimaging data due to the lack of MR contrast and its small size, therefore the definition of nbM in previous studies has heavily depended on an existing atlas. The accuracy of the definition of the region of interest (ROI) influences the accuracy of volumetric or functional measurements for the nbM. With an increasing number of neuroimaging studies focusing on structural changes of the nbM in patients and the functioning of the nbM in healthy groups, there is a pressing need to revisit the localisation of the nbM in these neuroimaging studies. In Chapter 2, we reviewed the human nbM ROI selection protocols used in recent MRI studies. We found a distinct lack of reporting nbM volume with meaningful physical units. Among studies

that did report the nbM volume with a physical unit, we found highly variable volume estimates. This variability could be due to the atlas used and the probabilistic threshold set, but also existed in studies using the same atlas and threshold. More importantly, we discovered that the accuracy of atlas-based volumetry is reduced when the atlas is applied to datasets with a much lower spatial resolution (1.3 mm isotropic and above). In addition to helping to interpret previous studies, this is especially critical information for future nbM (f)MRI studies, as the field moves towards higher resolution acquisition. It is then critical that researchers avoid analysis that converts high-resolution to much lower resolution, for example, 1.5 mm isotropic in standard MNI space from SPM DARTEL toolbox, 2/3 mm isotropic in functional space. While atlas-based methods have their limits, we have to acknowledge the fact that the nbM is still not visible in in vivo datasets despite the advancement of ultra-high field neuroimaging. By exploring ultra-high resolution post-mortem datasets, we showed that the nbM could be visualised on quantitative T_2^* dataset with 200 µm isotropic. To our knowledge, this is the first attempt to investigate which MR contrast would be beneficial to visualise this structure. This knowledge can be used in two ways: in the short-to-medium term it will be possible to build an nbM template based on ultra-high resolution post-mortem MR datasets to replace the existing nbM atlases created from a post-mortem T1 weighted dataset with close to 1.0 mm isotropic. Such an atlas could be especially relevant as the availability of submillimetre resolution (f)MRI (for which applying an atlas from lower resolution datasets is especially problematic) in daily research increases. In the longer term, with increasing advancement in MRI technology and techniques, it may eventually become possible to make individual in-vivo structural scans of the nbM for structural and functional investigations. Given the importance of the nbM in cognition, there will be future research focusing on its structure and function, on clinical application and on methods development for better study. Our efforts in Chapter 2 lay the groundwork and provide a potential vision for relevant studies in the future.

We next studied visual processes in the cortex, again using 7T fMRI. Our visual experience of the world is dominated by surfaces. However our understanding of the neuronal mechanisms of vision emphasises the processing of contrast edges. Exactly how our perception of surface interiors arises has been vigorously debated for over a century. In Chapter 3, we found a non-significant trend towards a positive early (corresponding to the positive-dominant BOLD averaged across 3 TRs) fMRI signals in the V1 representation of the probing region during luminance decrement of the inducer. In literature, there has been an ongoing debate about whether the early visual cortex participates in the processing of surface brightness. Although our results do not settle the debate, our efforts in Chapter 3 could be beneficial to future studies on the same topic. Our design was an adapted version from Van de ven et al. (2012) and was designed to be efficient in brightness induction and allow studying the cortical responses in each ROI for each luminance condition separately. Future investigations may consider using this, or a similar experimental design to uncover new information on cortical processing and the temporal response associated with surface processing. Meanwhile, we observed multiple temporal responses in different retinotopic regions for each luminance condition. This could imply different hemodynamic response function models in the region, which could suggest a different analysis procedure. We also suggest that future studies take the asymmetric responses of luminance increment and decrement into consideration. An effective method to balance the perception of the two luminance conditions is needed, for example, a staircase experiment could be arranged while the participant lies in the scanner before the experiment. Data quality is essential to the investigation of small cortical responses, such as the responses we observed in Chapter 3. In future studies, measures should be taken to improve the data quality. To reduce the effect of B1 inhomogeneity to data quality at 7T, one can use a dielectric pad during the acquisition or acquire SA2RAGE to correct the B1 map. Additionally, researchers should be aware of the asymmetric temporal signal-to-noise ratio (tSNR) between the two hemispheres for 7T fMRI experiments. Last but not least, our experience indicates that it would be wise to conduct a pilot experiment

with larger voxel size, either using 7T or 3T, to test the design before moving to the submillimetre resolution.

An additional avenue to explore in future investigations of surface perception is to use as powerful a stimulus as possible. To set up an experimental stimulus capable of inducing strong illusion for use in future investigations, in Chapter 4 we parametrically studied Anderson and Winawer' s textured stimulus and compared different testing methods using an online platform. The reason for using this stimulus is that it can produce dramatic illusions and allows a powerful control stimulus, generated by rotating the surround without changing the overall luminance. With the optimised stimulus, we discovered that the illusory perception can be induced by only varying the luminance of a small region of inducer near to the probing region' s border. Although the illusory effect from these experiments was small, and testing in the psychophysics laboratory will be necessary, it provides a new set up of stimuli that are potentially valuable for future behavioural and neuroimaging research. In our group there has already been an EEG study conducted using the stimulus developed in Chapter 4. It is a thrill to know that our work already inspires new research.

Although the findings from this thesis cannot be immediately translated into economic and practical applications, the process of scientific exploration could be intriguing to society. Nowadays, with the information explosion on the internet, we want to convey the message that the scientific community takes caution in the process of creating knowledge. Although each project has its own expectations, we did not let our expectations dominate the direction of our projects. Negative results can be personally upsetting, but the goal of the scientific endeavour is to pursue the objective truth and find new mysteries, rather than to force conclusions upon data that do not allow one to do so. Messages of caution, such as we give in our published work, are important in keeping the progress of science grounded in objective, observable phenomena. Thus, neuroimaging studies that suggest a shrinkage of the nbM associated with dementia

are in line with previous histological knowledge and appear valid, however the imaging methods used must themselves be valid for the work to add new knowledge. Furthermore, part of our projects studied the mechanisms of perception using illusory stimuli which produce a mismatch between the state of our perception and the actual sensory information. In addition to being interesting phenomena, these stimuli provide a powerful metaphor for a cautious approach to interpreting research findings. Thus, just as the brightness of two objectively identical surfaces may differ due to differences in the background, differences in the baseline during a neuroscience experiment can lead to apparently large differences between experimental conditions, even when none exist. Exciting research results, even and especially when they are in line with expectations, must therefore always be approached with scepticism and caution.

Finally, we are delighted to share our academic work with the scientific community and the public. This thesis and the work within has been or will be published in open access journals to facilitate accessibility to society. The publication is or will be accompanied by the release of analysis scripts and data that are necessary to perform the analysis. Projects have already been shared with research teams in Canada and France in order to promote science communication and collaboration. This may inspire future research and collaborations into the volumetry of subcortical structures and the neuronal mechanisms of surface perception.

Bibliography

Adelson, E. H. (1993). Perceptual Organization and the Judgment of Brightness. Science, **262**(5142), 2042–2044. DOI: 10.1126/science.8266102

Akkus, Z., Galimzianova, A., Hoogi, A., Rubin, D. L., & Erickson, B. J. (2017). Deep Learning for Brain MRI Segmentation: State of the Art and Future Directions. Journal of Digital Imaging, **30**(4), 449–459. DOI: 10.1007/s10278-017-9983-4

Albert, M. K. (2007). Occlusion, transparency, and lightness. Vision Research, **47**(24), 3061–3069. DOI: 10.1016/j.visres.2007.06.004

Albrecht, D. G., & Hamilton, D. B. (1982). Striate cortex of monkey and cat: Contrast response function. Journal of Neurophysiology, **48**(1), 217–237. DOI: 10.1152/jn.1982.48.1.217

Aldusary, N., Michels, L., Traber, G. L., Hartog-Keisker, B., Wyss, M., Baeshen, A., Huebel, K., Almalki, Y. E., Brunner, D. O., Pruessmann, K. P., Landau, K., Kollias, S., & Piccirelli, M. (2019). Lateral geniculate nucleus volumetry at 3T and 7T: Four different optimized magnetic-resonance-imaging sequences evaluated against a 7T reference acquisition. NeuroImage, **186**, 399–409. DOI: 10.1016/j.neuroimage.2018.09.046

Alkemade, A., Keuken, M. C., & Forstmann, B. U. (2013). A perspective on terra incognita: Uncovering the neuroanatomy of the human subcortex. Frontiers in Neuroanatomy, **7**. DOI: 10.3389/fnana.2013.00040

Alkemade, A., Mulder, M. J., Groot, J. M., Isaacs, B. R., van Berendonk, N., Lute, N., Isherwood, S. J., Bazin, P.-L., & Forstmann, B. U. (2020). The Amsterdam Ultra-high field adult lifespan database (AHEAD): A freely available multimodal 7 Tesla submillimeter magnetic resonance imaging database. NeuroImage, **221**, 117200. DOI: 10.1016/j.neuroimage.2020.117200

Alonso-Ortiz, E., Levesque, I. R., & Pike, G. B. (2018). Multi-gradient-echo myelin water fraction imaging: Comparison to the multi-echo-spin-echo technique. Magnetic Resonance in Medicine, **79**(3), 1439–1446. DOI: 10.1002/mrm.26809

Altmann, C. F., Bülthoff, H. H., & Kourtzi, Z. (2003). Perceptual Organization of Local Elements into Global Shapes in the Human Visual Cortex. Current Biology, **13**(4), 342–349. DOI: 10.1016/S0960-9822(03)00052-6

Amunts, K., Lepage, C., Borgeat, L., Mohlberg, H., Dickscheid, T., Rousseau, M.- ., Bludau, S., Bazin, P.-L., Lewis, L. B., Oros-Peusquens, A.-M., Shah, N. J., Lippert, T., Zilles, K., & Evans, A. C. (2013). BigBrain: An Ultrahigh-Resolution 3D Human Brain Model. Science, **340**(6139), 1472–1475. DOI: 10.1126/science.1235381

Amunts, K., Mohlberg, H., Bludau, S., Caspers, S., Eickhoff, S. B., & Pieperhoff, P. (2020). Whole-brain parcellation of the julich-brain cytoarchitectonic atlas (v2.0) [Data set]. EBRAINS. DOI: 10.25493/TAKY-64D

Amunts, K., & Zilles, K. (2015). Architectonic Mapping of the Human Brain beyond Brodmann. Neuron, **88**(6), 1086–1107. DOI: 10.1016/j.neuron.2015.12.001

Anderson, B. L. (1999). Stereoscopic Surface Perception. Neuron, **24**(4), 919–928. DOI: 10.1016/S0896-6273(00)81039-9

Anderson, B. L., & Winawer, J. (2005). Image segmentation and lightness perception. Nature, **434**(7029), 79–83. DOI: 10.1038/nature03271

Anderson, B. L., & Winawer, J. (2008). Layered image representations and the computation of surface lightness. Journal of Vision, **8**(7), 18. DOI: 10.1167/8.7.18

Ang, G. W. Y., Tang, C. S., Hay, Y. A., Zannone, S., Paulsen, O., & Clopath, C. (2021). The functional role of sequentially neuromodulated synaptic plasticity in behavioural learning. PLOS Computational Biology, **17**(6), e1009017. DOI: 10.1371/journal.pcbi.1009017

Anstis, S. White's effect in lightness, color and motion. In: In *Seeing spatial form*. 2006, p. 91.

Arendt, T., Bigl, V., Arendt, A., & Tennstedt, A. (1983). Loss of neurons in the nucleus basalis of Meynert in Alzheimer's disease, paralysis agitans and Korsakoff's Disease. Acta Neuropathologica, **61**(2), 101–108. DOI: 10.1007/BF00697388

Ashburner, J. (2007). A fast diffeomorphic image registration algorithm. NeuroImage, **38**(1), 95–113. DOI: 10.1016/j.neuroimage.2007.07.007

Ashburner, J., & Friston, K. J. (2005). Unified segmentation. NeuroImage, **26**(3), 839–851. DOI: 10.1016/j.neuroimage.2005.02.018

Ashida, H., & Scott-Samuel, N. E. (2014). Motion Influences the Perception of Background Lightness. i-Perception, **5**(1), 41–49. DOI: 10.1068/i0628

Atta-Ur-Rahman, T. I. (2012). *Nuclear magnetic resonance: Basic principles*. Springer Science & Business Media.

Avants, B., Tustison, N., & Song, G. (2009). Advanced Normalization Tools: V1.0. The Insight Journal, 681. Retrieved March 25, 2021, from http://hdl.handle.net/10380/3113

Avants, B. B., Tustison, N. J., Song, G., Cook, P. A., Klein, A., & Gee, J. C. (2011). A reproducible evaluation of ANTs similarity metric performance in brain image registration. NeuroImage, **54**(3), 2033–2044. DOI: 10.1016/j.neuroimage.2010.09.025

Bagnato, F., Hametner, S., & Welch, E. B. (2013). Visualizing iron in multiple sclerosis. Magnetic resonance imaging, **31**(3), 376–384. DOI: 10.1016/j.mri.2012.11.011

Ballinger, E. C., Ananth, M., Talmage, D. A., & Role, L. W. (2016). Basal forebrain cholinergic circuits and signaling in cognition and cognitive decline. Neuron, **91**(6), 1199–1218. DOI: 10.1016/j.neuron.2016.09.006

Barrett, M. J., Blair, J. C., Sperling, S. A., Smolkin, M. E., & Druzgal, T. J. (2018). Baseline symptoms and basal forebrain volume predict future psychosis in early Parkinson disease. Neurology, **90**(18), e1618–e1626. DOI: 10.1212/WNL.0000000000005421

Barth, M., & Poser, B. A. (2011). Advances in High-Field BOLD fMRI. Materials, **4**(11), 1941–1955. DOI: 10.3390/ma4111941

Beaulieu, C., & Allen, P. S. (1994). Water diffusion in the giant axon of the squid: Implications for diffusion-weighted MRI of the nervous system. Magnetic Resonance in Medicine, **32**(5), 579–583. DOI: 10.1002/mrm.1910320506

Beenen, G., Ling, K., Wang, X., Chang, K., Frankowski, D., Resnick, P., & Kraut, R. E. Using social psychology to motivate contributions to online communities. In: In *Proceedings of the 2004 ACM conference on Computer supported cooperative work*. CSCW '04. New York, NY, USA: Association for Computing Machinery, 2004, November, 212–221. ISBN: 978-1-58113-810-8. DOI: 10.1145/1031607.1031642.

Behnel, S., Bradshaw, R., Citro, C., Dalcin, L., Seljebotn, D. S., & Smith, K. (2011). Cython: The Best of Both Worlds. Computing in Science Engineering, **13**(2), 31–39. DOI: 10.1109/MCSE.2010.118

Bethlehem, R. a. I., Seidlitz, J., White, S. R., Vogel, J. W., Anderson, K. M., Adamson, C., Adler, S., Alexopoulos, G. S., Anagnostou, E., Areces-Gonzalez, A., Astle, D. E., Auyeung, B., Ayub, M., Bae, J., Ball, G., Baron-Cohen, S., Beare, R., Bedford, S. A., Benegal, V., (2022). Brain charts for the human lifespan. Nature, **604**(7906), 525–533. DOI: 10.1038/s41586-022-04554-y

Birnnbaum, M. H. (2000). *Psychological Experiments on the INTERNET*. Academic Press.

Bisley, J. W., & Goldberg, M. E. (2003). Neuronal Activity in the Lateral Intraparietal Area and Spatial Attention. Science, **299**(5603), 81–86. DOI: 10.1126/science.1077395

Bisley, J. W., & Goldberg, M. E. (2006). Neural Correlates of Attention and Distractibility in the Lateral Intraparietal Area. Journal of Neurophysiology, **95**(3), 1696–1717. DOI: 10.1152/jn.00848.2005

Blakeslee, B., & McCourt, M. E. (1999). A multiscale spatial filtering account of the White effect, simultaneous brightness contrast and grating induction. Vision Research, **39**(26), 4361–4377. DOI: 10.1016/S0042-6989(99)00119-4

Blazejewska, A., Hinds, O., & Polimeni, J. Improved tSNR of high-resolution fMRI with surface-based cortical ribbon smoothing. In: In *Annu. Meet. Organ.* 2016, 1728.

Blazejewska, A. I., Fischl, B., Wald, L. L., & Polimeni, J. R. (2019). Intracortical smoothing of small-voxel fMRI data can provide increased detection power without spatial resolution losses compared to conventional large-voxel fMRI data. NeuroImage, **189**, 601–614. DOI: 10.1016/j.neuroimage.2019.01.054

Bloom, F., Bjorklund, A., & Hokfelt, T. Handbook of chemical neuroanatomy. English. In: In *The primate nervous system, part i.* Vol. 13. Handbook of Chemical Neuroanatomy. Elsevier Science B.V., 1997, p. 553. ISBN: 0-444-82558-4.

Bock, N. A., Hashim, E., Janik, R., Konyer, N. B., Weiss, M., Stanisz, G. J., Turner, R., & Geyer, S. (2013). Optimizing T1-weighted imaging of cortical myelin content at 3.0T. NeuroImage, **65**, 1–12. DOI: 10.1016/j.neuroimage.2012.09.051

Bohnen, N. I., Albin, R. L., Müller, M. L. T. M., Petrou, M., Kotagal, V., Koeppe, R. A., Scott, P. J. H., & Frey, K. A. (2015). Frequency of cholinergic and caudate nucleus dopaminergic deficits across the predemented cognitive spectrum of Parkinson disease and evidence of interaction effects. JAMA neurology, **72**(2), 194–200. DOI: 10.1001/jamaneurol.2014.2757

Bohnen, N. I., Müller, M. L. T. M., Kotagal, V., Koeppe, R. A., Kilbourn, M. R., Gilman, S., Albin, R. L., & Frey, K. A. (2012). Heterogeneity of cholinergic denervation in Parkinson's disease without dementia. Journal of Cerebral Blood Flow and Metabolism: Official Journal of the International Society of Cerebral Blood Flow and Metabolism, **32**(8), 1609–1617. DOI: 10.1038/jcbfm.2012.60

Boucard, C. C., van Es, J. J., Maguire, R. P., & Cornelissen, F. W. (2005). Functional magnetic resonance imaging of brightness induction in the human visual cortex. NeuroReport, **16**(12), 1335–1338. DOI: 10.1097/01.wnr.0000175242.05343.50

Boyaci, H., Fang, F., Murray, S. O., & Kersten, D. (2007). Responses to Lightness Variations in Early Human Visual Cortex. Current Biology, **17**(11), 989–993. DOI: 10.1016/j.cub.2007.05.005

Briggs, F. (2020). Role of Feedback Connections in Central Visual Processing. Annual Review of Vision Science, **6**(1), 313–334. DOI: 10.1146/annurev-vision-121219-081716

Broadbent, D. E. (1958). *Perception and communication*. Pergamon Press.

Bruce, C, Desimone, R, & Gross, C. G. (1981). Visual properties of neurons in a polysensory area in superior temporal sulcus of the macaque. Journal of Neurophysiology, **46**(2), 369–384. DOI: 10.1152/jn.1981.46.2.369

Buckner, R., Bandettini, P., O' Craven, K., Savoy, R., Petersen, S., Raichle, M., & Rosen, B. (1996). Detection of cortical activation during averaged single trials of a cognitive task using functional magnetic resonance imaging. Proceedings of the National Academy of Sciences, **93**(25), 14878–14883. DOI: 10.1073/pnas.93.25.14878

Callaway, E. M. (2004). Feedforward, feedback and inhibitory connections in primate visual cortex. Neural Networks, **17**(5), 625–632. DOI: 10.1016/j.neunet.2004.04.004

Cantero, J. L., Atienza, M., Lage, C., Zaborszky, L., Vilaplana, E., Lopez-Garcia, S., Pozueta, A., Rodriguez-Rodriguez, E., Blesa, R., Alcolea, D., Lleo, A., Sanchez-Juan, P., Fortea, J., & Alzheimer' s Disease Neuroimaging Initiative. (2020). Atrophy of Basal Forebrain Initiates with Tau Pathology in Individuals at Risk for Alzheimer' s Disease. Cerebral Cortex, **30**(4), 2083–2098. DOI: 10.1093/cercor/bhz224

Cantero, J. L., Zaborszky, L., & Atienza, M. (2017). Volume Loss of the Nucleus Basalis of Meynert is Associated with Atrophy of Innervated Regions in Mild Cognitive Impairment. Cerebral Cortex (New York, N.Y.: 1991), **27**(8), 3881–3889. DOI: 10.1093/cercor/bhw195

Carruthers, S. P., Gurvich, C. T., & Rossell, S. L. (2015). The muscarinic system, cognition and schizophrenia. Neuroscience and

Biobehavioral Reviews, **55**, 393–402. DOI: 10.1016/j.neubiorev.2015.05.011

Casamitjana, A., & Iglesias, J. E. (2022). High-resolution atlasing and segmentation of the subcortex: Review and perspective on challenges and opportunities created by machine learning. NeuroImage, **263**, 119616. DOI: 10.1016/j.neuroimage.2022.119616

Chan-Palay, V. (1988). Galanin hyperinnervates surviving neurons of the human basal nucleus of meynert in dementias of alzheimer's and parkinson's disease: A hypothesis for the role of galanin in accentuating cholinergic dysfunction in dementia. Journal of Comparative Neurology, **273**(4), 543–557. DOI: 10.1002/cne.902730409

Chen, N., Sugihara, H., Sharma, J., Perea, G., Petravicz, J., Le, C., & Sur, M. (2012). Nucleus basalis-enabled stimulus-specific plasticity in the visual cortex is mediated by astrocytes. Proceedings of the National Academy of Sciences, **109**(41), E2832–E2841. DOI: 10.1073/pnas.1206557109

Chen, N., Sugihara, H., & Sur, M. (2015). An acetylcholine-activated microcircuit drives temporal dynamics of cortical activity. Nature Neuroscience, **18**(6), 892–902. DOI: 10.1038/nn.4002

Chen, N.-k., & Wyrwicz, A. M. (1999). Correction for EPI distortions using multi-echo gradient-echo imaging. Magnetic Resonance in Medicine, **41**(6), 1206–1213. DOI: 10.1002/(SICI)1522-2594(199906)41:6<1206::AID-MRM17>3.0.CO;2-L

Chui, H. C., Bondareff, W., Zarow, C., & Slager, U. (1984). Stability of neuronal number in the human nucleus basalis of Meynert with age. Neurobiology of Aging, **5**(2), 83–88. DOI: 10.1016/0197-4580(84)90035-6

Clay Reid, R., & Shapley, R. (1988). Brightness induction by local contrast and the spatial dependence of assimilation. Vision Research, **28**(1), 115–132. DOI: 10.1016/S0042-6989(88)80012-9

Cohen, A. D., Yang, B., Fernandez, B., Banerjee, S., & Wang, Y. (2021). Improved resting state functional connectivity sensitivity and reproducibility using a multiband multi-echo acquisition. NeuroImage, **225**, 117461. DOI: 10.1016/j.neuroimage.2020.117461

Connor, J. R., Menzies, S. L., Martin, S. M. S., & Mufson, E. J. (1990). Cellular distribution of transferrin, ferritin, and iron in normal and aged human brains. Journal of Neuroscience Research, **27**(4), 595–611. DOI: https://doi.org/10.1002/jnr.490270421

Corbetta, M., & Shulman, G. L. (2002). Control of goal-directed and stimulus-driven attention in the brain. Nature Reviews Neuroscience, **3**(3), 201–215. DOI: 10.1038/nrn755

Cornelissen, F. W., Wade, A. R., Vladusich, T., Dougherty, R. F., & Wandell, B. A. (2006). No Functional Magnetic Resonance Imaging Evidence for Brightness and Color Filling-In In Early Human Visual Cortex. Journal of Neuroscience, **26**(14), 3634–3641. DOI: 10.1523/JNEUROSCI.4382-05.2006

Cox, D. D., & Savoy, R. L. (2003). Functional magnetic resonance imaging (fMRI) "brain reading" : Detecting and classifying distributed patterns of fMRI activity in human visual cortex. NeuroImage, **19**(2), 261–270. DOI: 10.1016/S1053-8119(03)00049-1

Cox, M. A., & Maier, A. (2015). Serial versus parallel processing in mid-level vision: Filling-in the details of spatial interpolation. Neuroscience of Consciousness, **2015**(1), niv007. DOI: 10.1093/nc/niv007

Crowne, D. P. (1983). The frontal eye field and attention. Psychological Bulletin, **93**, 232–260. DOI: 10.1037/0033-2909.93.2.232

Darley, W. K., Blankson, C., & Luethge, D. J. (2010). Toward an integrated framework for online consumer behavior and decision making process: A review. Psychology & Marketing, **27**(2), 94–116. DOI: 10.1002/mar.20322

de Hollander, G., Keuken, M. C., van der Zwaag, W., Forstmann, B. U., & Trampel, R. (2017). Comparing functional MRI protocols for small, iron-rich basal ganglia nuclei such as the subthalamic nucleus at 7 T and 3 T. Human Brain Mapping, **38**(6), 3226–3248. DOI: 10.1002/hbm.23586

De Lacalle, S., Iraizoz, I., & Ma Gonzalo, L. (1991). Differential changes in cell size and number in topographic subdivisions of human basal nucleus in normal aging. Neuroscience, **43**(2), 445–456. DOI: 10.1016/0306-4522(91)90307-A

De Martino, F., Moerel, M., Ugurbil, K., Goebel, R., Yacoub, E., & Formisano, E. (2015). Frequency preference and attention effects across cortical depths in the human primary auditory cortex. Proceedings of the National Academy of Sciences, **112**(52), 16036–16041. DOI: 10.1073/pnas.1507552112

De Martino, F., Valente, G., Staeren, N., Ashburner, J., Goebel, R., & Formisano, E. (2008). Combining multivariate voxel selection and support vector machines for mapping and classification of fMRI spatial patterns. NeuroImage, **43**(1), 44–58. DOI: 10.1016/j.neuroimage.2008.06.037

De Martino, F., Yacoub, E., Kemper, V., Moerel, M., Uludağ, K., De Weerd, P., Ugurbil, K., Goebel, R., & Formisano, E. (2018). The impact of ultra-high field MRI on cognitive and computational neuroimaging. NeuroImage, **168**, 366–382. DOI: 10.1016/j.neuroimage.2017.03.060

De Valois, R. L., & De Valois, K. K. (1988). *Spatial vision.* Oxford University Press.

De Weerd, P., Karni, A., Kastner, S, Ungerleider, L., & Jezzard, P. An investigation of fMRI resolution in visual cortex. In: *5*. Neuroimage, 1997, S45.

Dennett, D. C. (1991). *Consciousness Explained.* Little, Brown; Co.

Dennett, D. C. Filling in versus finding out: A Ubiquitous Confusion in Cognitive Science (H. Pick, P. V. d. Broek, & D. Knill, Eds.). In: *Cognition: Conceptual and methodological issues* (H. Pick, P. V. d. Broek, & D. Knill, Eds.). Ed. by Pick, H., Broek, P. V. d., & Knill, D. American Psychological Association, 1992.

Desimone, R., Albright, T. D., Gross, C. G., & Bruce, C. (1984). Stimulus-selective properties of inferior temporal neurons in the macaque. Journal of Neuroscience, **4**(8), 2051–2062. DOI: 10.1523/JNEUROSCI.04-08-02051.1984

Desimone, R., Wessinger, M., Thomas, L., & Schneider, W. (1990). Attentional Control of Visual Perception: Cortical and Subcortical Mechanisms. Cold Spring Harbor Symposia on Quantitative Biology, **55**, 963–971. DOI: 10.1101/SQB.1990.055.01.090

Deutsch, J. A., & Deutsch, D. (1963). Attention: Some theoretical considerations. Psychological Review, **70**, 80–90. DOI: 10.1037/h0039515

Ding, S.-L., Royall, J. J., Sunkin, S. M., Ng, L., Facer, B. A. C., Lesnar, P., Guillozet-Bongaarts, A., McMurray, B., Szafer, A., Dolbeare, T. A., Stevens, A., Tirrell, L., Benner, T., Caldejon, S., Dalley, R. A., Dee, N., Lau, C., Nyhus, J., Reding, M., (2016). Comprehensive cellular-resolution atlas of the adult human brain. Journal of Comparative Neurology, **524**(16), 3127–3481. DOI: https://doi.org/10.1002/cne.24080

Ding, Z., Gore, J. C., & Anderson, A. W. (2005). Reduction of noise in diffusion tensor images using anisotropic smoothing. Magnetic Resonance in Medicine, **53**(2), 485–490. DOI: 10.1002/mrm.20339

Dinse, J., Härtwich, N., Waehnert, M. D., Tardif, C. L., Schäfer, A., Geyer, S., Preim, B., Turner, R., & Bazin, P. L. (2015). A cytoarchitecture-driven myelin model reveals area-specific signatures in human primary and secondary areas using ultra-high resolution in-vivo brain MRI. NeuroImage, **114**, 71–87. DOI: 10.1016/j.neuroimage.2015.04.023

Disney, A. A., Aoki, C., & Hawken, M. J. (2012). Cholinergic suppression of visual responses in primate V1 is mediated by GABAergic inhibition. Journal of Neurophysiology, **108**(7), 1907–1923. DOI: 10.1152/jn.00188.2012

Dixon, E., Shapiro, A., & Lu, Z.-L. (2014). Scale-invariance in brightness illusions implicates object-level visual processing. Scientific Reports, **4**(1), 3900. DOI: 10.1038/srep03900

Drayer, B, Burger, P, Darwin, R, Riederer, S, Herfkens, R, & Johnson, G. (1986). Mri of brain iron. American Journal of Roentgenology, **147**(1), 103–110. DOI: 10.2214/ajr.147.1.103

Driver, J., & Mattingley, J. B. (1998). Parietal neglect and visual awareness. Nature Neuroscience, **1**(1), 17–22. DOI: 10.1038/217

Du, Y. P., Chu, R., Hwang, D., Brown, M. S., Kleinschmidt-DeMasters, B. K., Singel, D., & Simon, J. H. (2007). Fast multislice mapping of the myelin water fraction using multicompartment analysis

of T decay at 3T: A preliminary postmortem study. Magnetic Resonance in Medicine, **58**(5), 865–870. DOI: 10.1002/mrm.21409

Dumoulin, S. O., Fracasso, A., van der Zwaag, W., Siero, J. C. W., & Petridou, N. (2018). Ultra-high field MRI: Advancing systems neuroscience towards mesoscopic human brain function. NeuroImage, **168**, 345–357. DOI: 10.1016/j.neuroimage.2017.01.028

Dumoulin, S. O., Harvey, B. M., Fracasso, A., Zuiderbaan, W., Luijten, P. R., Wandell, B. A., & Petridou, N. (2017). In vivo evidence of functional and anatomical stripe-based subdivisions in human V2 and V3. Scientific Reports, **7**(1), 733. DOI: 10.1038/s41598-017-00634-6

Duyn, J. H. (2012). The future of ultra-high field MRI and fMRI for study of the human brain. NeuroImage, **62**(2), 1241–1248. DOI: 10.1016/j.neuroimage.2011.10.065

Easton, A., Douchamps, V., Eacott, M., & Lever, C. (2012). A specific role for septohippocampal acetylcholine in memory? Neuropsychologia, **50**(13), 3156–3168. DOI: 10.1016/j.neuropsychologia.2012.07.022

Edlow, B. L., Mareyam, A., Horn, A., Polimeni, J. R., Witzel, T., Tisdall, M. D., Augustinack, J. C., Stockmann, J. P., Diamond, B. R., Stevens, A., Tirrell, L. S., Folkerth, R. D., Wald, L. L., Fischl, B., & van der Kouwe, A. (2019). 7 Tesla MRI of the ex vivo human brain at 100 micron resolution. Scientific Data, **6**(1), 244. DOI: 10.1038/s41597-019-0254-8

Eggenschwiler, F., Kober, T., Magill, A. W., Gruetter, R., & Marques, J. P. (2012). SA2RAGE: A new sequence for fast B1+-mapping. Magnetic Resonance in Medicine, **67**(6), 1609–1619. DOI: 10.1002/mrm.23145

Eichner, C., Paquette, M., Mildner, T., Schlumm, T., Pléh, K., Samuni, L., Crockford, C., Wittig, R. M., Jäger, C., Möller, H. E., Friederici, A. D., & Anwander, A. (2020). Increased sensitivity and signal-to-noise ratio in diffusion-weighted MRI using multi-echo acquisitions. NeuroImage, **221**, 117172. DOI: 10.1016/j.neuroimage.2020.117172

Eickhoff, Stephan, K. E., Mohlberg, H., Grefkes, C., Fink, G. R., Amunts, K., & Zilles, K. (2005a). A new SPM toolbox for combining probabilistic cytoarchitectonic maps and functional imaging data. NeuroImage, **25**(4), 1325–1335. DOI: 10.1016/j.neuroimage.2004.12.034

Eickhoff, Walters, N. B., Schleicher, A., Kril, J., Egan, G. F., Zilles, K., Watson, J. D. G., & Amunts, K. (2005b). High-resolution MRI reflects myeloarchitecture and cytoarchitecture of human cerebral cortex. Human Brain Mapping, **24**(3), 206–215. DOI: 10.1002/hbm.20082

Fazal, Z., Gomez, D. E. P., Llera, A., Marques, J. P. R. F., Beck, T., Poser, B. A., & Norris, D. G. (2022). A comparison of multiband and multiband multiecho gradient-echo EPI for task fMRI at 3 T. Human Brain Mapping, **n/a**(n/a). DOI: 10.1002/hbm.26081

Felleman, D. J., & Van Essen, D. C. (1991). Distributed hierarchical processing in the primate cerebral cortex. Cerebral cortex (New York, N.Y. **1**(1), 1–47. DOI: 10.1093/cercor/1.1.1-a

Fernández-Cabello, S., Kronbichler, M., Van Dijk, K. R. A., Goodman, J. A., Spreng, R. N., Schmitz, T. W., & on behalf of the Alzheimer's Disease Neuroimaging Initiative. (2020). Basal forebrain volume reliably predicts the cortical spread of Alzheimer's degeneration. Brain, **143**(3), 993–1009. DOI: 10.1093/brain/awaa012

Field, D. J., Hayes, A., & Hess, R. F. (1993). Contour integration by the human visual system: Evidence for a local "association field". Vision Research, **33**(2), 173–193. DOI: 10.1016/0042-6989(93)90156-Q

Filo, S., Shtangel, O., Salamon, N., Kol, A., Weisinger, B., Shifman, S., & Mezer, A. A. (2019). Disentangling molecular alterations from water-content changes in the aging human brain using quantitative MRI. Nature Communications, **10**(1), 3403. DOI: 10.1038/s41467-019-11319-1

Finn, E. S., Huber, L., & Bandettini, P. A. (2021). Higher and deeper: Bringing layer fmri to association cortex. Progress in Neurobiology, **207**, 101930. DOI: 10.1016/j.pneurobio.2020.101930

Fischer, J., & Whitney, D. (2012). Attention gates visual coding in the human pulvinar. Nature Communications, **3**(1), 1051. DOI: 10.1038/ncomms2054

Fischl, B. (2012). FreeSurfer. NeuroImage, **62**(2). DOI: 10.1016/j.neuroimage.2012.01.021

Fischl, B., & Dale, A. M. (2000). Measuring the thickness of the human cerebral cortex from magnetic resonance images. Proceedings of the National Academy of Sciences, **97**(20), 11050–11055. DOI: 10.1073/pnas.200033797

Formisano, E., De Martino, F., Bonte, M., & Goebel, R. (2008). "Who" Is Saying "What"? Brain-Based Decoding of Human Voice and Speech. Science, **322**(5903), 970–973. DOI: 10.1126/science.1164318

Forstmann, B. U., de Hollander, G., van Maanen, L., Alkemade, A., & Keuken, M. C. (2017). Towards a mechanistic understanding of the human subcortex. Nature Reviews Neuroscience, **18**(1), 57–65. DOI: 10.1038/nrn.2016.163

Forstmann, B. U., Keuken, M. C., Schafer, A., Bazin, P.-L., Alkemade, A., & Turner, R. (2014). Multi-modal ultra-high resolution structural 7-Tesla MRI data repository. Scientific Data, **1**(1), 140050. DOI: 10.1038/sdata.2014.50

Foster, D. H. (2011). Color constancy. Vision Research, **51**(7), 674–700. DOI: 10.1016/j.visres.2010.09.006

Fox, M. D., Corbetta, M., Snyder, A. Z., Vincent, J. L., & Raichle, M. E. (2006). Spontaneous neuronal activity distinguishes human dorsal and ventral attention systems. Proceedings of the National Academy of Sciences, **103**(26), 10046–10051. DOI: 10.1073/pnas.0604187103

Fracasso, A., Dumoulin, S. O., & Petridou, N. (2021). Point-spread function of the BOLD response across columns and cortical depth in human extra-striate cortex. Progress in Neurobiology, **202**, 102034. DOI: 10.1016/j.pneurobio.2021.102034

Fracasso, A., van Veluw, S. J., Visser, F., Luijten, P. R., Spliet, W., Zwanenburg, J. J. M., Dumoulin, S. O., & Petridou, N. (2016). Lines of Baillarger in vivo and ex vivo: Myelin contrast across

lamina at 7T MRI and histology. NeuroImage, **133**, 163–175. DOI: 10.1016/j.neuroimage.2016.02.072

Friedman, H. S., Zhou, H., & von der Heydt, R. (2003). The coding of uniform colour figures in monkey visual cortex. The Journal of Physiology, **548**(Pt 2), 593–613. DOI: 10.1113/jphysiol.2002.033555

Fritz, H. J., Ray, N., Dyrba, M., Sorg, C., Teipel, S. J., & Grothe, M. J. (2018). The corticotopic organization of the human basal forebrain as revealed by regionally selective functional connectivity profiles. Human Brain Mapping, **40**(3), 868–878. DOI: 10.1002/hbm.24417

Fukunaga, M., Li, T.-Q., Gelderen, P. v., Zwart, J. A. d., Shmueli, K., Yao, B., Lee, J., Maric, D., Aronova, M. A., Zhang, G., Leapman, R. D., Schenck, J. F., Merkle, H., & Duyn, J. H. (2010). Layer-specific variation of iron content in cerebral cortex as a source of MRI contrast. Proceedings of the National Academy of Sciences, **107**(8), 3834–3839. DOI: 10.1073/pnas.0911177107

Gallant, J. L., Shoup, R. E., & Mazer, J. A. (2000). A Human Extrastriate Area Functionally Homologous to Macaque V4. Neuron, **27**(2), 227–235. DOI: 10.1016/S0896-6273(00)00032-5

Gallichan, D., Marques, J. P., & Gruetter, R. (2016). Retrospective correction of involuntary microscopic head movement using highly accelerated fat image navigators (3D FatNavs) at 7T. Magnetic Resonance in Medicine, **75**(3), 1030–1039. DOI: https://doi.org/10.1002/mrm.25670

Gallotto, S., Duecker, F., Oever, S. t., Schuhmann, T., de Graaf, T. A., & Sack, A. T. (2020). Relating alpha power modulations to competing visuospatial attention theories. NeuroImage, **207**, 116429. DOI: 10.1016/j.neuroimage.2019.116429

Gang, M., Baba, T., Hosokai, Y., Nishio, Y., Kikuchi, A., Hirayama, K., Hasegawa, T., Aoki, M., Takeda, A., Mori, E., & Suzuki, K. (2020). Clinical and Cerebral Metabolic Changes in Parkinson's Disease With Basal Forebrain Atrophy. Movement Disorders, **35**(5), 825–832. DOI: https://doi.org/10.1002/mds.27988

Gao, F.-q., Pettersen, J. A., Bocti, C., Nestor, S. M., Kiss, A., & Black, S. E. (2013). Is encroachment of the carotid termination into the substantia innominata associated with its atrophy and cognition in Alzheimer's disease? Neurobiology of Aging, **34**(7), 1807–1814. DOI: 10.1016/j.neurobiolaging.2013.01.009

Gaspar, P., & Gray, F. (1984). Dementia in idiopathic Parkinson's disease. A neuropathological study of 32 cases. Acta Neuropathologica, **64**(1), 43–52. DOI: 10.1007/BF00695605

Gattass, R., Nascimento-Silva, S., Soares, J. G., Lima, B., Jansen, A. K., Diogo, A. C. M., Farias, M. F., Botelho, M. M., Eliã P, Mariani, O. S., Azzi, J., & Fiorani, M. (2005). Cortical visual areas in monkeys: Location, topography, connections, columns, plasticity and cortical dynamics. Philosophical Transactions of the Royal Society B: Biological Sciences, **360**(1456), 709–731. DOI: 10.1098/rstb.2005.1629

Gazzaniga, M. S., & Rakoff, J. S. (2010). *Judges' guide to neuroscience: A concise introduction* (A. S. Mansfield, Ed.). University of California, Santa Barbara.

George, S., Mufson, E., Leurgans, S., Shah, R., Ferrari, C., & deToledo Morrell, L. (2011). MRI-based volumetric measurement of the substantia innominata in amnestic MCI and mild AD. Neurobiology of aging, **32**(10), 1756–1764. DOI: 10.1016/j.neurobiolaging.2009.11.006

Gilchrist. (2007). Lightness and brightness. **17**(8), R267–R269.

Gilchrist, A. (2015). Theoretical Approaches to Lightness and Perception. Perception, **44**(4), 339–358. DOI: 10.1068/p7935

Gilchrist, A. L. (1977). Perceived Lightness Depends on Perceived Spatial Arrangement. Science, **195**(4274), 185–187. DOI: 10.1126/science.831266

Gilchrist, A. L. (1980). When does perceived lightness depend on perceived spatial arrangement? Perception & Psychophysics, **28**(6), 527–538. DOI: 10.3758/BF03198821

Gilchrist, A. L., & Jacobsen, A. (1983). Lightness constancy through a veiling luminance. Journal of Experimental Psychology: Human

Perception and Performance, **9**(6), 936–944. DOI: 10.1037/0096-1523.9.6.936

Goard, M., & Dan, Y. (2009). Basal forebrain activation enhances cortical coding of natural scenes. Nature Neuroscience, **12**(11), 1444–1449. DOI: 10.1038/nn.2402

Goense, J. B. M., & Logothetis, N. K. (2008). Neurophysiology of the BOLD fMRI Signal in Awake Monkeys. Current Biology, **18**(9), 631–640. DOI: 10.1016/j.cub.2008.03.054

Goldberg, M. E., Bisley, J., Powell, K. D., Gottlieb, J., & Kusunoki, M. (2002). The Role of the Lateral Intraparietal Area of the Monkey in the Generation of Saccades and Visuospatial Attention. Annals of the New York Academy of Sciences, **956**(1), 205–215. DOI: 10.1111/j.1749-6632.2002.tb02820.x

Goldberg, M. E., Bisley, J. W., Powell, K. D., & Gottlieb, J. Chapter 10 Saccades, salience and attention: The role of the lateral intraparietal area in visual behavior (S. Martinez-Conde, S. L. Macknik, L. M. Martinez, J. M. Alonso, & P. U. Tse, Eds.). en. In: *Progress in Brain Research* (S. Martinez-Conde, S. L. Macknik, L. M. Martinez, J. M. Alonso, & P. U. Tse, Eds.). Ed. by Martinez-Conde, S., Macknik, S. L., Martinez, L. M., Alonso, J. M., & Tse, P. U. Vol. 155. Visual Perception. Elsevier, 2006, January, pp. 157–175. DOI: 10.1016/S0079-6123(06)55010-1.

Gorgolewski, K. J., Auer, T., Calhoun, V. D., Craddock, R. C., Das, S., Duff, E. P., Flandin, G., Ghosh, S. S., Glatard, T., Halchenko, Y. O., Handwerker, D. A., Hanke, M., Keator, D., Li, X., Michael, Z., Maumet, C., Nichols, B. N., Nichols, T. E., Pellman, J., (2016). The brain imaging data structure, a format for organizing and describing outputs of neuroimaging experiments. Scientific Data, **3**(1), 160044. DOI: 10.1038/sdata.2016.44

Gracien, R.-M., Maiworm, M., Brüche, N., Shrestha, M., Nöth, U., Hattingen, E., Wagner, M., & Deichmann, R. (2020). How stable is quantitative MRI? –Assessment of intra- and inter-scanner-model reproducibility using identical acquisition sequences and

data analysis programs. NeuroImage, **207**, 116364. DOI: 10.1016/j.neuroimage.2019.116364

Greve, D. N., Billot, B., Cordero, D., Hoopes, A., Hoffmann, M., Dalca, A. V., Fischl, B., Iglesias, J. E., & Augustinack, J. C. (2021). A deep learning toolbox for automatic segmentation of subcortical limbic structures from MRI images. NeuroImage, **244**, 118610. DOI: 10.1016/j.neuroimage.2021.118610

Grinberg, L. T., & Heinsen, H. (2007). Computer-assisted 3D reconstruction of the human basal forebrain complex. Dementia & Neuropsychologia, **1**(2), 140–146. DOI: 10.1590/s1980-57642008dn10200005

Gritton, H. J., Howe, W. M., Mallory, C. S., Hetrick, V. L., Berke, J. D., & Sarter, M. (2016). Cortical cholinergic signaling controls the detection of cues. Proceedings of the National Academy of Sciences, **113**(8), E1089–E1097. DOI: 10.1073/pnas.1516134113

Grossberg, S. (1987a). Cortical dynamics of three-dimensional form, color, and brightness perception: I. Monocular theory. Perception & Psychophysics, **41**(2), 87–116. DOI: 10.3758/BF03204874

Grossberg, S. (1987b). Cortical dynamics of three-dimensional form, color, and brightness perception: II. Binocular theory. Perception & Psychophysics, **41**(2), 117–158. DOI: 10.3758/BF03204875

Grossberg, S., & Hong, S. (2006). A neural model of surface perception: Lightness, anchoring, and filling-in. Spatial Vision, **19**(2-4), 263–321. DOI: 10.1163/156856806776923399

Grossberg, S., & Mingolla, E. (1985). Neural dynamics of form perception: Boundary completion, illusory figures, and neon color spreading. Psychological Review, **92**(2), 173–211. DOI: 10.1037/0033-295X.92.2.173

Grothe, M., Heinsen, H., & Teipel. (2012). Atrophy of the cholinergic basal forebrain over the adult age range and in early stages of Alzheimer´s disease. Biological psychiatry, **71**(9), 805–813. DOI: 10.1016/j.biopsych.2011.06.019

Grothe, M., Heinsen, H., & Teipel, S. (2013). Longitudinal measures of cholinergic forebrain atrophy in the transition from healthy ag-

ing to Alzheimer's disease. Neurobiology of Aging, **34**(4), 1210–1220. DOI: 10.1016/j.neurobiolaging.2012.10.018

Grothe, M., Zaborszky, L., Atienza, M., Gil-Neciga, E., Rodriguez-Romero, R., Teipel, S. J., Amunts, K., Suarez-Gonzalez, A., & Cantero, J. L. (2010). Reduction of Basal Forebrain Cholinergic System Parallels Cognitive Impairment in Patients at High Risk of Developing Alzheimer's Disease. Cerebral Cortex (New York, NY), **20**(7), 1685–1695. DOI: 10.1093/cercor/bhp232

Grothe, M. J., Ewers, M., Krause, B., Heinsen, H., & Teipel. (2014a). Basal forebrain atrophy and cortical amyloid deposition in non-demented elderly subjects. Alzheimer's & dementia : the journal of the Alzheimer's Association, **10**(0), S344–S353. DOI: 10.1016/j.jalz.2013.09.011

Grothe, M. J., Schuster, C., Bauer, F., Heinsen, H., Prudlo, J., & Teipel, S. J. (2014b). Atrophy of the cholinergic basal forebrain in dementia with Lewy bodies and Alzheimer' s disease dementia. Journal of Neurology, **261**(10), 1939–1948. DOI: 10.1007/s00415-014-7439-z

Guérin, B., Villena, J. F., Polimeridis, A. G., Adalsteinsson, E., Daniel, L., White, J. K., & Wald, L. L. (2017). The ultimate signal-to-noise ratio in realistic body models. Magnetic Resonance in Medicine, **78**(5), 1969–1980. DOI: 10.1002/mrm.26564

Hall, H., Reyes, S., Landeck, N., Bye, C., Leanza, G., Double, K., Thompson, L., Halliday, G., & Kirik, D. (2014). Hippocampal Lewy pathology and cholinergic dysfunction are associated with dementia in Parkinson' s disease. Brain, **137**(9), 2493–2508. DOI: 10.1093/brain/awu193

Halliday, G. M., Cullen, K., & Cairns, M. J. (1993). Quantitation and three-dimensional reconstruction of Ch4 nucleus in the human basal forebrain. Synapse, **15**(1), 1–16. DOI: 10.1002/syn.890150102

Hamker. The role of feedback connections in task-driven visual search (D. Heinke, G. W. Humphreys, & A. Olson, Eds.). en. In: *Connectionist Models in Cognitive Neuroscience* (D. Heinke, G. W. Humphreys, & A. Olson, Eds.). Ed. by Heinke, D., Humphreys,

G. W., & Olson, A. Perspectives in Neural Computing. London: Springer, 1999, 252–261. ISBN: 978-1-4471-0813-9. DOI: 10.1007/978-1-4471-0813-9_22.

Hamker. (2005). The Reentry Hypothesis: The Putative Interaction of the Frontal Eye Field, Ventrolateral Prefrontal Cortex, and Areas V4, IT for Attention and Eye Movement. Cerebral Cortex, **15**(4), 431–447. DOI: 10.1093/cercor/bhh146

Hanna Al-Shaikh, F. S., Duara, R., Crook, J. E., Lesser, E. R., Schaeverbeke, J., Hinkle, K. M., Ross, O. A., Ertekin-Taner, N., Pedraza, O., Dickson, D. W., Graff-Radford, N. R., & Murray, M. E. (2020). Selective Vulnerability of the Nucleus Basalis of Meynert Among Neuropathologic Subtypes of Alzheimer Disease. JAMA Neurology, **77**(2), 225–233. DOI: 10.1001/jamaneurol.2019.3606

Harris, C. R., Millman, K. J., van der Walt, S. J., Gommers, R., Virtanen, P., Cournapeau, D., Wieser, E., Taylor, J., Berg, S., Smith, N. J., Kern, R., Picus, M., Hoyer, S., van Kerkwijk, M. H., Brett, M., Haldane, A., del Río, J. F., Wiebe, M., Peterson, P., (2020). Array programming with NumPy. Nature, **585**(7825), 357–362. DOI: 10.1038/s41586-020-2649-2

Harris, K. D., & Thiele, A. (2011). Cortical state and attention. Nature Reviews Neuroscience, **12**(9), 509–523. DOI: 10.1038/nrn3084

Hartline, H. K., Wagner, H. G., & Ratliff, F. (1956). INHIBITION IN THE EYE OF LIMULUS. The Journal of General Physiology, **39**(5), 651–673. Retrieved August 23, 2022, from https://www.ncbi.nlm.nih.gov/pmc/articles/PMC2147566/

Hasselmo. (2006). The role of acetylcholine in learning and memory. Current Opinion in Neurobiology, **16**(6), 710–715. DOI: 10.1016/j.conb.2006.09.002

Hasselmo, M. E. (1999). Neuromodulation: Acetylcholine and memory consolidation. Trends in Cognitive Sciences, **3**(9), 351–359. DOI: 10.1016/S1364-6613(99)01365-0

Hawkins, J., Ahmad, S., & Cui, Y. (2017). A Theory of How Columns in the Neocortex Enable Learning the Structure of the World. Frontiers in Neural Circuits, **11**. Retrieved November 23, 2022,

from https://www.frontiersin.org/articles/10.3389/fncir.2017.00081

Haxby, J. V., Gobbini, M. I., Furey, M. L., Ishai, A., Schouten, J. L., & Pietrini, P. (2001). Distributed and Overlapping Representations of Faces and Objects in Ventral Temporal Cortex. Science, **293**(5539), 2425–2430. DOI: 10.1126/science.1063736

Haynes, J.-D., Lotto, R. B., & Rees, G. (2004). Responses of human visual cortex to uniform surfaces. Proceedings of the National Academy of Sciences, **101**(12), 4286–4291. DOI: 10.1073/pnas.0307948101

Haynes, J.-D., & Rees, G. (2006). Decoding mental states from brain activity in humans. Nature Reviews Neuroscience, **7**(7), 523–534. DOI: 10.1038/nrn1931

Hedreen, J. C., Struble, R. G., Whitehouse, P. J., & Price, D. L. (1984). Topography of the magnocellular basal forebrain system in human brain. Journal of Neuropathology and Experimental Neurology, **43**(1), 1–21. DOI: 10.1097/00005072-198401000-00001

Heinsen, H., Hampel, H., & J., T. S. (2006). Response to Boban et al: Computer-assisted 3D reconstruction of the nucleus basalis complex, including the nucleus subputaminalis (Ayala's nucleus). Brain, **129**(4), E43. DOI: 10.1093/brain/awl026

Henson, R. Analysis of fMRI time series (R. Frackowiak, J. Ashburner, W. Penny, S. Zeki, K. Friston, C. Frith, R. Dolan, & C. Price, Eds.; Second). In: *Human Brain Function* (R. Frackowiak, J. Ashburner, W. Penny, S. Zeki, K. Friston, C. Frith, R. Dolan, & C. Price, Eds.; Second). Ed. by Frackowiak, R., Ashburner, J., Penny, W., Zeki, S., Friston, K., Frith, C., Dolan, R., & Price, C. Second. London: Academic press, 2004, pp. 793–822.

Herrero, J. L., Roberts, M. J., Delicato, L. S., Gieselmann, M. A., Dayan, P., & Thiele, A. (2008). Acetylcholine contributes through muscarinic receptors to attentional modulation in V1. Nature, **454**(7208), 1110–1114. DOI: 10.1038/nature07141

Hess, G., Aizenman, C. D., & Donoghue, J. P. (1996). Conditions for the induction of long-term potentiation in layer II/III horizontal

connections of the rat motor cortex. Journal of Neurophysiology, **75**(5), 1765–1778. DOI: 10.1152/jn.1996.75.5.1765

Heunis, S., Breeuwer, M., Caballero-Gaudes, C., Hellrung, L., Huijbers, W., Jansen, J. F., Lamerichs, R., Zinger, S., & Aldenkamp, A. P. (2021). The effects of multi-echo fMRI combination and rapid T2*-mapping on offline and real-time BOLD sensitivity. NeuroImage, **238**, 118244. DOI: 10.1016/j.neuroimage.2021.118244

Horton, J. C., & Adams, D. L. (2005). The cortical column: A structure without a function. Philosophical Transactions of the Royal Society B: Biological Sciences, **360**(1456), 837–862. DOI: 10.1098/rstb.2005.1623

Hubel, D. H., & Wiesel, T. N. (1962). Receptive fields, binocular interaction and functional architecture in the cat's visual cortex. The Journal of Physiology, **160**(1), 106–154.2. Retrieved January 19, 2022, from https://www.ncbi.nlm.nih.gov/pmc/articles/PMC1359523/

Hubel, D. H., & Wiesel, T. N. (1968). Receptive fields and functional architecture of monkey striate cortex. The Journal of Physiology, **195**(1), 215–243. Retrieved August 19, 2022, from https://www.ncbi.nlm.nih.gov/pmc/articles/PMC1557912/

Huber, L., Goense, J., Kennerley, A. J., Trampel, R., Guidi, M., Reimer, E., Ivanov, D., Neef, N., Gauthier, C. J., Turner, R., & Möller, H. E. (2015). Cortical lamina-dependent blood volume changes in human brain at 7T. NeuroImage, **107**, 23–33. DOI: 10.1016/j.neuroimage.2014.11.046

Huber, L., Handwerker, D. A., Hall, A., Jangraw, D. C., Gonzalez-Castillo, J., Guidi, M., Ivanov, D., Poser, B. A., & Bandettini, P. A. Cortical depth-dependent fMRI: Heterogeneity across tasks, across participants, across days and along the cortical ribbon. In: In *In Proceedings of the International Society of Magnetic Resonance in Medicine*. 2017, 237. DOI: http://dx.doi.org/10.7490/f1000research.1114368.1.

Hung, C. P., Ramsden, B. M., Chen, L. M., & Roe, A. W. (2001). Building surfaces from borders in Areas 17 and 18 of the cat. Vision

Research, **41**(10), 1389–1407. DOI: 10.1016/S0042-6989(01)00075-X

Hung, C. P., Ramsden, B. M., & Roe, A. W. (2007). A functional circuitry for edge-induced brightness perception. Nature Neuroscience, **10**(9), 1185–1190. DOI: 10.1038/nn1948

Hunter, J. D. (2007). Matplotlib: A 2D Graphics Environment. Computing in Science Engineering, **9**(3), 90–95. DOI: 10.1109/MCSE.2007.55

Iglesias, J. E., Augustinack, J. C., Nguyen, K., Player, C. M., Player, A., Wright, M., Roy, N., Frosch, M. P., McKee, A. C., Wald, L. L., Fischl, B., & Van Leemput, K. (2015). A computational atlas of the hippocampal formation using ex vivo, ultra-high resolution MRI: Application to adaptive segmentation of in vivo MRI. NeuroImage, **115**, 117–137. DOI: 10.1016/j.neuroimage.2015.04.042

Isaacson, J. S., & Scanziani, M. (2011). How Inhibition Shapes Cortical Activity. Neuron, **72**(2), 231–243. DOI: 10.1016/j.neuron.2011.09.027

Ito, M., & Gilbert, C. D. (1999). Attention Modulates Contextual Influences in the Primary Visual Cortex of Alert Monkeys. Neuron, **22**(3), 593–604. DOI: 10.1016/S0896-6273(00)80713-8

Jacobs, H. I. L., Müller-Ehrenberg, L., Priovoulos, N., & Roebroeck, A. (2018). Curvilinear locus coeruleus functional connectivity trajectories over the adult lifespan: A 7T MRI study. Neurobiology of Aging, **69**, 167–176. DOI: 10.1016/j.neurobiolaging.2018.05.021

Jenkinson, M., Bannister, P., Brady, M., & Smith, S. (2002). Improved Optimization for the Robust and Accurate Linear Registration and Motion Correction of Brain Images. NeuroImage, **17**(2), 825–841. DOI: 10.1006/nimg.2002.1132

Jenkinson, M., & Smith, S. (2001). A global optimisation method for robust affine registration of brain images. Medical Image Analysis, **5**(2), 143–156. DOI: 10.1016/S1361-8415(01)00036-6

Jorge, J., Figueiredo, P., van der Zwaag, W., & Marques, J. P. (2013). Signal fluctuations in fMRI data acquired with 2D-EPI and 3D-

EPI at 7 Tesla. Magnetic Resonance Imaging, **31**(2), 212–220. DOI: 10.1016/j.mri.2012.07.001

Kafaligonul, H., Breitmeyer, B. G., & Öğmen, H. (2015). Feedforward and feedback processes in vision. Frontiers in Psychology, **6**. Retrieved January 29, 2023, from https://www.frontiersin.org/articles/10.3389/fpsyg.2015.00279

Kalmbach, A., Hedrick, T., & Waters, J. (2012). Selective optogenetic stimulation of cholinergic axons in neocortex. Journal of Neurophysiology, **107**(7), 2008–2019. DOI: 10.1152/jn.00870.2011

Kanowski, M., Voges, J., Buentjen, L., Stadler, J., Heinze, H.-J., & Tempelmann, C. (2014). Direct Visualization of Anatomic Subfields within the Superior Aspect of the Human Lateral Thalamus by MRI at 7T. American Journal of Neuroradiology, **35**(9), 1721–1727. DOI: 10.3174/ajnr.A3951

Kashyap, S., Haast, R. A. M., Kirk, T. F., Vu, A. T., Kurban, D., Hellenbrand, R., Wiggins, C. J., Roebroeck, A., Khan, A. R., A. Feinberg, D., Poser, B. A., & Ivanov, D. (2021a). The impact of B1+ on the optimisation of high-resolution ASL acquisitions at 7T. DOI: 10.6084/m9.figshare.14445297.v2

Kashyap, S., Ivanov, D., Havlicek, M., Huber, L., Poser, B. A., & Uludağ, K. (2021b). Sub-millimetre resolution laminar fMRI using Arterial Spin Labelling in humans at 7 T. PLOS ONE, **16**(4), e0250504. DOI: 10.1371/journal.pone.0250504

Kastner, S., De Weerd, P., Desimone, R., & Ungerleider, L. G. (1998). Mechanisms of Directed Attention in the Human Extrastriate Cortex as Revealed by Functional MRI. Science, **282**(5386), 108–111. DOI: 10.1126/science.282.5386.108

Kastner, S., De Weerd, P., Pinsk, M. A., Elizondo, M. I., Desimone, R., & Ungerleider, L. G. (2001). Modulation of Sensory Suppression: Implications for Receptive Field Sizes in the Human Visual Cortex. Journal of Neurophysiology, **86**(3), 1398–1411. DOI: 10.1152/jn.2001.86.3.1398

Kastner, S., De Weerd, P., & Ungerleider, L. G. (2000). Texture Segregation in the Human Visual Cortex: A Functional MRI Study.

Journal of Neurophysiology, **83**(4), 2453–2457. DOI: 10.1152/jn.2000.83.4.2453

Kastner, S., Pinsk, M. A., De Weerd, P., Desimone, R., & Ungerleider, L. G. (1999). Increased Activity in Human Visual Cortex during Directed Attention in the Absence of Visual Stimulation. Neuron, **22**(4), 751–761. DOI: 10.1016/S0896-6273(00)80734-5

Kauffman, D. F., Zhao, R., & Yang, Y.-S. (2011). Effects of online note taking formats and self-monitoring prompts on learning from online text: Using technology to enhance self-regulated learning. Contemporary Educational Psychology, **36**(4), 313–322. DOI: 10.1016/j.cedpsych.2011.04.001

Keil, M. S., Cristóbal, G., Hansen, T., & Neumann, H. (2005). Recovering real-world images from single-scale boundaries with a novel filling-in architecture. Neural Networks, **18**(10), 1319–1331. DOI: 10.1016/j.neunet.2005.04.003

Keuken, M. C., Isaacs, B. R., Trampel, R., van der Zwaag, W., & Forstmann, B. U. (2018). Visualizing the Human Subcortex Using Ultra-high Field Magnetic Resonance Imaging. Brain Topography, **31**(4), 513–545. DOI: 10.1007/s10548-018-0638-7

Keuleers, E., Stevens, M., Mandera, P., & Brysbaert, M. (2015). Word knowledge in the crowd: Measuring vocabulary size and word prevalence in a massive online experiment. The Quarterly Journal of Experimental Psychology, **68**(8), 1665–1692. DOI: 10.1080/17470218.2015.1022560

Kilimann, I., Grothe, M., Heinsen, H., Alho, E. J. L., Grinberg, L., Amaro, E., dos Santos, G. A. B., da Silva, R. E., Mitchell, A. J., Frisoni, G. B., Bokde, A. L., Fellgiebel, A., Filippi, M., Hampel, H., Klöppel, S., & Teipel, S. J. (2014). Subregional Basal Forebrain Atrophy in Alzheimer's Disease: A Multicenter Study. Journal of Alzheimer's disease : JAD, **40**(3), 687–700. DOI: 10.3233/JAD-132345

Kim, J.-H., Jung, A.-H., Jeong, D., Choi, I., Kim, K., Shin, S., Kim, S. J., & Lee, S.-H. (2016). Selectivity of Neuromodulatory Projections from the Basal Forebrain and Locus Ceruleus to Primary Sensory Cortices. The Journal of Neuroscience: The Offi-

cial Journal of the Society for Neuroscience, **36**(19), 5314–5327. DOI: 10.1523/JNEUROSCI.4333-15.2016

Kim, S.-G., & Ogawa, S. (2012). Biophysical and Physiological Origins of Blood Oxygenation Level-Dependent fMRI Signals. Journal of Cerebral Blood Flow & Metabolism, **32**(7), 1188–1206. DOI: 10.1038/jcbfm.2012.23

Kingdom, F. A. A. (2011). Lightness, brightness and transparency: A quarter century of new ideas, captivating demonstrations and unrelenting controversy. Vision Research, **51**(7), 652–673. DOI: 10.1016/j.visres.2010.09.012

Kinoshita, M., & Komatsu, H. (2001). Neural Representation of the Luminance and Brightness of a Uniform Surface in the Macaque Primary Visual Cortex. Journal of Neurophysiology, **86**(5), 2559–2570. DOI: 10.1152/jn.2001.86.5.2559

Kirchberger, L., Mukherjee, S., Schnabel, U. H., van Beest, E., Barsegyan, A., Levelt, C. N., Heimel, A., Lorteije, J. A. M., van der Togt, C., Self, M. W., & Roelfsema, P. (2019, August). The Essential Role of Feedback Processing for Figure-Ground Perception in Mice. DOI: 10.2139/ssrn.3441074

Klein, J. C., Eggers, C., Kalbe, E., Weisenbach, S., Hohmann, C., Vollmar, S., Baudrexel, S., Diederich, N. J., Heiss, W. D., & Hilker, R. (2010). Neurotransmitter changes in dementia with Lewy bodies and Parkinson disease dementia in vivo. Neurology, **74**(11), 885–892. DOI: 10.1212/WNL.0b013e3181d55f61

Klein, J., Ardekani, B. A., Ashburner, J., Avants, B., Chiang, M.-C., Christensen, G. E., Collins, D. L., Gee, J., Hellier, P., Song, J. H., Jenkinson, M., Lepage, C., Rueckert, D., Thompson, P., Vercauteren, T., Woods, R. P., Mann, J. J., & Parsey, R. V. (2009). Evaluation of 14 nonlinear deformation algorithms applied to human brain MRI registration. NeuroImage, **46**(3), 786–802. DOI: 10.1016/j.neuroimage.2008.12.037

Klinkenberg, I., Sambeth, A., & Blokland, A. (2011). Acetylcholine and attention. Behavioural Brain Research, **221**(2), 430–442. DOI: 10.1016/j.bbr.2010.11.033

Kok, P., Bains, L., van Mourik, T., Norris, D., & de Lange, F. (2016). Selective Activation of the Deep Layers of the Human Primary Visual Cortex by Top-Down Feedback. Current Biology, **26**(3), 371–376. DOI: 10.1016/j.cub.2015.12.038

Komatsu, H. (2006). The neural mechanisms of perceptual filling-in. Nature Reviews Neuroscience, **7**(3), 220–231. DOI: 10.1038/nrn1869

Komatsu, H., Kinoshita, M., & Murakami, I. (2000). Neural Responses in the Retinotopic Representation of the Blind Spot in the Macaque V1 to Stimuli for Perceptual Filling-In. Journal of Neuroscience, **20**(24), 9310–9319. DOI: 10.1523/JNEUROSCI.20-24-09310.2000

Komatsu, H., Kinoshita, M., & Murakami, I. (2002). Neural responses in the primary visual cortex of the monkey during perceptual filling-in at the blind spot. Neuroscience Research, **44**(3), 231–236. DOI: 10.1016/S0168-0102(02)00149-9

Koopmans, P. J., Barth, M., & Norris, D. G. (2010). Layer-specific BOLD activation in human V1. Human Brain Mapping, **31**(9), 1297–1304. DOI: 10.1002/hbm.20936

Koshiyama, D., Fukunaga, M., Okada, N., Yamashita, F., Yamamori, H., Yasuda, Y., Fujimoto, M., Ohi, K., Fujino, H., Watanabe, Y., Kasai, K., & Hashimoto, R. (2018). Role of subcortical structures on cognitive and social function in schizophrenia. Scientific Reports, **8**(1), 1183. DOI: 10.1038/s41598-017-18950-2

Krauzlis, R. J., Lovejoy, L. P., & Zénon, A. (2013). Superior Colliculus and Visual Spatial Attention. Annual review of neuroscience, **36**, 10.1146/annurev–neuro–062012–170249. DOI: 10.1146/annurev-neuro-062012-170249

Kriegeskorte, N., Mur, M., & Bandettini, P. (2008). Representational similarity analysis - connecting the branches of systems neuroscience. Frontiers in Systems Neuroscience, **2**. Retrieved October 24, 2022, from https://www.frontiersin.org/articles/10.3389/neuro.06.004.2008

Krüger, G., & Glover, G. (2001). Physiological noise in oxygenation-sensitive magnetic resonance imaging. Magnetic Resonance in Medicine, **46**(4), 631–637. DOI: 10.1002/mrm.1240

Kuffler, S. W. (1953). Discharge patterns and functional organization of mammalian retina. Journal of Neurophysiology, **16**(1), 37–68. DOI: 10.1152/jn.1953.16.1.37

Kuhl, D. E., Minoshima, S., Fessler, J. A., Frey, K. A., Foster, N. L., Ficaro, E. P., Wieland, D. M., & Koeppe, R. A. (1996). In vivo mapping of cholinergic terminals in normal aging, Alzheimer's disease, and Parkinson's disease. Annals of Neurology, **40**(3), 399–410. DOI: 10.1002/ana.410400309

Kundu, P., Voon, V., Balchandani, P., Lombardo, M. V., Poser, B. A., & Bandettini, P. A. (2017). Multi-echo fMRI: A review of applications in fMRI denoising and analysis of BOLD signals. NeuroImage, **154**, 59–80. DOI: 10.1016/j.neuroimage.2017.03.033

Kurzawski, J. W., Gulban, O. F., Jamison, K., Winawer, J., & Kay, K. (2022). Non-Neural Factors Influencing BOLD Response Magnitudes within Individual Subjects. Journal of Neuroscience, **42**(38), 7256–7266. DOI: 10.1523/JNEUROSCI.2532-21.2022

Labadie, C., Lee, J.-H., Rooney, W. D., Jarchow, S., Aubert-Frécon, M., Springer, C. S., & Möller, H. E. (2014). Myelin water mapping by spatially regularized longitudinal relaxographic imaging at high magnetic fields. Magnetic Resonance in Medicine, **71**(1), 375–387. DOI: 10.1002/mrm.24670

Ladd, M. E., Bachert, P., Meyerspeer, M., Moser, E., Nagel, A. M., Norris, D. G., Schmitter, S., Speck, O., Straub, S., & Zaiss, M. (2018). Pros and cons of ultra-high-field MRI/MRS for human application. Progress in Nuclear Magnetic Resonance Spectroscopy, **109**, 1–50. DOI: 10.1016/j.pnmrs.2018.06.001

Lamme, V. A. (1995). The neurophysiology of figure-ground segregation in primary visual cortex. Journal of Neuroscience, **15**(2), 1605–1615. DOI: 10.1523/JNEUROSCI.15-02-01605.1995

Lamme, V. A. F., & Roelfsema, P. R. (2000). The distinct modes of vision offered by feedforward and recurrent processing. Trends in Neurosciences, **23**(11), 571–579. DOI: 10.1016/S0166-2236(00)01657-X

Lamme, V. A., Rodriguez-Rodriguez, V., & Spekreijse, H. (1999). Separate Processing Dynamics for Texture Elements, Boundaries

and Surfaces in Primary Visual Cortex of the Macaque Monkey. Cerebral Cortex, **9**(4), 406–413. DOI: 10.1093/cercor/9.4.406

Lamme, V. A., Supèr, H., & Spekreijse, H. (1998). Feedforward, horizontal, and feedback processing in the visual cortex. Current Opinion in Neurobiology, **8**(4), 529–535. DOI: 10.1016/S0959-4388(98)80042-1

Lammers, F., Borchers, F., Feinkohl, I., Hendrikse, J., Kant, I. M. J., Kozma, P., Pischon, T., Slooter, A. J. C., Spies, C., Montfort, S. J. T. v., Zacharias, N., Zaborszky, L., Winterer, G., & Consortium, T. B. (2018). Basal forebrain cholinergic system volume is associated with general cognitive ability in the elderly. Neuropsychologia, **119**, 145. DOI: 10.1016/j.neuropsychologia.2018.08.005

Lammers, F., Mobascher, A., Musso, F., Shah, N. J., Warbrick, T., Zaborszky, L., & Winterer, G. (2016). Effects of Ncl. Basalis Meynert volume on the Trail-Making-Test are restricted to the left hemisphere. Brain and Behavior, **6**(1). DOI: 10.1002/brb3.421

Land, E. H., & McCann, J. J. (1971). Lightness and Retinex Theory. JOSA, **61**(1), 1–11. DOI: 10.1364/JOSA.61.000001

Langkammer, C., Krebs, N., Goessler, W., Scheurer, E., Ebner, F., Yen, K., Fazekas, F., & Ropele, S. (2010). Quantitative MR Imaging of Brain Iron: A Postmortem Validation Study. Radiology, **257**(2), 455–462. DOI: 10.1148/radiol.10100495

Laule, C., Kozlowski, P., Leung, E., Li, D. K. B., MacKay, A. L., & Moore, G. R. W. (2008). Myelin water imaging of multiple sclerosis at 7 T: Correlations with histopathology. NeuroImage, **40**(4), 1575–1580. DOI: 10.1016/j.neuroimage.2007.12.008

Lee, J., Nam, Y., Choi, J. Y., Kim, E. Y., Oh, S.-H., & Kim, D.-H. (2017). Mechanisms of T2* anisotropy and gradient echo myelin water imaging. NMR in Biomedicine, **30**(4), e3513. DOI: 10.1002/nbm.3513

Lee, J., Shmueli, K., Kang, B.-T., Yao, B., Fukunaga, M., van Gelderen, P., Palumbo, S., Bosetti, F., Silva, A. C., & Duyn, J. H. (2012). The contribution of myelin to magnetic susceptibility-weighted

contrasts in high-field MRI of the brain. Neuroimage, **59**(4), 3967–3975. DOI: 10.1016/j.neuroimage.2011.10.076

Leergaard, T. B., & Bjaalie, J. G. (2022). Atlas-based data integration for mapping the connections and architecture of the brain. Science, **378**(6619), 488–492. DOI: 10.1126/science.abq2594

Lenzner, T., Kaczmirek, L., & Lenzner, A. (2010). Cognitive burden of survey questions and response times: A psycholinguistic experiment. Applied Cognitive Psychology, **24**(7), 1003–1020. DOI: 10.1002/acp.1602

Levine, S. M. (1991). Oligodendrocytes and myelin sheaths in normal, quaking and shiverer brains are enriched in iron. Journal of Neuroscience Research, **29**(3), 413–419. DOI: https://doi.org/10.1002/jnr.490290317

Levitt, M. H. (2013). *Spin dynamics: Basics of nuclear magnetic resonance* (second). John Wiley & Sons.

Li, Ide, J. S., Zhang, S., Hu, S., Chao, H. H., & Zaborszky, L. (2014). Resting state functional connectivity of the basal nucleus of Meynert in humans: In comparison to the ventral striatum and the effects of age. NeuroImage, **97**, 321–332. DOI: 10.1016/j.neuroimage.2014.04.019

Li, Q., Joo, S. J., Yeatman, J. D., & Reinecke, K. (2020). Controlling for Participants' Viewing Distance in Large-Scale, Psychophysical Online Experiments Using a Virtual Chinrest. Scientific Reports, **10**(1), 904. DOI: 10.1038/s41598-019-57204-1

Liang, H., Pan, Z., Qian, C., Liu, C., Sun, K., Weng, D., An, J., Zhuo, Y., Wang, D. J. J., Guo, H., & Xue, R. (2022). Multi-echo balanced SSFP with a sequential phase-encoding order for functional MR imaging at 7T. Magnetic Resonance in Medicine, **88**(3), 1303–1313. DOI: 10.1002/mrm.29301

Liu, Chang, R. C.-C., Pearce, R. K. B., & Gentleman, S. M. (2015). Nucleus basalis of Meynert revisited: Anatomy, history and differential involvement in Alzheimer' s and Parkinson' s disease. Acta Neuropathologica, **129**(4), 527–540. DOI: 10.1007/s00401-015-1392-5

Liu, X., de Zwart, J. A., Schölvinck, M. L., Chang, C., Ye, F. Q., Leopold, D. A., & Duyn, J. H. (2018). Subcortical evidence for a contribution of arousal to fMRI studies of brain activity. Nature Communications, **9**(1), 395. DOI: 10.1038/s41467-017-02815-3

Logothetis, N. K. (2008). What we can do and what we cannot do with fMRI. Nature, **453**(7197), 869–878. DOI: 10.1038/nature06976

Logothetis, N. K., Pauls, J., Augath, M., Trinath, T., & Oeltermann, A. (2001). Neurophysiological investigation of the basis of the fMRI signal. Nature, **412**(6843), 150–157. DOI: 10.1038/35084005

Lonsdale, K. Y., & Bragg, W. H. (1939). Diamagnetic anisotropy of organic molecules. Proceedings of the Royal Society of London. Series A. Mathematical and Physical Sciences, **171**(947), 541–568. DOI: 10.1098/rspa.1939.0083

Lowes-Hummel, P., Gertz, H. J., Ferszt, R., & Cervos-Navarro, J. (1989). The basal nucleus of Meynert revised: The nerve cell number decreases with age. Archives of Gerontology and Geriatrics, **8**(1), 21–27. DOI: 10.1016/0167-4943(89)90066-6

Lu, H. D., & Roe, A. W. (2007). Optical Imaging of Contrast Response in Macaque Monkey V1 and V2. Cerebral Cortex, **17**(11), 2675–2695. DOI: 10.1093/cercor/bhl177

Luo, Y., Kim, E. H., Flask, C. A., & Clark, H. A. (2018). Nanosensors for the Chemical Imaging of Acetylcholine Using Magnetic Resonance Imaging. ACS Nano, **12**(6), 5761–5773. DOI: 10.1021/acsnano.8b01640

Lutti, A., Dick, F., Sereno, M. I., & Weiskopf, N. (2014). Using high-resolution quantitative mapping of R1 as an index of cortical myelination. NeuroImage, **93**, 176–188. DOI: 10.1016/j.neuroimage.2013.06.005

Lüsebrink, F., Sciarra, A., Mattern, H., Yakupov, R., & Speck, O. (2017). T1-weighted in vivo human whole brain MRI dataset with an ultrahigh isotropic resolution of 250 m. Scientific Data, **4**. DOI: 10.1038/sdata.2017.32

MacEvoy, S. P., Kim, W., & Paradiso, M. A. (1998). Integration of surface information in primary visual cortex. Nature Neuroscience, **1**(7), 616–620. DOI: 10.1038/2849

Mackay, A., Whittall, K., Adler, J., Li, D., Paty, D., & Graeb, D. (1994). In vivo visualization of myelin water in brain by magnetic resonance. Magnetic Resonance in Medicine, **31**(6), 673–677. DOI: 10.1002/mrm.1910310614

Mai, V. G. T. J. K., Paxinos. (2008). *Atlas of the human brain* (3rd, Vol. 3). Elsevier.

Mansfield, P. (1977). Multi-planar image formation using NMR spin echoes. Journal of Physics C: Solid State Physics, **10**(3), L55. DOI: 10.1088/0022-3719/10/3/004

Markello, R. D., Spreng, R. N., Luh, W.-M., Anderson, A. K., & De Rosa, E. (2018). Segregation of the human basal forebrain using resting state functional MRI. NeuroImage, **173**, 287–297. DOI: 10.1016/j.neuroimage.2018.02.042

Marquardt, I., De Weerd, P., Schneider, M., Gulban, O. F., Ivanov, D., Wang, Y., & Uludağ, K. (2020). Feedback contribution to surface motion perception in the human early visual cortex (T. H. Donner, C. Büchel, T. Knapen, & L. Muckli, Eds.). eLife, **9**, e50933. DOI: 10.7554/eLife.50933

Marquardt, I., Schneider, M., Gulban, O. F., Ivanov, D., & Uludağ, K. (2018). Cortical depth profiles of luminance contrast responses in human V1 and V2 using 7 T fMRI. Human Brain Mapping, **39**(7), 2812–2827. DOI: 10.1002/hbm.24042

Marques, J. P., Kober, T., Krueger, G., van der Zwaag, W., Van de Moortele, P.-F., & Gruetter, R. (2010). MP2RAGE, a self bias-field corrected sequence for improved segmentation and T1-mapping at high field. NeuroImage, **49**(2), 1271–1281. DOI: 10.1016/j.neuroimage.2009.10.002

Maton, A. (1993). *Human biology and health*. Englewood Cliffs, N.J. : Prentice Hall. Retrieved October 20, 2022, from http://archive.org/details/humanbiologyheal00scho

Maunsell, J. H., & Essen, D. v. (1983). The connections of the middle temporal visual area (MT) and their relationship to a cortical hierarchy in the macaque monkey. Journal of Neuroscience, **3**(12), 2563–2586. DOI: 10.1523/JNEUROSCI.03-12-02563.1983

McAdams, C. J., & Reid, R. C. (2005). Attention Modulates the Responses of Simple Cells in Monkey Primary Visual Cortex. Journal of Neuroscience, **25**(47), 11023–11033. DOI: 10.1523/JNEUROSCI.2904-05.2005

McAlonan, K., Cavanaugh, J., & Wurtz, R. H. (2008). Guarding the gateway to cortex with attention in visual thalamus. Nature, **456**(7220), 391–394. DOI: 10.1038/nature07382

McCourt, M. E., & Foxe, J. J. (2004). Brightening prospects for early cortical coding of perceived luminance: A high-density electrical mapping study. NeuroReport, **15**(1), 49–56. Retrieved January 25, 2022, from https://journals.lww.com/neuroreport/Fulltext/2004/01190/Brightening_prospects_for_early_cortical_coding_of.11.aspx

McGeer, P. L., McGeer, E. G., Suzuki, J., Dolman, C. E., & Nagai, T. (1984). Aging, Alzheimer's disease, and the cholinergic system of the basal forebrain. Neurology, **34**(6), 741–741. DOI: 10.1212/WNL.34.6.741

McGuire, B. A., Gilbert, C. D., Rivlin, P. K., & Wiesel, T. N. (1991). Targets of horizontal connections in macaque primary visual cortex. Journal of Comparative Neurology, **305**(3), 370–392. DOI: 10.1002/cne.903050303

Mendola, J. D., Conner, I. P., Sharma, S., Bahekar, A., & Lemieux, S. (2006). fMRI Measures of Perceptual Filling-in in the Human Visual Cortex. Journal of Cognitive Neuroscience, **18**(3), 363–375. DOI: 10.1162/089892906775990624

Mesulam, M. M., & Geula, C. (1988). Nucleus basalis (Ch4) and cortical cholinergic innervation in the human brain: Observations based on the distribution of acetylcholinesterase and choline acetyltransferase. The Journal of Comparative Neurology, **275**(2), 216–240. DOI: 10.1002/cne.902750205

Mesulam, M. M., Mufson, E. J., Levey, A. I., & Wainer, B. H. (1983). Cholinergic innervation of cortex by the basal forebrain: Cytochemistry and cortical connections of the septal area, diagonal band nuclei, nucleus basalis (substantia innominata), and hy-

pothalamus in the rhesus monkey. The Journal of Comparative Neurology, **214**(2), 170–197. DOI: 10.1002/cne.902140206

Metere, R., Kober, T., Möller, H. E., & Schäfer, A. (2017). Simultaneous quantitative mri mapping of t1, t2* and magnetic susceptibility with multi-echo mp2rage. PLOS ONE, **12**(1), e0169265. DOI: 10.1371/journal.pone.0169265

Minces, V., Pinto, L., Dan, Y., & Chiba, A. A. (2017). Cholinergic shaping of neural correlations. Proceedings of the National Academy of Sciences, **114**(22), 5725–5730. DOI: 10.1073/pnas.1621493114

Mitsushima, D., Sano, A., & Takahashi, T. (2013). A cholinergic trigger drives learning-induced plasticity at hippocampal synapses. Nature Communications, **4**(1), 2760. DOI: 10.1038/ncomms3760

Moeller, S., Pisharady, P. K., Ramanna, S., Lenglet, C., Wu, X., Dowdle, L., Yacoub, E., Uğurbil, K., & Akçakaya, M. (2021). Noise reduction with distribution corrected (nordic) pca in dmri with complex-valued parameter-free locally low-rank processing. NeuroImage, **226**, 117539. DOI: 10.1016/j.neuroimage.2020.117539

Moeller, S., Yacoub, E., Olman, C. A., Auerbach, E., Strupp, J., Harel, N., & Uğurbil, K. (2010). Multiband multislice GE-EPI at 7 tesla, with 16-fold acceleration using partial parallel imaging with application to high spatial and temporal whole-brain fMRI. Magnetic Resonance in Medicine, **63**(5), 1144–1153. DOI: 10.1002/mrm.22361

Moore, T., & Fallah, M. (2004). Microstimulation of the Frontal Eye Field and Its Effects on Covert Spatial Attention. Journal of Neurophysiology, **91**(1), 152–162. DOI: 10.1152/jn.00741.2002

Moran, J., & Desimone, R. (1985). Selective Attention Gates Visual Processing in the Extrastriate Cortex. Science, **229**(4715), 782–784. DOI: 10.1126/science.4023713

Morikawa, K., & Papathomas, T. V. (2002). Influences of Motion and Depth on Brightness Induction: An Illusory Transparency Effect? Perception, **31**(12), 1449–1457. DOI: 10.1068/p3439

Morris, C. M., Candy, J. M., Oakley, A. E., Bloxham, C. A., & Edwardson, J. A. (1992). Histochemical distribution of non-haem

iron in the human brain. Acta Anatomica, **144**(3), 235–257. DOI: 10.1159/000147312

Motter, B. C. (1993). Focal attention produces spatially selective processing in visual cortical areas V1, V2, and V4 in the presence of competing stimuli. Journal of Neurophysiology, **70**(3), 909–919. DOI: 10.1152/jn.1993.70.3.909

Mouritzen Dam, A. (1979). Shrinkage of the brain during histological procedures with fixation in formaldehyde solutions of different concentrations. Journal Fur Hirnforschung, **20**(2), 115–119.

Mugler, J. P., & Brookeman, J. R. (1991). Rapid three-dimensional T1-weighted MR imaging with the MP-RAGE sequence. Journal of Magnetic Resonance Imaging, **1**(5), 561–567. DOI: 10.1002/jmri.1880010509

Mugler III, J. P., & Brookeman, J. R. (1990). Three-dimensional magnetization-prepared rapid gradient-echo imaging (3D MP RAGE). Magnetic Resonance in Medicine, **15**(1), 152–157. DOI: 10.1002/mrm.1910150117

Möller, H. E., Bossoni, L., Connor, J. R., Crichton, R. R., Does, M. D., Ward, R. J., Zecca, L., Zucca, F. A., & Ronen, I. (2019). Iron, Myelin, and the Brain: Neuroimaging Meets Neurobiology. Trends in Neurosciences, **42**(6), 384–401. DOI: 10.1016/j.tins.2019.03.009

Müller, J. R., Philiastides, M. G., & Newsome, W. T. (2005). Microstimulation of the superior colliculus focuses attention without moving the eyes. Proceedings of the National Academy of Sciences, **102**(3), 524–529. DOI: 10.1073/pnas.0408311101

Müller, M. L. T. M., Bohnen, N. I., Kotagal, V., Scott, P. J. H., Koeppe, R. A., Frey, K. A., & Albin, R. L. (2015). Clinical markers for identifying cholinergic deficits in Parkinson's disease. Movement Disorders, **30**(2), 269–273. DOI: 10.1002/mds.26061

Nagai, T., McGeer, P. L., Peng, J. H., McGeer, E. G., & Dolman, C. E. (1983). Choline acetyltransferase immunohistochemistry in brains of Alzheimer's disease patients and controls. Neuroscience Letters, **36**(2), 195–199. DOI: 10.1016/0304-3940(83)90264-1

Nagai, T., Beer, R. D., Krizay, E. A., & MacLeod, D. I. A. (2011). Spatiotemporal averaging of perceived brightness along an apparent motion trajectory. Journal of Vision, **11**(7), 5. DOI: 10.1167/11.7.5

Nakaizumi, K., Ouchi, Y., Terada, T., Yoshikawa, E., Kakimoto, A., Isobe, T., Bunai, T., Yokokura, M., Suzuki, K., & Magata, Y. (2018). In vivo Depiction of 7 Nicotinic Receptor Loss for Cognitive Decline in Alzheimer' s Disease. Journal of Alzheimer's Disease, **61**(4), 1355–1365. DOI: 10.3233/JAD-170591

Nakano, I., & Hirano, A. (1984). Parkinson's disease: Neuron loss in the nucleus basalis without concomitant Alzheimer's disease. Annals of Neurology, **15**(5), 415–418. DOI: 10.1002/ana.410150503

Naselaris, T., Kay, K. N., Nishimoto, S., & Gallant, J. L. (2011). Encoding and decoding in fMRI. NeuroImage, **56**(2), 400–410. DOI: 10.1016/j.neuroimage.2010.07.073

Nemy, M., Cedres, N., Grothe, M. J., Muehlboeck, J.-S., Lindberg, O., Nedelska, Z., Stepankova, O., Vyslouzilova, L., Eriksdotter, M., Barroso, J., Teipel, S., Westman, E., & Ferreira, D. (2020). Cholinergic white matter pathways make a stronger contribution to attention and memory in normal aging than cerebrovascular health and nucleus basalis of Meynert. NeuroImage, **211**, 116607. DOI: 10.1016/j.neuroimage.2020.116607

Nieoullon, A. (2002). Dopamine and the regulation of cognition and attention. Progress in Neurobiology, **67**(1), 53–83. DOI: 10.1016/S0301-0082(02)00011-4

Oakden, W., Bock, N. A., Al-Ebraheem, A., Farquharson, M. J., & Stanisz, G. J. (2017). Early regional cuprizone-induced demyelination in a rat model revealed with MRI. NMR in Biomedicine, **30**(9), e3743. DOI: 10.1002/nbm.3743

Obermayer, J., Verhoog, M. B., Luchicchi, A., & Mansvelder, H. D. (2017). Cholinergic Modulation of Cortical Microcircuits Is Layer-Specific: Evidence from Rodent, Monkey and Human Brain. Frontiers in Neural Circuits, **11**. DOI: 10.3389/fncir.2017.00100

Ogawa, S, Lee, T. M., Kay, A. R., & Tank, D. W. (1990). Brain magnetic resonance imaging with contrast dependent on blood oxygenation. Proceedings of the National Academy of Sciences of the United States of America, **87**(24), 9868–9872. Retrieved October 20, 2022, from https://www.ncbi.nlm.nih.gov/pmc/articles/PMC55275/

Ogawa, S., & Lee, T.-M. (1990). Magnetic resonance imaging of blood vessels at high fields: In vivo and in vitro measurements and image simulation. Magnetic Resonance in Medicine, **16**(1), 9–18. DOI: 10.1002/mrm.1910160103

Okada, H., Ouchi, Y., Ogawa, M., Futatsubashi, M., Saito, Y., Yoshikawa, E., Terada, T., Oboshi, Y., Tsukada, H., Ueki, T., Watanabe, M., Yamashita, T., & Magata, Y. (2013). Alterations in $\alpha 4\beta 2$ nicotinic receptors in cognitive decline in Alzheimer' s aetiopathology. Brain, **136**(10), 3004–3017. DOI: 10.1093/brain/awt195

Onwuegbuzie, A. J. (2000, November). *Expanding the Framework of Internal and External Validity in Quantitative Research* (tech. rep.). Retrieved November 18, 2022, from https://eric.ed.gov/?id=ED448205

Palombo, M., Ianus, A., Guerreri, M., Nunes, D., Alexander, D. C., Shemesh, N., & Zhang, H. (2020). SANDI: A compartment-based model for non-invasive apparent soma and neurite imaging by diffusion MRI. NeuroImage, **215**, 116835. DOI: 10.1016/j.neuroimage.2020.116835

Parigi, P., Santana, J. J., & Cook, K. S. (2017). Online Field Experiments: Studying Social Interactions in Context. Social Psychology Quarterly, **80**(1), 1–19. DOI: 10.1177/0190272516680842

Pauli, W. M., Nili, A. N., & Tyszka, J. M. (2018). A high-resolution probabilistic in vivo atlas of human subcortical brain nuclei. Scientific Data, **5**(1), 180063. DOI: 10.1038/sdata.2018.63

Pauling, L., & Coryell, C. D. (1936). The Magnetic Properties and Structure of Hemoglobin, Oxyhemoglobin and Carbonmonoxyhemoglobin. Proceedings of the National Academy of Sciences

of the United States of America, **22**(4), 210–216. https://www.ncbi.nlm.nih.gov/pmc/articles/PMC1076743/

Peirce, J. W. (2007). PsychoPy—Psychophysics software in Python. Journal of Neuroscience Methods, **162**(1-2), 8–13. DOI: 10.1016/j.jneumeth.2006.11.017

Peirce, J. W. (2009). Generating Stimuli for Neuroscience Using PsychoPy. Frontiers in Neuroinformatics, **2**. DOI: 10.3389/neuro.11.010.2008

Pereverzeva, M., & Murray, S. O. (2008). Neural activity in human V1 correlates with dynamic lightness induction. Journal of Vision, **8**(15), 8. DOI: 10.1167/8.15.8

Perna, A., Tosetti, M., Montanaro, D., & Morrone, M. C. (2005). Neuronal Mechanisms for Illusory Brightness Perception in Humans. Neuron, **47**(5), 645–651. DOI: 10.1016/j.neuron.2005.07.012

Peters, A. M., Brookes, M. J., Hoogenraad, F. G., Gowland, P. A., Francis, S. T., Morris, P. G., & Bowtell, R. (2007). T2* measurements in human brain at 1.5, 3 and 7 T. Magnetic Resonance Imaging, **25**(6), 748–753. DOI: 10.1016/j.mri.2007.02.014

Petersen, S. E., Robinson, D. L., & Morris, J. D. (1987). Contributions of the pulvinar to visual spatial attention. Neuropsychologia, **25**(1, Part 1), 97–105. DOI: 10.1016/0028-3932(87)90046-7

Picciotto, M. R., Higley, M. J., & Mineur, Y. S. (2012). Acetylcholine as a neuromodulator: Cholinergic signaling shapes nervous system function and behavior. Neuron, **76**(1), 116–129. DOI: 10.1016/j.neuron.2012.08.036

Pinto, L., Goard, M. J., Estandian, D., Xu, M., Kwan, A. C., Lee, S.-H., Harrison, T. C., Feng, G., & Dan, Y. (2013). Fast modulation of visual perception by basal forebrain cholinergic neurons. Nature Neuroscience, **16**(12), 1857–1863. DOI: 10.1038/nn.3552

Poiriehr, F. J. A. M. (2009). The Anderson-Winawer illusion: It' s not occlusion. Attention, Perception, & Psychophysics, **71**(6), 1353–1359. DOI: 10.3758/APP.71.6.1353

Poirier, F. J. A. M., Gosselin, F., & Arguin, M. (2012). Clouds are not normal occluders, and other oddities: More interactions between

textures and lightness illusions. Journal of Vision, **12**(1), 21. DOI: 10.1167/12.1.21

Polimeni, J. R., Fischl, B., Greve, D. N., & Wald, L. L. (2010). Laminar analysis of 7T BOLD using an imposed spatial activation pattern in human V1. NeuroImage, **52**(4), 1334–1346. DOI: 10.1016/j.neuroimage.2010.05.005

Polimeni, J. R., Renvall, V., Zaretskaya, N., & Fischl, B. (2018). Analysis strategies for high-resolution UHF-fMRI data. NeuroImage, **168**, 296–320. DOI: 10.1016/j.neuroimage.2017.04.053

Poser, B. A., Koopmans, P. J., Witzel, T., Wald, L. L., & Barth, M. (2010). Three dimensional echo-planar imaging at 7 Tesla. NeuroImage, **51**(1), 261–266. DOI: 10.1016/j.neuroimage.2010.01.108

Poser, B. A., & Norris, D. G. (2009). Investigating the benefits of multi-echo EPI for fMRI at 7 T. NeuroImage, **45**(4), 1162–1172. DOI: 10.1016/j.neuroimage.2009.01.007

Posse, S., Wiese, S., Gembris, D., Mathiak, K., Kessler, C., Grosse-Ruyken, M.-L., Elghahwagi, B., Richards, T., Dager, S. R., & Kiselev, V. G. (1999). Enhancement of BOLD-contrast sensitivity by single-shot multi-echo functional MR imaging. Magnetic Resonance in Medicine, **42**(1), 87–97. DOI: 10.1002/(SICI)1522-2594(199907)42:1<87::AID-MRM13>3.0.CO;2-O

Pouget, A., & Driver, J. (2000). Relating unilateral neglect to the neural coding of space. Current Opinion in Neurobiology, **10**(2), 242–249. DOI: 10.1016/S0959-4388(00)00077-5

Prasloski, T., Rauscher, A., MacKay, A. L., Hodgson, M., Vavasour, I. M., Laule, C., & Mädler, B. (2012). Rapid whole cerebrum myelin water imaging using a 3D GRASE sequence. NeuroImage, **63**(1), 533–539. DOI: 10.1016/j.neuroimage.2012.06.064

Quester, R., & Schröder, R. (1997). The shrinkage of the human brain stem during formalin fixation and embedding in paraffin. Journal of Neuroscience Methods, **75**(1), 81–89. DOI: 10.1016/S0165-0270(97)00050-2

Rajananda, S., A.K. Peters, M., Lau, H., & Odegaard, B. (2018). Visual psychophysics on the web: Open-access tools, experiments, and

results using online platforms. Journal of Vision, **18**(10), 299. DOI: 10.1167/18.10.299

Reynolds, J. H., Chelazzi, L., & Desimone, R. (1999). Competitive Mechanisms Subserve Attention in Macaque Areas V2 and V4. Journal of Neuroscience, **19**(5), 1736–1753. DOI: 10.1523/JNEUROSCI.19-05-01736.1999

Rinne, J. O., Kaasinen, V., Järvenpää, T., Någren, K., Roivainen, A., Yu, M., Oikonen, V., & Kurki, T. (2003). Brain acetylcholinesterase activity in mild cognitive impairment and early Alzheimer's disease. Journal of Neurology, Neurosurgery, and Psychiatry, **74**(1), 113–115. DOI: 10.1136/jnnp.74.1.113

Roberts, M. J., Zinke, W., Guo, K., Robertson, R., McDonald, J. S., & Thiele, A. (2005). Acetylcholine Dynamically Controls Spatial Integration in Marmoset Primary Visual Cortex. Journal of neurophysiology, **93**(4), 2062–2072. DOI: 10.1152/jn.00911.2004

Roberts, M. J., & Thiele, A. (2008). Spatial integration and its moderation by attention and acetylcholine. Frontiers in Bioscience: A Journal and Virtual Library, **13**, 3742–3759. DOI: 10.2741/2963

Robinson, D. L., & Kertzman, C. (1995). Covert orienting of attention in macaques. III. Contributions of the superior colliculus. Journal of Neurophysiology, **74**(2), 713–721. DOI: 10.1152/jn.1995.74.2.713

Rockland, K. S., & Pandya, D. N. (1979). Laminar origins and terminations of cortical connections of the occipital lobe in the rhesus monkey. Brain Research, **179**(1), 3–20. DOI: 10.1016/0006-8993(79)90485-2

Rodriguez, R., Kallenbach, U., Singer, W., & Munk, M. H. J. (2004). Short- and long-term effects of cholinergic modulation on gamma oscillations and response synchronization in the visual cortex. The Journal of Neuroscience: The Official Journal of the Society for Neuroscience, **24**(46), 10369–10378. DOI: 10.1523/JNEUROSCI.1839-04.2004

Roe, A. W., Lu, H. D., & Hung, C. P. (2005). Cortical processing of a brightness illusion. Proceedings of the National Academy of Sciences, **102**(10), 3869–3874. DOI: 10.1073/pnas.0500097102

Roebroeck, A., Sengupta, S., Bastiani, M., Schillak, S., Tramm, B., Waks, M., Lataster, A., Herrler, A., Tse, D., & Poser, B. High resolution MRI neuroanatomy in whole human brains post mortem with a specialized 9.4T RF-coil [Poster]. In: Toronto, 2015, July. DOI: 10.13140/RG.2.2.21380.07041.

Roelfsema, P. R., Lamme, V. A. F., & Spekreijse, H. (1998). Object-based attention in the primary visual cortex of the macaque monkey. Nature, **395**(6700), 376–381. DOI: 10.1038/26475

Rogers, J. D., Brogan, D., & Mirra, S. S. (1985). The nucleus basalis of Meynert in neurological disease: A quantitative morphological study. Annals of Neurology, **17**(2), 163–170. DOI: https://doi.org/10.1002/ana.410170210

Rooney, W. D., Johnson, G., Li, X., Cohen, E. R., Kim, S.-G., Ugurbil, K., & Springer Jr., C. S. (2007). Magnetic field and tissue dependencies of human brain longitudinal 1H2O relaxation in vivo. Magnetic Resonance in Medicine, **57**(2), 308–318. DOI: 10.1002/mrm.21122

Rossi, A. F., & Paradiso, M. A. (1999). Neural Correlates of Perceived Brightness in the Retina, Lateral Geniculate Nucleus, and Striate Cortex. Journal of Neuroscience, **19**(14), 6145–6156. DOI: 10.1523/JNEUROSCI.19-14-06145.1999

Rossi, A. F., Rittenhouse, C. D., & Paradiso, M. A. (1996). The representation of brightness in primary visual cortex. Science, **273**(5278), 1104–1107. DOI: 10.1126/science.273.5278.1104

Rudd, M. E., & Zemach, I. K. (2007). Contrast polarity and edge integration in achromatic color perception. JOSA A, **24**(8), 2134–2156. DOI: 10.1364/JOSAA.24.002134

Ruff, D. A., Brainard, D. H., & Cohen, M. R. (2018). Neuronal population mechanisms of lightness perception. Journal of Neurophysiology, **120**(5), 2296–2310. DOI: 10.1152/jn.00906.2017

Saalmann, Y. B., Pinsk, M. A., Wang, L., Li, X., & Kastner, S. (2012). The Pulvinar Regulates Information Transmission Between Cortical Areas Based on Attention Demands. Science, **337**(6095), 753–756. DOI: 10.1126/science.1223082

Sabri, O., Becker, G.-A., Meyer, P. M., Hesse, S., Wilke, S., Graef, S., Patt, M., Luthardt, J., Wagenknecht, G., Hoepping, A., Smits, R., Franke, A., Sattler, B., Habermann, B., Neuhaus, P., Fischer, S., Tiepolt, S., Deuther-Conrad, W., Barthel, H., (2015). First-in-human PET quantification study of cerebral 4 2* nicotinic acetylcholine receptors using the novel specific radioligand (−)-[18F]Flubatine. NeuroImage, **118**, 199–208. DOI: 10.1016/j.neuroimage.2015.05.065

Sagi, Y., Tavor, I., Hofstetter, S., Tzur-Moryosef, S., Blumenfeld-Katzir, T., & Assaf, Y. (2012). Learning in the fast lane: New insights into neuroplasticity. Neuron, **73**(6), 1195–1203. DOI: 10.1016/j.neuron.2012.01.025

Salmela, V. R., & Vanni, S. (2013). Brightness and transparency in the early visual cortex. Journal of Vision, **13**(7), 16. DOI: 10.1167/13.7.16

Sara, S. J. (2009). The locus coeruleus and noradrenergic modulation of cognition. Nature Reviews Neuroscience, **10**(3), 211–223. DOI: 10.1038/nrn2573

Saranathan, M., Tourdias, T., Bayram, E., Ghanouni, P., & Rutt, B. K. (2015). Optimization of white-matter-nulled magnetization prepared rapid gradient echo (MP-RAGE) imaging. Magnetic Resonance in Medicine, **73**(5), 1786–1794. DOI: 10.1002/mrm.25298

Sarter, M., Parikh, V., & Howe, W. M. (2009). Phasic acetylcholine release and the volume transmission hypothesis: Time to move on. Nature Reviews Neuroscience, **10**(5), 383–390. DOI: 10.1038/nrn2635

Sasaki, Y., & Watanabe, T. (2004). The primary visual cortex fills in color. Proceedings of the National Academy of Sciences, **101**(52), 18251–18256. DOI: 10.1073/pnas.0406293102

Schafer, R. J., & Moore, T. (2007). Attention Governs Action in the Primate Frontal Eye Field. Neuron, **56**(3), 541–551. DOI: 10.1016/j.neuron.2007.09.029

Schall, J. D. (2004). On the role of frontal eye field in guiding attention and saccades. Vision Research, **44**(12), 1453–1467. DOI: 10.1016/j.visres.2003.10.025

Schenck, J. F., & Zimmerman, E. A. (2004). High-field magnetic resonance imaging of brain iron: Birth of a biomarker? NMR in Biomedicine, **17**(7), 433–445. DOI: 10.1002/nbm.922

Schmierer, K., Tozer, D. J., Scaravilli, F., Altmann, D. R., Barker, G. J., Tofts, P. S., & Miller, D. H. (2007). Quantitative magnetization transfer imaging in postmortem multiple sclerosis brain. Journal of Magnetic Resonance Imaging, **26**(1), 41–51. DOI: 10.1002/jmri.20984

Schmitz, T. W., Mur, M., Aghourian, M., Bedard, M.-A., & Spreng, R. N. (2018). Longitudinal alzheimer' s degeneration reflects the spatial topography of cholinergic basal forebrain projections. Cell Reports, **24**(1), 38–46. DOI: 10.1016/j.celrep.2018.06.001

Schmitz, T. W., & Nathan Spreng, R. (2016). Basal forebrain degeneration precedes and predicts the cortical spread of Alzheimer' s pathology. Nature Communications, **7**(1), 13249. DOI: 10.1038/ncomms13249

Schmitz, T. W., Soreq, H., Poirier, J., & Spreng, R. N. (2020). Longitudinal basal forebrain degeneration interacts with trem2/c3 biomarkers of inflammation in presymptomatic Alzheimer's Disease. Journal of Neuroscience, **40**(9), 1931–1942. DOI: 10.1523/JNEUROSCI.1184-19.2019

Schneider, D., Beste, C., & Wascher, E. (2012). On the time course of bottom-up and top-down processes in selective visual attention: An EEG study. Psychophysiology, **49**(11), 1660–1671. DOI: 10.1111/j.1469-8986.2012.01462.x

Schneider, M. (2019). *Representational content in human cortical systems and visual consciousness* (Doctoral dissertation). Maastricht University. DOI: 10.26481/dis.20191009ms

Schulz, J., Pagano, G., Fernández Bonfante, J. A., Wilson, H., & Politis, M. (2018). Nucleus basalis of Meynert degeneration precedes and predicts cognitive impairment in Parkinson' s disease. Brain, **141**(5), 1501–1516. DOI: 10.1093/brain/awy072

Schwabe, L., Obermayer, K., Angelucci, A., & Bressloff, P. C. (2006). The Role of Feedback in Shaping the Extra-Classical Receptive Field of Cortical Neurons: A Recurrent Network Model. Journal

of Neuroscience, **26**(36), 9117–9129. DOI: 10.1523/JNEUROSCI.1253-06.2006

Sejnowski, T. J., Churchland, P. S., & Movshon, J. A. (2014). Putting big data to good use in neuroscience. Nature Neuroscience, **17**(11), 1440–1441. DOI: 10.1038/nn.3839

Semba, K. The Cholinergic Basal Forebrain: A Critical Role in Cortical Arousal (T. C. Napier, P. W. Kalivas, & I. Hanin, Eds.). en. In: *The Basal Forebrain: Anatomy to Function* (T. C. Napier, P. W. Kalivas, & I. Hanin, Eds.). Ed. by Napier, T. C., Kalivas, P. W., & Hanin, I. Advances in Experimental Medicine and Biology. Boston, MA: Springer US, 1991, pp. 197–218. ISBN: 978-1-4757-0145-6. DOI: 10.1007/978-1-4757-0145-6_10.

Semmelmann, K., & Weigelt, S. (2017). Online psychophysics: Reaction time effects in cognitive experiments. Behavior Research Methods, **49**(4), 1241–1260. DOI: 10.3758/s13428-016-0783-4

Sengupta, S., Fritz, F. J., Harms, R. L., Hildebrand, S., Tse, D. H. Y., Poser, B. A., Goebel, R., & Roebroeck, A. (2018). High resolution anatomical and quantitative MRI of the entire human occipital lobe ex vivo at 9.4T. NeuroImage, **168**, 162–171. DOI: 10.1016/j.neuroimage.2017.03.039

Sereno, M. I., Dale, A. M., Reppas, J. B., Kwong, K. K., Belliveau, J. W., Brady, T. J., Rosen, B. R., & Tootell, R. B. H. (1995). Borders of Multiple Visual Areas in Humans Revealed by Functional Magnetic Resonance Imaging. Science, **268**(5212), 889–893. DOI: 10.1126/science.7754376

Setsompop, K., Gagoski, B. A., Polimeni, J. R., Witzel, T., Wedeen, V. J., & Wald, L. L. (2012). Blipped-controlled aliasing in parallel imaging for simultaneous multislice echo planar imaging with reduced g-factor penalty. Magnetic Resonance in Medicine, **67**(5), 1210–1224. DOI: 10.1002/mrm.23097

Shih, Y.-Y. I., Chen, Y.-Y., Chen, C.-C. V., Chen, J.-C., Chang, C., & Jaw, F.-S. (2008). Whole-brain functional magnetic resonance imaging mapping of acute nociceptive responses induced by formalin in rats using atlas registration-based event-related anal-

ysis. Journal of Neuroscience Research, **86**(8), 1801–1811. DOI: 10.1002/jnr.21638

Shimojo, S., Paradiso, M., & Fujita, I. (2001). What visual perception tells us about mind and brain. Proceedings of the National Academy of Sciences, **98**(22), 12340–12341. DOI: 10.1073/pnas.221383698

Shmuel, A., Yacoub, E., Chaimow, D., Logothetis, N. K., & Ugurbil, K. (2007). Spatio-temporal point-spread function of fMRI signal in human gray matter at 7 Tesla. NeuroImage, **35**(2), 539–552. DOI: 10.1016/j.neuroimage.2006.12.030

Siero, J. C., Petridou, N., Hoogduin, H., Luijten, P. R., & Ramsey, N. F. (2011). Cortical Depth-Dependent Temporal Dynamics of the BOLD Response in the Human Brain. Journal of Cerebral Blood Flow & Metabolism, **31**(10), 1999–2008. DOI: 10.1038/jcbfm.2011.57

Simić, G., Mrzljak, L., Fucić, A., Winblad, B., Lovrić, H., & Kostović, I. (1999). Nucleus subputaminalis (Ayala): The still disregarded magnocellular component of the basal forebrain may be human specific and connected with the cortical speech area. Neuroscience, **89**(1), 73–89. DOI: 10.1016/s0306-4522(98)00304-2

Sitek, K. R., Gulban, O. F., Calabrese, E., Johnson, G. A., Lage-Castellanos, A., Moerel, M., Ghosh, S. S., & De Martino, F. (2019). Mapping the human subcortical auditory system using histology, postmortem MRI and in vivo MRI at 7T (J. E. Peelle, B. G. Shinn-Cunningham, & I. S. Johnsrude, Eds.). eLife, **8**, e48932. DOI: 10.7554/eLife.48932

Sled, J. G. (2018). Modelling and interpretation of magnetization transfer imaging in the brain. NeuroImage, **182**, 128–135. DOI: 10.1016/j.neuroimage.2017.11.065

Smith, S. M. (2002). Fast robust automated brain extraction. Human Brain Mapping, **17**(3), 143–155. DOI: 10.1002/hbm.10062

Solano-Castiella, E., Schäfer, A., Reimer, E., Türke, E., Pröger, T., Lohmann, G., Trampel, R., & Turner, R. (2011). Parcellation of human amygdala in vivo using ultra high field structural MRI.

NeuroImage, **58**(3), 741–748. DOI: 10.1016/j.neuroimage.2011.06.047

Soranzo, A., & Gilchrist, A. (2019). Layer and framework theories of lightness. Attention, Perception, & Psychophysics, **81**(5), 1179–1188. DOI: 10.3758/s13414-019-01736-1

Sprawls Jr, P. Chapter 7 Gradient Echo Imaging Methods. eng. In: In *Magnetic Resonance Imaging Principles, Methods,and Techniques*. Madison, Wisconsin: Medical Physics Publishing Corporation, 2000, July, p. 74. ISBN: 0-944838-97-9. https://open.library.emory.edu/publications/emory\%3As2p3d/

Stenbacka, L., & Vanni, S. (2007). Central luminance flicker can activate peripheral retinotopic representation. NeuroImage, **34**(1), 342–348. DOI: 10.1016/j.neuroimage.2006.08.029

Stüber, C., Morawski, M., Schäfer, A., Labadie, C., Wähnert, M., Leuze, C., Streicher, M., Barapatre, N., Reimann, K., Geyer, S., Spemann, D., & Turner, R. (2014). Myelin and iron concentration in the human brain: A quantitative study of MRI contrast. NeuroImage, **93**, 95–106. DOI: 10.1016/j.neuroimage.2014.02.026

Sweeney, J. C., Webb, D., Mazzarol, T., & Soutar, G. N. (2014). Self-Determination Theory and Word of Mouth about Energy-Saving Behaviors: An Online Experiment. Psychology & Marketing, **31**(9), 698–716. DOI: 10.1002/mar.20729

Tadmor, Y., & Tolhurst, D. J. (2000). Calculating the contrasts that retinal ganglion cells and LGN neurones encounter in natural scenes. Vision Research, **40**(22), 3145–3157. DOI: 10.1016/S0042-6989(00)00166-8

Tagliavini, F., Pilleri, G., Bouras, C., & Constantinidis, J. (1984). The basal nucleus of Meynert in idiopathic Parkinson's disease. Acta Neurologica Scandinavica, **70**(1), 20–28. DOI: 10.1111/j.1600-0404.1984.tb00798.x

Tanaka, K. (1996). Inferotemporal Cortex and Object Vision. Annual Review of Neuroscience, **19**(1), 109–139. DOI: 10.1146/annurev.ne.19.030196.000545

Taragin, M. I. (2019). Learning from negative findings. Israel Journal of Health Policy Research, **8**(1), 38. DOI: 10.1186/s13584-019-0309-5

Taylor, M. M., Sedigh-Sarvestani, M., Vigeland, L., Palmer, L. A., & Contreras, D. (2018). Inhibition in Simple Cell Receptive Fields Is Broad and OFF-Subregion Biased. The Journal of Neuroscience, **38**(3), 595–612. DOI: 10.1523/JNEUROSCI.2099-17.2017

Teipel, Cavedo, E., Grothe, M. J., Lista, S., Galluzzi, S., Colliot, O., Chupin, M., Bakardjian, H., Dormont, D., Dubois, B., Hampel, H., Godefroy, O., Deramond, H., Etcharry Bouyx, F., Pasco Papon, A., Dartigues, J., Allard, M., Rouaud, O., Ricolfi, F., (2016a). Predictors of cognitive decline and treatment response in a clinical trial on suspected prodromal Alzheimer's disease. Neuropharmacology, **108**, 128–135. DOI: 10.1016/j.neuropharm.2016.02.005

Teipel, Cavedo, E., Hampel, H., & Grothe, M. J. (2018). Basal Forebrain Volume, but Not Hippocampal Volume, Is a Predictor of Global Cognitive Decline in Patients With Alzheimer's Disease Treated With Cholinesterase Inhibitors. Frontiers in Neurology, **9**. DOI: 10.3389/fneur.2018.00642

Teipel, Flatz, W., Ackl, N., Grothe, M., Kilimann, I., Bokde, A. L., Grinberg, L., Amaro, E., Kljajevic, V., Alho, E., Knels, C., Ebert, A., Heinsen, H., & Danek, A. (2014a). Brain atrophy in primary progressive aphasia involves the cholinergic basal forebrain and Ayala' s nucleus. Psychiatry research, **221**(3), 187–194. DOI: 10.1016/j.pscychresns.2013.10.003

Teipel, Flatz, W. H., Heinsen, H., Bokde, A. L. W., Schoenberg, S. O., Stöckel, S., Dietrich, O., Reiser, M. F., Möller, H.-J., & Hampel, H. (2005). Measurement of basal forebrain atrophy in Alzheimer's disease using MRI. Brain, **128**(11), 2626–2644. DOI: 10.1093/brain/awh589

Teipel, S., Raiser, T., Riedl, L., Riederer, I., Schroeter, M. L., Bisenius, S., Schneider, A., Kornhuber, J., Fliessbach, K., Spottke, A., Grothe, M. J., Prudlo, J., Kassubek, J., Ludolph, A.,

Landwehrmeyer, B., Straub, S., Otto, M., & Danek, A. (2016b). Atrophy and structural covariance of the cholinergic basal forebrain in primary progressive aphasia. Cortex, **83**, 124–135. DOI: 10.1016/j.cortex.2016.07.004

Teipel, S. J., Heinsen, H., Amaro, E., Grinberg, L. T., Krause, B., & Grothe, M. (2014b). Cholinergic basal forebrain atrophy predicts amyloid burden in Alzheimer' s disease. Neurobiology of aging, **35**(3), 482–491. DOI: 10.1016/j.neurobiolaging.2013.09.029

Teipel, S. J., Meindl, T., Grinberg, L., Grothe, M., Cantero, J. L., Reiser, M. F., Möller, H., Heinsen, H., & Hampel, H. (2011). The cholinergic system in mild cognitive impairment and Alzheimer's disease: An in vivo MRI and DTI study. Human Brain Mapping, **32**(9), 1349–1362. DOI: 10.1002/hbm.21111

Teller, D. Y. (1984). Linking propositions. Vision Research, **24**(10), 1233–1246. DOI: 10.1016/0042-6989(84)90178-0

Thiele, A., & Bellgrove, M. A. (2018). Neuromodulation of Attention. Neuron, **97**(4), 769–785. DOI: 10.1016/j.neuron.2018.01.008

Thomas, B. P., Welch, E. B., Niederhauser, B. D., Whetsell Jr, W. O., Anderson, A. W., Gore, J. C., Avison, M. J., & Creasy, J. L. (2008). High-resolution 7T MRI of the human hippocampus in vivo. Journal of Magnetic Resonance Imaging, **28**(5), 1266–1272. DOI: 10.1002/jmri.21576

Thompson, K. G., Biscoe, K. L., & Sato, T. R. (2005). Neuronal Basis of Covert Spatial Attention in the Frontal Eye Field. Journal of Neuroscience, **25**(41), 9479–9487. DOI: 10.1523/JNEUROSCI.0741-05.2005

Toi, P. T., Jang, H. J., Min, K., Kim, S.-P., Lee, S.-K., Lee, J., Kwag, J., & Park, J.-Y. (2022). In vivo direct imaging of neuronal activity at high temporospatial resolution. Science, **378**(6616), 160–168. DOI: 10.1126/science.abh4340

Tourdias, T., Saranathan, M., Levesque, I. R., Su, J., & Rutt, B. K. (2014). Visualization of intra-thalamic nuclei with optimized white-matter-nulled MPRAGE at 7T. NeuroImage, **84**, 534–545. DOI: 10.1016/j.neuroimage.2013.08.069

Triantafyllou, C., Hoge, R. D., Krueger, G., Wiggins, C. J., Potthast, A., Wiggins, G. C., & Wald, L. L. (2005). Comparison of physiological noise at 1.5 T, 3 T and 7 T and optimization of fMRI acquisition parameters. NeuroImage, **26**(1), 243–250. DOI: 10.1016/j.neuroimage.2005.01.007

Triantafyllou, C., Hoge, R. D., & Wald, L. L. (2006). Effect of spatial smoothing on physiological noise in high-resolution fMRI. NeuroImage, **32**(2), 551–557. DOI: 10.1016/j.neuroimage.2006.04.182

Triantafyllou, C., Polimeni, J. R., & Wald, L. L. (2011). Physiological noise and signal-to-noise ratio in fMRI with multi-channel array coils. NeuroImage, **55**(2), 597–606. DOI: 10.1016/j.neuroimage.2010.11.084

Tsao, D. Y., & Livingstone, M. S. (2008). Mechanisms of Face Perception. Annual Review of Neuroscience, **31**(1), 411–437. DOI: 10.1146/annurev.neuro.30.051606.094238

Tucker, T. R., & Fitzpatrick, D. (2006). Luminance-Evoked Inhibition in Primary Visual Cortex: A Transient Veto of Simultaneous and Ongoing Response. The Journal of Neuroscience, **26**(52), 13537–13547. DOI: 10.1523/JNEUROSCI.3723-06.2006

Ugurbil, K. (2016). What is feasible with imaging human brain function and connectivity using functional magnetic resonance imaging. Philosophical Transactions of the Royal Society B: Biological Sciences, **371**(1705), 20150361. DOI: 10.1098/rstb.2015.0361

Uludağ, K., & Blinder, P. (2018). Linking brain vascular physiology to hemodynamic response in ultra-high field MRI. NeuroImage, **168**, 279–295. DOI: 10.1016/j.neuroimage.2017.02.063

Uludağ, K., Müller-Bierl, B., & Uğurbil, K. (2009). An integrative model for neuronal activity-induced signal changes for gradient and spin echo functional imaging. NeuroImage, **48**(1), 150–165. DOI: 10.1016/j.neuroimage.2009.05.051

Uludağ, K., Uğurbi, K., & Berliner, L. (Eds.). (2005). *Fmri: From nuclear spins to brain functions* (1st ed.). Springer New York, NY. DOI: https://doi.org/10.1007/978-1-4899-7591-1

Uğurbil, K. (2014). Magnetic Resonance Imaging at Ultrahigh Fields. IEEE Transactions on Biomedical Engineering, **61**(5), 1364–1379. DOI: 10.1109/TBME.2014.2313619

Uğurbil, K., Toth, L., & Kim, D.-S. (2003). How accurate is magnetic resonance imaging of brain function? Trends in Neurosciences, **26**(2), 108–114. DOI: 10.1016/S0166-2236(02)00039-5

van Dalen, J. W., Caan, M. W., van Gool, W. A., & Richard, E. (2017). Neuropsychiatric symptoms of cholinergic deficiency occur with degradation of the projections from the nucleus basalis of Meynert. Brain Imaging and Behavior, **11**(6), 1707–1719. DOI: 10.1007/s11682-016-9631-5

Van de Moortele, P.-F., Auerbach, E. J., Olman, C., Yacoub, E., Uğurbil, K., & Moeller, S. (2009). T1 weighted brain images at 7 Tesla unbiased for Proton Density, T2 contrast and RF coil receive B1 sensitivity with simultaneous vessel visualization. NeuroImage, **46**(2), 432–446. DOI: 10.1016/j.neuroimage.2009.02.009

Van de ven, V., Jans, B., Goebel, R., & De Weerd, P. (2012). Early Human Visual Cortex Encodes Surface Brightness Induced by Dynamic Context. Journal of Cognitive Neuroscience, **24**(2), 367–377. DOI: 10.1162/jocn_a_00126

van der Weijden, C. W. J., García, D. V., Borra, R. J. H., Thurner, P., Meilof, J. F., van Laar, P.-J., Dierckx, R. A. J. O., Gutmann, I. W., & de Vries, E. F. J. (2021). Myelin quantification with MRI: A systematic review of accuracy and reproducibility. NeuroImage, **226**, 117561. DOI: 10.1016/j.neuroimage.2020.117561

Vaughan, J., Garwood, M., Collins, C., Liu, W., DelaBarre, L., Adriany, G., Andersen, P., Merkle, H., Goebel, R., Smith, M., & Ugurbil, K. (2001). 7T vs. 4T: RF power, homogeneity, and signal-to-noise comparison in head images. Magnetic Resonance in Medicine, **46**(1), 24–30. DOI: 10.1002/mrm.1156

Verheyen, C., & Göritz, A. S. (2009). Plain texts as an online mood-induction procedure. Social Psychology, **40**, 6–15. DOI: 10.1027/1864-9335.40.1.6

Verma, G., & Balchandani, P. (2019). Ultrahigh field mr neuroimaging. Topics in magnetic resonance imaging : TMRI, **28**(3), 137–144. DOI: 10.1097/RMR.0000000000000210

Vinke, L. N., & Ling, S. (2020). Luminance potentiates human visuocortical responses. Journal of Neurophysiology, **123**(2), 473–483. DOI: 10.1152/jn.00589.2019

Virtanen, P., Gommers, R., Oliphant, T. E., Haberland, M., Reddy, T., Cournapeau, D., Burovski, E., Peterson, P., Weckesser, W., Bright, J., van der Walt, S. J., Brett, M., Wilson, J., Millman, K. J., Mayorov, N., Nelson, A. R. J., Jones, E., Kern, R., Larson, E., (2020). SciPy 1.0: Fundamental algorithms for scientific computing in Python. Nature Methods, **17**(3), 261–272. DOI: 10.1038/s41592-019-0686-2

Vogels, O. J., Broere, C. A., ter Laak, H. J., ten Donkelaar, H. J., Nieuwenhuys, R., & Schulte, B. P. (1990). Cell loss and shrinkage in the nucleus basalis Meynert complex in Alzheimer's disease. Neurobiology of Aging, **11**(1), 3–13. DOI: 10.1016/0197-4580(90)90056-6

Vossel, S., Geng, J. J., & Fink, G. R. (2014). Dorsal and Ventral Attention Systems: Distinct Neural Circuits but Collaborative Roles. The Neuroscientist, **20**(2), 150–159. DOI: 10.1177/1073858413494269

Vovk, A., Cox, R. W., Stare, J., Suput, D., & Saad, Z. S. (2011). Segmentation Priors From Local Image Properties: Without Using Bias Field Correction, Location-based Templates, or Registration. NeuroImage, **55**(1), 142–152. DOI: 10.1016/j.neuroimage.2010.11.082

Vu, A. T., Auerbach, E., Lenglet, C., Moeller, S., Sotiropoulos, S. N., Jbabdi, S., Andersson, J., Yacoub, E., & Ugurbil, K. (2015). High resolution whole brain diffusion imaging at 7T for the Human Connectome Project. NeuroImage, **122**, 318–331. DOI: 10.1016/j.neuroimage.2015.08.004

Wagstyl, K., Larocque, S., Cucurull, G., Lepage, C., Cohen, J. P., Bludau, S., Palomero-Gallagher, N., Lewis, L. B., Funck, T., Spitzer, H., Dickscheid, T., Fletcher, P. C., Romero, A., Zilles,

K., Amunts, K., Bengio, Y., & Evans, A. C. (2020). BigBrain 3D atlas of cortical layers: Cortical and laminar thickness gradients diverge in sensory and motor cortices. PLOS Biology, **18**(4), e3000678. DOI: 10.1371/journal.pbio.3000678

Walter, S., Quigley, C., & Mueller, M. M. (2014). Competitive interactions of attentional resources in early visual cortex during sustained visuospatial attention within or between visual hemifields: Evidence for the different-hemifield advantage. Journal of Cognitive Neuroscience, **26**(5), 938–954. DOI: 10.1162/jocn_a_00547

Wan, L., Huang, H., Schwab, N., Tanner, J., Rajan, A., Lam, N. B., Zaborszky, L., Li, C. R., Price, C. C., & Ding, M. (2018). From eyes-closed to eyes-open: Role of cholinergic projections in EC-to-EO alpha reactivity revealed by combining EEG and MRI. Human Brain Mapping, **40**(2), 566–577. DOI: 10.1002/hbm.24395

Wang, T., Han, Z., Yang, Y., Tian, R., Zhou, W., Ren, P., Wang, P., Zong, J., Hu, Y., & Jiang, Q. (2019). Polygenic Risk Score for Alzheimer' s Disease Is Associated With Ch4 Volume in Normal Subjects. Frontiers in Genetics, **10**. DOI: 10.3389/fgene.2019.00519

Weerd, P. D., Gattass, R., Desimone, R., & Ungerleider, L. G. (1995). Responses of cells in monkey visual cortex during perceptual filling-in of an artificial scotoma. Nature, **377**(6551), 731–734. DOI: 10.1038/377731a0

Wehrl, H. F., Bezrukov, I., Wiehr, S., Lehnhoff, M., Fuchs, K., Mannheim, J. G., Quintanilla-Martinez, L., Kohlhofer, U., Kneilling, M., Pichler, B. J., & Sauter, A. W. (2015). Assessment of murine brain tissue shrinkage caused by different histological fixatives using magnetic resonance and computed tomography imaging. Histology and Histopathology, **30**(5), 601–613. DOI: 10.14670/HH-30.601

Weiskopf, N., Edwards, L. J., Helms, G., Mohammadi, S., & Kirilina, E. (2021). Quantitative magnetic resonance imaging of brain

anatomy and in vivo histology. Nature Reviews Physics, 1–19. DOI: 10.1038/s42254-021-00326-1

Weiskopf, N., Suckling, J., Williams, G., Correia, M. M., Inkster, B., Tait, R., Ooi, C., Bullmore, E. T., & Lutti, A. (2013). Quantitative multi-parameter mapping of R1, PD*, MT, and R2* at 3T: A multi-center validation. Frontiers in Neuroscience, **7**, 95. DOI: 10.3389/fnins.2013.00095

Welvaert, M., & Rosseel, Y. (2013). On the Definition of Signal-To-Noise Ratio and Contrast-To-Noise Ratio for fMRI Data. PLOS ONE, **8**(11), e77089. DOI: 10.1371/journal.pone.0077089

Wen, Q., Kelley, D. A. C., Banerjee, S., Lupo, J. M., Chang, S. M., Xu, D., Hess, C. P., & Nelson, S. J. (2015). Clinically feasible NODDI characterization of glioma using multiband EPI at 7 T. NeuroImage: Clinical, **9**, 291–299. DOI: 10.1016/j.nicl.2015.08.017

West, K. L., Kelm, N. D., Carson, R. P., Gochberg, D. F., Ess, K. C., & Does, M. D. (2018). Myelin volume fraction imaging with MRI. NeuroImage, **182**, 511–521. DOI: 10.1016/j.neuroimage.2016.12.067

Whitehouse, P. J., Price, D. L., Clark, A. W., Coyle, J. T., & DeLong, M. R. (1981). Alzheimer disease: Evidence for selective loss of cholinergic neurons in the nucleus basalis. Annals of Neurology, **10**(2), 122–126. DOI: 10.1002/ana.410100203

Whitehouse, P. J., Hedreen, J. C., White, C. L., & Price, D. L. (1983a). Basal forebrain neurons in the dementia of Parkinson disease. Annals of Neurology, **13**(3), 243–248. DOI: 10.1002/ana.410130304

Whitehouse, P., Parhad, I., Hedreen, J., Clark, A., White, C., Struble, R., & Price, D. (1983b). Integrity of the nucleus basalis of Meynert in normal aging. Neurology, **33**(Suppl. 2), 159.

Whittall, K. P., & MacKay, A. L. (1989). Quantitative interpretation of NMR relaxation data. Journal of Magnetic Resonance (1969), **84**(1), 134–152. DOI: 10.1016/0022-2364(89)90011-5

Wiggins, G. C., Polimeni, J. R., Potthast, A., Schmitt, M., Alagappan, V., & Wald, L. L. (2009). 96-Channel receive-only head coil for 3

Tesla: Design optimization and evaluation. Magnetic Resonance in Medicine, **62**(3), 754–762. DOI: 10.1002/mrm.22028

Winterburn, J. L., Pruessner, J. C., Chavez, S., Schira, M. M., Lobaugh, N. J., Voineskos, A. N., & Chakravarty, M. M. (2013). A novel in vivo atlas of human hippocampal subfields using high-resolution 3t magnetic resonance imaging. NeuroImage, **74**, 254–265. DOI: 10.1016/j.neuroimage.2013.02.003

Wisse, Adler, D. H., Ittyerah, R, Pluta, J. B., Robinson, J. L., Schuck, T, Trojanowski, J. Q., Grossman, M, Detre, J. A., Elliott, M. A., Toledo, J. B., Liu, W, Pickup, S, Das, S. R., Wolk, D. A., & Yushkevich, P. A. (2017). Comparison of In Vivo and Ex Vivo MRI of the Human Hippocampal Formation in the Same Subjects. Cerebral Cortex (New York, NY), **27**(11), 5185–5196. DOI: 10.1093/cercor/bhw299

Wisse, Gerritsen, L., Zwanenburg, J. J. M., Kuijf, H. J., Luijten, P. R., Biessels, G. J., & Geerlings, M. I. (2012). Subfields of the hippocampal formation at 7T MRI: In vivo volumetric assessment. NeuroImage, **61**(4), 1043–1049. DOI: 10.1016/j.neuroimage.2012.03.023

Wisse, Kuijf, H. J., Honingh, A. M., Wang, H., Pluta, J. B., Das, S. R., Wolk, D. A., Zwanenburg, J. J. M., Yushkevich, P. A., & Geerlings, M. I. (2016). Automated Hippocampal Subfield Segmentation at 7T MRI. American Journal of Neuroradiology, **37**(6), 1050–1057. DOI: 10.3174/ajnr.A4659

Wolf, D., Grothe, M., Fischer, F. U., Heinsen, H., Kilimann, I., J., T. S., & Fellgiebel, A. (2014). Association of basal forebrain volumes and cognition in normal aging. Neuropsychologia, **53**, 54–63. DOI: 10.1016/j.neuropsychologia.2013.11.002

Woolrich, M. W., Ripley, B. D., Brady, M., & Smith, S. M. (2001). Temporal Autocorrelation in Univariate Linear Modeling of FMRI Data. NeuroImage, **14**(6), 1370–1386. DOI: 10.1006/nimg.2001.0931

Wu, J., Ishikawa, M., Zhang, J., & Hashimoto, K. (2010). Brain imaging of nicotinic receptors in Alzheimer's disease. International

Journal of Alzheimer's Disease, **2010**, 548913. DOI: 10.4061/2010/548913

Xing, D., Yeh, C.-I., Gordon, J., & Shapley, R. M. (2014). Cortical brightness adaptation when darkness and brightness produce different dynamical states in the visual cortex. Proceedings of the National Academy of Sciences of the United States of America, **111**(3), 1210–1215. DOI: 10.1073/pnas.1314690111

Yacoub, E., Shmuel, A., Pfeuffer, J., Van De Moortele, P.-F., Adriany, G., Andersen, P., Vaughan, J. T., Merkle, H., Ugurbil, K., & Hu, X. (2001). Imaging brain function in humans at 7 Tesla. Magnetic Resonance in Medicine, **45**(4), 588–594. DOI: 10.1002/mrm.1080

Yang, Y., Wang, T., Li, Y., Dai, W., Yang, G., Han, C., Wu, Y., & Xing, D. (2022). Coding strategy for surface luminance switches in the primary visual cortex of the awake monkey. Nature Communications, **13**(1), 286. DOI: 10.1038/s41467-021-27892-3

Yuan, R., Biswal, B. B., & Zaborszky, L. (2019). Functional Subdivisions of Magnocellular Cell Groups in Human Basal Forebrain: Test–Retest Resting-State Study at Ultra-high Field, and Meta-analysis. Cerebral Cortex, **29**(7), 2844–2858. DOI: 10.1093/cercor/bhy150

Yushkevich, P. A., Piven, J., Hazlett, H. C., Smith, R. G., Ho, S., Gee, J. C., & Gerig, G. (2006). User-guided 3D active contour segmentation of anatomical structures: Significantly improved efficiency and reliability. NeuroImage, **31**(3), 1116–1128. DOI: 10.1016/j.neuroimage.2006.01.015

Zaborszky, Hoemke, L., Mohlberg, H., Schleicher, A., Amunts, K., & Zilles, K. (2008). Stereotaxic probabilistic maps of the magnocellular cell groups in human basal forebrain. NeuroImage, **42**(3), 1127–1141. DOI: 10.1016/j.neuroimage.2008.05.055

Zaborszky, Hoemke, L., Mohlberg, H., Schleicher, A., Amunts, K., & Zilles, K. (2019). Probabilistic cytoarchitectonic map of Ch 4 (Basal Forebrain) (v4.2)[Data set]. Human Brain Project Neuroinformatics Platform. DOI: 10.25493/VZJ5-8WJ

Zampetakis, L. A., & Melas, C. (2021). The health belief model predicts vaccination intentions against COVID-19: A survey experiment approach. Applied Psychology: Health and Well-Being, **13**(2), 469–484. DOI: 10.1111/aphw.12262

Zarow, C., Lyness, S. A., Mortimer, J. A., & Chui, H. C. (2003). Neuronal loss is greater in the locus coeruleus than nucleus basalis and substantia nigra in Alzheimer and Parkinson diseases. Archives of Neurology, **60**(3), 337–341. DOI: 10.1001/archneur.60.3.337

Zavagno, D., Daneyko, O., & Liu, Z. (2018). The Influence of Physical Illumination on Lightness Perception in Simultaneous Contrast Displays. i-Perception, **9**(4), 2041669518787212. DOI: 10.1177/2041669518787212

Zhang, H., Trollor, J. N., Wen, W., Zhu, W., Crawford, J. D., Kochan, N. A., Slavin, M. J., Brodaty, H., Reppermund, S., Kang, K., Mather, K. A., & Sachdev, P. S. (2011). Grey matter atrophy of basal forebrain and hippocampus in mild cognitive impairment. Journal of Neurology, Neurosurgery, and Psychiatry, **82**(5), 487–493. DOI: 10.1136/jnnp.2010.217133

Zhou, H., Schafer, R. J., & Desimone, R. (2016). Pulvinar-Cortex Interactions in Vision and Attention. Neuron, **89**(1), 209–220. DOI: 10.1016/j.neuron.2015.11.034

Zinke, W., Roberts, M. J., Guo, K., McDonald, J. S., Robertson, R., & Thiele, A. (2006). Cholinergic modulation of response properties and orientation tuning of neurons in primary visual cortex of anaesthetized Marmoset monkeys. The European journal of neuroscience, **24**(1), 314–328. DOI: 10.1111/j.1460-9568.2006.04882.x

Acknowledgments

This academic journey would not have been possible without the invaluable help and support from many individuals who I hold in high regard.

Peter, I want to express my deep gratitude for many things that you have done for me but four in particular. Firstly, thank you for assembling a professional and supportive supervision team that has been an invaluable resource throughout all of my projects. Whenever I am faced with a challenge or problem, I know that I can turn to someone for guidance and advice. I also enjoy our meetings, where we exchange ideas and work together to make them a reality. Secondly, I also want to thank you for being a role model of a rigorous and critical researcher. Your positive attitude and unwavering support towards the career development of young researchers is truly admirable and has left a lasting impact on me. Thirdly, I would like to thank you for resolving the housing crisis I faced due to the housing agency. Your efforts in providing temporary storage for my furniture, negotiating with the agency, and ultimately helping me find a new place to stay have been a lifesaver. Last but not least, thank you for creating a safe space to communicate thoughts and ideas beyond the confines of academia. Your willingness to listen with an open mind and provide valuable feedback has been invaluable to me, and I am grateful for the time we have spent together.

Mark, I recall the excitement when I received your email about the PhD position and the ambitious plan on investigating the source of attention using 7T (f)MRI. Although the project did not go exactly as planned, I believe we are all pleased with the outcome. Regardless of the setbacks, we are one step closer to solving the puzzle. I have no regrets about my decision, and I hope you feel the same way. I would also like to express my deep gratitude for your inspiration, expertise, support and guidance along the journey, especially in the last months.

Thank you for being there for me and believing in me. I will always be grateful for the positive impact you have had on my life.

Sri, the wiseman! I feel very fortunate to have had you on my supervision team and also as my friend. I want to express my sincere appreciation for the countless hours we spent together on scanning, data analysis, project discussions, and more, especially during the challenging times of the pandemic. Your dedication to our work and other projects and your willingness to share your expertise and insights have been truly inspiring and motivating. Your encouragement has been particularly meaningful during moments of self-doubt, and I am so thankful for your unwavering belief in my abilities. May you continue to thrive in your academic pursuits and achieve all of your goals and dreams.

Minye, my non-official supervisor and friend. My gratitude is beyond words. Your selfless statement of 'I just want to help you' will remain a lasting memory in my heart and mind. Your exceptional critical thinking, your extensive expertise and your generosity in sharing your knowledge and insights have been truly inspiring. Your ability to excel in both science and art is truly admirable. I am also deeply thankful for your warm hospitality, the numerous insightful discussions we've had, and the memorable trips we've taken together. I am confident that you will continue to make remarkable contributions to your field and achieve great success in all aspects of your life. May our path cross again in the future.

Federico, it has been an amazing experience working with you for some time. During this period, I have not only gained valuable knowledge for my projects but also for my personal life. Your approach towards 'closure' in research has been a great source of inspiration for me. Your dedication and enthusiasm towards research and life have been truly motivating and encouraging. I also want to express my sincere gratitude to you and **Michelle** for offering me a place to stay when I was in need. I am forever thankful for your kindness and generosity. Wishing you all the best in your future endeavors, and I hope our paths cross again someday.

Marian and **Ingo**, thanks for bringing so many sparkles in my Maastricht life and being such a good friend. I struggle to find the right words to convey just how grateful and happy I am. Despite all the support and good times together, thanks to you, I have begun to introspect and reconsider some of the values and ideas that I previously held as absolute truth. Additionally, your presence has helped me realize the significance of certain things that I may have otherwise overlooked. I am constantly inspired and encouraged by the friendship between you two and together with **Faruk**. You all have shown me different aspects of a true friendship. I am grateful that **Faruk** continues his career in Maastricht at the moment, which 'unexpectedly' benefits me (thank you for all the support and wisdom imparted). That moment when you said 'Better to be lost and moving than to be stagnant and still' has stayed with me ever since. It was a simple but powerful reminder. But beyond that, I also hold deep gratitude for all the tasty food you shared with me over the years. Thank you all for being a part of this experience with me and for making it all more enjoyable and meaningful. Here's to future reunions filled with laughter and joy!

Linda, I remember my first day in the office when you told me all these useful tips on how I could quickly settle down in this city. I also remember how you opened your home for me when you found out that I had missed the train after the boat party. And there was another time when you magically found my bike on a dark night, even though I had given you the wrong information. There are many many things happened along the way and I guess this is how our friendship grow and strengthened. I am so grateful and fortunate to have such an amazing friend and will cherish it forever. **Geraldine**, I appreciate the time we spent together during my first year in Maastricht, and I'm thankful that our friendship has endured even after you graduated. The cards you sent, the gifts you gave, and the spicy snacks you brought along made me feel pampered like a little sister. I am amazed by your extensive network in the city and inspired by your optimistic attitude towards life. **Miriam**, your company at our office and on Zoom has meant a lot to me. Thank you for being there for me during moments

of self-doubt and always having an open ear. I feel fortunate to have you with me during the second half of this PhD. I am grateful to this small office for introducing me to these amazing women and creating memorable experiences together. I hope that the positive energy of our office continues to attract new people and the magic of our time together is passed on to them.

Manli, the one shining with the brilliance of insight. I am grateful to have you as my friend, and such an honest one. You are sensible, steady, decisive and caring. Your way of approaching the world and those around you with logic and passion is very admirable. Thank you for all the support and wonderful time along the way. **Qian**, I feel thankful that Maastricht has brought such a wonderful friend into my life. There might be some cosmic connection brought us together to the same flight (together with **Huahua**). I recall the early days when we were attempting to find our way around the city as well as getting to know each other. As we got to know each other, we realized how much we had in common, and how easy it was to talk to each other. The city brought us together, but it's our friendship that has made my life so much richer and fulfilling. I'm grateful for the experiences we've shared, the laughs we've had, and the lessons we've learned together. **Luotong**, I am grateful that life gave me a new friend in the very last moments of this journey. Your encouragement and kindness have been a source of comfort and strength during difficult times, and I'm truly grateful for your presence in my life.

A big thank you to all of my CN/FPN friends and colleagues for creating such a welcoming and supportive environment. Some of them are associated with the **Lunch group** or the **Layer seminar**, or both. Those people gave me so much laugh, inspiration and motivation along the way. **Fabian**, the daily lunch alarm, known as 'statistics and excel wiz'. Thank you for all the hallway talk, fun moments, voluntarily participating all my projects (same gratitude also goes to **Deni**) and creating such wonderful images for the country. I am still wondering how you make that shining blue drink. **Marta**, looking back on my first year

in Maastricht, I am glad to have had you round. Thanks for making the transition to this new environment much smoother for me. Our connection became closer through **Minye**, and I am grateful for the bond that we share. **Alix**, I really enjoyed our conversation with you and **Bob** at the boat party when I first arrived in Maastricht. Talking to you always gave me a boost of energy. With your passion and enthusiasm, there's no doubt that you will excel in anything you set your mind to. **Alicia**, I am grateful for the many times you have assisted me with testing my eye-tracking experiments. Thank you for all the wonderful moments we shared during our time together. **Chen**, it is great to know you at the last moments of my maastricht life. Thank you so much for coming all the way to participate in the study. And also thanks for many pleasant conversations and help when I am in need. I also want to express my special gratitude to **Renzo**, **Vincent**, **Selma**, **Hannah**, **Alex Kroner**, **Alexandra K. Emmendorfer**, **Mario E. Archila-Melendez**, **Deni**, **Vaish**, **Amaia**, **Shruti**, **Anita**, **Laurien**, **Shanice**, **Kirsten**, **Mario Senden**, **Arko**, **Andreas**, **Salil**, **Niels**, and **Sven**, for your insightful contributions, cheerful greetings in the corridors and wonderful lunch time. I see the **Layer seminar** as the seed/development of science and feel the passion, sense, creativity and critical-thinking within it. **Renzo**, **Faruk**, **Miriam**, **Sebastian**, **Lonike**, **Alessandra**, **Johannes**, **Kenshu** and all the new members, thank you all for creating such a wonderful atmosphere together. During times when I was struggling with negative experiences, it was a source of motivation to remember the original reason why I chose research. Let the fire of scientific innovation and progress burn on, fueled by the curiosity and dedication of those who seek to expand our understanding of the world.

Christl, **José**, **Eva**, **Riny** and **Andra**, I am very grateful for your support and assistance in many occasions, which makes my life a lot easier.

My genuine thanks also go to my old fellas. **Feng zi**, having you in my life has been an absolute delight and a true blessing. It's incredible

how time flies; it seems like only yesterday that we first met during our early days at university, and yet here we are, nearly 14 years later, still sharing a special bond that has only grown stronger with time. It's remarkable to consider how many things could have turned out differently without your influence. Thank you for being the amazing person that you are, and for making such a positive impact on my life. Sister **Ding Cui**, as my friend and mentor, you've been there for me through thick and thin, offering guidance, support, and encouragement every step of the way. Your unwavering resilience and determination make you a true embodiment of 'The Invincible Jack Bauer'. Witnessing your unrelenting pursuit of your goals has been a constant source of inspiration and motivation for me. Take very good care! Sister **Liqin**, despite being on different continents, we communicate as if we are in the same time zone. The comfort and ease I feel in our friendship is something that I hold dear to my heart. In a world that can sometimes feel chaotic and overwhelming, it is a true blessing to have someone like you in my life. The fond memories of us enjoying rice noodles together on the second floor still remain fresh in my mind. You are the one who has earned my utmost respect when it comes to handling spicy food. We should do it again! May all your worries fade away and happiness be the only path ahead of you. **Baoge**, I have graduated, finally! When the night is dark and quiet across Asia and Europe, there are still you and **Feng zi** in the states keeping me company, and offering your advice and support. Thanks for having faith in my abilities. I will always cherish the memories we've shared together. Wishing you both all the best as you continue your (academic) pursuits in Beijing, and may your endeavors be filled with innovation and breakthroughs.

在这里，也要感谢**爸妈**一直以来的关心与支持！有人说，到不了的地方是远方，回不去的世界叫做家乡。于我来说，你们所在的那片土地才是家乡。疫情之下，自从上次一别，已有数年，即使在当今网络十分发达的时代，也是很久了。离家十余载，我以为你们早已习惯了我长期不在家的时光，却未想到这种思念会随着岁月的沉淀愈加深刻。如今，已过而立之年的我，虽然依然青涩，但还是想带你们来看这数年里我看到的、感受到的世界，就像你们曾经在我牙牙学语之际带我走进这个世

界一样。还要感谢国内所有的亲人、好友，在这期间对我以及家里的关心与关照。无论是在远方还是在家乡，希望我们都可以在未来的某一天重新相遇。

Onne, my love and my best friend, thank you for all your sparkles and support. You often mention how fortunate I am, but I know the real luck is having you in my life. You are amazingly gifted to uplift my spirit when I was down, and inspire me when I feel lost. Words cannot do justice to how much I cherish everything you do. You are truly a wonderful surprise that life has given me. I cannot wait to see what the future holds for us!

Yawen Wang
Maastricht
28-06-2023

List of Publications

Peer-reviewed publications

Wang, Y., Zhan, M., Roebroeck, A., De Weerd, P., Kashyap S., Roberts, M.J. (2022). Inconsistencies in atlas-based volumetric measures of the human nucleus basalis of Meynert: A need for high-resolution alternatives. *NeuroImage*, 119421.

Marquardt, I., De Weerd, P., Schneider, M., Gulban, O. F., Ivanov, D., Wang, Y., Uludağ, K. (2020). Feedback contribution to surface motion perception in the human early visual cortex. *eLife*, 9, e50933.

Manuscripts in preparation

Wang, Y., Kashyap S., Zhan, M., Roberts, M.J., De Weerd, P. (in preparation). Cortical responses to illusory surface brightness perception at 7T fMRI.

Wang, Y., Maiocchi C., Kazan C., De Weerd, P., Roberts, M.J. (in preparation). Developing a novel stimulus for brightness illusion using online psychophysics.

Conference contributions

Wang, Y., Kashyap, S., Zhan, M., Roberts, M. J., De Weerd, P. (2021). Poster: Neural responses of illusory surface brightness perception at 7T fMRI. In the 27th Annual Meeting of OHBM (Virtual).

About the author

Yawen Wang was born on January 13^{th} 1993 in bayannur, China. She graduated from high school at Fendou Middle School in 2009 and then pursued a Bachelor's degree in Veterinary Medicine at Northwest A&F University from 2009 to 2014. During her undergraduate studies, she participated in an exchange program on animal husbandry and wine-making at the University of Western Australia.

Following her undergraduate degree, she enrolled in a master program in Neuroscience and Neuroimaging at Sino-Danish Center from 2014 to 2017. Under the supervision of Prof. Rong Xue, Dr. Zuxiang Liu and Dr. Christopher Bailey, she investigated behavioral differences of zebrafish larva with laser lesion and modelled the motion of larva using machine learning algorithms. She obtained double degree of Master of Science in Neuroscience & Neuroimaging from Aarhus University and Master of Neurobiology from Unviersity of Chinese Academy of Sciences.

In October 2017, she continued her scientific journey as a PhD candidate at the department of Cognitive Neuroscience in Maastricht University. Her research focused on attention and perception using 7T (f)MRI under the supervision of Prof. Peter De Weerd, Dr. Mark J Roberts, and Dr. Sriranga Kashyap. Upon completion of her PhD, she continues to pursue her interests in multidisciplinary science.